UNIVERSITÄT ZU LÜBECK

From the Institute for Experimental and Clinical

Pharmacology and Toxicology

of the University of Lübeck

"The NF-kappa-B essential modulator (NEMO) is crucial for the functionality of brain endothelial properties."

Dissertation

for Fulfillment of

Requirements

for the Doctoral Degree

of the University of Lübeck

from the Department of Natural Sciences

Submitted by

Josephine Lampe

from Parchim (Germany)

Lübeck 2021

First referee:	Prof. Dr. Markus Schwaninger
Second referee:	Prof. Dr. Kristina Kusche-Vihrog
Date of oral examination:	20.04.2022
Approved for printing:	26.04.2022

Table of contents

List of figures

List of tables

Abbreviations

ABC	ATP binding cassette
ABIN	A20-binding inhibitor of NF-kappa-B activation
AD	Alzheimer's disease
AJ	Adherens junctions
Ang	Angiopoietin
AIF	Apoptosis-inducing factor
ATP	Adenosine triphosphate
BBB	Blood-brain barrier
Bcl-2	B-cell lymphoma 2
BEC	Brain endothelial cell
beKO (e.g. *Nemo*^{beKO})	Brain endothelial knockout
BSA	Bovine serum albumin
Casp	Caspase
ca (e.g. *IKK2*^{ca})	Constitutively active
CD (e.g. CD31)	Cluster of differentiation
cIAP	Cellular inhibitors of apoptosis
CNS	Central nervous system
Coll IV	Collagen IV
Cre	Cyclisation recombinase
CreER^{T2}	Cre fused to a mutant estrogen ligand-binding domain (ERctT2)
cSVD	Cerebral small vessel disease
Ct	Cycle threshold
Cy (e.g. Cy3)	Cyanine
DAPI	4′,6-diamidino-2-phenylindole
DEPC	Diethyl pyrocarbonate
DHA	Docosahexaenoic acid
DMSO	Dimethyl sulfoxide
dUTP	Deoxyuridine triphosphate
ECL	Extracellular loops
ERG	ETS-related gene
ESCRT	Endosomal sorting complexes required for transport
ETS	Erythroblast transformation-specific
FADD	Fas-associated protein with death domain
FasL	Fas ligand
FasR	Fas receptor

Fc	Fragment crystallizable
FcR_n	Neonatal Fc receptor
FDR	False discovery rate
FITC	Fluorescein isothiocyanate
fl (e.g. *$Nemo^{fl}$*)	Floxed
GFAP	Glial fibrillary acidic protein
GLUT1	Facilitated glucose transporter member 1
GSH	Glutathione
GTPase	Guanosine triphosphate hydrolase
HRP	Horseradish peroxidase
i. p.	Intraperitoneal
i. v.	Intravenous
Iba1	Ionized calcium-binding adaptor molecule 1
IgG	Immunoglobulin G
IHC	Immunohistochemistry
IκB-α	Nuclear factor of kappa light polypeptide gene enhancer in B-cells inhibitor alpha
IKK	IκB kinase
IL (e.g Il1b)	Interleukin
IP	Incontinentia pigmenti
JAM	Junctional adhesion molecules
Ki67	Kiel67
LAMP2	Lysosome-associated membrane protein 2
LRP	Low-density lipoprotein receptor-related protein
LUBAC	Linear ubiquitin assembly complex
MAGUK	Membrane-associated guanylate kinases
MCAO	Middle cerebral artery occlusion
MCT	Monocarboxylate transporter
MDR	Multidrug resistance protein
Mfsd2a	Major facilitator superfamily domain containing 2A protein
MLKL	Mixed lineage kinase domain-like protein
MMP	Matrix metalloproteinase
M^{pro}	Main protease
MRP	Multidrug resistance-related protein
N-CAM	Neural cell adhesion molecule
Nec	Necrostatin
NEMO	NF-κB essential modulator

NF-κB	Nuclear factor “kappa-light-chain-enhancer” of activated B-cells
p- (e.g. pMLKL)	Phospho-
p. i.	Post-injection
PBS	Phosphate-buffered saline
PCA	Principal component analysis
PDGFβ	Platelet-derived growth factor β
PDGFRβ	PDGFβ receptor
PFA	Paraformaldehyde
P-gp	P-glycoprotein
qPCR	Quantitative polymerase chain reaction
Rab	Ras-related protein
RACK	Receptor for activated C kinase
RhoA	Ras homolog family member A
RIPK	Receptor-interacting serine/threonine-protein kinase
RT	Room temperature
SAH	Subarachnoid haemorrhage
SARS-CoV-2	Severe acute respiratory syndrome coronavirus type 2
SDS	Sodium dodecyl sulphate
SEM	Standard error of the mean
Slco1c1	Solute carrier organic anion transporter family member 1C1
Slcert	Slco1c1-CreER^{T2}
SMA	Smooth muscle actin
STED	Stimulated emission depletion
TAB	TAK1-binding protein
TAE	Tris base, acetic acid and EDTA
Tak1	Transforming growth factor beta-activated kinase 1
TEMED	N,N,N',N'-Tetramethylethylendiamine
TfR	Transferrin receptor
TGFβ	Transforming growth factor β
TGFβR	TGFβ receptor
Tie	Tyrosine-protein kinase receptor 2
TJ	Tight junctions
TNF	Tumour necrosis factor
TNFR1	TNF receptor 1
TRADD	TNFR1-associated death domain protein
TRAF2	TNFR-associated factor 2

TUNEL	Terminal deoxynucleotidyl transferase-mediated dUTP-biotin nick end labelling
UBAN	Ubiquitin binding domain in ABIN proteins and NEMO
VEGF	Vascular endothelial growth factor
Wnt	Portmanteau of “Wingless” and “Int-1”
ZO	Zonula occludens

Abstract

NF-κB is a transcription factor present in all cell types of the body and is involved in various essential processes, such as immunity and cell proliferation. The NF-κB essential modulator (NEMO) is a subunit of the IκB kinase complex, and a crucial factor for activating NF-κB. Genetic inactivation of *IKBKG*, the gene which is encoding NEMO, or NEMO cleavage in brain endothelial cells cause severe vascular defects in the cerebral small vessel disease Incontinentia pigmenti and COVID-19. A brain endothelial-specific conditional knockout of *Ikbkg* (*Nemo^{beKO}*) in mice has been used to investigate the underlying mechanisms. Thus, vessel rarefaction, increased occurrence of so-called string vessels and massive blood-brain barrier leakage have been detected in former studies.

This study indicates that string vessels are remnants from dead vessels and are primarily localised in higher branch orders of the vascular tree, where they reflect the ablation of capillaries. Since previous reports showed NEMO ablation associated with TNF-induced apoptosis or necroptosis, we considered deletion and inhibition of cell death executioners, such as RIPK1, RIPK3, and FADD. Thus, we aimed to prevent the neurological pathology caused by the absence of endothelial NEMO. Interestingly, only the ubiquitous knockout of *Ripk3 (Ripk3$^{-/-}$)* could rescue the vascular defects detected in *Nemo^{beKO}* mice shortly after knockout induction. In addition, we observed less brain parenchymal extravasation for specific molecules than in *Nemo^{beKO}* mice. The remaining blood-brain barrier defects were not arising from endothelial tight junction interruptions, but instead, we detected impaired transcytosis in the endothelium.

Moreover, increased angiogenesis due to the absence of NEMO is only partially improved by the ablation of RIPK3, suggesting a RIPK3-independent effect of NEMO on brain endothelial transcytosis and angiogenesis. Notably, little is known about the mechanisms leading to restricted brain endothelial transcytosis in the healthy brain and transcytotic changes in several neurological diseases. Thus, the NF-κB pathway might be an attractive target for future investigations on brain endothelial transcytosis.

However, our long-term studies showed that the *Ripk3* knockout could not prevent the *Nemo^{beKO}* phenotype at later stages, possibly due to RIPK1-induced apoptosis. To date, it is unknown if the initial attenuation of the phenotype is sufficient to prevent neurological symptoms, such as seizures. Additional investigations on this issue and further characterisation of cell death induced by NEMO ablation might help develop a pharmacological intervention to treat Incontinentia pigmenti- and COVID-19-induced brain pathology.

Zusammenfassung

NF-κB ist ein Transkriptionsfaktor, der in allen Körperzellen exprimiert wird und in verschiedenen Prozessen, wie Immunität und Zellproliferation, involviert ist. Der NF-κB essentielle Modulator (NEMO) ist Bestandteil des IκB Komplexes und essentiell für die NF-κB induzierte Genexpression. Genetische Inaktivierung oder Spaltung des NEMO-Proteins in Gehirnendothelzellen kann zu schweren vaskulären Defekten führen, wie sie für zerebrale Mikroangiopathien des Syndroms Incontinentia pigmenti und für COVID-19 gezeigt wurden. Um zugrunde liegende Mechanismen zu untersuchen, wurde ein Mausmodell genutzt, in dem *Ikbkg,* das für NEMO codierende Gen, spezifisch in Gehirnendothelzellen mittels eines konditionalen Knockouts deletiert werden kann. In früheren Studien konnte damit gezeigt werden, dass NEMO-Defizienz mit einer geringeren Gefäßdichte, einem erhöhten Vorkommen sogenannter „string vessels“ und einer massiven Störung der Bluthirnschranke einhergeht.

Die Ergebnisse dieser Studie weisen darauf hin, dass „string vessels“ Rudimente toter Gefäße darstellen und vor allem in den höher verzweigten Kapillaren des Gefäßbaums vorkommen. Somit nimmt die Anzahl kleinerer Gefäße in den Gehirnen von *Nemo*^{beKO} Tieren ab. Da vorherige Studien zeigen konnten, dass die Deletion von NEMO mit TNF-induzierter Apoptose und Nekroptose assoziiert ist, haben wir in dieser Studie Auswirkungen der Deletion oder Inhibierung von Proteinen untersucht, die für die Ausführung des Zelltods und nachfolgenden Neuropathologien essentiell sind. Zu diesen Proteinen gehören RIPK1, RIPK3 und FADD. Interessanterweise war es nur durch den ubiquitären Knockout von RIPK3 möglich, den vaskulären Defekten der *Nemo*^{beKO} Tiere kurz nach der Induktion des Knockouts vorzubeugen. Zusätzlich wiesen diese Tiere eine geringere Extravasation für bestimmte Moleküle in das Gehirnparenchym auf als die *Nemo*^{beKO} Mäuse. Der verbleibende Defekt der Bluthirnschranke konnte nicht auf Unterbrechungen der endothelialen Tight-Junction Struktur zurückgeführt werden, jedoch wurde eine gestörte endotheliale Transzytose festgestellt.

Des Weiteren konnte die durch die *Ikbkg*-Deletion bedingte Aktivierung von Angiogenese nur partiell durch die RIPK3-Defizienz vermindert werden, weswegen wir einen RIPK3-unabhängigen Effekt von NEMO auf die Transzytose und Angiogenese im Hirnendothel vermuten. Es sei dabei erwähnt, dass bislang wenig über die Mechanismen bekannt ist, die zu einer starken Limitation der Transzytose im Gehirnendothel des gesunden Gehirns und zu Störungen der Transzytose in zahlreichen neurologischen Erkrankungen führen. Deshalb stellt der NF-κB Signalweg ein interessantes Ziel für zukünftige Untersuchungen hinsichtlich der Transzytose in Gehirnendothelzellen dar.

Nachfolgende Langzeitstudien zeigten, dass der *Ripk3*-Knockout den vaskulären Defekten nicht nachhaltig vorbeugen kann, sondern eher zu einer Verzögerung des Phänotyps der *Nemo*^{beKO} Mäuse führt. Wir vermuten, dass RIPK1-induzierte Apoptose in der verzögerten Ausbildung der vaskulären Defekte eine Rolle spielen könnte. Derzeitig ist nicht bekannt, ob das verzögerte Auftreten des Phänotyps ausreichend für die Verhinderung neurologischer Symptome wie zum Beispiel epileptischer Anfälle ist. Zusätzliche Untersuchungen diesbezüglich und eine weitere Charakterisierung des durch NEMO-Defizienz ausgelösten Zelltodes könnte bei der Entwicklung pharmakologischer Interventionen zur Behandlung neurologischer Pathologien bei Incontinentia pigmenti und COVID-19 helfen.

1. Introduction

1.1. Structure and pivotal functions of the blood-brain barrier (BBB)

The brain has to fulfil enormous computational functions and thus, consumes energy sufficient to power a 20-W-light bulb (Ková, 2010). Therefore, it utilizes 20 % of the cardiac output, although it only accounts for 2 % of the body weight (Clarke & Sokoloff, 1999). Within the brain tissue, a dense vascular network guarantees efficient and flexible distribution of nutrients and oxygen. Indeed, it is assumed that every neuron is supplied by its own capillary (Pardridge, 2002). Neuronal tissue is very sensitive to ionic changes, pathogens and toxins, and hence, requires a highly selective semipermeable membrane barrier between blood circulation and brain parenchyma to ensure regulated homeostasis. This so-called blood-brain barrier (BBB) is predominantly formed by highly specialized endothelial cells. In contrast to other endothelial cells of the body, a minimal paracellular and transcellular transport resulting from a unique expression of tight junctions (TJ) and transporters characterises the brain endothelium.

1.1.1. The cellular structure of the BBB

Although the BBB is mainly formed by endothelial cells, it is well known that other cells and structures are also crucial for a functional BBB (Figure 1). In accordance, Kutuzov et al. have coined the term “tripartite” BBB consisting of the endothelium, the extravascular compartment and, in addition, the glycocalyx (Kutuzov et al., 2018). The glycocalyx is formed by a gel-like layer of various sugars attached to the proteins and lipids of the luminal side of endothelial cells. This layer coats approximately 40 % of the surface of cerebral capillaries (Ando et al., 2018; Möckl, 2020). It is assumed that it represents the first barrier limiting the transport of macromolecules towards the brain parenchyma (Ando et al., 2018; Kutuzov et al., 2018; J. Zhu et al., 2018). The next barrier is characterised by the endothelial expression of various adherens junctions (AJ) and TJ, excluding fenestrations and thus restricting paracellular transport. Moreover, the transcellular transport of the brain endothelium is limited by low transcytosis rates and specialized transporters that deliver only selected molecules through the BBB and exclude many others. Brain endothelial cells (BEC) are in close contact with pericytes wrapped around the abluminal side and embedded in the same basement membrane. For endothelial-pericyte signalling, gap junctions, adhesion plaques and “peg-socket” junctions serve as exchanging platforms (Caruso et al., 2009; Fujimoto, 1995; Larson et al., 1987). Reciprocal signalling between both cell types contributes to various processes such as angiogenesis, TJ formation, and transendothelial trafficking (Daneman et al., 2010; Teichert et al., 2017; Villaseñor, Kuennecke, et al., 2017). In addition, pericytes are described as contractile cells essential for regulating the cerebral blood flow according to the neurons' need for oxygen and glucose, also known as functional hyperemia (Hall et al., 2014; Iadecola, 2004).

Further outside, astrocytic processes surround the complex of endothelial cells, pericytes and basement membrane. Astrocytes possess various functions, such as a supportive role for neuronal tissue, and they contribute to tissue repair and scar formation in inflammatory or ischemic conditions (Kimelberg & Nedergaard, 2010; Sofroniew, 2015). Further, they mediate functional hyperemia by transmitting neuronal signals to the vasculature (Attwell et al., 2010). Like pericytes, astrocytes are also considered to mediate the permeability of the BBB by initiating TJ biogenesis and endothelium angiogenesis (Arthur et al., 1987; Salhia et al., 2000).

Some investigators also include microglia as a component of the BBB, even if it is not clear if microglia contributes to BBB regulation in the healthy state. Microglia in inflammatory conditions can migrate to the cerebral vasculature and mediate paracellular transport (Haruwaka et al., 2019; Mehrabadi et al., 2017).

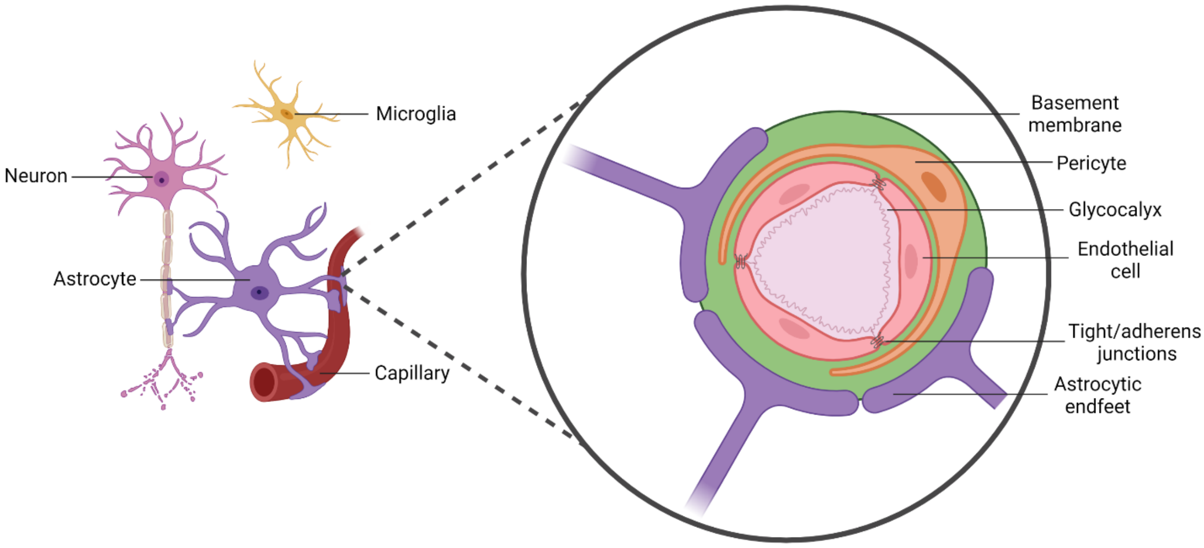

Figure 1: Cellular structure of the BBB. *The first barrier limiting extravasation from the blood vessels to the brain parenchyma is the glycocalyx formed by BEC. Endothelial TJ and AJ limit paracellular transport. The endothelium is embedded by a basement membrane which is also enwrapping pericytes. Astrocytic endfeet are in contact with the BBB and mediate communication between BECs and neurons. The role of microglial cells for the BBB is still under debate. The figure was created with BioRender.*

1.1.2. The molecular structure of the BBB

Paracellular transport

Paracellular transport is restricted by AJ and TJ, which are apical intercellular junctional complexes, visualized as “kissing points” or branching fibrils of various lengths (Kniesel & Wolburg, 2000). By using freeze-fracturing and ultrathin sections in electron microscopy techniques, it has been shown that TJ consist of transmembrane, cytoplasmatic scaffolding and associated proteins (Kniesel & Wolburg, 2000; Luissint et al., 2012). By forming dimers with the TJ of adjacent endothelial cells, they fulfil three main functions: Restricting paracellular transport of blood-borne substances to the brain parenchyma, maintaining endothelial polarity, and forming a signalling platform for intra- and extracellular signals (Luissint et al., 2012; Zihni et al., 2016).

The essential transmembrane proteins regulating the paracellular transport at the BBB are claudin-5 and occludin. Despite, other TJ proteins such as claudin-3 or claudin-12 were detected at the BBB, but their function for limiting the paracellular transport is disputed (Castro Dias, Coisne, Baden, et al., 2019; Castro Dias, Coisne, Lazarevic, et al., 2019). Claudin-5 and other claudins consist of four transmembrane domains, an intracellular NH2 terminus, a long COOH terminus, a short intracellular loop and two extracellular loops (ECL), in which the first extracellular loop (ECL1) held the critical function for the TJ sealing properties (Greene et al., 2019). Claudin-5 restricts the paracellular transport of molecules smaller than 800 Da and leads to a transendothelial electrical resistance up to 1500 Ωcm^2 in BBB vessels of rats (Butt et al., 1990; Nitta et al., 2003). The deficiency of claudin-5 is lethal within 10 days after birth, while its downregulated expression and dysfunction are involved in severe neurological pathologies such as multiple sclerosis, stroke, epilepsy or various psychiatric disorders (Greene et al., 2019; Nitta et al., 2003).

In contrast to claudin-5 deficient mice, the loss of occludin is not lethal and does not compromise the development of functional TJ strands (Saitou et al., 2000). Nevertheless, other studies indicate the importance of occludin for BBB integrity, especially in pathologic conditions such as ischemic stroke (Eum et al., 2015; W. Liu et al., 2014; Yuan Zhang et al., 2021). Occludin was first identified in chick liver in 1993 by Furuse et al. as 65-kDa integral membrane protein (Furuse et al., 1993). It has a similar structure as the claudins, with ECL2 as the primary domain for interacting with other TJ proteins (Bellmann et al., 2014).

Another category of TJ transmembrane proteins is the junctional adhesions molecules (JAM). JAM have a supportive function for BBB integrity and leukocyte migration in pathologic states, but it is not clear if JAM are directly involved in the sealing function of TJ (Jia et al., 2013; Martìn-Padura et al., 1998; Stamatovic et al., 2012).

TJ transmembrane proteins connect to scaffold proteins through a PDZ binding motif localised on their C-termini (Cummins, 2011; Rüffer & Gerke, 2004). Scaffolding proteins include members of the membrane-associated guanylate kinases (MAGUK) family, such as the zonula occludens (ZO) proteins ZO-1, ZO-2 and ZO-3 (Anerson et al., 1988; González-Mariscal et al., 2000; Gumbiner et al., 1991; Haskins et al., 1998). In general, the ZO proteins function as a cross-linker to the actin cytoskeleton, represent a platform enabling signal transduction molecules to interact with the TJ and thus, are also involved in cell proliferation, survival and differentiation (Zihni et al., 2016).

AJ, such as cadherins, CD31 and Nectin, are not known to have a meaningful role in limiting the paracellular transport but rather in forming and maintaining endothelial cell-cell contacts (Stamatovic et al., 2012). Their structure is similar to that of TJ, and they connect to the actin cytoskeleton via catenins and desmoplakin (Bazzoni et al., 2000; Reynolds et al., 1992; Shibamoto et al., 1995). AJ and TJ mediate actin cytoskeleton reorganisation via scaffold proteins and associated molecules, such as members of the Ras homolog family member A (RhoA)/ receptor for activated C kinase (RACK) 2 signalling pathway (Feng et al., 2018). Actin-polymerisation and -depolymerisation are required to maintain BBB integrity functions and modulate permeability due to shear stress, angiogenesis or immune cell infiltration in inflammatory conditions (Colgan et al., 2007; DeOre et al., 2020; DeStefano et al., 2017; Shi et al., 2016; Tornavaca et al., 2015).

Intensive crosstalk between the endothelial cells and other BBB cells ensures the expression of TJ and AJ during development and subsequent maintenance. Essential for TJ regulation are astrocytic released Wnt molecules interacting with the Frizzle/low-density lipoprotein receptor-related protein (LRP) 5/6 receptor complex on BECs. Subsequent stabilisation of β-catenin promotes the expression of various genes increasing TJ protein expression and stability (Guérit et al., 2020; Liebner et al., 2008). In addition, astrocytes promote TJ expression by releasing the Sonic Hedgehog protein, which binds to the Patched-1 receptor on endothelial cells (Alvarez et al., 2011). Following receptor binding, Smoothened is activated and induces TJ protein expression. Pericytes and endothelial cells communicate through bidirectional and reciprocal angiopoietin (Ang) 1/ tyrosine-protein kinase receptor 2 (Tie-2), platelet-derived growth factor β (PDGFβ)/ PDGFβ receptor (PDGFRβ) and transforming growth factor β (TGFβ)/TGFβ receptor (TGFβR) signalling pathways to improve TJ expression and functionality (Geranmayeh et al., 2019; Hori et al., 2004; Shen et al., 2019). Conversely, in inflammatory states, microglia-derived cytokines, such as the tumour necrosis factor (TNF) and interleukin (IL)-1β induce the opening of the BBB by delocalisation or degradation of TJ. Both molecules induce the nuclear factor ''kappa-light-chain-enhancer' of activated B-cells (NF-κB) mediated signalling in pericytes, leading to increased matrix metalloproteinase (MMP) 9 expression, an enzyme degrading different TJ structures (Qin et al., 2019; Takata et al., 2011; Tsuge et al., 2010). Further, the stability or delocalisation of TJ is regulated through phosphorylation and ubiquitylation processes. Depending on the phosphorylation site and underlying pathways, phosphorylation can either decrease BBB permeability (e.g. phosphokinase A mediated threonine phosphorylation of claudin-5) or increase BBB extravasation (e.g. phosphorylation of serine, threonine or tyrosine residues of occludin) (Y. S. Chen et al., 2007; DeMaio et al., 2006; Ishizaki et al., 2003; Morgan et al., 2007). Ubiquitylation is an essential mechanism for the degradation of occludin and, thus, enhanced BBB permeability (Murakami et al., 2009; Traweger et al., 2002). Ubiquitinated occludin is internalized by clathrin-mediated endocytosis and transported to proteasomes for degradation (Murakami et al., 2009). Deubiquitinases, such as A20, can prevent occludin delocalisation and thus, might increase BBB integrity (Kolodziej et al., 2011).

Transcellular transport

In 1967, Reese and Karnovsky described the distribution of intravenously injected horseradish peroxidase (HRP) in the cerebral cortex. In contrast to organs in the periphery, such as skeletal muscle or heart, they could not observe any extravasation of HRP into the central nervous system (CNS) and found only some micropinocytotic vesicles localised in the BECs (Reese & Karnovsky, 1967). At this time, they assumed that TJ rather than the restricted vesicular trafficking is the leading cause of limited transport to the brain parenchyma. Nowadays, it is well known that the restriction of brain endothelial trafficking is an essential factor for BBB integrity. Thus, dysregulation of BEC intracellular trafficking can lead to BBB leakage, although TJ functionality is not impaired (Andreone et al., 2017; Ben-Zvi et al., 2014).

Several carrier-mediated transporters, ATP binding cassette (ABC) transporters, and various endocytotic mechanisms mediate the influx and efflux of hydrophilic substances and macromolecules. Thus, the uptake of nutrients and precursor molecules is guaranteed, while several efflux transporters largely exclude xenobiotics. Preservation of this highly selective permeability in BEC requires extremely high metabolic activity rates and energy-consuming processes compared to other endothelium types (Oldendorf, Cornford, & Brown, 1977).

Carrier-mediated transport and efflux

Carrier-mediated transporters for glucose, monocarboxylate, amino acids, and peptides are localised at the abluminal and luminal membrane of BECs. Glucose transport through BECs is mediated by the insulin-independent facilitated glucose transporter member 1 (GLUT1), which is crucial for the development of the BBB and is oxygen-dependently expressed (Bruckner et al., 1999; Zheng et al., 2010). This transporter has an obligatory function since the brain is the primary consumer of glucose (Erbsloh et al., 1958). Alternatively, the brain can also metabolize monocarboxylic acid, i.e. lactate or ketone bodies, transported by the proton-coupled monocarboxylate transporter (MCT)-1 or -2 (Pierre et al., 2000; Poole & Halestrap, 1993). Nucleoside transport through the BBB exists, but little is known about its mechanisms. Chishty et al. suggest at least four nucleoside carrier systems, including two sodium-dependent secondary active transporters and two systems mediating facilitated diffusion (Chishty et al., 2003). Amino acid and peptide transport are carried out by various transporter systems and depends on the branching and hydrophilic characteristics of the reactive group of amino acids. Thus, the transporters are classified in system L, y+, and Xc^- (Barar et al., 2016). System L, a sodium-independent bidirectional transporter for branched and aromatic neutral amino acids, hosts a crucial therapeutic function for drug delivery across the BBB. It delivers externally supplied L-DOPA used for the treatment of Parkinson's disease (Kageyama et al., 2000).

The efflux of BEC, especially the exclusion of xenobiotics, is mainly regulated by ABC transporters. These transporters include the multidrug resistance protein (MDR), the multidrug resistance-related protein (MRP), and the breast cancer resistance protein (BCRP) (Mahringer & Fricker, 2016). Localised at the luminal membrane of BEC, these proteins work unidirectional and utilize energy by binding and hydrolyzing adenosine triphosphate (ATP) (Linton, 2007). The most investigated efflux transporter at the BBB is probably the P-glycoprotein (P-gp), a member of the MDR family. It regulates the efflux of various phospholipids, sphingolipids, aldosterone, and amyloid-β. However, it prevents also the transport of many therapeutics to the brain tissue, such as chemotherapeutics and several antiepileptics (Lagas et al., 2009; Luna-Tortós et al., 2008; Tang et al., 2012).

Transcytosis

As in non-CNS tissue, transcytosis at the BBB starts with receptor-mediated, adsorptive, or fluid-phase endocytosis of molecules. Receptor-mediated transcytosis is typical for insulin, transferrin, and low-density lipoprotein transport and is based on the specific ligand-receptor binding (Pulgar, 2019). In contrast, the fluid phase and adsorptive endocytosis are relatively non-selective, and substrate transport depends on charge interactions (Preston et al., 2014; Xiao & Gan, 2013).

Endocytosis is usually subdivided into caveolae-, clathrin-dependent, and clathrin-independent pathways, which mediates invagination of the plasma membrane and subsequent internalisation of molecules in vesicles. Clathrin-dependent endocytosis is the most investigated pathway and promotes receptor-mediated transport (Villaseñor et al., 2019). It relies on the recruitment of clathrin coat components to the plasma membrane and subsequent organisation as trimers of heterodimers, termed the triskeleton (Kumari et al., 2010). In contrast, the coat protein caveolin is an integral membrane protein forming caveolae dependent on the availability of cholesterol (Fielding & Fielding, 2000). Caveolae are assumed to promote the transport of fluid-phase or adsorptive molecules such as dextran and albumin, while their role for receptor-mediated transport remains elusive (Villaseñor et al., 2019). Both processes are completed by the fission reaction in which the dynamin guanosine triphosphate hydrolase (GTPase) cuts off the vesicles for the next step of transport, the intracellular trafficking (Shpetner & Vallee, 1989). First, the coat of the vesicles is shredded, and vesicles are transported to the early endosome. Recent investigations have shown that sorting tubules regulate the intracellular trafficking network in BEC. These dynamic structures regulate vesicular fate after the transport to the early endosome, such as recycling or lysosomal degradation, and are regulated by the expression of the small GTPase Ras-related protein (Rab) 17 (Villaseñor, Schilling, et al., 2017). It is unclear which signals determine degradation, recycling, or transport to the brain parenchyma. Recently, some studies indicated that the affinity of the cargo to its receptor might be relevant. For example, investigations on a brain shuttle platform addressing the transferrin receptor (TfR) at the BBB have shown that high binding affinity and bivalent antibody binding to the receptor leads to degradation. In contrast, TfR monovalent antibodies with lower binding affinity are sorted for transcytosis (Villaseñor, Schilling, et al., 2017). Similar results have been achieved using polymersomes functionalized with LRP1 targeting moieties with tuneable avidity to LPR1 (Tian et al., 2020). High-avidity cargo was sorted for endothelial degradation, while mid-avidity cargo has shown rapid transport to the abluminal side.

Although rapid progress in the field of brain endothelial trafficking has been made, it is still uncertain how transcytosis at BEC is kept at exceptionally low levels. Recently, several investigations have focussed on the role of lipids and the major facilitator superfamily domain containing 2A protein (Mfsd2a). Mfsd2a is a transmembrane protein with high expression in the brain, placenta, and testis (Ben-Zvi et al., 2014; Esnault et al., 2008; Nguyen et al., 2014). According to Andreone and colleagues, Mfsd2a-regulated transport of docosahexaenoic acid (DHA) from the outer to the inner membrane leaflet leads to a unique lipid composition in BEC, hindering the formation of caveolae-mediated transcytotic vesicles (Andreone et al., 2017). Indeed, in a subarachnoid haemorrhage (SAH) rat model, DHA deficiency exacerbated BBB damage by increased caveolae-based transcellular transport (Zhao et al., 2020). Overexpression of Mfsd2a reversed effects caused by SAH, proposing a protective role of DHA and Mfsda2 for the BBB in disease conditions. However, exact pathways and the regulation for specific molecules are still unknown. Investigating these pathways is of significant interest since the development of potential therapeutics against neurological pathologies often fails due to the inability to penetrate the BBB.

1.2. The impact of endothelial cell death in the brain

1.2.1. Classification of cell death

Although brain endothelial death is viewed as a component of many neurological pathologies, it is also known for its necessity for physiological processes such as brain development, remodelling and repair (Rizzo & Leaver, 2010). In neurological diseases, endothelial cell death is primarily caused by the loss of supply with oxygen and nutrients. Eventually, endothelial cell death affects other cells of the neurovascular unit and might lead to inflammatory, ischemic and degenerative processes (Rizzo & Leaver, 2010; Zille et al., 2019).

To date, various modes of cell death have been described, and many of them have been shown involved in brain pathologies, such as necrosis, apoptosis, necroptosis, apoptosis-related cell death (e.g. autophagy) or ferroptosis (A. Q. Chen et al., 2019; Kim et al., 2020; Q. Li et al., 2017; Song et al., 2017; Wei et al., 2004). The most common types of endothelial cell death are necrosis and apoptosis, which can be distinguished by numerous morphological and biochemical features (Table 1; D. Chen et al., 2016; Galluzzi et al., 2018; Kroemer et al., 2005, 2009; C. Liu et al., 2018). Usually, necrosis occurs as a sign of extrinsic or intrinsic cell stress such as hypoxia, noxious physical and chemical agents, as well as immunologic reactions (Khalid & Azimpouran, 2021). Since necrosis leads to the release of intracellular materials into neighbouring tissue, inflammation and subsequent tissue damage are often associated with this type of cell death (Khalid & Azimpouran, 2021). In contrast, apoptotic cells rarely release substances that lead to cell death in surrounding tissue and are removed in an efficient and highly controlled way. Apoptosis can be induced by either the intrinsic or extrinsic pathway. The intrinsic pathway can be triggered by oxidative stress products, toxins, radiation or the loss of anti-apoptotic factors (Elmore, 2007). Upon its activation, the mitochondrial permeability transition pore is formed, and apoptotic effectors are released under the control of the B-cell lymphoma 2 (Bcl-2) family of proteins (Cory & Adams, 2002). The binding of death ligands initiates the extrinsic apoptosis pathway to their death receptors, such as TNF/TNF receptor 1 (TNFR1) and Fas ligand (FasL)/Fas receptor (FasR) (Chau et al., 2004; Holmström et al., 1999; H. Liu et al., 2004). In both pathways, cleavage of certain procaspases leads to activation of the executioner enzyme caspase (Casp)-3. Finally, apoptosis is determined by DNA degradation and cytoskeletal reorganisation (Elmore, 2007).

Several years ago, a cell death type carrying features of necrosis and apoptosis, termed necroptosis, was discovered. Necroptosis shows most morphological characteristics of necrosis but is activated by ligand-receptor interactions and mediated in an ATP- and enzyme-dependent manner such as apoptosis (Manolis Pasparakis & Vandenabeele, 2015). Although similar stimuli activate necroptosis as apoptosis, most investigations on necroptosis include its stimulation by TNF. Upon ligand binding, an alternative pathway is induced, including the formation of the necrosome consisting of the receptor-interacting serine/threonine-protein kinase (RIPK) 1, RIPK3 and mixed lineage kinase domain-like protein (MLKL) (Manolis Pasparakis & Vandenabeele, 2015). This complex represents the core platform of necroptosis, and its formation is dependent on the kinase activity of RIPK1 and the inhibition or deletion of the Fas-associated protein with death domain (FADD) or Casp8 (Manolis Pasparakis & Vandenabeele, 2015). Notably, RIPK1 is also involved in the TNF-induced complex I, which induces NF-κB activation and blocks cell death. Here, RIPK1 kinase activity is inhibited by phosphorylation at Ser25 by the IκB kinase (IKK) complex, and RIPK1 interacts as a scaffold molecule (Dondelinger et al., 2019).

After induction of RIPK1 kinase activity, RIPK3 is recruited and phosphorylated by RIPK1, leading to homodimerisation of RIPK3 and autophosphorylation (Manolis Pasparakis & Vandenabeele, 2015). Phosphorylated RIPK3 recruits and phosphorylates MLKL. After the MLKL auto-inhibitory region is dissociated, mediated by inositol phosphate kinase activity, necroptosis is executed by MLKL oligomerisation, subsequent membrane translocation and pore formation (Dovey et al., 2018). This event leads to Ca^{2+} influx, phosphatidylserine externalisation, and loss of plasma membrane integrity (Gong, Guy, Crawford, et al., 2017). Although this event is often described as the last and irreversible step of necroptosis, Gong and colleagues reported that $pMLKL^{+}$ cells do not undergo cell death if active MLKL is inhibited before cell lysis. Deactivation of pMLKL, as well as cell lysis, is presumably regulated by the endosomal sorting complexes required for transport (ESCRT)-III machinery (Gong, Guy, Olauson, et al., 2017)

Apoptosis	Necrosis	Necroptosis
	Morphological characteristics	
Cytoplasmatic shrinkage Little or no modification of cytoplasmatic organelles	Cytoplasmatic swelling (oncosis) Organelle swelling and rupture	Cytoplasm swelling and vacuolisation Organelle swelling and rupture
Chromatin condensation (pyknosis) Nuclear fragmentation (karyorrhexis)	Moderate chromatin condensation Nuclear fragmentation can occur**	Moderate chromatin condensation Nuclear fragmentation can occur**
Plasma membrane blebbing and formation of apoptotic bodies, degradation by phagocytosing cells	Plasma membrane swelling and rupture	Plasma membrane swelling and rupture
	Biochemical characteristics	
Programmed cell death Activation of caspase cascade* ATP-dependent Inflammation of the surrounding tissue is unlikely	Unregulated ATP-independent Inflammation of the surrounding tissue is likely	Programmed cell death, Caspase inhibition necessary Formation of the necrosome (pRIPK1, pRIPK3 and pMLKL) ATP-dependent Inflammation of the surrounding tissue is likely

Table 1: Morphological and biochemical features of apoptosis, necrosis and necroptosis. **In some cases, apoptosis can also occur in a caspase-independent but apoptosis-inducing factor (AIF) dependent manner* (Candé et al., 2004)*. **Initially, necrosis and necroptosis have been described as cell death without nuclear fragmentation. However, nuclear fragmentation has been observed in apoptotic secondary necrosis* (Silva et al., 2008)*.*

String vessels – a special feature of endothelial cell death

Occasionally, the death of endothelial cells has been reported to be associated with the formation of pruning vessels or so-called string vessels (Brown, 2010; Hunter et al., 2012; Ridder et al., 2015; Zille et al., 2019). String vessels are often described as thin connective tissue strands and remnants of capillaries lacking endothelial cells and not carrying blood (Brown, 2010; Ridder et al., 2015). They have been discovered already in 1838 and have been thought to occur with ageing and pathologies for a long time, but only in the beginning of the 1990s, the occurrence of string vessels in neurological diseases such as Alzheimer’s diseases (AD) has been proved (V. R. Challa et al., 2004; Henle, 1838). Since then, string vessels have been observed in several neurological diseases (Forsberg et al., 2018; Y. Hase et al., 2019; Reinecke et al., 1962; Ridder et al., 2015; P. Yang et al., 2015). There are still ongoing debates about the origin and functions of string vessels. Chen and colleagues observed vessel pruning during the development of midbrain vasculature due to haemodynamic changes and in association with endothelial cell migration (Q. Chen et al., 2012). They concluded that vessel pruning reduces the complexity of developing brain vasculature to improve efficient blood flow. Besides, the occurrence of string vessels has also been observed in adulthood. Such observations have been interpreted as spontaneous obstructing vessels, which are recanalized in 75-80 % of all cases (Reeson et al., 2018). Others describe string vessels as newly formed capillary tubes, probably as a sign of angiogenesis (Bennett et al., 2018). However, Alarcon-Martinez and colleagues argue against the theory that these tubes are remnants from regressing vessels or newly formed capillaries but instead identify string vessels as nanotube-like processes that connect two “bona fide” pericytes in different capillary systems (Alarcon-Martinez et al., 2020). According to their conclusion, pericyte-derived string vessels regulate neurovascular coupling by conducting intercellular calcium waves between separate capillary systems. In conclusion, it is plausible that string vessels might arise from diverse origins and thus, can fulfil different functions.

1.2.2. The role of brain endothelial cell death in neurological diseases

Endothelial cell death can lead to grave damage and inflammation in the brain resulting in severe neuropathologies such as stroke, SAH, cerebral cavernous malformations or AD (Rizzo & Leaver, 2010). Often, several cell death modes can be observed in these diseases.

A study by Chen et al. proved increased apoptosis and necroptosis after middle cerebral artery occlusion (MCAO), a mouse stroke model (A. Q. Chen et al., 2019). Notably, apoptosis markers were upregulated soon after MCAO but declined later, while the necroptosis marker levels increased continuously at later stages. According to their study, necroptosis significantly exacerbated subsequent ischemia-reperfusion injury by increasing BBB permeability. Chen and colleagues proposed a mechanism by which increased NF-κB-mediated TNF expression by microglia leads to the activation of necroptosis in BECs. This process could be attenuated by the treatment with Infliximab, a TNF inhibitor and Necrostatin-1s (Nec-1s), a RIPK1 inhibitor. Other studies observed BBB defects mediated by transcytotic changes. For example, at the early stages of stroke or cerebral ischemia, caveolae-dependent transcytosis is dysregulated resulting in TJ defects, such as occludin degradation or claudin dissociation (Choi et al., 2016; Knowland et al., 2014; J. Liu et al., 2012).

On the contrary, only a few studies describe BBB defects as the trigger of endothelial cell death in neurological diseases. In dementia and AD, alterations in brain endothelial transcytosis might trigger amyloid-beta aggregation and thus, lead to endothelial cell death. In accordance, LRP1-mediated efflux of amyloid-beta at the BBB is critical to prevent toxic amyloid-beta aggregations, which subsequently cause vascular apoptosis (M. Hase et al., 1997; Shibata et al., 2000; Storck et al., 2016). Polymorphisms in the *LRP1* gene might lead to disturbed transcytosis and promote AD development, but this hypothesis is still debated (Kang et al., 1997; Y. Wang et al., 2017). Although AD is known for neuronal cell death and subsequent loss of neuronal connections, it becomes clearer that vascular defects play an essential role in the initiation and progression of the disease (Govindpani et al., 2019).

Interestingly, AD, stroke and several other brain diseases affecting the microvasculature have been associated with a pathology called cerebral small vessel disease (cSVD). Mainly, cSVD occurs sporadically and increases the risk for AD, stroke, Parkinson’s disease, depression, epilepsy, dementia, and mental disability, primarily in the elderly (Cuadrado-Godia et al., 2018; Müller et al., 2017). Although the exact mechanisms of pathogenesis are still unknown, classical risk factors, such as hypertension and diabetes mellitus, are associated with cSVD (Pantoni, 2010). Nonetheless, numerous studies summarized elsewhere indicate endothelial dysfunction and BBB breakdown as the main reason for cSVD’s symptoms (Cuadrado-Godia et al., 2018). Thus, endothelial cell death, the increased formation of string vessels and vessel rarefaction have been observed as morphological characteristics for this disease (Y. Jiang et al., 2020; Müller et al., 2017). For some types of cSVD, genetic factors play a crucial role in the onset of the disease (Cuadrado-Godia et al., 2018; Müller et al., 2017). This circumstance might offer a chance to determine proteins that are important for brain endothelial integrity and uncover possible targets for pharmacological interventions to treat cSVD.

1.3. The NF-κB pathway

1.3.1. Regulation of the NF-κB pathway

NF-κB is present in all cell types, and its target genes are involved in various essential processes, such as immunity and cell proliferation (Oeckinghaus & Ghosh, 2009). Activation of NF-κB occurs either via the canonical or the non-canonical pathway. The canonical pathway involves the IKK complex, which includes the NF-κB essential modulator (NEMO), and regulates the activation of the NF-κB proteins p105/p50, p65 and c-Rel (T. Liu et al., 2017; Sun, 2017). This pathway is induced by numerous stimuli and responds relatively fast but only transitory (Sun, 2017; Yu et al., 2020). The non-canonical pathway has a considerably longer reaction time, but the response is persistent. This pathway is initiated by only a few stimuli and transmits the response predominantly via p100/p52 and RelB (Sun, 2017). In contrast to the canonical pathway, the non-canonical pathway does not involve the entire IKK complex inclusive NEMO. While the non-canonical pathway is thought to be explicitly involved in the development of the immune system and the immune response, the canonical pathway bears a broad spectrum of functions (T. Liu et al., 2017; Sun, 2017). Like the non-canonical pathway, it is also involved in many aspects of the immune response and can act with the non-canonical pathway synergistically or antagonistically depending on the cell type and the stimuli (Gray et al., 2014; Kendellen et al., 2014). In addition, the canonical NF-κB pathway holds essential functions in neuronal survival, angiogenesis and is often involved in cancerogenesis (Tabruyn et al., 2009; Wooten, 1999; Xia et al., 2014).

Stimuli for the canonical NF-κB pathway include cytokines, growth factors, mitogens, microbial components, stress agents, or even ultraviolet or gamma radiation (T. Liu et al., 2017; Wenzel & Schwaninger, 2016). In many cell types, activation of NF-κB by TNF plays an important role. Upon binding on TNFR1 and receptor trimerisation, the TNFR1-associated death domain protein (TRADD), RIPK1, the E3 ubiquitin ligases cellular inhibitors of apoptosis (cIAP1 and cIAP2) and the TNFR1-associated factor 2 (TRAF2) are recruited (Kondylis et al., 2017; Kim Newton, 2020; Manolis Pasparakis & Vandenabeele, 2015). The cIAPs ubiquitinate RIPK1 and other complex components predominantly with K63-linked ubiquitin chains, resulting in the formation of the linear ubiquitin assembly complex (LUBAC) (Kondylis et al., 2017). Subsequently, the TAK1-binding protein (TAB) 2 and 3 are recruited, adaptor proteins for the transforming growth factor beta-activated kinase 1 (TAK1) (Kanayama et al., 2004). In addition, the IKK complex binds to the ubiquitin chains via the ubiquitin-binding domain in ABIN proteins and NEMO (UBAN) (Rahighi et al., 2009). The close proximity of TAK1 and the IKK complex induces activation of TAK1, which then phosphorylates the I-κB kinase complex (IKK), which consists of two kinase subunits, IKKα and IKKβ, and Nemo (IKKγ) (May et al., 2000; Mercurio et al., 1997; Takaesu et al., 2003). In the following, IKKβ phosphorylates I-κBα at two N-terminal serines in the presence of NEMO and thus, induces ubiquitin-dependent proteasomal degradation of the nuclear factor of kappa light polypeptide gene enhancer in B-cells inhibitor alpha (IκB-α) (Zandi et al., 1997). Consequently, NF-κB dimers are translocated into the nucleus, and, primarily, gene expression is activated. The TNF-induced reaction chain, including the NF-κB pathway, is also termed TNF-induced complex I (Figure 2; Manolis Pasparakis & Vandenabeele, 2015).

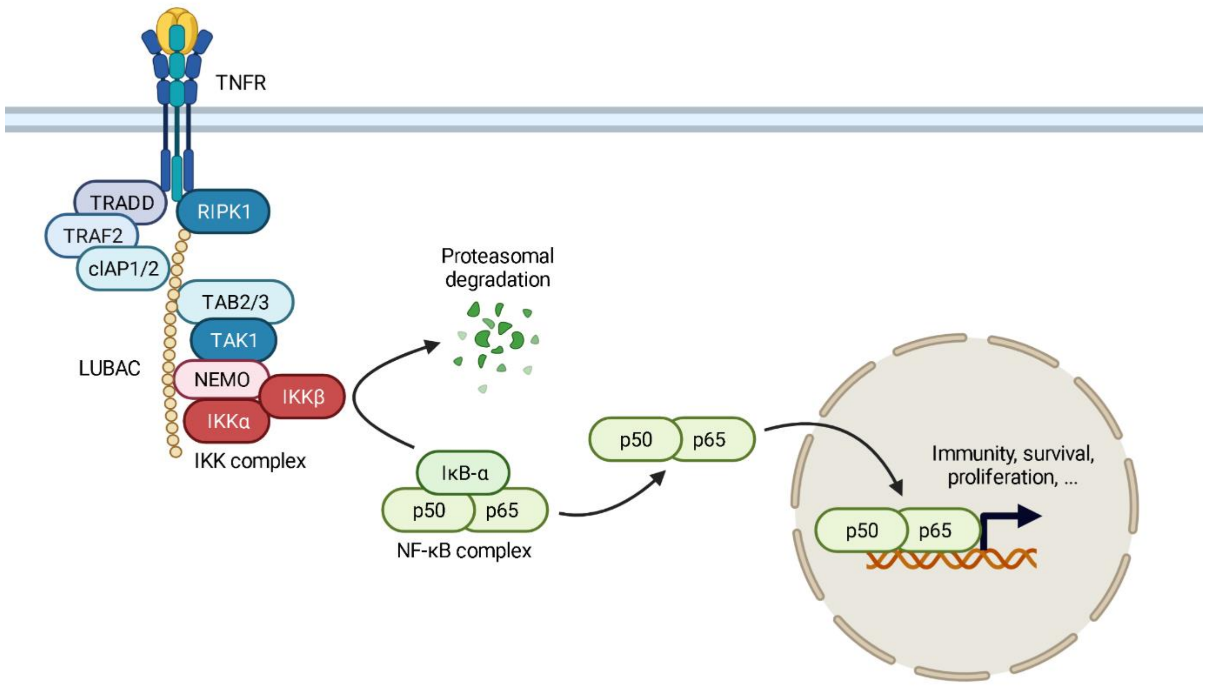

***Figure 2: TNF-induced complex I and canonical NF-κB pathway**. TNF binding to its receptor (TNFR) leads to the recruitment of TRADD, TRAF2, cIAP1/2 and RIPK1. Several ubiquitination events initiate the formation of LUBAC and the binding of TAB2/3/TAK1. Subsequently, the IKK complex is recruited and activated, leading to phosphorylation and degradation of IκB-α, an inhibitory subunit of the NF-κB complex. NF-κB dimers, such as p50 and p65, are released and translocated to the nucleus, where gene expression of NF-κB targets is induced. The figure was created with Biorender.com.*

Activation of the TNF-induced complex I is limited by several feedback loops acting on each level of the NF-κB pathway. Hence, they can interfere with receptor function, produce dominant-negative signal transducers, reverse posttranslational modifications, degrade signalling proteins or even inhibit nuclear NF-κB activity (Renner & Schmitz, 2009). Negative feedback regulators are often NF-κB targets themselves and thus, act in a time-delaying manner. For example, the deubiquitinase A20, whose expression is induced by NF-κB, binds to NEMO and prevents the phosphorylation of IKK by TAK1 (Shembade & Harhaj, 2012). Mice deficient for A20 suffer from multi-organ inflammation due to NF-κB overactivation (Lee et al., 2000). Coordinated activation of positive and negative feedback loops leads to oscillations in NF-κB activation, which might be involved in cell cycle activity and circadian rhythms (Inoue et al., 2016).

1.3.2. The role of NF-κB in diseases

In general, increased NF-κB activation is associated mainly with increased inflammation, tissue damage and carcinogenesis. Thus, increased NF-κB activation participates in the inflammatory phenotypes of progressive diabetic nephropathy, arthritis, asthma or gastritis (Han et al., 1998; Hart et al., 1998; Mezzano et al., 2004; van den Brink et al., 2000).

In the brain, the NF-κB pathway is activated by the same stimuli as in any other organ, but in addition, the neural cell adhesion molecule (N-CAM), neurotrophins or amyloid-beta are also potent NF-κB inducers (Behl et al., 1994; Carter et al., 1996; Krushel et al., 1999). High NF-κB activation is often associated with enhanced inflammation and brain damage after injuries and in neurodegenerative disorders. For example, NF-κB is strongly activated in the inflammatory phenotype of aneurysm walls in subarachnoid haemorrhage (SAH), and additional neuronal NF-κB activation leads to delayed brain injury (Frösen et al., 2019; You et al., 2013). Further, NF-κB is contributing to extensive neuroinflammation observed in AD (Grilli et al., 1996; Ju Hwang et al., 2017; Valerio et al., 2006). Hwang and colleagues suggest a model in which enhanced NF-κB activity leads to activation of amyloidogenesis by beta-secretase, TNF-induced neuroinflammation and subsequent neuronal cell death. AD and many other brain diseases involving inflammation are associated with increased permeability of the BBB (Obermeier et al., 2013; Sweeney et al., 2018). Although the opening of the BBB has crucial immunological functions such as immune cell infiltration and subsequent clearance of pathogens, neuronal damage and CNS defects can occur if BBB integrity is disrupted chronically (Wenzel & Schwaninger, 2016). If NF-κB contributes to the process of BBB opening is still elusive. A recent study investigated NF-κB's role at the BBB in traumatic shock by inducing a hypovolemic status in Sprague-Dawley rats (Deng et al., 2019). The authors found enhanced NF-κB p65 protein expression in cortical brain tissue accompanied by decreased occludin and claudin-5 levels. Inhibition of NF-κB by pyrrolidine dithiocarbamate could at least partially increase occludin and claudin-5 expression, suggesting disruption of the BBB by NF-κB-dependent degradation of TJ proteins. Further, it is known that NF-κB activation induces the expression of MMP which are able to degrade the BBB basement membrane, possibly leading to increased BBB permeability (Bell et al., 2012). While these studies did not differentiate between different types of brain cells, another study specifically investigated brain endothelial NF-κB. Here, the authors could show that dysfunctional transcytosis due to methamphetamine toxicity could be prevented by NF-κB pathway inhibition in brain endothelial cells (Coelho-Santos et al., 2015).

In contrast, basal activity of NF-κB independent of inflammatory stimuli has shown to be needed for learning and memory in mice, protection of neurons against toxins such as amyloid-beta and ensuring the survival of neural stem cells (Kaltschmidt & Kaltschmidt, 2009). Thus, ablation of NEMO, the regulatory subunit of the IKK complex, might have severe consequences.

In humans, the genetic inactivation of *IKBKG*, the gene encoding NEMO, leads to the development of a neurocutaneous syndrome known as Incontinentia pigmenti (IP). Patients suffer from typical cutaneous manifestations such as neonatal vesicular rashes, linear atrophic alopecic lesions and hyperpigmentations. These symptoms can be accompanied by dental abnormalities, alopecia, nail abnormalities and retinal disorders (Poziomczyk et al., 2014). A significant problem of this disease are the neurological symptoms observed in 30 % of all patients (Meuwissen & Mancini, 2012). These include seizures, intellectual disability, and stroke. Neurological pathologies and symptoms found in humans – such as epileptic seizures – have been reproduced in a mouse model with a tamoxifen-inducible knockout of *Ikbkg* ($Nemo^{beKO}$) specific for BECs (Ridder et al., 2015). Detailed investigations have observed massive BBB breakdown shown by higher immunoglobulin G (IgG) and albumin extravasation, increased leakage for dextrans of different sizes, and high water content in the brains of $Nemo^{beKO}$ mice (Ridder et al., 2015). Further, an enormously increased formation of string vessels, rarefaction of brain microvessels and a decreased perfusion in brain vessels have been detected, suggesting cell death in the absence of NEMO. In addition, the expression of the TJ protein occludin was lower than in the control group, while other TJ protein levels were not altered. In the mouse model, the symptoms did include not only epileptic seizures but also behavioural consequences such as increased anxiety-like behaviour and reduced social interactions with littermates.

Interestingly, the main protease of the severe acute respiratory syndrome coronavirus type 2 (SARS-CoV-2), M^{pro}, cleaves NEMO and patients who suffer from neurological manifestations show symptoms similar to the neurological phenotype of IP (Meuwissen & Mancini, 2012; Wenzel, Lampe, Müller-Fielitz et al., 2021). In accordance, patients with coronavirus disease 2019 (COVID-19) and mice which received a M^{pro}-coding vector showed increased string vessel formation. Therefore it can be assumed that despite the brain damage caused by increased NF-κB activation in inflammatory conditions, a basal level of NF-κB seems necessary to maintain BBB functions and ensure endothelial survival. As suggested by Wenzel et al., the relationship between NF-κB activity and BBB integrity might be explained best by a bell-shaped curve (Figure 3; Wenzel & Schwaninger, 2016).

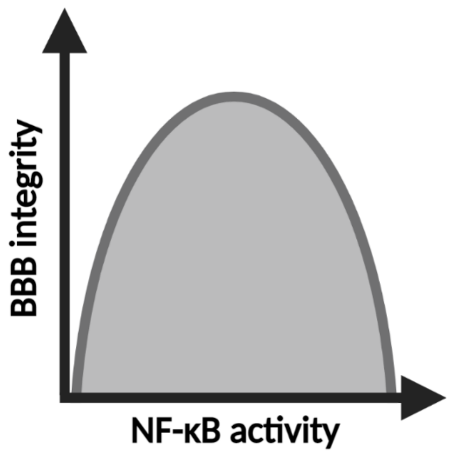

Figure 3: Contradicting findings of NF-κB's role for the BBB can be explained by a bell-shaped relationship between NF-κB activity and BBB integrity. *Basal levels of NF-κB activity ensures endothelial survival and BBB integrity, while high activation of NF-κB induces inflammation and damage at the BBB. The figure was created with Biorender.com.*

1.4. Aims of the study

In previous work, BBB leakage and vascular defects have been observed for *Nemo*^{beKO} mice, a mouse model for IP (Ridder et al., 2015). From these findings, IP has been associated with the pathology observed in cSVD (Y. Jiang et al., 2020). In this study, we aim to further investigate the vascular phenotype of *Nemo*^{beKO} mice, and thus, planned a comprehensive characterisation of string vessels.

Moreover, we would like to inhibit cell death in NEMO deficient endothelial cells to improve vascular defects and BBB interruptions. For this reason, we want to target crucial executioners of TNF-induced cell death, such as RIPK1, RIPK3 and FADD, by genetic and pharmacological approaches. Since recent researches showed brain endothelial transcytosis dysregulation in several neurological diseases, we also aim to include transcytosis analysis in the phenotype investigations of the *Nemo*^{beKO} mice lacking the cell death executioner proteins (Villaseñor et al., 2019). Besides, we would like to test if cell death inhibition has long-lasting effects on the *Nemo*^{beKO} phenotype. A positive outcome of this study might help develop pharmacological interventions to treat at least neurological symptoms in IP patients and COVID-19.

More specifically, we want to address the following questions:

1. Which characteristics do string vessels have in *Nemo*^{beKO} mice, and which other vascular anomalies can be found in these mice?
2. Is cell death inhibition sufficient for preventing vascular defects and BBB impairment in *Nemo*^{beKO} mice? If yes, are these effects persistent?
3. Is brain endothelial transcytosis affected by the ablation of NEMO?

2. Material

2.1. Chemicals

Name	Vendor
100 bp DNA Ladder (Quick-Load)® 50 µg/ml	New England BioLabs (Frankfurt, Germany)
2,2,2-Tribromoethanol (Avertin)	Sigma-Aldrich (St. Louis, USA)
2-Methylbutane	Carl Roth GmbH & Co. KG (Karlsruhe, Germany)
4',6-diamidino-2-phenylindole (DAPI)	Thermo Fisher Scientific (Waltham, USA)
4-Hydroxy-2,2,6,6-tetramethyl piperidinyl oxyl (4-Hydroxy-TEMPO)	Sigma-Aldrich (St. Louis, USA)
Acetic acid	Carl Roth GmbH & Co. KG (Karlsruhe, Germany)
Acetone	J.T.Baker (Deventer, The Netherlands)
Acrylamide 40 %	Sigma-Aldrich (St. Louis, USA)
Agarose (low-melt)	Carl Roth GmbH & Co. KG (Karlsruhe, Germany)
Agarose (NEEO Ultraquality)	Carl Roth GmbH & Co. KG (Karlsruhe, Germany)
Alizarin Red S	Abcam (Cambridge, United Kingdom)
Ammonium hydroxide 28-30 %	Thermo Fisher Scientific (Waltham, USA)
Ammonium persulfate (APS)	Sigma-Aldrich (St. Louis, USA)
Araldite	Sigma-Aldrich (St. Louis, USA)
Bovine serum albumin (BSA)	Sigma-Aldrich (St. Louis, USA)
Calcium chloride ($CaCl_2$)	Merck KGaA (Darmstadt, Germany)
Cell Lysis Buffer (CLB) 10x	Cell Signaling Technologies (Danvers, USA)
Desinfection	BODE Chemie GmbH (Hamburg, Germany)
Diethyl pyrocarbonate	Sigma-Aldrich (St. Louis, USA)
Dimethylsulfoxid (DMSO)	Sigma-Aldrich (St. Louis, USA)
dNTP Mix 10 mM	Thermo Fisher Scientific (Waltham, USA)

Dream Taq Green Buffer 20mM	Thermo Fisher Scientific (Waltham, USA)
Dulbecco's Modified Eagle Medium /Nutrient Mixture F-12 (DMEM-F12, without glutamine)	Gibco /Thermo Fisher Scientific (Waltham, USA)
Dulbecco's Phosphate Buffered Saline (PBS)	Biowest (Nuaillé, France)
Ethanol (absolute)	Carl Roth GmbH & Co. KG (Karlsruhe, Germany)
Ethanol 70 % (denatured)	Th. Geyer GmbH & Co. KG (Renningen, Germany)
Ethidium bromide 10 mg/ml	Carl Roth GmbH & Co. KG (Karlsruhe, Germany)
Ethylenediaminetetraacetic acid dihydrate (EDTA)	Sigma-Aldrich (St. Louis, USA)
FITC-dextran 4 kDa	TdB Consultancy AB, (Uppsala, Sweden)
Fluorescent mounting medium	Dako (Glostrup, Denmark)
Gel Loading dye Purple 6x	New England BioLabs (Frankfurt, Germany)
Glycerol	Carl Roth GmbH & Co. KG (Karlsruhe, Germany)
Green buffer (10x)	Thermo Fisher Scientific (Waltham, USA)
Guanidine Hydrochloride 8 M	Sigma-Aldrich (St. Louis, USA)
Heparin sodium 25 000 U/5 ml	Ratiopharm (Ulm, Germany)
Hydrochloric acid (HCl) 1 M	Carl Roth GmbH & Co. KG (Karlsruhe, Germany)
Isoflurane	Baxter (Deerfield, USA)
Isopropanol	J.T.Baker (Deventer, The Netherlands)
Ketamine 100 mg/ml	Dr. E. Graeub AG (Bern, Switzerland)
L-Glutamine 200 mM	Gibco/Thermo Fisher Scientific (Waltham, USA)
Lead citrate ready-to-use solution	Leica Biosystems (Richmond, USA)
Magnesium chloride ($MgCl_2$) 50 mM	Thermo Fisher Scientific (Waltham, USA)
Methacrylic acid N-hydroxy succinimidyl ester (MA-NHS)	Sigma-Aldrich (St. Louis, USA)

Methanol	Th. Geyer GmbH & Co. KG (Renningen, Germany)
Methylenebisacrylamide solution 2 %	Sigma-Aldrich (St. Louis, USA)
Miglyol 812	Caesar & Loretz GmbH (Hilden, Germany)
Mowiol® 4-88 MW~31 000 g/mol	Carl Roth GmbH & Co. KG (Karlsruhe, Germany)
N,N,N',N'-Tetramethylethylendiamine (TEMED)	Carl Roth GmbH & Co. KG (Karlsruhe, Germany)
Necrostatin-1s (Nec-1s, ab221984)	Abcam (Cambridge, United Kingdom)
Paraformaldehyde (PFA)	Sigma-Aldrich (St. Louis, USA)
Penicillin/Streptomycin (Penicillin G 10.000 E/ml und Streptomycin 10 mg/ml, 100 x)	Merck KGaA (Darmstadt, Germany)
Platinum SYBR green Supermix	Thermo Fisher Scientific (Waltham, USA)
Potassium chloride (KCl)	Sigma-Aldrich (St.Louis, USA)
Potassium dihydrogen phosphate (KH_2PO_4)	Merck KGaA (Darmstadt, Germany)
Potassium hydroxide (KOH)	Merck KGaA (Darmstadt, Germany)
Propylene oxide	Sigma-Aldrich (Munich, Germany)
Puromycin	Sigma-Aldrich (St.Louis, USA)
Random Primers	Promega (Madison, USA)
Ringer's solution	Berlin-Chemie AG (Berlin, Germany)
RNasin	Promega (Madison, USA)
Sodium Acrylate 97%	Sigma-Aldrich (St.Louis, USA)
Sodium cacodylate trihydrate	Sigma-Aldrich (St. Louis, USA)
Sodium chloride (NaCl)	Sigma-Aldrich (St. Louis, USA)
Sodium chloride solution 0.9%	Berlin-Chemie AG (Berlin, Germany)
Sodium citrate, dihydrate	J.T.Baker (Deventer, The Netherlands)
Sodium dodecyl sulphate (SDS)	Sigma-Aldrich (St. Louis, USA)
Sodium hydroxide (NaOH)	Thermo Fisher Scientific (Waltham, USA)
Sodium phosphate dibasic dihydrate ($Na_2HPO_4 \cdot 2H_2O$)	Sigma-Aldrich (St. Louis, USA)

Sucrose	Carl Roth GmbH & Co. KG (Karlsruhe, Germany)
Tamoxifen	Sigma-Aldrich (St. Louis, USA)
Tetramethylethylenediamine	Sigma-Aldrich (St. Louis, USA)
Tissue freezing medium	Leica Biosystems (Richmond, USA)
Tris-hydrochloride (Tris-HCl) pH 8.0	Carl Roth GmbH & Co. KG (Karlsruhe, Germany)
Triton-X-100	Promega (Madison, USA)
TWEEN-20	MP Biomedicals, LLC (Illkirch, France)
Type F Immersion Liquid	Leica Biosystems (Richmond, USA)
Type N Immersion Liquid	Leica Biosystems (Richmond, USA)
UHU superglue	UHU (Bühl/Baden, Germany)
Uranyl acetate ready-to-use solution	Leica Biosystems (Richmond, USA)
Xylazine (Rompun®) 2 %	Bayer Vital GmbH (Leverkusen, Germany)
Xylole	Merck KGaA (Darmstadt, Germany)

2.2. Kits

Name	Type	Vendor
In Situ Cell Death Detection Kit (TUNEL)	Fluorescein	Roche Life Science (Mannheim, Germany)
RNA extraction (for microarray)	RNeasy Mini Kit	Qiagen (Venlo, The Netherlands)
RNA extraction and DNase digestion (for RT-PCR)	NucleoSpin® RNA mini	Macherey-Nagel GmbH & Co. KG (Düren, Germany)

2.3. Enzymes

Name	Vendor
Dream Taq DNA Polymerase 5 U/µl	Thermo Fisher Scientific (Waltham, USA)
Proteinase K 10 mg/ml (= 800 units/ml), expansion microscopy	Sigma-Aldrich (St. Louis, USA)
Proteinase K 20 mg/ml, genotyping	Carl Roth GmbH & Co. KG (Karlsruhe, Germany)
Reverse Transcriptase (MMLV)	Promega (Madison, USA)
Taq-Polymerase DyNAzyme (incl. 10x reaction buffer)	Thermo Fisher Scientific (Waltham, USA)

2.4. Solutions and Buffers

Name	Preparation	
10x Phosphate buffered saline (PBS)	400 g/l	NaCl in aqua bidest
	10 g/l	KCl
	57,5 g/l	Na_2HPO_4 x $2H_2O$
	10 g/l	KH_2PO_4
	adjusted to pH 7.4 by 1 N HCl	
Alizarin Red S solution	20 g/ml	Alizarin red S ml in aqua bidest (w/v)
	adjusted to pH 4.2 by 10 % ammonium hydroxide	
Blocking solution (for cryosections)	1 %	BSA in 1x PBS
	0.3 %	Triton-X-100

Blocking solution (for free-floating sections)	3 %	BSA (w/v) in 1x PBS
	0.3 %	Triton-X-100
DEPC water	1 g/l	Diethyl pyrocarbonate (w/v) in aqua bidest
Dextran solution 18 % m/v (vessel fragment isolation)	Per preparation:	
	5,4 g	Dextran (w/v) diluted in 30 ml 1x PBS
	300 µl	Penicillin/Streptomycin
	300 µl	L-Glutamine
Digestion buffer (Expansion microscopy)	0.8 M	Guanidine HCl in 1x TAE buffer
	0.5 %	Triton-X-100
	8 units/ml	Proteinase K
Gelation solution	0.2 %	APS (w/w) in monomer solution
	0.2 %	TEMED (w/w)
	0.01 %	4-hydroxy-TEMPO
Glutaraldehyde fixative	2 %	PFA in 1x PBS
	2.5 %	glutaraldehyde
Lysis buffer gDNA preparation	20 mM	Tris-HCl in aqua bidest
	5 mM	EDTA (pH 8.0)
	400 mM	NaCl
	1 %	SDS
	400 µg/ml	Proteinase K
Mastermix qPCR	2 µl	dNTP Mix (25 mM)
	10 µl	Reaction buffer (5x)
	1 µl	Random hexamer primers
	1 µl	RNasin
	1 µl	Reverse transcriptase (MMLV)
Monomer solution	2 M	NaCl in aqua bidest
	2.5 %	Acrylamide
	0.15 %	Methyl-bis Acrylamide
	8.625 %	Sodium acrylate
	adjusted to pH 7.35	
Monti-Graziadei solution	0.06 M	Sodium cacodylate
	2 %	Glutaraldehyde
	0.6 %	PFA
	0.03 %	$CaCl_2$
Paraformaldehyde fixation buffer 2 %	2 %	PFA in 1x PBS
	200 µl	5 M KOH per 100 ml 1x PBS
	dissolved by heating up to 60 °C, filtered by Whatman prepleated qualitative filter paper and adjusted to pH 7.4 by KOH	
Reaction mix PCR for genotyping	0.18 mM	dNTP in DEPC-water
	1.79 mM	10x Dream Taq Green Buffer
	0.89 mM	$MgCl_2$ (only for “NEMO” PCR)

	0.34 µM	of each primer (NEMO: 0.27 µM; IKK2: 0.68 µM)
	1 U	Dream Taq DNA Polymerase
Ringer's solution with heparin	10 U/ml	heparin in Ringer's solution
Sodium citrate buffer 10 mM	2.94 g/l	Sodium citrate dihydrate in aqua bidest (w/v)
	0.05 %	Tween-20
	adjusted to pH 6.0 by 1 N HCl	
Supermix qPCR	per sample:	
	9 µl	DEPC water
	12.5 µl	Platinum SYBR green Supermix
	0.75 µl	forward primer (30 nM)
	0.75 µl	reverse primer (30 nM)
TAE Buffer (10x)	1.2 M	Tris Base in aqua bidest
	30 mM	EDTA
	Adjusted to pH 8.3 with acetic acid	
Tamoxifen	Per preparation:	
	100 mg	Tamoxifen (w/v)
	500 µl	Ethanol (abs.)
	4.5 ml	Miglyol 812
Tribromoethanol 1.5 %	1.2 ml	Avertin (7,073 M in 2 Methyl butan-2-ol)
	100 ml	NaCl solution (0.9 %)
Working medium (vessel fragment isolation)	For two preparations:	
	20 ml	DMEM/F12
	200 µl	Penicillin/Streptomycin (10 mg/ml)
	200 µl	L-Glutamine (200 mM)

2.5. Reagents

Name	Type	Vendor
6 Well glass bottom plates	#1.5H	Cellvis (Mountain Viwe, USA)
Agarose gel chambers	SUB-CELL®GT	BIO-RAD
Aluminium foil	30 M	Fipp Handelsmarken (Hamburg, Germany)
Beaker glasses	10-5000 ml	Schott Duran (Wertheim, Germany)

Cannula	27G x 3/4’’ (0.4 x 19 mm)	TERUMO COOPERATION (Hamburg, Germany)
	Safety-Multifly ® cannula 21G	Sarstedt (Nümbrecht, Germany)
Cell culture plates	Cellstar® (6-, 24-, 96-Well)	Greiner AG (Kremsmünster, Austria)
Cell scraper	28 cm	Greiner AG (Kremsmünster, Austria)
Cell strainer	40 µm	Becton Dickinson (New Jersey, USA)
Combitips advanced	0.5 ml, 5 ml, 10 ml	Eppendorf AG (Hamburg, Germany)
Coplin jar		Glaswerk Wertheim (Wertheim, Germany)
Coverslips	24 x 40 mm 24 x 50 mm 24 x 60 mm ⌀ 24 mm	Carl Roth GmbH & Co. KG (Karlsruhe, Germany)
Falcon tubes	15 ml, 50 ml	Greiner AG (Kremsmünster, Austria)
Fatty Pen	DAKO pen	Agilent Technologies, Santa Clara (USA)
Filter paper	MN 615 1/4 (Ø 240 mm)	Macherey-Nagel (Düren, Germany)
	Whatman pre-pleated qualitative filter paper Grade 0858 1/2, grained	Sigma-Aldrich (St. Louis, USA)
Forceps	HWC 110-10	Karl Hammacher GmbH (Solingen, Germany)
Gloves	Peha-soft nitrile FINO	PAUL HARTMANN AG, (Heidenheim, Germany)
Individually ventilated green line cages	500 cm^2	Tecniplast (Buguggiate, Italy)
Parafilm	M	Pechiney Plastic Packaging (Akron, USA)

PCR-96-well plate	Without skirt	SARSTEDT AG & Co. KG (Nümbrecht, Germany)
Petri dishes		Schott Duran (Wertheim, Germany)
Pipet help		Hirschmann Laborgeräte GmbH & Co. KG (Eberstadt, Germany)
Pipet tips	10 µl, 200 µl, 1000 µl, transparent	Sarstedt AG & Co KG, (Nümbrecht, Germany)
Pipettes	10 µl, 100 µl, 200 µl, 1000 µl	Eppendorf AG (Hamburg, Germany)
Razor blades	Classic	Wilkinson Sword (London, UK)
Reaction tube	0.2 ml, 0.5 ml, 1.5 ml, 2 ml	Eppendorf AG (Hamburg, Germany)
Scalpel	FeatherTM disposable scalpel No 10, 11, 22	Electron Microscopy Sciences (Hatfield, USA)
Sealing tape	Optically clear	Sarstedt (Nümbrecht, Germany)
Serological pipettes	Cellstar® (5 ml, 10 ml, 25 ml, 50 ml)	Greiner AG (Kremsmünster, Austria)
Slides	SUPERFROST®PLUS	ThermoScientific (Braunschweig, Germany)
Surgery tools		Fine Science Tools (Heidelberg, Germany)
Syringe	1 ml Plastipak, Luer	Becton Dickinson (New Jersey, USA)
	Original Perfusor 50 ml	B.Braun Melsungen AG (Melsungen, Germany)
Tissue	WypAll	Kimberly-Clark Corp. (Irving, USA)
	Facial tissues 6210	Abena A/S (Aaabenraa, Denmark)
Tissue Grinder	Dounce	Sigma-Aldrich (St. Louis, USA)
Vials for free-floating sections storage	Wide-Mouth Straight-Sided PPCO Jars with Closure	Thermo Fisher Scientific (Waltham, USA)

2.6. Hardware

Name	Type	Vendor
Autoclave	Systec V-65	Systec GmbH (Linden, Germany)
Bench	SAFE 2020	Thermo Fisher Scientific (Waltham, USA)
Centrifuges	5415R	Eppendorf AG (Hamburg, Germany)
	Micro200R	Andreas Hettich GmbH & Co. KG (Tuttlingen, Germany)
	Micro220R	Andreas Hettich GmbH & Co. KG (Tuttlingen, Germany)
	Universal 320R	Andreas Hettich GmbH & Co. KG (Tuttlingen, Germany)
Confocal Laser Scanning Microscope	Leica TCS SP5	Leica Microsystems AG (Wetzlar, Germany)
	Leica TCS SP8	Leica Microsystems AG (Wetzlar, Germany)
	Olympus BX61WI-F	Olympus (Hamburg, Germany)
Contrasting system for ultrathin sections	Leica EM AC20	Leica Microsystems AG (Wetzlar, Germany)
Cryostat	CM3050	Leica Biosystems GmbH (Nussloch, Germany)
Disperser	Ultra-Turrax® T 18	IKA®-Werke GmbH & CO. KG (Staufen, Germany)
Electron microscope	Jeol JEM 1011	JEOL GmbH (Eching, Germany)
Fluorescence microscope	Leica DMI6000 B	Leica Microsystems AG (Wetzlar, Germany)
Freezer -20 °C	MediLinie	Liebherr International AG, (Bulle, Switzerland)
Freezer -80 °C	KM-DU73Y1	Panasonic Corp. (Osaka, Japan)
Fridge 4 °C	MedLine	Liebherr International AG, (Bulle, Switzerland)

Gel electrophorese -power supply	PowerPac 300	Bio-Rad Laboratories (München, Germany)
Gel electrophoresis system	Sub-Cell GT Cell	Bio-Rad Laboratories (München, Germany)
Heating block	Thermomixer compact	Eppendorf AG (Hamburg, Germany)
	Thermomixer 5436	Eppendorf AG (Hamburg, Germany)
Heating plate	Combimag Ret/Rch	Janke & Kunkel IKA-Werke GmbH & Co KG (Staufen, Germany)
Hot Air Sterilisers	UT 6060	Heraeus GmbH & Co. KG (Hanau, Germany)
Hybridisation Incubator with Shaking Platform	#11655	HYBAID LIMITED (Altrincham, UK)
Ice machine	AF-10	Intercontinentale Ziegra Eismaschinen GmbH (Isernhagen, Germany)
Infrared light lamp	R95E Infrared 100 W	Koninklijke Philips N. V. (Eindhoven, The Netherlands)
Laboratory Scales		
Precision Scale	MC1 LC220S	Sartorius AG (Göttingen, Germany)
Coarse Scale	ABT-100-SM	Kern & Sohn GmbH (Balingen, Germany)
Animal Scale	LC 4200 S	Sartorius AG (Göttingen, Germany)
Microplate reader	CLARIOstar®	BMG LABTECH GmbH (Ortenberg, Germany)
Microwave	MG28F301TJS	Samsung Group (Seoul Korea)
Objectives		
10x objective (DMI6000 B)	HCX PL FLUOSTAR 20X 0.30 DRY	
20x objective (DMI6000 B)	HCX PL FLUOSTAR L 20X 0.40 DRY	

20x objective (SP5)	HC PL APO CS 20X 0.7 IMM	
20x objective (SP8)	HC PL APO 20x/0.75 IMM CS2	Leica Microsystems AG (Wetzlar, Germany)
40x objective (SP8)	HC PL APO 40x/1.30 Oil CS2	
40x objective (SP8)	HC PL APO CS2 40x/1.10 water objective	
63x objective (SP5)	HC PL APO CS 63X 1,4 oil	
63x objective (SP8)	HC PL APO CS 63X 1,4 oil CS2	
100x objective (STED)	Olympus UPlanSApo, 1.4NA	Olympus (Hamburg, Germany)
Perfusion pump	TSE 540100	TSE Systems GmbH & CO KG (Tuttlingen, Germany)
pH meter	SevenCompact™S210	Mettler-Toledo AG (Schwerzenbach, Switzerland)
qPCR Cycler	ABI PRISM® 7000 Sequence Detection System	Thermo Fisher Scientific (Waltham, USA)
Shaker	MTS4	IKA® Labortechnik (Staufen, Germany)
Spectrophotometer	NanoDrop 2000	Thermo Fisher Scientific (Waltham, USA)
STED	Custom-made	Abberior Instruments GmbH (Göttingen, Germany)
STED beam scanner	QUADScan	Abberior Instruments GmbH (Göttingen, Germany)
STED focus drive	PIFOC® focus drive	Abberior Instruments GmbH (Göttingen, Germany)
Sterile Bench	Safe 2020	Unity Lab Services, Thermo Fisher Scientific Inc. (Waltham, USA)
	BHA48	Faster SRL (Cornaredo, Italy)
Taumelrollenmischer	CAT RM 5	Ingenieurbüro CAT M. Zipper GmbH (Staufen-Etzenbach, Germany)

Thermocycler	2720 Thermal Cycler	Thermo Fisher Scientific (Waltham, USA)
	TGradient	Biometra GmbH (Göttingen, Germany)
	TADVANCED	Biometra GmbH (Göttingen, Germany)
Ultra-Low Temperature Freezer (-80 °C)	HERAfreezeTM HFU T-series	Thermo Fisher Scientific (Waltham, USA)
Vibratome	VT 1000S, VT 1200S	Leica Microsystems AG (Wetzlar, Germany)
Vortex	REAX 2000	Heidolph Instruments (Schwabach, Germany)
	Vortex Genie 2	Scientific Industries Inc. (New York, USA)
Water bath	850 022	Lauda (Lauda-Königshofen, Germany)
	GFL 1083	Werner Hassa Laborbedarf GmbH (Lübeck, Germany)
Water purification system	Milli-Q® Integral System	Merck Millipore (Billerica, USA)

2.7. Software

Name	Version	Vendor
BioRender		BioRender (Toronto, Canada)
DAVID Bioinformatics Resources	6.8	Laboratory of Human Retrovirology and Immunoinformatics (Frederick, USA)
G Power	3.1.9.2	Franz Faul (Kiel, Germany)
GelDoc Launcher		NIPPON Genetics EUROPE (Düren, Germany)
GraphPad Prism	8.0	GraphPad Software (La Jolla, USA)
ImageJ	1.51s (Fiji) Java 1.8.0_66 (64-bit)	NIH (Bethesda, USA)
Imaris	9.3.0	Bitplane AG (Zurich, Switzerland)
Inkscape	1.0.2.	Software Freedom Conservancy (New York, USA)
Leica Application Suite (LAS) AF Software	2.5.1.6757	Leica Microsystems AG (Wetzlar, Germany)
Leica Application Suite Advanced Fluorescence	2.5.0.6735	Leica Microsystems AG (Wetzlar, Germany)
Mendeley	1.19.8.	Elsevier (Amsterdam, The Netherlands)
MotionTracking	MPI-CBG, v8	Zerial lab,Max-Planck institute, Dresde (Germany)
NanoDrop 2000/2000c	1.5	Thermo Fisher Scientific (Waltham, USA)
Transcriptome Analysis Console	TAC 4.0	Thermo Fisher Scientific (Waltham, USA)

2.8. Primer

2.8.1. Quantitative polymerase chain reaction (qPCR)

Name	Direction	Sequence
Cyclophilin A	Forward reverse	5’-AGGTCCTGGCATCTTGTCCAT-3’ 5’-GAACCGTTTGTGTTTGGTCCA-3’
Tnf	Forward reverse	5’-CCACCACGCTCTTCTGTCTA-3’ 5’-AGGGTCTGGGCCATAGAACT-3’

2.8.2. Genotyping

Name	Direction	Sequence
Fadd	Forward Reverse Reverse	5’-TCACCGTTGCTCTTTGTCTAC-3’ 5’-GTAATCTCTGTAGGGAGCCCT-3’ 5’-CTAGCGCATAGGATGATCAGA-3’
Ikk2	Forward Reverse Reverse	5’-AAAGTCGCTCTGAGTTGTTATC-3’ 5’-GATATGAAGTACTGGGCTCTT-3’ 5’-TCGGCATGGACGAGCTGTAC-3’
Ikbkg	Reverse Reverse Forward	5’-CGTGGACCTGCTAAATTGTCT-3’ 5’-ATCACCTCTGCAAATCACCAG-3’ 5’-ATGTGCCCAAGAACCATCCAG-3’
Il2 (internal control for *Slco1c1*)	Forward Reverse	5’-CTAGGCCACAGAATTGAAAGATCT-3’ 5’-GTAGGTGGAAATTCTAGCATCATCC-3’
Ripk3	Forward Forward Reverse	5’-GCCTGCCCATCAGCAACTC-3’ 5’-CCAGAGGCCACTTGTGTAGCG-3’ 5’-CGCTTTAGAAGCCTTCAGGTTGAC-3’
Slco1c1	Forward Reverse	5’-GCTATTCATGTCTTGGAAGCC-3’ 5’-CAGGTTCTTCCTGACTTCATC-3’
Tak1	Forward Reverse	5’-GGCTTTCATTGTGGAGGTAAGCTGAGA-3’ 5’-GGAACCCGTGGATAAGTGCACTTGAAT-3’

2.9. Antibodies

2.9.1. Primary antibodies

Target	Host	Vendor (catalogue no.)	Dilution	IgG Type	RRID	Usage
Albumin	goat	Bethyl (A90-134)	1:600	polyclonal	AB_67120	free-floating (PFA)
Alpha-GFAP	rabbit	Dako (Z033429-2)	1:1000 (3.2 µg/ml)	polyclonal	Not available	free-floating (PFA)
Cleaved caspase-3	rabbit	Cell Signaling Technology (9664S)	1:400	monoclonal	AB_2070042	free-floating (PFA)
CD13	goat	R&D Systems (AF2335)	1:200 (1 µg/ml)	polyclonal	AB_2227288	free-floating (PFA)
CD31	rat	Bio Rad (MCA2388)	1:200 (5 µg/ml)	monoclonal	AB_2161024	free-floating (PFA)
CD31	rat	BD-Pharmingen (553370)	1:500 (1 µg/ml)	monoclonal	Not available	Cryosection, (RS)
Collagen IV	goat	Bio Rad (134001)	1:200 (2 µg/ml)	polyclonal	AB_2082646	free-floating (PFA), cryosection (PFA)
Collagen IV	rabbit	Abcam (ab6586)	1:1000 (1 µg/ml)	polyclonal	AB_305584	Cryosection (RS)
ERG	Rabbit	Abcam (ab92513)	1:200 (4.4 µg/ml)	monoclonal	AB_2630401	Cryosection (PFA)
Fibrinogen	rabbit	Dako (A0080)	1:200 (31.0 µg/ml)	polyclonal	Not available	free-floating (PFA)
Iba1	rabbit	FUJIFILM Wako Pure Chemical Corporation (019-19741)	1:100 (5 µg/ml)	polyclonal	AB_839504	free-floating (PFA)

Ki67	rabbit	Abcam (ab16667)	1:200 (0.2 µg/ml)	mono-clonal	AB_302459	Cryo-section (RS)
LAMP2	rat	Fitzgerald (10R-CD107BBMSP)	1:200 (2.5 µg/ml)	mono-clonal	Not available	free-floating (PFA)
Occludin	rabbit	Thermo Fisher Scientific (71-1500)	1:200 (1.25 µg/ml)	polyc-lonal	AB_2533977	free-floating (PFA)
Smooth muscle actin	mouse	Millipore (C6198-100UL)	1:100 (15 µg/ml)	mono-clonal	AB_476856	free-floating (PFA)
Transferrin Receptor	rabbit	Abcam (ab84036)	1:200 (5 µg/ml)	polyc-lonal	AB_10673794	free-floating (PFA)
ZO-1	rat	Thermo Fisher Scientific (14-9776-82)	1:200 (2.5 µg/ml)	mono-clonal	AB_2573026	free-floating (PFA)

2.9.2. Secondary antibodies

Target	Host	Vendor (catalogue no.)	Dilution	IgG Type	RRID	Usage
Goat IgG Alexa Fluor 488	donkey	Thermo Fisher Scientific (A-11055)	1:400 (5 µg/ml)	polyc-lonal	AB_2534102	Cryo-section (RS), free-floating (PFA)
Goat IgG Alexa Fluor 647	donkey	ThermoFisher (A-21447)	1:400 (5 µg/ml)	polyc-lonal	AB_2535864	free-floating (PFA)
Goat IgG Cy3	donkey	Jackson ImmunoResearch (705-165-147)	1:400 (3.75 µg/ml)	polyc-lonal	AB_2307351	Cryo-section (PFA), free-floating (PFA)
Mouse IgG Alexa Fluor 488	goat	Thermo Fisher Scientific (A11001)	1:100 (20 µg/ml)	polyc-lonal	AB_2534069	free-floating (PFA)
Mouse IgG Alexa Fluor 555	goat	Thermo Fisher Scientific (A21422)	1:100 (20 µg/ml)	polyc-lonal	AB_2535844	free-floating (PFA)

Mouse IgG Alexa Fluor 594	donkey	Thermo Fisher Scientific (A-21203)	1:100 (20 µg/ml)	polyc-lonal	AB_2535789	free-floating (PFA)
Mouse IgG Alexa Fluor 647	donkey	Thermo Fisher Scientific (A31571)	1:100 (20 µg/ml)	polyc-lonal	AB_162542	free-floating (PFA)
Mouse IgG Cy3	donkey	Jackson (715-165-151)	1:400 (3.75 µg/ml)	polyc-lonal	AB_2315777	free-floating (PFA)
Rabbit IgG Alexa Fluor 488	donkey	Thermo Fisher Scientific (A-21206)	1:400 (5 µg/ml)	polyc-lonal	AB_2535792	free-floating (PFA)
Rabbit IgG Alexa Fluor 647	donkey	Thermo Fisher Scientific (A-31573)	1:400 (5 µg/ml)	polyc-lonal	AB_2536183	Cryo-section (PFA), free-floating (PFA)
Rabbit IgG Cy3	donkey	Jackson (711-165-152)	1:400 (3.75 µg/ml)	polyc-lonal	AB_2307443	Cryo-section (RS), free-floating (PFA)
Rat IgG Alexa Fluor 488	donkey	Thermo Fisher Scientific (A-21208)	1:400 (5 µg/ml)	polyc-lonal	AB_2535794	free-floating (PFA)
Rat IgG Cy3	donkey	Jackson (712-165-150)	1:400 (3.75 µg/ml)	polyc-lonal	AB_2340666	free-floating (PFA)

3. Methods

3.1. Animals

All animals were obtained by “Gemeinsame Tierhaltung der Universität Lübeck” (GTH) and cared by professional animal caretakers. Mice were housed by sex (max. five animals per group) in individually ventilated green line cages (500 cm^2) with dust-free wooden bedding under a 12-hour light/dark cycle (artificial light, lights on at 7:00 a. m.). The mice were fed an autoclaved-pelleted mouse diet *ad libitum* (#1314, Altromin Spezialfutter GmbH & Co. KG) and had free access to tap water at any time. Home cages were enriched by straw as nesting material. Once a week, home cages were cleaned and equipped with new bedding.

All studies were performed following the German Animal Welfare Act and the corresponding regulation. Breeding, husbandry, and the execution of experimental procedures were approved by the local animal ethics committee (Ministerium für Energiewende, Landwirtschaft, Umwelt, Natur und Digitalisierung, Kiel, Germany).

3.1.1. Mouse lines

All mouse lines of this study were established on a C57BL/6 background. In all experiments, littermate mice at the age of 8 weeks to 15 weeks were used that were age- and sex-matched between experimental groups.

For endothelial knockout of *Fadd, Ikbkg, and Tak1* and constitutive activation of *Ikk2,* mice with the respective loxP flanked-alleles were crossed with the BAC-transgenic *Slco1c1-CreER^{T2}* line (Ridder et al., 2011, 2015), which expresses the tamoxifen-inducible CreER^{T2} under the control of the mouse *Slco1c1* regulatory sequences in BECs and epithelial cells of the choroid plexus. Besides, Nemo^{fl}*; Slco1c1-CreERT2* mice and *Nemo^{fl}* mice were crossed with *Ripk3* deleted mice (*Ripk3$^{-/-}$*; ubiquitous knockout). *Ripk3$^{-/-}$* mice have been reported previously (Kim Newton et al., 2004). The nomenclature and MGI number of the used mouse lines are shown in Table 2. Ear biopsies were taken shortly after birth to analyze the genotype, and tail tips were used after transcardial perfusion to confirm the genotype.

Mouse line	Nomenclature	MGI number
Fadd$^{fl/fl}$	B6.Cg-Thy1^{a}-Fadd^{tm1Mpa}	3700154
Nemo^{fl}	B6.Cg-Thy1^{a}-Ikbkg$^{tm1.1Mpa}$	2679024
Ripk3$^{-/-}$	B6.129-Ripk3^{tm1Vmd}	3028853
Slco1c1-CreER^{T2}	B6.D/2-Tg(Slco1c1-icre/ERT2)1Mrks	5301361
Tak1$^{fl/fl}$	B6-Map3k7$^{tm1.1Aki}$	3664194
IKK2ca	B6(Cg)-Gt(ROSA)26Sortm4(Ikbkb)Rsky/J	3687199

Table 2: Nomenclature and MGI number of the mouse lines used in this study.

3.1.2. Recombination induction

Mice were injected intraperitoneally (i. p.) with 2 mg/kg tamoxifen twice daily for five consecutive days (see section 2.4 for details). After the treatment with tamoxifen, mice with floxed alleles were referred to as either "*[name of floxed allel]*^{beKO}" or "*[name of floxed allel]*^{ca}" while the control littermates lacking the cyclisation recombinase (Cre) but receiving tamoxifen injection were termed as "*[name of floxed allel]*^{fl}" or "*[name of floxed allel]*$^{fl/fl}$". If not mentioned otherwise, mice were perfused 14 days after receiving the first dose of tamoxifen.

3.1.3. Nec-1s treatment

According to the protocol of Seifert and colleagues (Seifert et al., 2016), mice were injected intraperitoneal with 2 mg/kg Nec-1s in dimethyl sulfoxide (DMSO). The treatment started simultaneously with the recombination induction and was continued until the day of transcardial perfusion. In contrast to Seifert et al., Nec-1s was injected every 12 h instead of daily doses. As recommended by the manufacturer, we prepared Nec-1s stock solutions (15 mg/ml in DMSO) and stored aliquots at -20 °C. Every day, the required number of aliquots were thawed and diluted with PBS to a concentration of 0.75 mg/ml.

3.1.4. Transcardial perfusion and brain isolation

Mice were anaesthetized by i. p. injection of 1 g/ml triboromoethanol solution (20 µl/g body weight) or ketamine-xylazine solution (70 mg/kg and 14 mg/kg body weight). Before fixation of the animal, anaesthesia was assessed by pedal reflex (firm toe pinch), and an additional dose was administered if necessary. After the chest wall was opened and the heart was exposed, the needle of the perfusion pump was inserted into the left ventricle. Then, the right atrium was cut while the perfusion was started (speed: 450 ml/h). Subsequently, mice were decapitated and the brain was isolated, weighed, and stored according to the following experimental procedure. The tail tip (1-2 mm) was collected in a tube and stored at -20 °C for subsequent genotyping to confirm the genotype.

3.2. Histological stainings

Histological stainings were performed as described by our publication (Wenzel, Lampe, Müller-Fielitz et al., 2021).

3.2.1. Immunohistological stainings on free-floating sections

For high-resolution microscopy, brains were postfixed in 2 % PFA in PBS for 7 h at 4 °C, washed in PBS, and stored in PBS at 4 °C. After five days at the latest, brains were sectioned using a vibratome. To fix the brains to the specimen plate, they were first embedded in 4 % agarose in PBS and horizontally glued to obtain sagittal sections. The specimen plate was inserted into the vibratome tray filled with PBS. After installing and adjusting the razor blade, 100-µm thick sections were collected at a speed of 0.3-0.6 mm/s and a vibration amplitude of 1.00 mm. Sections were stored in straight-sided wide-mouth jars filled with 50 % glycerol in PBS at -20 °C. Before performing IHC, vibratome sections were washed two times in Dulbecco's PBS in a 24-well plate for 5 min at RT. Then, PBS was exchanged against the blocking solution (section 2.4). After blocking for 6 h at RT, sections were incubated with primary antibodies in blocking solution at 4 °C for 72 h. Subsequently, sections were washed (Dulbecco's PBS, 3x, 10 min) and then incubated with secondary antibodies in blocking solution at 4 °C overnight. The next day, sections were washed (Dulbecco's PBS, 3x, 10 min), and nuclei were counterstained using DAPI in PBS for 5 min. After two more washing steps (Dulbecco's PBS, 5 min), sections were mounted on SUPERFROST slides and sealed with coverslips by Dako fluorescent mounting medium. During the whole staining procedure, sections were gently shaken. Slides were stored light protected at 4 °C.

3.2.2. Immunohistological stainings on cryosections

Mice were perfused with 20 ml of Ringer's solution with heparin, and brains were frozen on dry ice and stored at -80 °C. Before starting sectioning, brains were kept at -20 °C for approximately 12 h. The cerebellum was removed and stored at -80 °C for western blot analysis. Brains were glued vertically onto a metal specimen disc with tissue freezing medium without the cerebellum. Cutting was performed at -20 °C, and obtained sections were coronal and with a thickness of 20 µm. Sections were taken starting at corpus callosum and attached to SUPERFROST slides. Subsequently, they dried at room temperature (RT) for 20 min and were stored at -20 °C until immunofluorescence was performed. Sections were postfixed for 10 min in methanol at -20 °C. After postfixation, slides were washed in PBS (2x, 5 min, RT), and sections were surrounded by a fatty pen. Subsequently, sections were blocked with either 1 % BSA in PBS (methanol postfixation and TUNEL assay) or 1 % BSA and 0.1 % Triton X-100 in PBS (PFA postfixation). After one hour of incubation in blocking solution, sections were incubated with primary antibodies in blocking buffer overnight at 4 °C. The next day, sections were washed (3x, 5 min, RT) and incubated with the secondary antibodies and DAPI in blocking buffer for two hours at RT. Again, slides were washed (3x, 5 min, RT) and sealed with coverslips using MOWIOL.

3.2.3. Alizarin Red S

Cryosections were obtained as described in 3.2.2. Sections were washed in PBS and postfixed for 6 min in a 1:1 acetone-methanol mixture at RT. After slides were washed in distilled water for 10 min, the sections were surrounded by a Dako pen, and Alizarin Red S solution was incubated for 60 s. Excessive dye was removed, and slides were dipped in acetone (20x), 1:1 acetone-xylol mixture (20x), xylol (20x) and sealed with coverslips using MOWIOL.

3.2.4. TdT-mediated dUTP-biotin nick end labelling (TUNEL) assay

Animals were perfused with 15 ml of Ringer's solution with heparin and 15 ml 4 % PFA in PBS. After removal, brains were postfixed in 4 % PFA in PBS at 4 °C overnight and transferred to a 30 % sucrose solution the next day. The following day, brains were dried on tissue and shock-frozen in 2-methylbutane on dry ice. After freezing, the brains were stored at -80 °C. Preparation of cryosections (coronal, 40 µm) and IHC was performed as described in section 3.2.2. For the TUNEL assay, no further postfixation was necessary.

Heat-induced epitope retrieval was performed by using a 10 mM sodium citrate buffer. A coplin jar filled with buffer was put in a water bath and heated up to 95 °C. Then, slides were transferred to the coplin jar, and the temperature was kept for another 20 min. When the time was elapsed, the coplin jar was placed at RT until the buffer was cooled down to 25-30 °C.

TUNEL assay was applied after IHC staining according to the manufacturer's kit information. In brief, the enzyme solution was diluted at 1:10 in label solution. Sections were incubated with 50 µl of the reaction mix for 60 min in a humidified atmosphere in the incubator at 37 °C in the dark. Then, sections were washed in PBS, stained with DAPI, and imaged by confocal microscopy using the argon laser for excitation (488 nm).

3.2.5. Expansion microscopy

Expansion of the free-floating sections was performed after immunofluorescence staining as described in section 3.2.1. The sections were incubated with methacrylic acid N-hydroxy succinimidyl ester (1 mM in PBS) for 1 hour at RT in a 24-well plate. After washing in PBS (2x, 10 min), monomer solution was added for 45 min at RT. Subsequently, sections were transferred to a coverslip with 2 spacer cover glasses at each side and topped by another cover glass. Gelation solution was added to the sections by carefully pipetting below the coverslip. Samples were incubated for 2-2.5 hours at 37 °C in a humidified environment. The excessive gel was removed, and sections were transferred carefully to a glass-bottom 6-well dish. Then, the samples were incubated in digestion buffer at 37 °C overnight. The following day, expansion was performed by incubating the sections 3-4 times in distilled water for 20 min and subsequent embedding in agarose (0.8 % in aqua bidest) for immobilisation. Images were taken with an HC PL APO CS2 40x/1.10 water objective. Expansion microscopy was used for the qualitative representation of occludin and ZO-1 morphology.

3.3. Imaging and image analysis

3.3.1. Fluorescence microscopy

Imaging was done by the fluorescence microscope Leica DMI6000 B equipped with a DFC360FX camera, and the LAS software was used for the appropriate settings. The filter cubes were chosen depending on excitation and emission (Table 3). The 10x objective was used for qualitative tile scans from IgG and Alizarin Red S staining and imaging on cryosections for vessel and angiogenesis analysis.

Filter Cube	Fluorochrom
A4	DAPI
L5	Alexa488
N3	Cy3, Alexa594

Table 3: Filter cubes and related fluorochromes used for fluorescence microscopy.

Vessel analysis

Kristin Müller performed imaging of the samples. String vessel length and vessel length analysis were done by Kristin Müller and me (Wenzel, Lampe, Müller-Fielitz et al., 2021). String vessels were identified as collagen IV^{+} (Coll IV) tube-like structures negative for the vessel marker CD31. By using the “Freehand Line” tool of ImageJ, string vessels were manually tracked, and the length and the total number were reported. Total vessel length analysis was performed on CD31 stained sections automatically using the “Skeleton” plugin. The total length of string vessels was normalized to the total vessel length.

Angiogenesis

Cells positive for Kiel67 (Ki67) and Coll IV were counted and normalized to the image area. For each animal, 12 images were obtained.

3.3.2. Laser-scanning confocal microscopy

Immunostaining images were taken by either TCS SP5 or TCS SP8 confocal laser scanning microscope, and the LAS AF software was used for the appropriate settings. The 405-Diode and three different lasers were used for excitation: Argon, HeNe 543, and HeNe 633. Emission of the fluorochromes was detected by PhotoMultiplier Tubes, and the range of emission detection was manually adjusted according to the individual emission and excitation spectra of the used fluorochromes.

All images were taken as z-stacks with 12-bit (SP8) or 16-bit (SP5) colour depth. The LAS AF software calculated optimal z-stack step sizes according to optical characteristics of the objective, emission wavelength and pinhole. Laser intensity and gain settings were adjusted to optimize the pixel saturation of the target structure.

All methods used in section 3.3.2 are published (Wenzel, Lampe, Müller-Fielitz et al., 2021).

Transcytosis and extravasation

For IgG transcytosis, stacks of approximately 9 µm were taken with the HCX PL APO CS 63x/1.4 oil (CS2) objective (Leica TCS SP5 and SP8). Deconvolution was performed based on the default settings for confocal microscopy and dependent on the used fluorochrome by the Huygens Software. Then, IgG-filled vesicles were analyzed using Imaris 9.3.0. First, 3D vasculature masks were generated from either Coll IV or CD31 immunostained tissue and smoothed under 1.0 µm (Coll IV) or 0.8 µm (CD31) surface details by using the “Surface” function (Figure 4). By using the “Spots” function, vesicles were identified by “Quality” and an estimated diameter of 0.5 µm. The vesicle number was normalized by the volume of the vessel mask. IgG extravasation was quantified by measuring the IgG intensity outside the vessel mask, and the values were normalized to the parenchymal volume.

IgG vesicle and IgG extravasation quantifications were achieved from 10-15 images per animal. Images were taken from the cortex if not stated otherwise. The same procedure was performed to analyse fibrinogen, lysosome-associated membrane protein 2 (LAMP2), and TfR vesicles. Ümit Özorhan analyzed albumin extravasation by measuring albumin mean intensity outside the vessels using ImageJ.

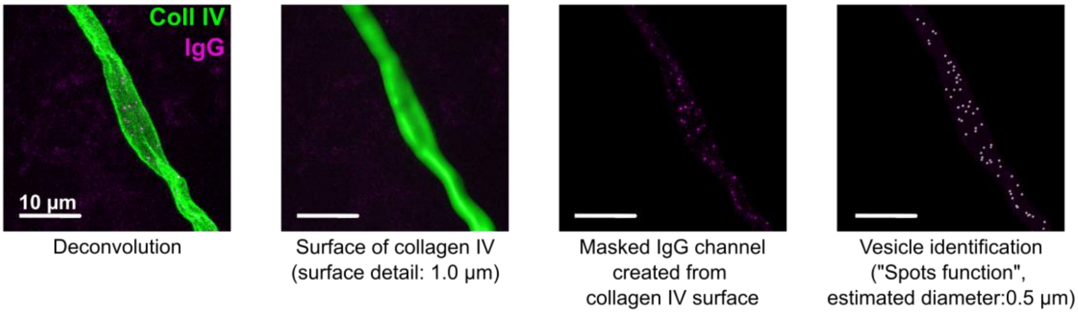

Figure 4: Scheme showing the procedure of IgG vesicle analysis in vessels.

String vessel and astrocyte analysis

For string vessel analysis from free-floating sections and glial fibrillary acidic protein (GFAP) analysis, stacks of approximately 30 µm were taken with an HCX PL APO CS 20x/0.7 IMM objective (Leica TCS SP5).

String vessels and $GFAP^+$ astrocytes were analyzed by the ImageJ software. String vessels were identified as described above (section 3.3.1.). For total vessel length, Coll IV staining was analyzed by the “Skeleton” plugin of ImageJ. A mask of the GFAP staining was created, and $GFAP^+$ astrocytes were quantified as the percentage of the whole image area. Quantifications were obtained from 4-6 images per animal. Images were taken from the cortex if not stated otherwise.

The HC PL APO CS2 40x/1.30 OIL CS2 objective was used for the vascular tree analysis, and images with a z-size of approximately 30 µm were taken (Leica TCS SP8).

String vessels were counted manually and tracked in tile scans from the cortex, hippocampus, and hypothalamus. For the starting point of the vascular tree, we selected α- smooth muscle actin $(\alpha\text{-SMA})^+$ vessels, which mainly represent arterioles and arteries. String vessels adjacent to arteriole vessels were termed as first-order capillary string vessels, etc. (Figure 5). The number of string vessels was normalized to the area of the image.

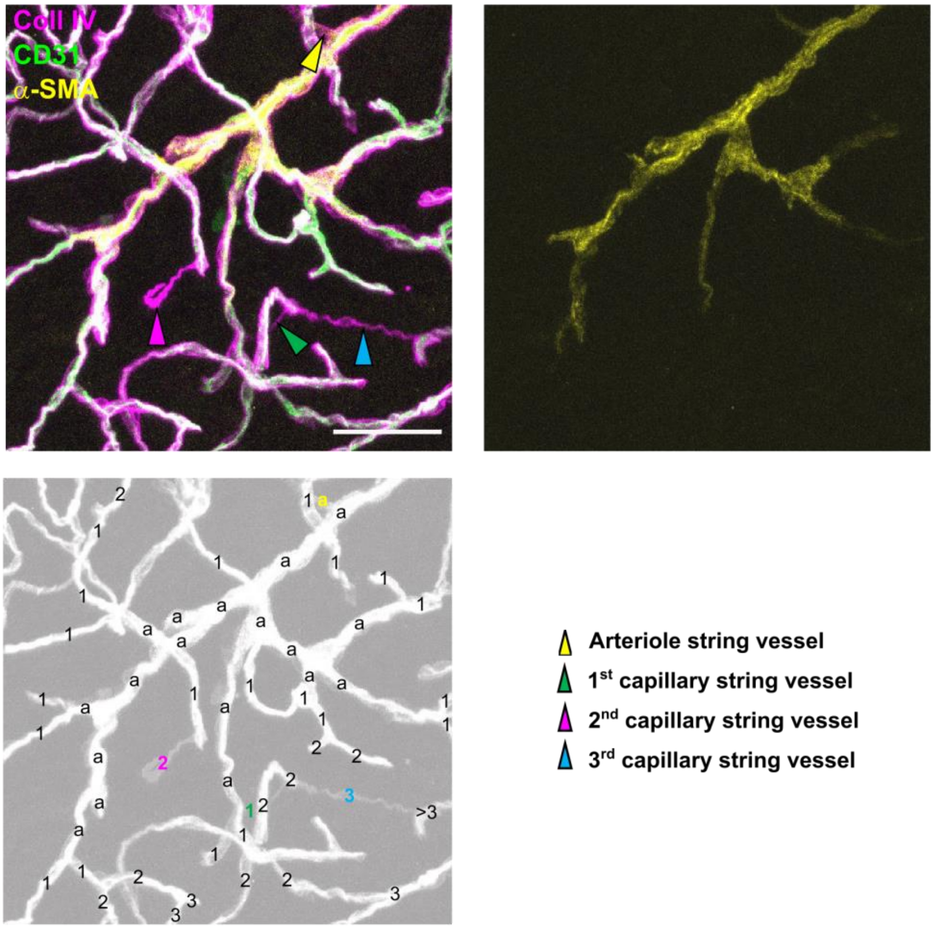

Figure 5: Vascular tree analysis. *Upper and lower images show arteriole, 1st capillary, 2nd capillary and 3rd capillary string vessels. Arteriole vessels were identified by colocalisation of Coll IV with α-SMA (upper images). String vessels adjacent to arteriole vessels were termed as 1st order capillary string vessels, etc. (lower image).*

Pericyte coverage and vessel diameter

Images for pericyte quantification had a stack size of 18 µm and were taken using the HC PL APO CS2 40x/1.30 OIL objective (Leica TCS SP8). Analysis was performed with the Motion-Tracking software. In short, the $CD13^+$ area inside the Coll IV^+ vessels was measured and normalized to the total Coll IV^+ area. The Coll IV staining of the same images has been analyzed in ImageJ by the “DiameterJ” plugin to measure the frequency of vessel diameters in a histogram. For both analyses, ten images per animal were used.

Endothelial cell death

Images were achieved with a stack size of 33 µm using an HCX PL APO CS 20x/0.7 IMM objective (Leica TCS SP5). Endothelial cell death was identified by $TUNEL^+$ and Coll IV^+ vessels normalized to the image area. For each animal, four images were analysed.

TJ interruptions

For quantitative analysis of occludin interruptions, 15 images per animal with a stack size of 12.6 µm have been taken with an HC PL APO 40×/1.3 oil objective. The occludin and ZO-1 TJ lengths were traced manually using the Simple Neurite Tracer plugin. Subsequently, occludin length was normalized to ZO-1 length.

3.3.3. Stimulated emission depletion (STED) microscopy

Markus Krohn performed STED microscopy of IgG-filled vesicles (Wenzel, Lampe, Müller-Fielitz et al., 2021). A 100x objective was utilized, and 485- and 561-nm diode excitation lasers and 775-nm STED laser were used. All were pulsed at 40 MHz. A doughnut-shaped (2D-STED) or a top-hat (3D-STED) phase mask was produced by a spatial light modulator (Hamamatsu), which shapes different depletion beams without changing the optical setup. In addition, photobleaching was reduced at an optimal signal to noise ratio by using DyMIN® adaptive illumination. A beam scanner was used for xy-scanning and a PIFOC® focus drive for z-scanning. All images were produced using the same setting.

IgG transcytosis

IgG-filled vesicles were analyzed as described before (section 3.3.2) using Imaris 9.3.0. The 3D vasculature masks were created and smoothed under 0.4 µm surface details. The settings for the quantification of the vesicle number remained the same.

IgG-filled vesicle quantifications were achieved from 3 images per animal using four animals per group. Images were taken from the cortex.

3.3.4. Electron microscopy

Sample preparation

As described in our publication (Wenzel, Lampe, Müller-Fielitz et al., 2021), mice were perfused with 15 ml Ringer's solution with heparin and 15 ml freshly prepared glutaraldehyde fixative. Brains were removed and postfixed in Monti-Graziadei solution for at least 48 h at 4 °C. Brain cortices were cut into cubes to a size of approximately 1 mm^3 using a matrix for mouse brains and razor blades. Further sample preparation and electron microscopy imaging were organized by Peter König and performed by Christo Örün (Institute of Anatomy, University of Lübeck). Samples were fixed in 1 % osmium tetroxide in 0.1 M cacodylate buffer for 2 h. Then, samples were dehydrated in ascending series of ethanol and incubated in propylene oxide followed by a 1:1 mixture of propylene oxide and araldite and embedded in araldite for subsequent sectioning. Ultrathin sections with a size of 80 nm were moved to copper grids and contrasted in a contrasting system for ultrathin sections using uranyl acetate ready-to-use solutionand lead citrate ready-to-use-solution.

Imaging and analysis

Imaging from vessels smaller than 10 µm was performed using an electron microscope. First of all, an overview image of a capillary cross-section was taken. A collage of partially overlapping images (4-8 images/vessel) was taken with higher magnification from this area. Using Inkscape's transparency function, the images were assembled to the original vessel cross-section using the overview images as a template. For the manual quantification of cytosolic vesicles, images were analyzed by ImageJ. By using the elliptical selection tool, vesicles were encircled, and for the determination as a vesicle, different criteria points selected by previous reports had to be fulfilled:

- Vesicles showed a boundary line which distinguished the vesicle from the cytoplasm (Jastrow, 2018; Zhou et al., 2021).
- The diameter range of a vesicle was between 30 nm (minimal diameter exosomes) and 200 nm (maximal diameter clathrin-coated vesicles) (Brodsky, 2016; Mondal et al., 2019).
- The lumen of the vesicles was either transparent/white (caveolin-coated vesicles) or grey with electron-dense areas close to the vesicle boundary (clathrin-coated vesicles) (Zhou et al., 2021). Structures with electron-dense, black lumen were considered as artefacts (Varga et al., 2020).
- Structures that fulfilled the former criteria but clearly showed irregular formed structures (neither round nor elliptical) or showed rather a tube-like structure (typical for dictyosomes) were not considered to be vesicles (*Golgi-Apparat Dr.Jastrows EM-Atlas*, n.d.).

The total number of counted vesicles per vessel was normalized to the length of the luminal membrane in µm. Three vessels were analyzed per animal.

3.4. Dextran extravasation

Fluorescein isothiocyanate (FITC)-labelled dextran (4 kDa) was suspended in PBS (12 mg/ml) and intravenously injected (100 µl per mouse) 30 min before perfusion (Ringer’s solution with heparin, 20 ml) (Wenzel, Lampe, Müller-Fielitz et al., 2021). Brains were removed and stored at -80 °C. From now on, brains were protected from light whenever possible. One hemisphere per brain was homogenized in 500 µl Tris-HCl (50 mM, pH 8.0) in 2-ml reaction tubes using a disperser. After centrifugation (16,100 g for 30 min, RT), supernatants (ca. 350 µl) were transferred to fresh tubes, and the same volume of methanol was added. After another centrifugation (16,100 g for 15 min, RT), 150 µl of the supernatants were transferred to a 96-well plate. A serial dilution of the 12 mg/ml dextran stock solution was prepared starting with 187.5 pg/ml as the highest concentration to determine absolute dextran concentration from a standard curve. A microplate reader detected fluorescence in supernatants at 530 nm with an excitation wavelength of 483 nm.

3.5. Nucleic acid analysis

3.5.1. Quantitative PCR

Ribonucleic acid (RNA) isolation and cDNA synthesis

For tissue lysis, 600 µl of the lysis buffer (RA1) were added to 240-µm coronal sections from midbrains. Samples were vortexed and pipetted into the NucleoSpin filter in a 2-ml reaction tube. Then, tubes were centrifuged (11,000 g, 1 min, RT), the supernatant was transferred to a new reaction tube, and 600 µl of 70 % ethanol was mixed with the supernatant.

RNA columns were placed into a 2-ml reaction tube for RNA isolation, and the supernatant-ethanol solution was added. Tubes were centrifuged (11,000 g, 30 s, RT), 350 µl of membrane desalting buffer was added to the columns, and tubes were centrifuged again (11,000 g, 1 min, RT). The filtrate was discarded, and the column was incubated with 95 µl of DNase reaction mix (10 µl rDNase + 90 µl reaction buffer) for 15 min at RT.

After DNA digestion, the membrane was washed and dried. First, the reaction was stopped by 200 µl inactivation buffer (RAW2), and tubes were centrifuged (11,000 g, 30 s, RT). Membranes were washed with 600 µl washing buffer (RAW2), centrifuged (11,000 g, 30 s, RT), washed again with 250 µl washing buffer and centrifuged (11,000 g, 2 min, RT). The column was placed into a nuclease-free collection tube (1.5 ml, supplied), and RNA was eluted using 60 µl of RNase-free H_2O (supplied with the Kit). Tubes were centrifuged (11,000 g, 1 min, RT), and the column was discarded. RNA concentration was measured at 260 nm using a spectrophotometer (NanoDrop). In the following, RNA solution was diluted with diethyl pyrocarbonate (DEPC) water to 400 ng (in a total volume of 35 µl) and stored at -80 °C.

For cDNA synthesis, the master mix solution was prepared as indicated in 2.4 and added to 35 µl of the diluted RNA samples. After 10 min of incubation at RT, samples were incubated for 90 min at 37 °C.

qPCR

Quantitative PCR was performed with undiluted cDNA samples (*Tnf*) or diluted 1:8 in DEPC water (*Cyclophilin A*). For qPCR, 23 µl of the super mix was mixed with 2 µl cDNA solution for each sample in a PCR-96-well plate. In addition, 2 wells were filled with super mix solution and DEPC water as a negative control. Well-plates were sealed with optically clear sealing tape. The qPCR was performed by a qPCR cycler as described in Table 4.

Step	Temperature	time	No. of cycles
Preincubation	50 °C	120 s	1x
Initial denaturation	95 °C	120 s	
Denaturation	95 °C	15 s	40x
Annealing	60 °C	60 s	
Denaturation	95 °C	15 s	1x
Final elongation	60 °C	20 s	
Melting curve	95 °C	15 s	

Table 4:Time course of qPCR

Subsequently, the quality of the qPCR was checked by the melting curve. Since the primers for the housekeeping gene *Cyclophilin A* are well established, but the primers for *Tnf* were not tested in our laboratory before, the qPCR product was separated with gel load buffer in a 2.5 % ethidium bromide agarose gel. Thus, the theoretical size of the PCR product of 103 bp could be confirmed by a band at approximately 100 bp. By using the cycle threshold (Ct) values achieved by the amplification curves, the relative fold gene expression of *Tnf* was calculated by the delta-delta Ct method ($2^{-\Delta\Delta Ct}$). In the first step, Ct values were averaged for the three technical replicates of each sample for *Tnf* and *Cyclophilin A* PCR. ΔCt values were calculated using the newly created average Ct values as described below. Then, the mean of all ΔCt values of the reference group, the *Nemo*^{fl} mice, were calculated. To achieve the ΔΔCt value, the mean ΔCt value from the *Nemo*^{fl} group was subtracted from each ΔCt value. Finally, the fold gene expression was achieved by two to the power of negative ΔΔCt. The formulas are shown below.

$$\Delta Ct = Ct(\text{Tnf}) - Ct(\text{Cyclophilin A})$$

$$\Delta\Delta Ct = \Delta Ct - mean_{\Delta Ct}(\text{Nemo}^{\text{fl}})$$

$$Fold\ gene\ expression = 2^{-\Delta\Delta Ct}$$

3.5.2. Microarray analysis

Jan Wenzel and Beate Lembrich carried out tamoxifen treatment and sample preparation for microarray analysis.

Vessel fragment isolation

For vessel fragment isolation, glassware, surgery tools, and solutions were autoclaved (180 °C, 3 h) or purchased sterile whenever it was possible.

First, media and solutions have been prepared as described in section 2.4. The next day, mouse brains were isolated. Mice were deeply anaesthetized by isoflurane and decapitated quickly. Heads were dipped in 70 % ethanol on ice, and brains were transferred to sterile and ice-cold PBS. Meninges were removed in the cell culture hood by rolling the brain on Whatman paper, and cerebellum and olfactory bulb were cut out and discarded. The cerebrum was cut into four pieces before they were transferred to a tissue grinder with 5 ml of working medium (4 °C). Homogenisation in the tissue grinder was performed using two pistils of different sizes (30 strokes with pistil A, 25 strokes with pistil B).

Homogenized tissue was transferred to a 50-ml Falcon tube, and the grinder was cleaned by another 5 ml of the working medium, which was subsequently added to the Falcon tube with the brain lysate. After centrifugation (3500 rpm, 5 min, 4 °C), the supernatant was aspirated gently, and the pellet was resuspended in 15 ml of a dextran solution (4 °C). After 2 min of vortexing, the solution was centrifuged to separate the myelin layer (8000 rpm, 10 min, 4 °C). The foamy myelin layer was removed using a 10-ml pipette, and the pellet was resuspended in dextran solution and centrifugated (8000 rpm, 10 min,4 °C). Subsequently, the pellet was washed in 10 ml of PBS and centrifuged again (3500 rpm, 5 min, RT). Then, the pellet was suspended in 5 ml PBS and transferred to a 40 µm cell strainer. The cell strainer was placed reversely on a petri dish. Vessel fragments were extracted from the cell strainer by rinsing with 2 ml PBS and using a cell scraper. The suspension was centrifuged (14,000g, 5 min, 4 °C), and the pellet was resuspended in 1x CLB buffer, mixed, and stored at -20 °C.

RNA extraction and microarray analysis

The RNA extractions from vessel fragments were performed with the RNeasy Mini Kit. RNA concentration was determined by a spectrophotometer at 260 nm (NanoDrop). Samples were sent to the working group of Norbert Hübner at the Max-Delbrück-Center for molecular medicine in Berlin. There, the RNA quality was controlled, and microarray analysis was performed.

Statistical analysis

Statistical analysis of the data was performed using the Transcriptome Analysis Console and DAVID Bioinformatics Resources. Genes with a false discovery rate (FDR) p-value < 0.05 and at least two-fold changed were considered as regulated. DAVID Bioinformatics Resources was used to perform gene enrichment analysis and functional annotation analysis. For this purpose, the databases of GOterm Biological Pathways Direct, KEGG pathway, and BioCarta have been chosen.

3.5.3. Genotyping

gDNA extraction

Ear or tail biopsies were collected in 1.5-ml reaction tubes and incubated with lysis buffer overnight at 56 °C. The next day, samples were vortexed and centrifuged (16,100 g, 3 min, RT). The supernatant was transferred to new 1.5-ml reaction tubes and acclimatized to 4 °C for 10 min. Then, 600 ml of ice-cold ethanol (absolute) were added, and tubes were swivelled 6-8 times. Subsequently, samples were centrifuged (14,000 rpm, 8 min, 4 °C), and the pellet was washed with 500 µl 70 % ethanol and centrifuged again (14,000 rpm, 8 min, 4 °C). The supernatant was discarded, the pellet was dried at 56 °C for 10 min and resuspended in 200 µl aqua bidest.

Amplification

The reaction mix was prepared as shown in section 2.4., and 20 µl were added to 2 µl of gDNA sample (8 µl for the *Ikbkg* PCR). PCR was performed as shown in Table 5.

	Fadd	***Ikk2***	***Ikbkg***	***Ripk3***	***Slco1c1***	***Tak1***
	4 °C					
Initialisation	94 °C, 5 min					
Denaturation	94 °C, 30 s					
Annealing	55 °C, 30 s	60 °C, 30 s	60 °C, 30 s	60 °C, 30 s	60 °C, 30 s	65 °C, 30 s
Extension/Elongation	72 °C, 45 s					
No. of cycles	*35x*	*35x*	*35x*	*35x*	*30x*	*35x*
Final Elongation	72 °C, 10 min					
Final hold	4 °C					

Table 5: PCR procedure for mouse gDNA amplification*. The grey background indicates a repeating process.*

PCR products and a 100-bp-marker were run on a 2 % agarose gel for 30-40 min at 190 V to analyze the genotypes.

3.6. Statistical analysis

Data were analyzed using GraphPad Prism 8 and SPSS 25 with the advice of Sonja Binder (Wenzel, Lampe, Müller-Fielitz et al., 2021). Sample sizes were chosen according to former publications (Ridder et al., 2011, 2015; Villasenõr et al., 2016). Significance was considered if $p < 0.05$ if not mentioned otherwise. Statistical methods are specified in the figure legends. Parametric statistics (e.g., t-Test, ANOVA) were only used if variances were not significantly different between the groups (tested by Brown-Forsythe, Levene's or F-test). If variances were significantly different or the sample size was very small, non-parametric methods were used as designated in the figure legends. All data were analyzed without an outlier test if not stated otherwise. Graphs show data with the standard error of the mean (SEM).

In all animal experiments, animals were randomly assigned to treatment groups but matched with regard to age-, sex-, and littermate conditions.

4. Results

4.1. Brain endothelial deficiency of NEMO leads to endothelial cell death and cSVD characteristics

In the last decade, research from our laboratory could show severe brain vascular defects if NEMO is absent in BECs (Körbelin et al., 2016; Ridder et al., 2015). To further study the function of NEMO in BECs, we used the tamoxifen-inducible *Nemo^{FL}; Slco1c1-CreER^{T2}* mouse line. Mice with floxed *Ikbkg* allele and carrying the recombinase were termed *Nemo^{beKO},* while mice carrying the floxed *Ikbkg* allele but missing the recombinase were termed *Nemo^{fl}*. The selectivity of the recombination for BECs but not for cells in peripheral tissues has been proved elsewhere (Ridder et al., 2011). Previous work showed that brain endothelial deletion of *Ikbkg* leads to a 60 % reduction of NEMO protein expression in primary BECs derived from *Nemo^{beKO}* mice (Ridder et al., 2015).

As observed in the former work, we could show a solid increase in string vessel formation in *Nemo^{beKO}* mice after tamoxifen injection (Körbelin et al., 2016; Ridder et al., 2015). String vessels were observed as thin tubes positive for the basement membrane marker Coll IV but negative for the endothelial cell marker CD31. While these structures are scarce in *Nemo^{fl}* mice, many were found in *Nemo^{beKO}* mice (Figure 6a). High-resolution imaging using STED microscopy characterised string vessels as thin tubes with a typical diameter of 0.5-1 µm (Figure 6b). In addition to the occurrence of string vessels, a previous report by Ridder and colleagues revealed vessel rarefaction accompanied by a reduced blood flow in *Nemo^{beKO}* mice (Ridder et al., 2015). Since blood flow is also dependent on vessel diameter, we investigated whether this parameter is changed in *Nemo^{beKO}* mice. Accordingly, we analysed confocal images from Coll IV-stained brain sections (Figure 6c and d). By measuring the frequency of Coll IV$^+$ vessel diameters, we observed a shift from smaller diameters towards bigger diameters in *Nemo^{beKO}* mice, suggesting that smaller-diameter vessels were primarily lost. This finding might indicate reduced constriction of brain vessels in *Nemo^{beKO}* mice. Since pericytes have a crucial function for pre-capillary arteriole constriction, we checked if pericyte loss decreases the blood flow by dysregulation of the vessel's diameter (Fernández-Klett & Priller, 2015). Quantification of pericyte coverage, stained by a CD13-antibody, showed a slight but significant reduction in *Nemo^{beKO}* mice. In conclusion, loss of small-diameter vessels in *Nemo^{beKO}* mice could result from increased vasodilation due to pericyte loss.

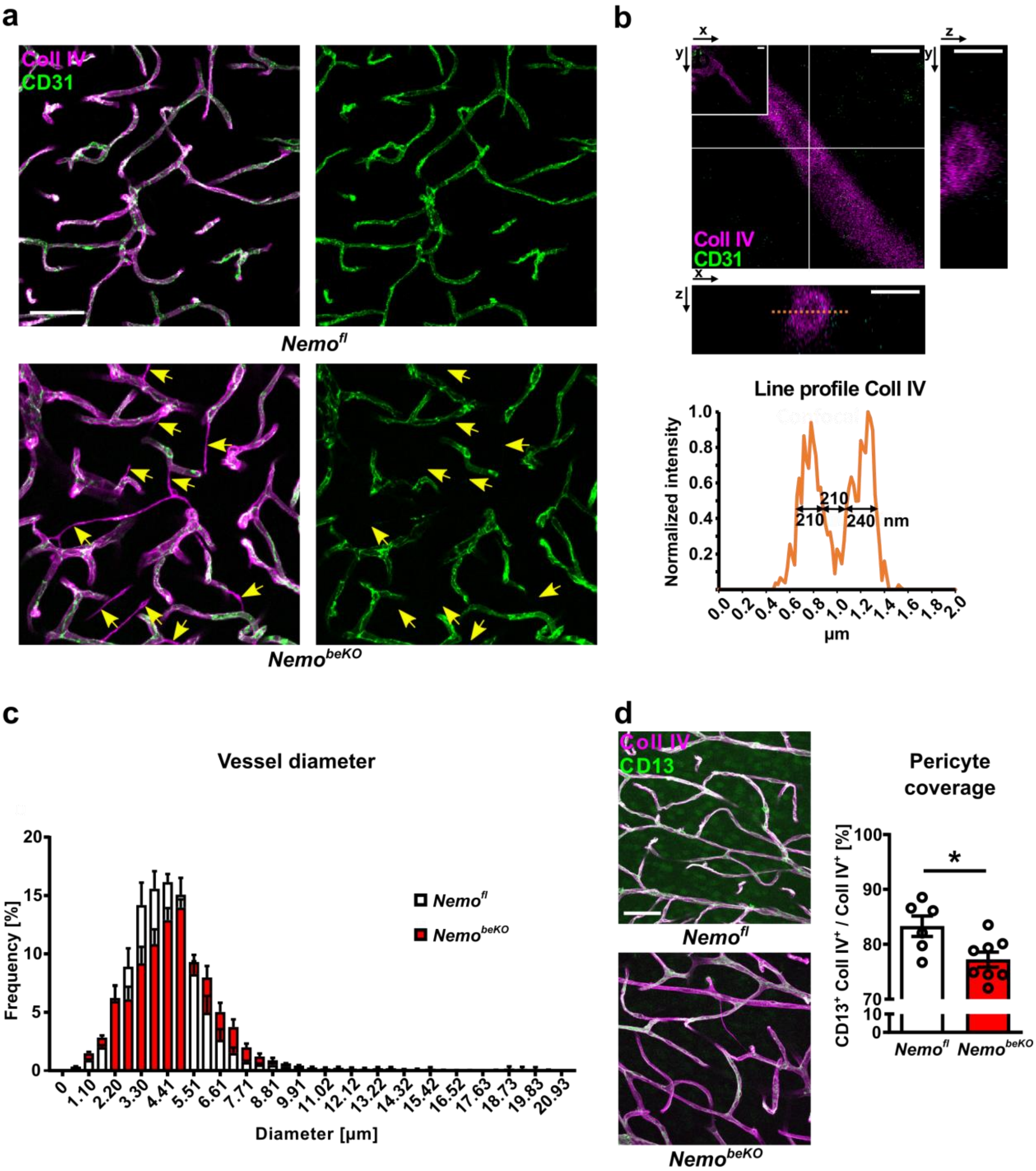

Figure 6: Ablation of NEMO led to vascular abnormalities. *(a) Representative images showed the cerebral vasculature of* Nemo^{fl} *and* Nemo^{beKO} *mice. Arrowheads indicate the massive occurrence of string vessels in* Nemo^{beKO} *mice which are positive for the basement membrane marker Coll IV but lack the endothelial marker CD31. Scale bar, 50 µm. (b) Super-resolution microscopy (STED) indicated string vessels as thin tubes with a diameter of 0.5 to 1.0 µm. An exemplary line profile of a string vessel is shown below. Scale bars, 1 µm. (c) Vessel diameter analysis of* Nemo^{fl} *and* Nemo^{beKO} *mice observed a shift from smaller towards bigger vessels in* Nemo^{beKO} *mice. The histogram shows the diameters of Coll IV^{+} vessels. Statistical analysis was not performed due to a low N-number (N = 3 animals/group). (d)* Nemo^{beKO} *mice show a significantly lower pericyte coverage. Scale bar, 50 µm. Unpaired t-test, T (12) = 2.7, p = 0.019, N = 6-8 animals/group. * p < 0.05. All figures are published (Wenzel, Lampe, Müller-Fielitz et al., 2021).*

Vessel rarefaction and pericyte loss can be typical symptoms of cSVD. Further, it is known that cSVD's pathologies are related to the capillary bed. Thus, we investigated if string vessels are emerging from brain capillaries. Inspired by the vascular tree analysis Hill and colleagues did, we performed stainings of Coll IV, CD31, and α-SMA in brain sections of *Nemo*^{fl} and *Nemo*^{beKO} mice to determine the localisation of string vessels in the vascular tree (Hill et al., 2015). As described by Figure 5, string vessels positive for α-SMA are defined as arteriolar string vessels, and adjacent string vessels are termed as first, second, third and higher-numbered (or venous) capillary string vessels. For this analysis, the cortex, hippocampus and hypothalamus were investigated. Tracking of string vessels in three brain areas showed a significantly higher number of string vessels present in higher branch orders of the vascular tree (Figure 7). Altogether, these data suggest that brain endothelium specific deletion of *Ikbkg* mainly affects capillaries.

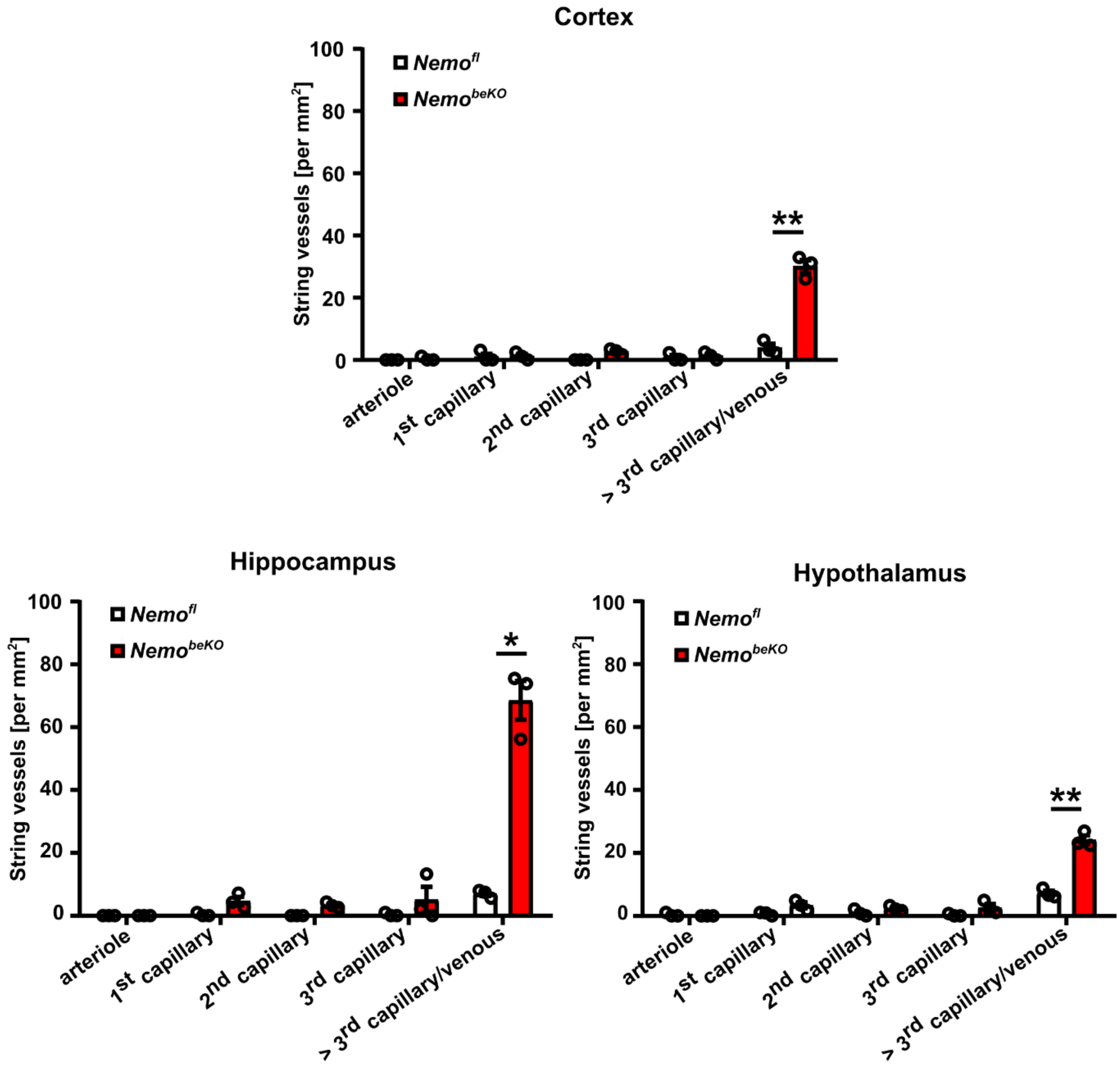

***Figure 7: Vascular tree analysis observed string vessels in higher branch orders**. String vessel formation in* Nemo^{beKO} *mice was significantly increased in the higher branch orders in the cortex, hippocampus, and hypothalamus. Repeated measures ANOVA followed by Sidak's post-hoc tests (cortex: genotype: $F(1,4) = 171.6$, $p = 0.002$; branch order: $F(1.9,7.8) = 103.9$, $p < 0.001$; interaction: $F(4,16) = 63.8$, $p < 0.001$; hippocampus: genotype: $F(1,4) = 77.2$, $p < 0.001$; branch order: $F(1.8,7.2) = 95.0$, $p < 0.001$; interaction: $F(4,16) = 62.32$, $p < 0.001$; hypothalamus: genotype: $F(1,4) = 67.2$, $p = 0.001$; branch order: $F(1.6,6.2) = 153.2$, $p < 0.001$; interaction: $F(4,16) = 45.23$, $p < 0.001$; N = 3 animals/group). * $p < 0.05$; ** $p < 0.01$. All figures are published (Wenzel, Lampe, Müller-Fielitz et al., 2021).*

Several studies interpret string vessels as a consequence of endothelial cell death (Brown, 2010; Hunter et al., 2012; Y. Jiang et al., 2020; Ridder et al., 2015; Zille et al., 2019). Thus, co-staining of Coll IV and cell death markers, such as cleaved Casp3 and TUNEL reaction, were performed for *Nemo^beKO^* mice. While Casp3 is a specific marker for apoptosis, the TUNEL assay is based on the enzymatic attachment of fluorochrome-tagged deoxynucleotides to free 3'-hydroxyl termini of DNA double-strand breaks. Although DNA breaks or fragmentation have been often declaimed as a characteristic marker of apoptosis, it is well-investigated that DNA fragmentation can also occur in necrosis (Kraupp et al., 1995; W. P. Li et al., 1997; Zhivotovsky & Orrenius, 2001). Therefore, the TUNEL reaction offers no conclusions about a specific type of cell death but rather indicates cell death in general. Due to the lack of cells in string vessels, we could not observe any string vessels positive for cleaved Casp3 or TUNEL but instead often found adjacent vessels to be positive for the cell death markers (Figure 8a). Co-staining for ETS-related gene (ERG) transcription factor, a marker specific for endothelial cells, localised the dead cells in the endothelium and not in pericytes (Figure 8b). Quantification of TUNEL$^+$ vessels observed a significant increase of BEC death in *Nemo*^{beKO} mice (Figure 8c). Since NEMO deficiency has been linked to TNF-induced cell death, we validated TNF mRNA expression by quantitative PCR in brain lysates of *Nemo*^{beKO} mice (Pescatore et al., 2016). TNF mRNA expression in *Nemo*^{beKO} mice is approximately 2.5-fold higher than in the control mice (Figure 8d).

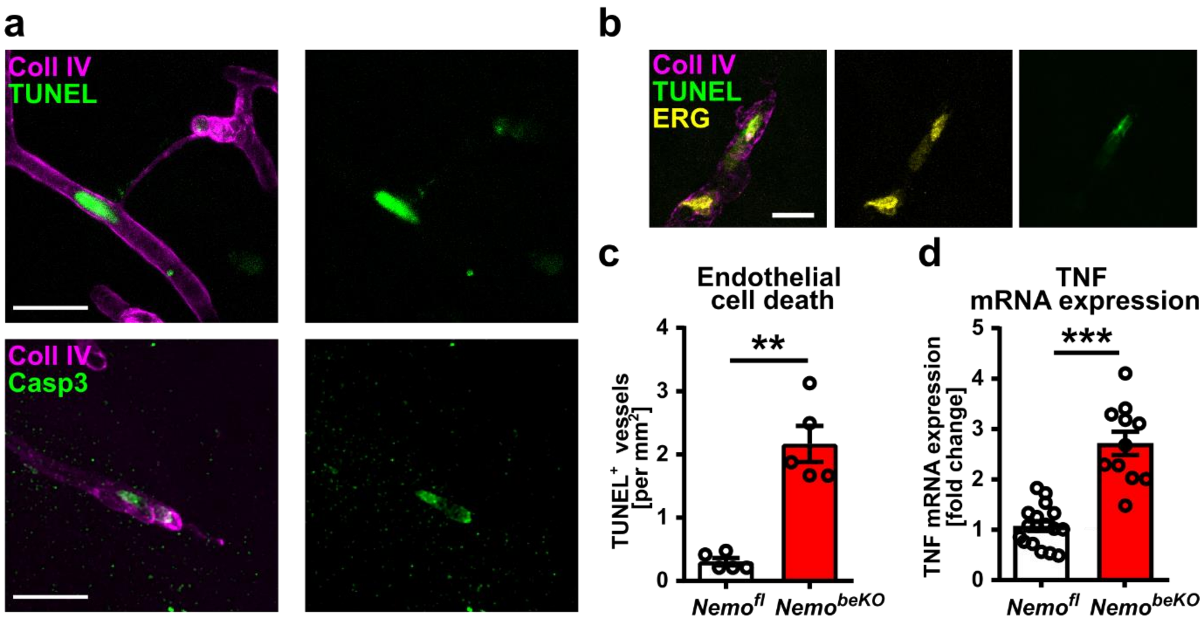

Figure 8: Endothelial cell death and TNF mRNA expression were increased in **Nemo**^{beKO} ***mice.*** *A) Adjacent vessels to string vessels were often TUNEL-positive or positive for the apoptosis marker cleaved caspase-3 (Casp3). B) Co-staining for ERG, an endothelial cell marker, indicated cell death in the endothelium. C) Quantification of TUNEL*$^+$ *vessels revealed increased endothelial cell death in* Nemo^{beKO} *mice. One-tailed Mann-Whitney U test, p = 0.004, N = 5 animals/group. D) TNF mRNA expression in* Nemo^{beKO} *lysates is significantly increased. Two-tailed Mann-Whitney U test, p < 0.001, N = 11-17 animals/group. ** p < 0.01; ***p < 0.001. Figures 8a-c are published (Wenzel, Lampe, Müller-Fielitz et al., 2021).*

TNF can induce NF-κB signalling, leading to the expression of genes that are important for pro-survival, proliferative and inflammatory processes (Oeckinghaus & Ghosh, 2009). In the absence of NEMO, TNF is known to activate alternative pathways leading to cell death (Figure **9**) (Pasparakis & Vandenabeele, 2015). The combination of higher TNF-expression and activation of alternative TNF-induced pathways might be the reason for BEC death followed by string vessel formation in *Nemo*^{beKO} mice. RIPK1 and RIPK3 are essential executors of apoptosis and necroptosis and, therefore, an interesting target to prevent TNF-induced cell death in *Nemo*^{beKO} mice. In a small pilot study, we tried inhibition of RIPK1-mediated cell death by the small-molecule Nec-1s. The treatment for 14 days after the start of tamoxifen injection failed to prevent the vasculature phenotype observed with NEMO deficiency (Supplement Figure 32a and b). Also, the gain in brain weight and the loss in body weight after tamoxifen injection was not reversed by this pharmacological intervention (Supplement Figure 32c). In the next step, we proceeded with a genetic approach in which mice of the Nemo^{fl}*; Slco1c1-CreER*^{T2} mouse line were crossed with mice with a floxed *Fadd* gene or an ubiquitous knockout of *Ripk3*.

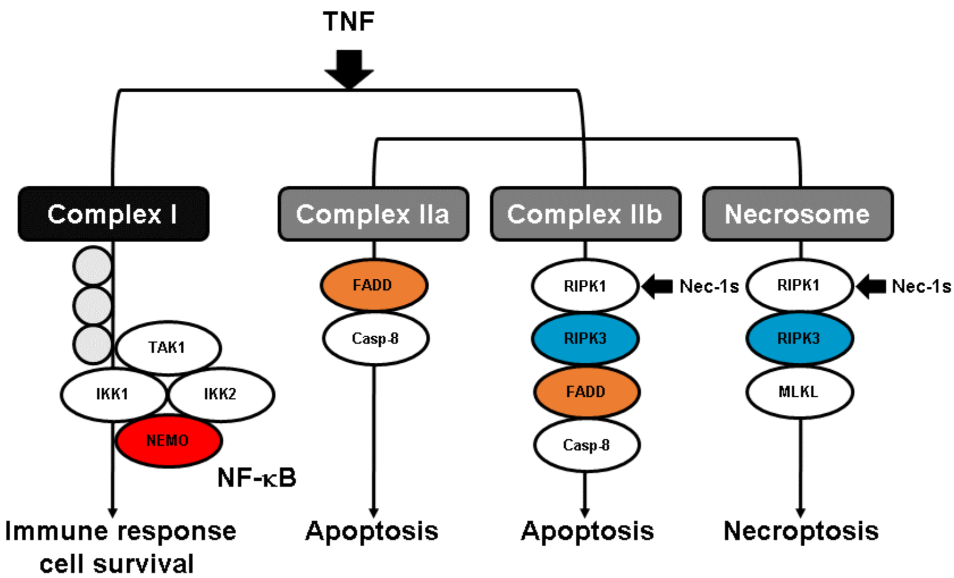

Figure 9: TNF-induced signalling pathways. *Binding ofTNF to its receptor leads to the activation of several adaptor proteins and kinases, such as TAK1. TAK1 induces activation of the IκB kinase (IKK) complex, which leads to translocation of NF-κB into the nucleus and the expression of target genes involved in immune response, cell survival, and other processes. NEMO is the regulatory subunit of the IKK complex, and its absence blocks complete formation complex I. Instead, alternative complexes are formed. These complexes mediate apoptosis or necroptosis by RIPK1, RIPK3, and FADD. In this study, pharmacological inhibition of RIPK1 or genetic ablation of FADD or RIPK3 has been used to inhibit cell death induced by NEMO deficiency. A review by Pasparakis and colleagues served as a template for the figure (Pasparakis & Vandenabeele, 2015). The figure is published (Wenzel, Lampe, Müller-Fielitz et al., 2021).*

First, we analyzed the mortality of all mice. In the past, it has been shown that *Nemo*^{beKO} mice have an increased mortality rate, probably due to vasogenic brain oedema (Ridder et al., 2015). Approximately 30 % of *Nemo*^{beKO} mice died until the end of the experiment, whereas all

Nemo^{beKO} animals with additional FADD deficiency died within 9 days after the start of tamoxifen injection (Figure 10a). Noteworthy, FADD deficiency without any other deficiency already led to a slightly higher mortality rate. Importantly, none of the *Nemo*^{beKO}*Ripk3*$^{-/-}$ mice died. In addition, *Nemo*^{beKO} mice with additional *Ripk3* deletion did not show an increase in string vessel formation and no reduction in vessel length, while FADD deficiency induced a vascular phenotype similar to the phenotype observed in *Nemo*^{beKO} mice (Figure 10b). Deleting both *Fadd* and *Ripk3* in NEMO deficient mice led to a reduced mortality rate compared to *Nemo*^{beKO} mice and did not lead to a significant increase in string vessel formation or a significant reduction of vessel length. Notably, *Fadd* and *Ripk3* deletion alone showed no increase in string vessel formation but a significantly reduced vessel length.

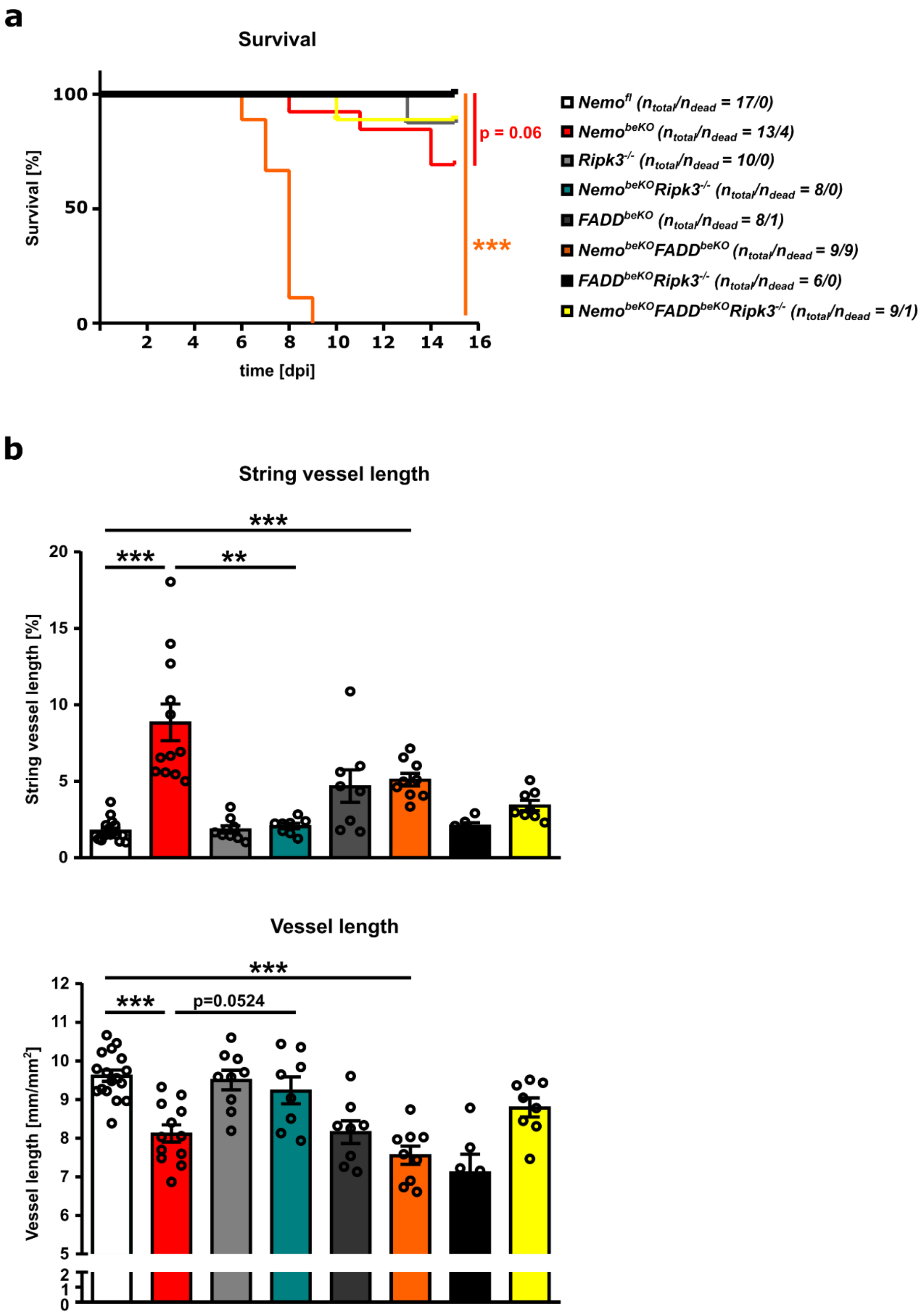

Figure 10: **Ripk3** ***but not*** **Fadd** ***deletion rescued the vascular phenotype observed in NEMO deficient mice.***
A) While approximately 30 % of all Nemo^{beKO} *mice died 14 days after the start of tamoxifen injection, all* Nemo^{beKO}FADD^{beKO} *mice died within nine days after tamoxifen injection. In contrast, none of the* Nemo^{beKO}Ripk3$^{-/-}$ *died after Cre induction. All groups with a 100 % survival rate are depicted with a black line. The initial number of animals* (n_{total}) *and the number of animals that died before the experiment finished* (n_{dead}) *were presented in the legend. Mantel-Cox test;* $\chi^2(7) = 102.1$; $p < 0.001$. *p-values were adjusted for multiple comparisons by Bonferroni (n = 4,* Nemo^{fl} – Nemo^{beKO}, Nemo^{fl} – Nemo^{beKO}Ripk3$^{-/-}$, Nemo^{fl} – Nemo^{beKO}FADD^{beKO}, Nemo^{fl} – Nemo^{beKO}FADD^{beKO}Ripk3$^{-/-}$*) B) Deleting* Nemo *and* Fadd *in BECs led to significantly increased formation of string vessels and reduced vessel length.* Ripk3 *deletion prevented these effects in* Nemo^{beKO} *mice. Kruskal-Wallis test followed by Dunn's multiple*

comparison test (string vessel length: $\chi^2(7) = 54.3$, $p < 0.001$, N = 6-17 animals/group) and ordinary one-way ANOVA followed by Tukey's posthoc test (vessel length; $F(7,69) = 12.8$; $p < 0.001$, N = 6-17 animals/group). The graphs show only the significant changes between Nemo^{beKO}, Nemo^{beKO}Ripk3$^{-/-}$, Nemo^{beKO}FADD^{beKO}, Nemo^{beKO}FADD^{beKO}Ripk3$^{-/-}$ *compared to the* Nemo^{fl} *group and between the* Nemo^{beKO} *and* Nemo^{beKO}Ripk3$^{-/-}$ *groups.** $p < 0.01$; ***$p < 0.001$. All figures are published (Wenzel, Lampe, Müller-Fielitz et al., 2021).*

4.2. BBB disruption caused by NEMO deficiency can be attenuated by *Ripk3* knockout

BBB breakdown in *Nemo^{beKO}* mice is associated with epileptic seizures and is well-characterised by Ridder and colleagues (Ridder et al., 2015). Western blot analysis showed elevated concentrations of IgG and albumin in brain lysates of *Nemo^{beKO}* mice compared to control mice. Interestingly, BBB defects did not lead to size-selective extravasation since intravenously injected fluorochrome-tagged tracers of different sizes were all significantly increased in *Nemo^{beKO}* brain extracts. By using immunohistological staining of IgG, albumin and fibrinogen, and intravenous (i. v.) injection of a fluorescently labelled tracer before transcardiac perfusion, we could confirm higher extravasation into the brain parenchyma of *Nemo^{beKO}* mice compared to *Nemo^{fl}* mice (Figure 11). Since RIPK3 deficiency reversed the vascular phenotype of *Nemo^{beKO}* mice, we wondered if the lack of cell death is sufficient to inhibit increased BBB extravasation in *Nemo^{beKO}* mice. Qualitative observations on tile-scans of brain sections from *Nemo^{beKO}Ripk3$^{-/-}$* mice revealed less IgG extravasation when compared with sections from *Nemo^{beKO}* mice (Figure 11a). However, IgG intensity seems to be higher in *Nemo^{beKO}Ripk3$^{-/-}$* mice when compared with the control group (*Ripk3$^{-/-}$*) and *Nemo^{fl}* mice. Quantitative analysis of IgG intensity outside the brain vessels obtained no significant difference in IgG extravasation between *Nemo^{beKO}* and *Nemo^{beKO}Ripk3$^{-/-}$* mice, but an almost significant increase in extravasation when comparing *Ripk3$^{-/-}$* and *Nemo^{beKO}Ripk3$^{-/-}$* mice (Figure 11b). However, there was no significant elevation in fibrinogen and albumin intensity for *Nemo^{beKO}Ripk3$^{-/-}$* mice compared with the control group (Figure 11c and d). In the next step, we proceeded with a tracer-based study in which we injected fluorescently labelled 4-kDa dextran 30 min before transcardiac perfusion. The tracer is much smaller than the investigated blood-borne molecules (albumin: 67 kDa, IgG: 150 kDa, fibrinogen: 340 kDa) and reflects acute BBB defects. In this experiment, brain extracts from *Nemo^{beKO}Ripk3$^{-/-}$* mice showed similar concentrations of 4-kDa dextran as observed in *Nemo^{beKO}* mice, indicating that increased BBB permeability for smaller molecules could not be prevented (Figure 11d). In summary, these results suggest that the BBB in *Nemo^{beKO}* mice with *Ripk3* deletion is still interrupted, but not to the same extent as in *Nemo^{beKO}* mice without *Ripk3* deletion.

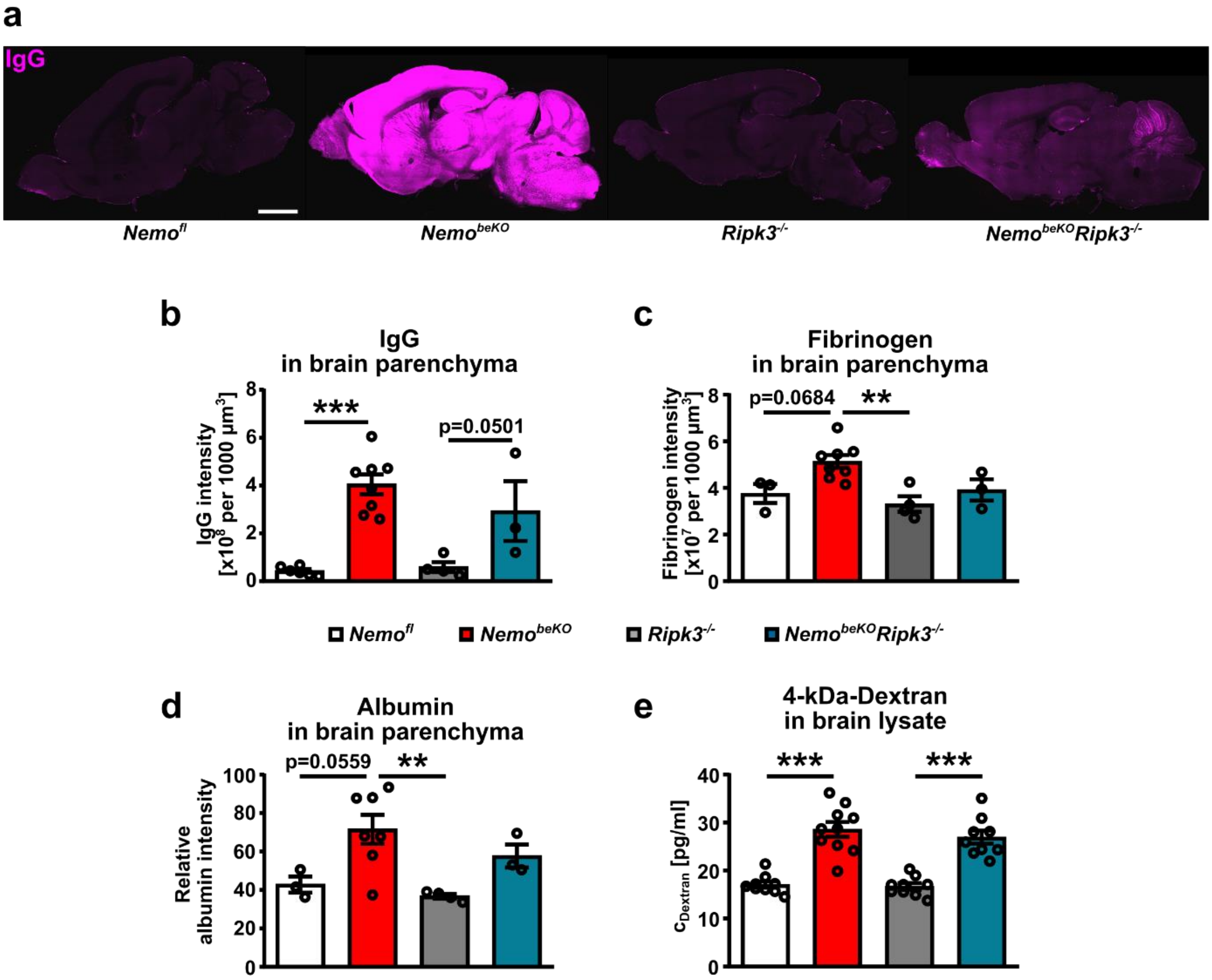

Figure 11: Increased extravasation into the brain parenchyma in* Nemo^{beKO} *mice could be partially reversed by additional RIPK3 deficiency. *A) Whole-brain tile-scans showed a higher IgG intensity in brain sections of* Nemo^{beKO} *mice, and RIPK3 deficiency could not fully rescue increased IgG extravasation in* Nemo^{beKO} *mice. Scale bars, 2 mm. b-e) Graphs show significantly higher or the tendency towards increased extravasation of several molecules in the brains of* Nemo^{beKO} *mice. The increased extravasation could be partially reversed by additional RIPK3 deficiency. Immunofluorescent stainings determined IgG, fibrinogen and albumin extravasation (b-d). In addition, a fluorescently labelled exogenous marker (4-kDa FITC-dextran) was injected intravenously 30 min before perfusion, and the extravasation of the marker was measured by the fluorescence intensity in the brain lysates. One-way ANOVA with Tukey's posthoc test (IgG: $F(3,17) = 16.7$, $p < 0.001$; N = 3-8 animals/group; fibrinogen: $F(3,14) = 6.5$, $p = 0.005$, N = 3-8 animals/group; albumin: $F(3,13) = 5.9$, $p = 0.009$, N = 3-7 animals/group; dextran: $F(3,33) = 29.6$; $p < 0.001$, N = 9-10 animals/group).*** $p < 0.01$; ****$p < 0.001$. Figure 11b and 11e are published (Wenzel, Lampe, Müller-Fielitz et al., 2021).*

Although endothelial cell death was prevented in *Nemo^{beKO}Ripk3$^{-/-}$* mice, brain parenchymal extravasation was not normalized. Previous investigation of specific brain endothelial TJ proteins revealed a reduced occludin expression in *Nemo^{beKO}* mice (Ridder et al., 2015). Here, we investigated occludin TJ morphology in detail using expansion microscopy and tested if TJ interruptions are responsible for increased BBB permeability in *Nemo^{beKO}Ripk3$^{-/-}$* mice. The junction protein ZO-1 served as a reference protein since it is not affected by brain endothelial *Ikbkg* knockout and colocalises with occludin (Ridder et al., 2015). Expansion microscopy images revealed interruptions in the occludin TJ structure of *Nemo^{beKO}* animals (Figure 12a). These interruptions occurred either as a complete loss or disintegration of occludin, leading to a 17.7 % loss of occludin structure when normalized to the ZO-1 reference structure (Figure 12b). In *Nemo*^{beKO} mice with additional RIPK3 deficiency, we could not find an interrupted occludin TJ morphology. These findings suggest that increased BBB extravasation in *Nemo*^{beKO}*Ripk3*$^{-/-}$ mice did not occur via the paracellular route.

However, occludin and pericyte deficiency have been shown to cause brain calcifications, which are typical for small-vessel diseases (Saitou et al., 2000; Zarb et al., 2019). Occludin interruptions and a reduction in pericyte coverage were observed in *Nemo*^{beKO} mice in our study. These findings prompted us to investigate if calcifications exist in *Nemo*^{beKO} brains. Therefore, we stained with Alizarin Red S, a dye that forms a red complex if calcium deposits are present. Nevertheless, staining for Alizarin-Red S did not obtain any calcifications in the brains of *Nemo*^{beKO} mice which were sacrificed 2 weeks, 8 weeks or 12 weeks after the start of tamoxifen injection (Figure 33).

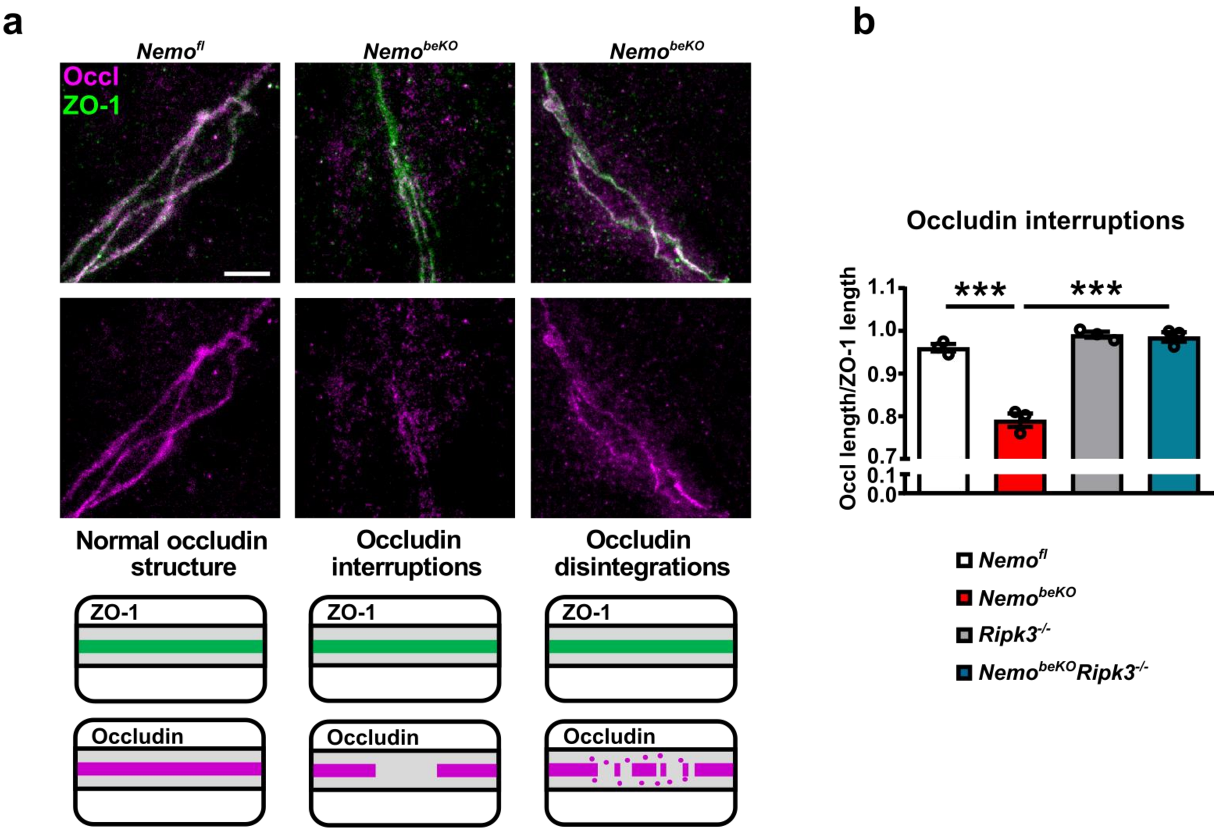

Figure 12: Interruptions in the occludin TJ morphology in **Nemo**^{beKO} ***mice were prevented by*** **Ripk3** ***deletion.*** *A) Representative immunostainings of ZO-1 and occludin (Occl) obtained by expansion microscopy in* Nemo^{fl} *and* Nemo^{beKO}*mice showed a disrupted structure in* Nemo^{beKO} *but not in* Nemo^{fl} *mice. Scale bar, 10 µm (corresponding to approximately 2.5 µm initial size). We classified TJ structures as occludin interruptions or disintegrations (middle). B) Quantification of occludin TJ length relative to ZO-1 TJ length revealed loss of occludin structure in* Nemo^{beKO} *mice, but not in* Nemo^{beKO}Ripk3$^{-/-}$ *mice. One-way ANOVA with Tukey's posthoc test,* $F(3,8) = 72.7$*,* $p < 0.001$*,* $N = 3$ *animals/group.****$p < 0.001$*. All figures are published (Wenzel, Lampe, Müller-Fielitz et al., 2021).*

4.3. Ablation of NEMO leads to disturbed IgG transcytosis

The findings above do not support the idea that TJ interruptions increase BBB extravasation in *Nemo*^{beKO}*Ripk3*$^{-/-}$ mice. Thus, we investigated if the transcellular route might be dysregulated and consequently influences extravasation at the BBB. It is well-known that transcellular transport in the brain endothelium is strictly limited (Stewart, 2000; Villaseñor et al., 2019). Such molecular insights have been mainly achieved by electron microscopy. By injection of HRP into the blood circulation and subsequent analysis of mouse brain sections, Reese and colleagues observed no extravasation to the brain parenchyma, and only a few vesicles were found in BECs (Reese & Karnovsky, 1967). For several brain pathological conditions, an increase in brain endothelial vesicles has been shown (Hirano et al., 1994; Villaseñor et al., 2019). To investigate transcytosis in *Nemo*^{beKO} mice, we followed a perfusion protocol by Peter König from the Institute of Anatomy Lübeck (section 3.3.4). Christo Örün performed electron microscopy. Quantifying vesicles according to defined parameters described in section 3.3.4 revealed no significant differences in *Nemo*^{beKO} mice compared to *Nemo*^{fl} mice (Figure 13).

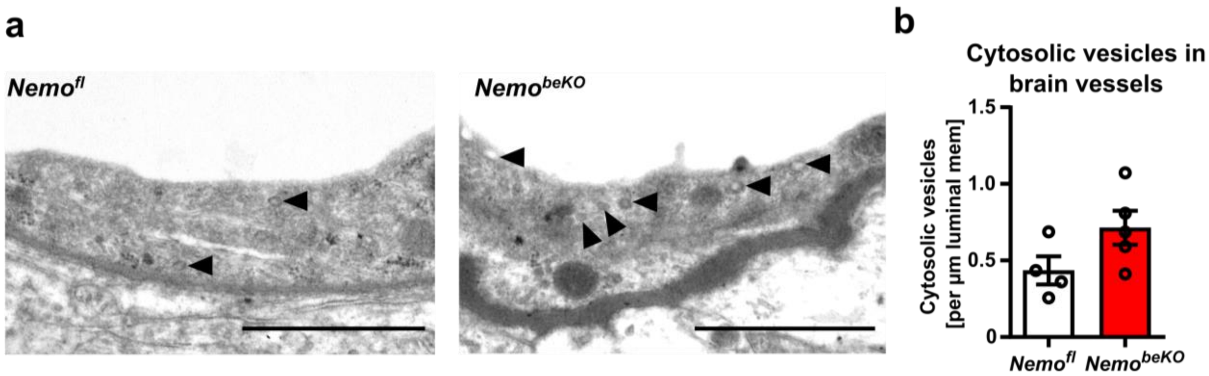

Figure 13: Electron microscopy showed endothelial vesicles in* Nemo^{fl} *and* Nemo^{beKO} *mice. *Analysis of electron microscopy images (a) obtained no differences in the total number of brain capillary vesicles in* Nemo^{beKO} *mice compared to* Nemo^{fl} *mice (b). Quantification was obtained by defined parameters as described in section 3.3.4. Scale bar, 1 µm. Two-tailed unpaired t-test, T(7) = 1.9, p = 0.1034, N = 4-5 animals/group. All figures are published (Wenzel, Lampe, Müller-Fielitz et al., 2021).*

Although electron microscopy is a reliable method with a powerful magnification to observe vesicular structures at the BBB, vesicle analysis is impacted by several disadvantages, such as the lack of distinguishing between different types of vesicles and other factors that are discussed elsewhere (section 5.2.2.)

In recent papers, fluorochrome-based approaches have been used to characterise specific vesicular transport machinery in BECs by conventional confocal or two-photon microscopy (Mathiesen Janiurek et al., 2019; Ruano-Salguero & Lee, 2020; Villasenõr et al., 2016; Villaseñor, Kuennecke, et al., 2017). To overcome the disadvantages of electron microscopy, we used such techniques. We visualized transcellular IgG transport in brain capillaries according to the protocol of Villasenor and colleagues in our laboratory. Staining with a fluorescently labelled anti-mouse IgG antibody revealed numerous IgG puncta in brain capillaries (Figure 14a). To confirm the specificity of the IgG vesicle staining, we used three other anti-mouse IgG antibodies, and, indeed, we observed the same pattern. Further, we detected no IgG-filled vesicular structures when using antibodies against rabbit IgG, confirming the specificity of the mouse antibodies (Figure 14b).

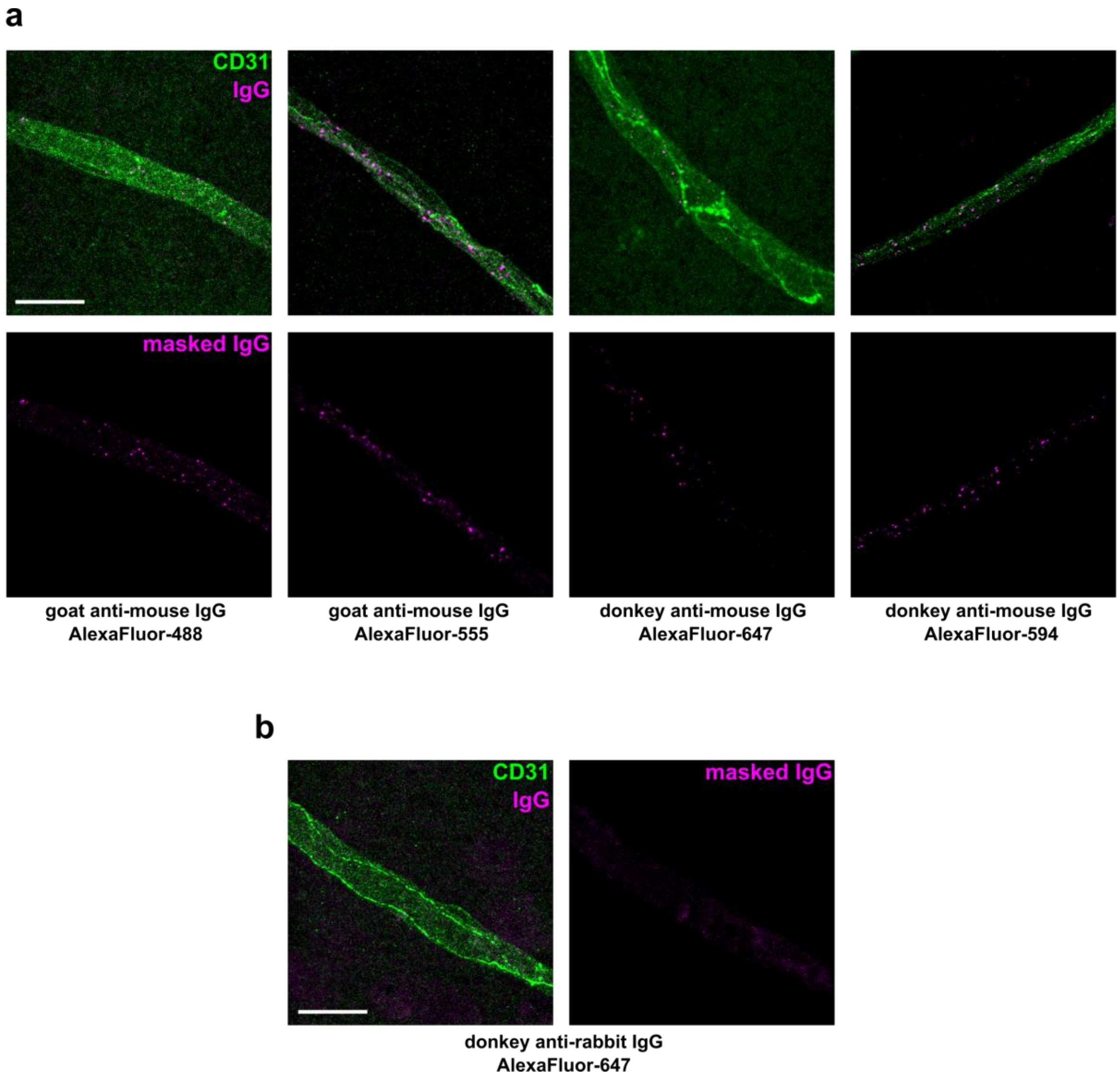

Figure 14: Anti-mouse IgG antibodies stained IgG-filled vesicles. *A) Different anti-mouse IgG antibodies labelled by a fluorochrome showed vesicular structures in wild-type mouse brain vessels. B) IgG vesicles could not be observed when using anti-IgG antibodies for other species than mice. Scale bar, 10 µm.*

We now performed IgG staining to quantify IgG-filled vesicles inside of brain capillaries. Thus, we imaged 10-15 capillaries per animal and IgG^+ puncta were counted inside the capillaries and normalized to the vessel volume using Imaris. Confocal images and quantification revealed a significant reduction of IgG-filled vesicles by more than half in *Nemo*^{beKO} mice

(Figure 15). Additionally, we analyzed images from *Ripk3*$^{-/-}$ and *Nemo*^{beKO}*Ripk3*$^{-/-}$ mice. Interestingly, the IgG vesicle number in *Nemo*^{beKO}*Ripk3*$^{-/-}$ mice decreased similarly as already detected for *Nemo*^{beKO} mice. In conclusion, NEMO deficiency led to defects in IgG transcytosis, which could not be prevented by *Ripk3* knockout.

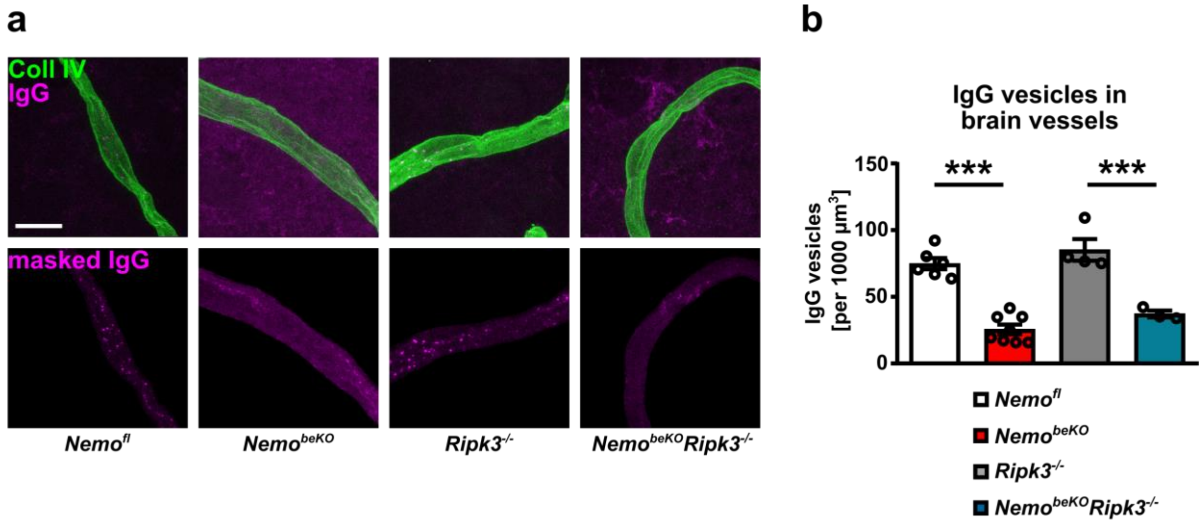

Figure 15: NEMO deficient mice showed reduced numbers of IgG-filled vesicles in brain capillaries independent of the presence of RIPK3**. A) Confocal images showed fewer IgG-vesicles in Coll IV-stained vessels in NEMO-deficient mice. Scale bar, 10 µm. b) Counting IgG-filled vesicles and normalisation for the vessel volume by Imaris revealed a significantly reduced number of IgG vesicles in* Nemo^{beKO} *and* Nemo^{beKO}Ripk3$^{-/-}$ *mice compared to their control groups. One-way ANOVA with Tukey's posthoc test (*$F_{(3,17)} = 37.4$, $p < 0.001$; $N = 3$-8 *animals/group).*$p < 0.001$*. All figures are published (Wenzel, Lampe, Müller-Fielitz et al., 2021).*

To confirm the findings obtained by confocal microscopy, we performed super-resolution imaging by STED microscopy with brain sections from *Nemo*^{fl} and *Nemo*^{beKO} mice. We used only a small sample size (3 images/animal; N = 4 animals/group) and performed the quantification as described before for confocal imaging. Notably, significantly fewer vesicles were observed for *Nemo*^{beKO} mice, as shown before (Figure 16b and Figure 15b). Compared to confocal images, IgG-filled vesicles had an apparent smaller diameter but showed a similar pattern as already observed by confocal microscopy (Figure 16a and Figure 15a).

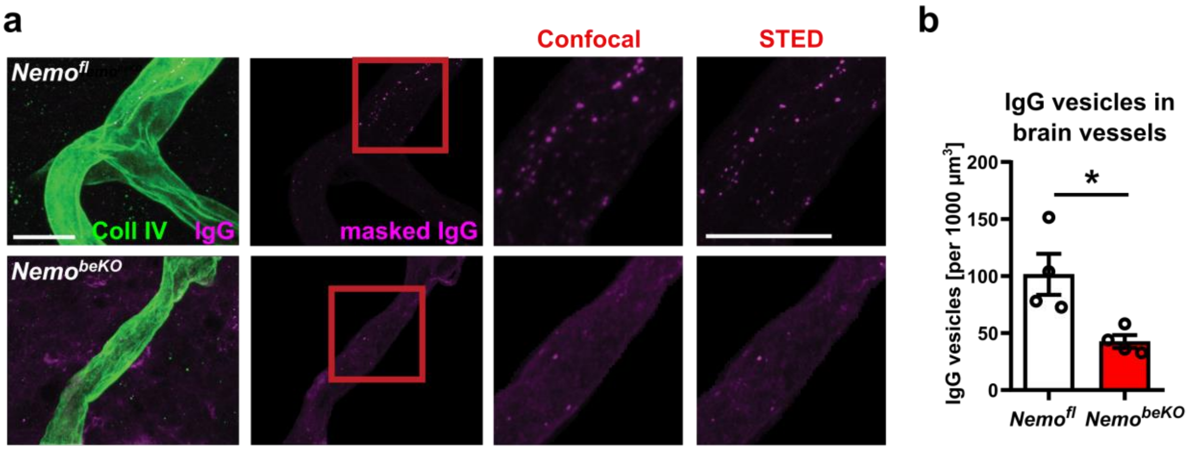

***Figure 16: STED microscopy showed IgG-filled vesicles and revealed fewer vesicles in Nemo^{beKO} mice**. A) STED images of* Nemo^{fl} *and* Nemo^{beKO} *showed an increased number of IgG-filled vesicles with an apparent smaller diameter compared to the corresponding confocal images. Scale bar, 10 µm B) Quantification of STED images observed a decrease of IgG-filled vesicles in* Nemo^{beKO}*. Mann-Whitney U-test, $p = 0.029$; N = 4 animals/group. *$p < 0.05$. All figures are published (Wenzel, Lampe, Müller-Fielitz et al., 2021).*

In the following, we performed stainings for intracellular compartment markers to identify the sorting pathways affected by NEMO deficiency. For this reason, we stained for LAMP2, a marker for lysosomes, TfR, a marker for recycling endosomes, and Coll IV as a marker for vessels (Hua et al., 1998; Ober et al., 2004). Vesicular structures could be observed for both stainings (Figure 17). Unlike the IgG staining, LAMP2$^+$ and TfR$^+$ vesicles were present in higher numbers and were also found outside the brain vessels in the *Nemo^{fl}* group, indicating their presence also in other cell types. However, counting TfR$^+$ and LAMP2$^+$ puncta inside brain vessels and normalisation to the vessel volume revealed a significant reduction in the number of TfR$^+$ recycling endosomes in *Nemo^{beKO}* mice, whereas the number of LAMP2$^+$ lysosomes remained unchanged.

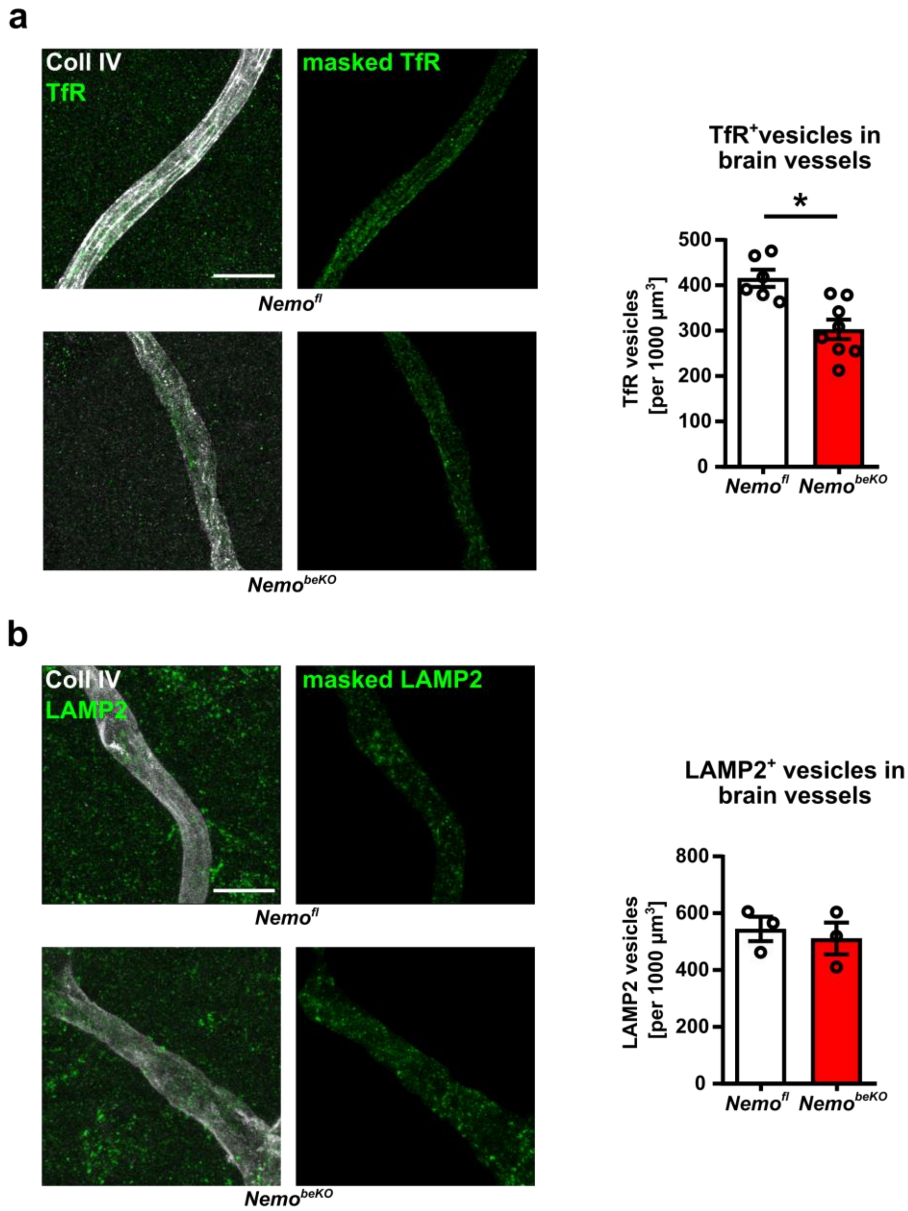

Figure 17: Ablation of NEMO led to a reduction of recycling endosomes but not to a decrease of lysosomes. *A) TfR^{+} vesicles in brain vessels were significantly reduced in* Nemo^{beKO} *mice. Scale bar, 10 µm. Unpaired t-test, T (12) = 3.8, p = 0.003, N = 6-8 animals/group. b) No differences in the number of LAMP2^{+} lysosomes could be observed for brain vessels of* Nemo^{beKO} *mice. Scale bar, 10 µm. Mann-Whitney U-test, p = 0.700, N = 3 animals/group.*p < 0.05.*

When analyzing the confocal images of IgG vesicle staining, we also observed IgG-filled structures outside the vessels in *Nemo^{beKO}* and *Nemo^{beKO}Ripk3$^{-/-}$* mice that were reminiscent of glial processes. Co-staining of IgG with the astrocytic marker GFAP (images not shown) and the microglial marker ionized calcium-binding adaptor molecule 1 (Iba1) revealed colocalisation of these IgG structures with microglia, but not with astroglia (Figure 18a). Using the expansion microscopy technique, we observed these IgG structures as IgG puncta or IgG-filled vesicles concentrating at microglial processes, suggesting that parenchymal IgG is interacting with microglial cells (Figure 18b).

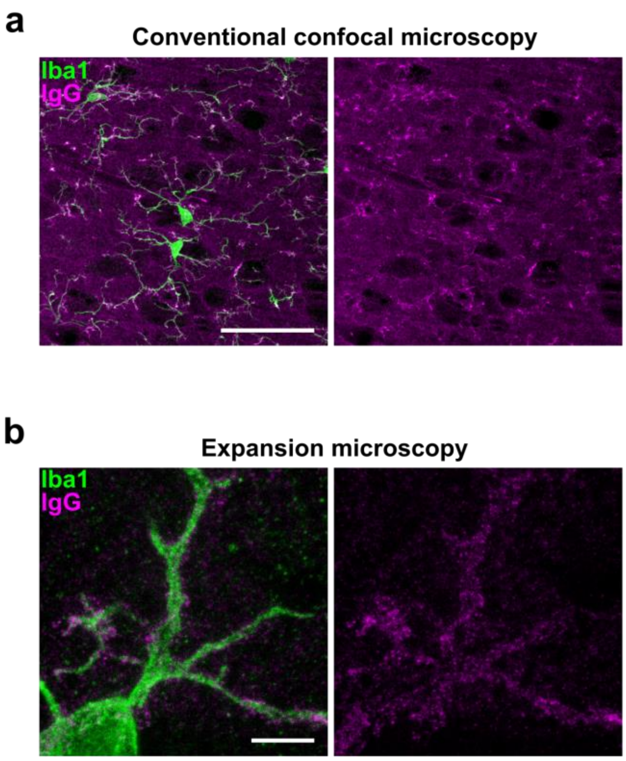

Figure 18: Parenchymal IgG colocalised with microglia. *A) Conventional confocal microscopy images from* Nemo^{beKO} *mice showed IgG structures in the brain parenchyma that might be colocalised with Iba1^{+} microglia. Scale bar, 50 µm. b) Sample expansion with prior IgG and Iba1 staining revealed IgG puncta colocalised with microglia processes. Scale bar, 10 µm.*

In addition to IgG, we searched for other markers to visualize the transcellular transport of plasma proteins. The fibrinogen staining revealed a puncta-like structure similar to the IgG^{+} vesicles (Figure 19a). *Nemo^{beKO}* mice showed a reduction in fibrinogen-filled vesicles (Figure 19b), but unlike IgG vesicle analysis, ablation of RIPK3 normalized the decrease in fibrinogen-filled vesicles. Thus, RIPK3 deficiency seems to prevent defects in fibrinogen transcytosis but not in IgG transcytosis. In addition, almost no colocalisation of IgG- and fibrinogen-filled vesicles were observed when stained together (Figure 19c). In conclusion, both molecules might be transported differently through the endothelium.

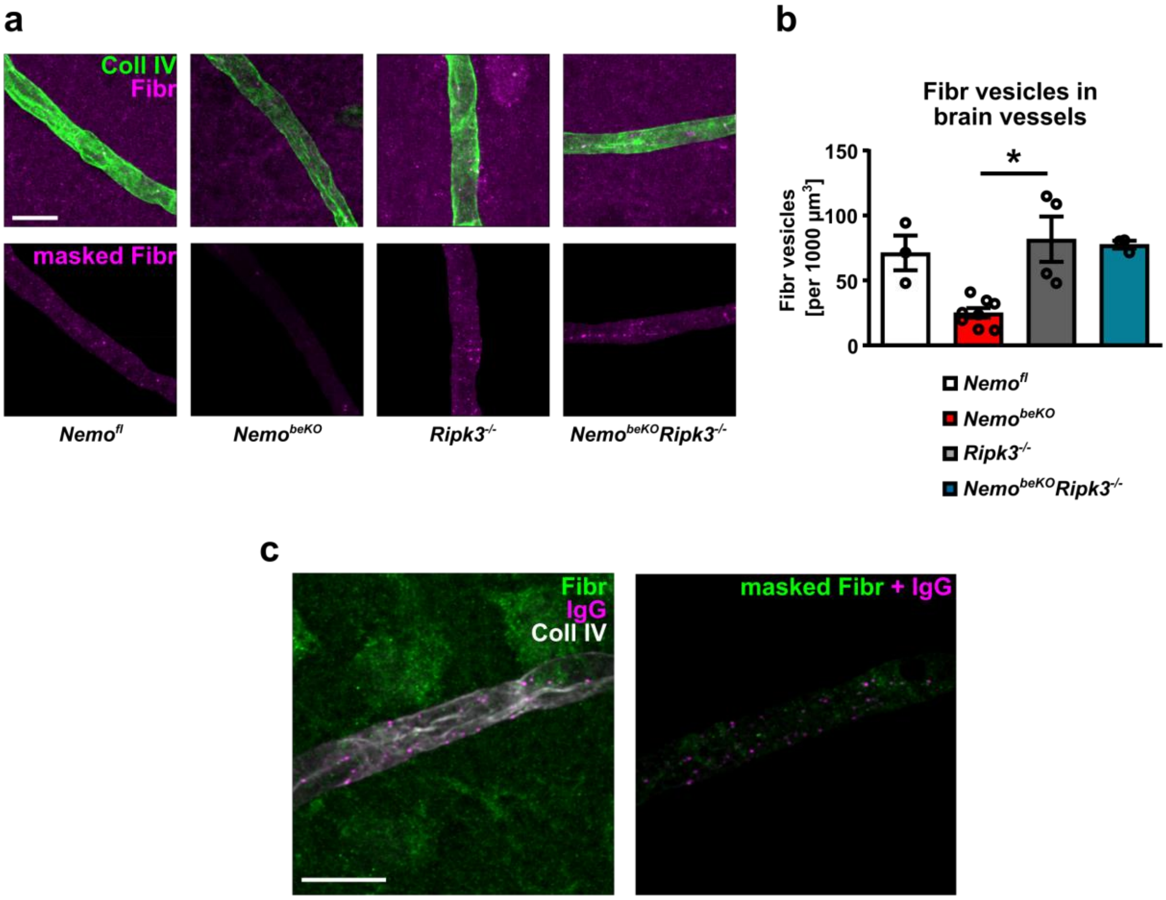

Figure 19: RIPK3 deficiency prevented the decrease in the number of fibrinogen-filled vesicles in brain capillaries of* Nemo^{beKO} *mice. *A) Confocal images showed fewer fibrinogen-filled vesicles in Coll IV-stained vessels in NEMO deficient mice but not in* Nemo^{beKO}Ripk3$^{-/-}$ *mice. Scale bar, 10 µm. b) Counting fibrinogen-filled vesicles and normalisation for the vessel volume using Imaris revealed a significantly reduced number of IgG vesicles in* Nemo^{beKO} *which is prevented by additional* Ripk3 *deletion. Kruskal-Wallis test with Dunn's posthoc test ($\chi^2(3) = 12.8$,* p *< 0.001; N = 3-8 animals/group). c) Co-staining of IgG and fibrinogen vesicles revealed only rare colocalisation in brain vessels. Scale bar, 10 µm. ***p < 0.001.*

Previous experiments have shown that brain endothelial deletion of *Tak1*, an upstream kinase of the IκB complex, leads to vascular defects and IgG extravasation at the BBB, as observed before for brain endothelial deletion of *Nemo* (Ridder et al., 2015). The expression of a constitutively active *Ikk2* mutant (*IKK2ca*) is predicted to be sufficient to activate NF-κB in the absence of TAK1 (Pasparakis et al., 2006). Thus, in *Tak1^{beKO}IKK2^{ca}* mice, mortality rate, IgG extravasation and brain weights were reduced. To date, BBB transcytosis in *Tak1^{beKO}* mice has not been investigated. Thus, we performed IgG transcytosis stainings on brain sections from *Tak1^{beKO}* mice, and in addition, we used the constitutively active *Ikk2* mutant to examine its effects on IgG transcytosis in TAK1 deficient mice. As detected before, TAK1 deficiency in BECs led to body weight loss as a sign of general malaise after tamoxifen injection (Figure 20a). An explanation for the increased general malaise in these animals might be a potential occurrence of epileptic seizures and increased anxiety, similar to what was detected for *Nemo^{beKO} mice* (Ridder et al., 2015). *Tak1^{beKO}* mice with constitutive IKK2 activation did not reach the same level of body weight as control mice (*Tak1*^{fl} and *IKK2*$^{+/+}$) but gained significantly more body weight than *Tak1*^{beKO} mice after 14 days of the first tamoxifen dose. As shown before, TAK1 deficiency also led to higher brain weights as a sign of brain oedema and massive extravasation, but this effect could be prevented by constitutive *Ikk2* activation (Figure 20b). *Tak1*^{beKO} mice showed a substantial increase in IgG brain extravasation, and although *Tak1*^{beKO}*IKK2*^{ca} *mice* did not show any increase in brain weight, we could observe a similar level of IgG extravasation as shown for *Tak1*^{beKO} mice (Figure 20c). In line with the findings for *Nemo*^{beKO} mice, fewer IgG-filled vesicles were counted in *Tak1*^{beKO} mice (Figure 20d). However, constitutive *Ikk2* activation could not increase the number of IgG-filled vesicles in *Tak1*^{beKO} mice.

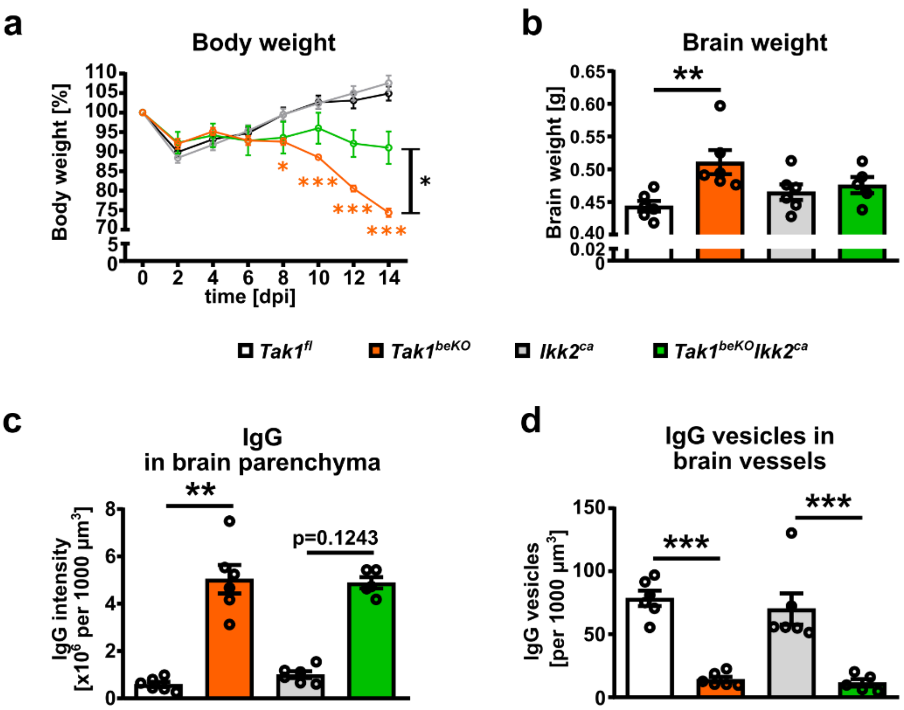

Figure 20:Constitutive **Ikk2** ***activation in TAK1 deficient mice did not prevent the increase in IgG extravasation and the decrease in IgG vesicle number.*** *A) Time course of body weight showed a dramatic drop of body weight in* Tak1^{beKO} *mice compared to* Tak1^{fl} *mice starting eight days after the first dose of tamoxifen. The decrease in body weight could be partially prevented by constitutive* Ikk2 *activation. The orange symbols indicate a significant difference between* Tak1^{beKO} *and* Tak1^{fl} *mice. The black symbol indicates a significant difference between* Tak1^{beKO} *and* Tak1^{beKO}IKK2^{ca} *mice. Repeated two-way ANOVA followed by Tukey's posthoc test; genotype: F (3,19)) = 7.6, p = 0.0015; time: F (2.8, 53.3) = 27.0, p < 0.0001; interaction: F (21, 133) = 35.1, p< 0.0001, subject: F(19,133) = 18.1; N = 5-6 animals/group. B)* Tak1^{beKO} *mice showed significantly increased brain weights compared to* Tak1^{beKO} *mice with constitutive* Ikk2 *activation. Ordinary one-way ANOVA followed by Tukey's posthoc test, F(3,19) = 4.6, p = 0.014, N = 5-6 animals/group. C) IgG extravasation was elevated in TAK1 deficient animals and cannot be rescued by constitutive* Ikk2 *activation. Kruskal-Wallis test followed by Dunn's posthoc test,* $\chi^2(3) = 17.5$*; p < 0.001, N = 5-6 animals/group. D) Number of IgG vesicles was reduced in* Tak1^{beKO} *mice and* Tak1^{beKO}IKK2^{ca} *mice. Ordinary one-way ANOVA followed by Tukey's posthoc test, F(3,19) = 22.8, p < 0.001, N = 5-6 animals/group.***p < 0.001, **p < 0.01.*

4.4. Commonly regulated genes in *Nemo*^{beKO} and *Nemo*^{beKO}*Ripk3*$^{-/-}$ mice revealed increased expression of angiogenesis-related genes

The previous results showed changes in IgG transcytosis accompanied by increased IgG extravasation in *Nemo*^{beKO} mice. These changes could not be fully reversed by deleting the cell death mediator *Ripk3*, suggesting that IgG transcytosis might be independently regulated of TNF-induced cell death. Instead, NF-κB-mediated gene expression might influence brain endothelial transcytosis. Interestingly, constitutive *Ikk2* activation in *Tak1*^{beKO} mice did not reverse the effect of *Tak1* deletion on IgG transcytosis. However, it is unclear if constitutive *Ikk2* activation recovers physiological NF-κB activity in TAK1 deficient mice or shifts NF-κB activation to the right side of the bell-shaped NF-κB activity curve leading to increased BBB integrity by overactivation (Figure 3).

Gene expression microarrays were performed from brain vessel fragment RNA from *Nemo*^{beKO} mice by Kristin Müller to observe the effect of NEMO ablation on the transcriptome (Y. Jiang et al., 2020). The data analysis showed 1097 regulated genes (counted were genes with an FDR-adjusted p-value < 0.05, which are at least two-fold regulated). Since increased endothelial cell death and activation of inflammation were observed in *Nemo*^{beKO} mice, many of that genes might be regulated secondary to NF-κB pathway inactivation. RIPK3 deficiency might prohibit these effects and better reflect direct gene expression changes due to NF-κB pathway inactivation. Thus, we extracted RNA from vessel fragments of *Nemo*^{beKO}*Ripk3*$^{-/-}$ and *Ripk3*$^{-/-}$ mice (performed by Beate Lembrich and Jan Wenzel). For subsequent microarray analysis, samples were sent to the group of Norbert Hübner (Berlin, Germany).

Principal component analysis (PCA) provided information on the overall variance of the transcriptomic data and was performed by Transcriptome Analysis Console 4.0. Figure 21 shows a clear separation of the *Nemo*^{beKO}*Ripk3*$^{-/-}$ dataset from the control group *Ripk3*$^{-/-}$ indicating genomic differences between the groups. Within the *Nemo*^{beKO}*Ripk3*$^{-/-}$ group, samples were distributed relatively homogenously, while samples in the *Ripk3*$^{-/-}$ dataset showed a more heterogeneous distribution. An explanation for these differences might be the unequal distribution of sex between the groups. Due to breeding problems and an unexpectedly high mortality rate during tamoxifen injection in both groups, we obtained samples from 6 females for the *Nemo*^{beKO}*Ripk3*$^{-/-}$ group and two females and four males for the *Ripk3*$^{-/-}$ group. Previous examinations showed no differences in the *Nemo*^{beKO} phenotype between males and females (data not shown). Considering this fact, we continued with analysing the gene expression microarray data.

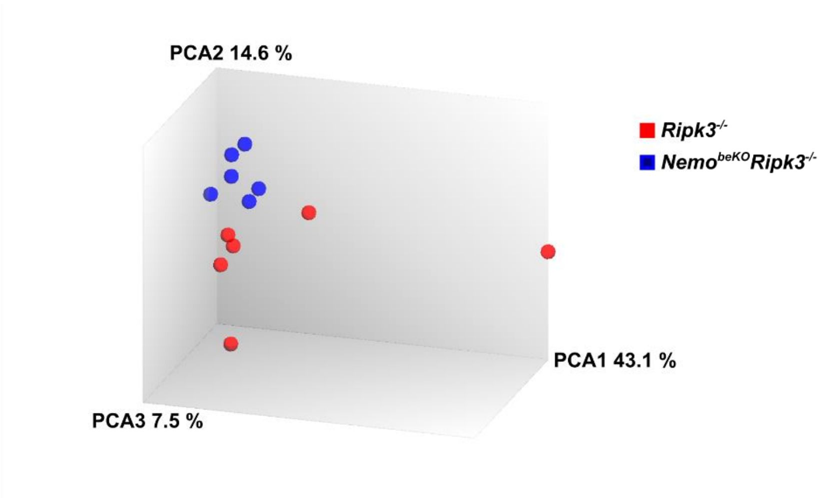

Figure 21: Principle component analysis (PCA) from gene expression microarray data from **Ripk3$^{-/-}$** ***and*** **Nemo^{beKO}Ripk3$^{-/-}$** ***mice showed the overall variance of the transcriptomic data.***

Analysis of the dataset revealed 25 regulated genes in vessel fragments of *Nemo^{beKO}Ripk3$^{-/-}$* mice, in which 22 genes were upregulated, and three genes were downregulated. The regulated genes were sorted by the descending order of fold change in

Table 6.

Average intensity (log2) $Nemo^{beKO}Ripk3^{-/-}$	Average intensity (log2) $Ripk3^{-/-}$	Fold change	FDR p-value	Gene symbol	Description
11.78	6.62	**35.71**	1.82E-10	**TC 17549068**	Xist-related non-coding RNA
9.2	6.02	**9.05**	4.38E-06	**Apln**	Apelin
9.71	7.67	**4.09**	7.43E-05	**Adm**	Adrenomedullin
8.25	6.55	**3.24**	0.0003	**Plaur**	Plasminogen activator uro-kinase receptor
9.08	7.41	**3.19**	0.0047	**F5**	Coagulation factor V
7.09	5.45	**3.13**	0.0218	**Mki67**	Antigen identified by mono-clonal antibody Ki67
8.04	6.43	**3.06**	0.0036	**Angpt2**	Angiopoietin 2
9.28	7.7	**2.99**	1.66E-05	**Ccnd1**	Cyclin D1
7.7	6.29	**2.67**	0.0099	**TC 17550474**	VL30 RNA
10.24	8.86	**2.61**	1.66E-05	**Mall**	Mal. T cell differentiation pro-tein-like
11.1	9.76	**2.52**	0.0257	**Cdkn1a**	Cyclin-dependent kinase in-hibitor 1A (P21)
8.01	6.7	**2.49**	0.0047	**Tubb6**	Tubulin. beta 6 class V
9.93	8.66	**2.42**	0.0002	**Clic1**	Chloride intracellular channel 1
7.6	6.33	**2.41**	0.0048	**Abca4**	ATP-binding cassette. sub-family A (ABC1) member 4
8.82	7.6	**2.33**	0.0316	**H2afx**	H2A histone family member X
5.53	4.32	**2.32**	0.0138	**Cdk1**	Cyclin-dependent kinase 1
8.1	6.93	**2.25**	0.03	**Tnfrsf12a**	Tumour necrosis factor re-ceptor superfamily member 12a
6.71	5.58	**2.18**	0.0078	**Pgf**	Placental growth factor
7.48	6.36	**2.17**	0.0143	**Sesn2**	Sestrin 2
7.06	5.98	**2.12**	0.0234	**TC 17267418**	VL30 RNA
8.71	7.63	**2.11**	0.0182	**Adamts9**	Disintegrin-like and metallopeptidase (reprolysin type) with thrombospondin type 1 motif. 9
8.73	7.69	**2.04**	0.0022	**Phlda3**	Pleckstrin homology-like do-main. family A member 3
6.54	7.79	**-2.37**	0.0373	**TC 17549150**	Non-coding RNA
8.1	9.83	**-3.32**	0.0022	**Gkn3**	Gastrokine 3
5.82	7.76	**-3.86**	0.019	**Krtap28-13**	Keratin associated protein 28-13

Table 6: Up- and downregulated genes in vessel fragments of **$Nemo^{beKO}Ripk3^{-/-}$** ***mice.*** *The table shows the average intensity for each gene for both groups, the fold change in gene expression of the* $Nemo^{beKO}Ripk3^{-/-}$ *group compared to the* $Ripk3^{-/-}$ *group, the FDR-adjusted p-value, the gene symbol, and the name of the translated protein or transcribed RNA (description). Data were statistically analyzed by Empirical Bayes Analysis. The p-value was adjusted for the false-discovery rate (FDR). Genes with an FDR p-value < 0.05 and at least two-fold changed were considered as regulated.*

A hierarchical clustering heatmap visualizes the intensities for the significantly two-fold regulated genes from each sample and suggests clusters (Supplement Figure 34). According to the heatmap, samples can be clearly separated by their genotype. Moreover, analysis by DAVID Functional Annotation Clustering was performed to uncover clusters of pathways and terms that might be associated with the regulated genes from vessel fragments of *Nemo*^{beKO}*Ripk3*$^{-/-}$ mice. Only 21 out of 25 regulated genes were analysed since the rest of the genes is transcribed to non-coding RNA. The algorithm used a kappa statistic score to measure relationships among common genes and thus, classified clusters of similar annotations. Table 7 shows enriched terms grouped by two clusters and sorted by the descending order of p-values. The most enriched term found in both clusters is “organ regeneration”, associated with a third of the regulated genes. In general, both clusters contain several terms associated with proliferation, such as “positive regulation of angiogenesis”, “cyclins and cell cycle regulation”, or “cell cycle”.

Database	Terms	Count (%)	Genes	p-value	Benjamini
Annotation Cluster 1 (ES = 4.98)					
GOterm BP Direct	**Organ regeneration**	7/21 (33.3 %)	Adm, Angpt2, Mki67, Ccnd1, Cdk1, Cdnk1a, Pgf	**1.2E-11**	3.2E-9
GOterm BP Direct	**Positive regulation of angiogenesis**	3/21 (14.3 %)	Adm, Angpt2, Pgf	**6.3E-3**	2.4E-1
GOterm BP Direct	**Response to hypoxia**	3/21 (14.3 %)	Adm, Angpt2, Pgf	**1.5E-2**	3.7E-1
Annotation Cluster 2 (ES = 3.23)					
GOterm BP Direct	**Organ regeneration**	7/21 (33.3 %)	Adm, Angpt2, Mki67, Ccnd1, Cdk1, Cdnk1a, Pgf	**1.2E-11**	3.2E-9
KEGG pathway	**P53 signaling pathway**	4/21 (19.0%)	Ccnd1, Cdk1, Cdnk1a, Sesn2	**9.95E-5**	4.9E-3
GOterm BP Direct	**Response to organonitrogen compound**	3/21 (14.3 %)	Ccnd1, Cdk1, Cdnk1a	**2.3E-4**	3.1E-2
BioCarta	**Cyclins and Cell cyle regulation**	3/21 (14.3 %)	Ccnd1, Cdk1, Cdnk1a	**9.9e-4**	1.4E-2
BioCarta	**Cell cycle**	3/21 (14.3 %)	Ccnd1, Cdk1, Cdnk1a	**1.3E-3**	1.4E-2
GOterm BP Direct	**Cell cycle**	5/21 (23.8 %)	H2afx, Mki67, Ccnd1, Cdk1, Cdnk1a	**2.8E-3**	1.9E-1
GOterm BP Direct	**Response to drug**	4/21 (19.0%)	Ccnd1, Cdk1, Cdnk1a, Pgf	**4.3E-3**	2.3E-1
KEGG pathway	**PI3K-Akt signaling pathway**	4/21 (19.0%)	Angpt2, Ccnd1, Cdnk1a, Pgf	**1.2E-2**	2.1E-1
KEGG pathway	**Cell cycle**	3/21 (14.3 %)	Ccnd1, Cdk1, Cdnk1a	**1.3E-2**	2.1E-1
KEGG pathway	**Viral carcinogenesis**	3/21 (14.3 %)	Ccnd1, Cdk1, Cdnk1a	**4.1E-2**	4.0E-1

Table 7: DAVID Functional Annotation Cluster. *The software used several commercially available databases to analyze enriched terms associated with the list of regulated genes. The minimal number of genes for the corresponding terms were reported by count (%). Shown are only clusters with an EASE score (ES) > 1.0 and annotations with a p-Value < 0.05. Modified Fisher exact p-value (Benjamini) has been reported but not used for the selection of data.*

Increased regulation of cell cycle-related pathways might indicate elevated endothelial proliferation in the brains of *Nemo*^{beKO}*Ripk3*$^{-/-}$ mice. Indeed, it is already investigated that brain endothelial *Ikbkg* deletion induces endothelial cell proliferation (Y. Jiang et al., 2020). In the following, we used the microarray data of vessel fragments from *Nemo*^{beKO} and *Nemo*^{fl} mice (achieved by Kristin Müller) to observe commonly regulated genes in *Nemo*^{beKO}*Ripk3*$^{-/-}$ and *Nemo*^{beKO} mice. Out of 25 genes regulated in *Nemo*^{beKO}*Ripk3*$^{-/-}$ vessel fragments, 21 were also regulated in *Nemo*^{beKO} vessel fragments (Figure 22). Genes regulated in *Nemo*^{beKO} *Ripk3*$^{-/-}$ samples, but not in *Nemo*^{beKO} samples, are coding for non-translational RNA, an ABC1 transporter member, the H2A histone and the keratin-associated protein 28-13, and are not of interest for our investigations.

In conclusion, these findings indicate that RIPK3 deficiency reduces gene expression that is not directly linked to *Ikbkg* deletion but rather to secondary effects, such as cell death and inflammation. The commonly regulated genes suggest that NEMO deficiency is primarily linked to the upregulation of proliferation pathways, such as angiogenesis.

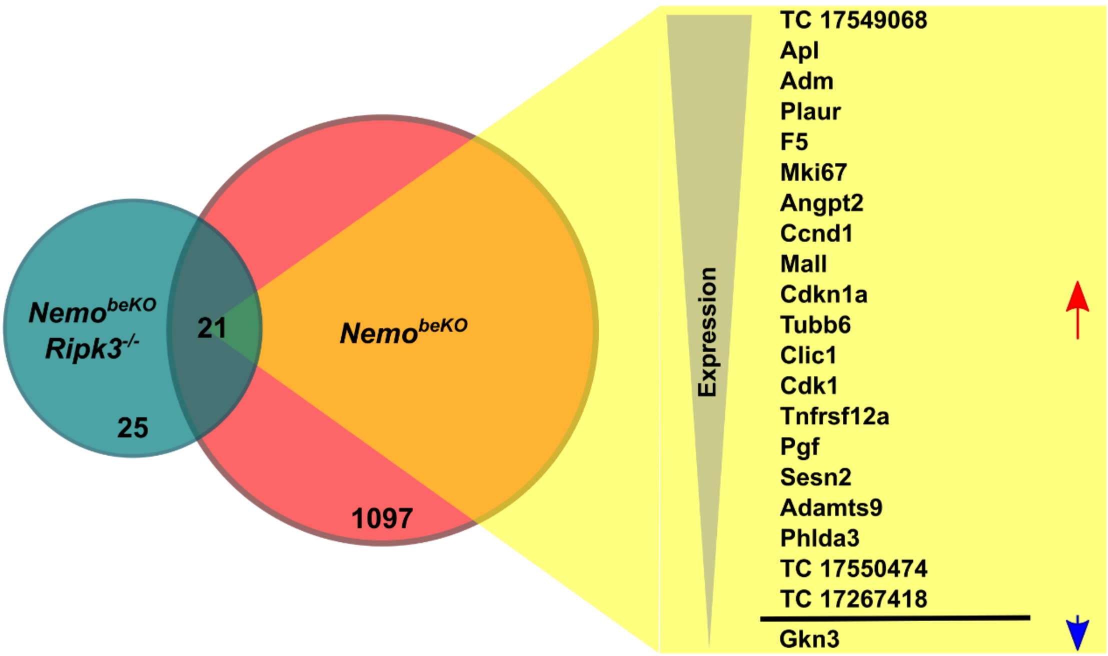

Figure 22: Commonly regulated genes in* Nemo^{beKO} *and* Nemo^{beKO}Ripk3$^{-/-}$ *mice. *Out of 25 significantly two-fold regulated genes from vessel fragments of* Nemo^{beKO}Ripk3$^{-/-}$ *mice, 21 were shown to be regulated in* Nemo^{beKO} *mice as well. The gene symbols are sorted by the descending order of fold change in* Nemo^{beKO}Ripk3$^{-/-}$ *vessel fragments. A red arrow indicates commonly upregulated genes, while a blue arrow indicates commonly downregulated genes.*

Since the DAVID Functional Annotation Cluster analysis results might indicate increased angiogenesis in *Nemo*^{beKO}*Ripk3*$^{-/-}$ mice, we investigated brain endothelial proliferation by staining Coll IV and Ki67, a marker for mitosis (Figure 23a). Counting of Ki67^{+}Coll IV^{+} cells revealed approximately three-fold increased endothelial proliferation in *Nemo*^{beKO}*Ripk3*$^{-/-}$ mouse brains (Figure 23b).

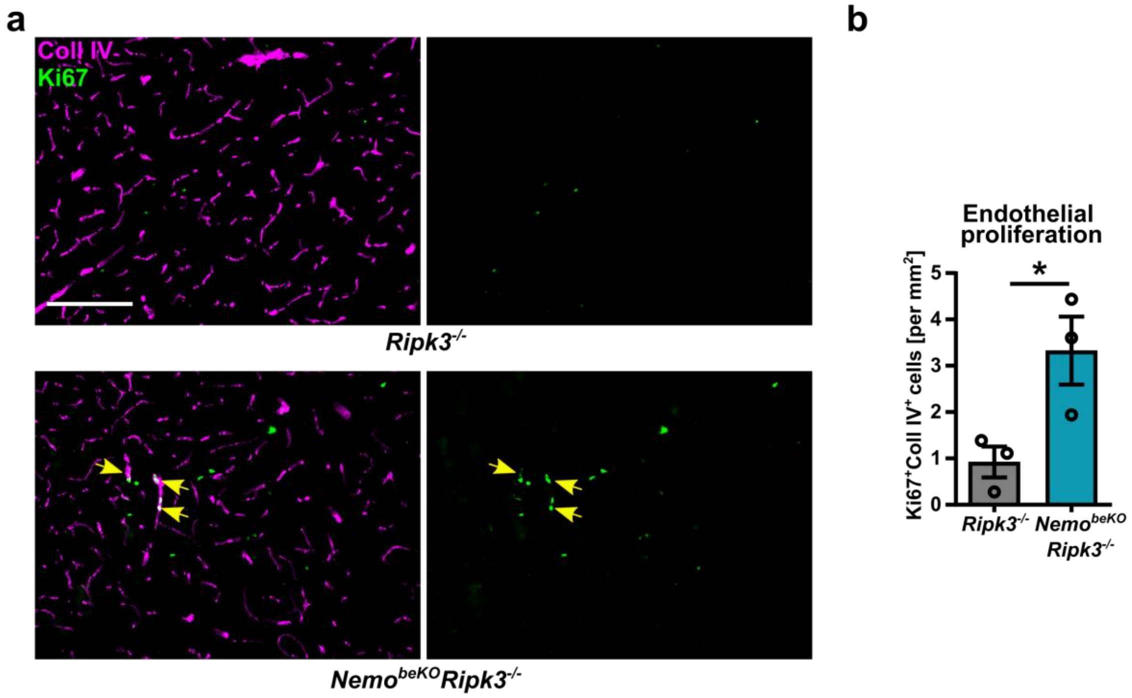

Figure 23: Increased angiogenesis was observed in* Nemo^{beKO}Ripk3$^{-/-}$ *mice. *A) Angiogenesis is indicated by staining of Ki67 and Coll IV. The yellow arrows indicate endothelial proliferation. Scale bar, 200 µm. B) Endothelial proliferation is significantly enhanced in the brains of* Nemo^{beKO}Ripk3$^{-/-}$ *mice compared to* Ripk3$^{-/-}$ *mice. Unpaired t-test, $F(4)=3.0$, $p = 0.0406$, N = 3 animals/group. *$p < 0.05$.*

4.5. RIPK3 deficiency delays but does not prevent the vascular phenotype of *Nemo*^{beKO} mice

The previous experiments showed that *Nemo*^{beKO} mice have a higher mortality rate and develop brain endothelial defects that can be prevented by RIPK3 ablation. To this point, mice were only examined 14 days after the first tamoxifen dose. Thus, we were wondering if RIPK3 deficiency is preventing the phenotype at any time after induction of *Ikbkg* deletion and – more importantly – if RIPK3 deficiency protects against the vascular defects even after a long time. For this purpose, a time-course experiment was performed. *Nemo*^{fl}, *Nemo*^{beKO}, *Ripk3*$^{-/-}$ and *Nemo*^{beKO}*Ripk3*$^{-/-}$ mice were sacrificed before and in range of 2-301 days after the start of tamoxifen injection. Notably, only one *Nemo*^{beKO} animal was found dead 14 days after the first tamoxifen treatment. The other animals survived until they were sacrificed for perfusion.

As an indicator of the health and well-being of the animals, body weight was measured every two days after the start of the tamoxifen treatment until day 28. Then, body weights were detected weakly (Figure 24). As observed before, *Nemo*^{beKO} mice started losing weight after eight days of tamoxifen injection (Ridder et al., 2015). They started gaining weight again after reaching a minimum weight approximately 20 days after the first tamoxifen dose. Later, their body weight was not significantly different from those in the *Nemo*^{fl} group. However, *Nemo*^{beKO} mice with RIPK3 deficiency showed no reduction in body weight until 28 days after the first tamoxifen injection. At this time point, their body weight was significantly reduced compared to the *Ripk3*$^{-/-}$ mice but still significantly higher than in the *Nemo*^{beKO} group. From this time point on, *Nemo*^{beKO}*Ripk3*$^{-/-}$ mice showed slightly reduced but not significantly different body weights from the control groups. In summary, the NEMO ablation led to a general malaise of the mice soon after inducing the knockout, but animals recovered fully approximately four weeks later. *Ripk3* deletion completely prevented the loss of body weight until 28 days after the start of tamoxifen injection and was not associated with a dramatic drop in body weight at any time.

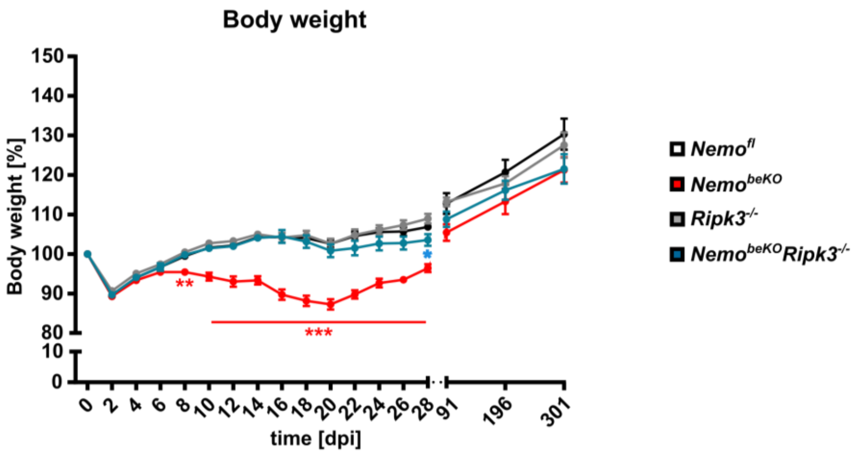

Figure 24: The body weight course showed a significant weight drop of* Nemo^{beKO} *mice which could be improved by additional RIPK3 ablation. *A) Shown is the overall body weight course. Body weight is shown as the percentage of the measured body weight before tamoxifen injection. Until day 28, mice were weighed every two days. Then, weight was taken weakly. Data for the time points 29 days-90 days, 92 days-195 days, and 197 days-300 days were not shown in the graph.* Nemo^{beKO} *mice had a significantly lower body weight than* Nemo^{fl} *mice from 8 to at least 28 days after the first tamoxifen dose. Then, no significant difference was observed.* Nemo^{beKO}Ripk3$^{-/-}$ *mice had a significantly reduced body weight compared to the* Ripk3$^{-/-}$ *group at 28 days after the first tamoxifen injection. Weight differences between* Nemo^{beKO} *mice and* Nemo^{beKO}Ripk3$^{-/-}$ *mice were significantly different from day 8-28 (significances not shown in the graph). Mixed-effects model with Geisser-Greenhouse correction (ε = 0.161) followed by Tukey's posthoc test, $\chi 2(1) = 448.6$; $p < 0.001$; genotype: $F(3,134) = 76.4$, time: $F(2.7,152.2) = 294.7$, $p < 0.001$; interaction: $F(51,943) = 14.6$ $p < 0.001$, N = 6 – 36 animals/group and time point.* * $p < 0.05$; ** $p < 0.01$, ***$p < 0.001$.

We next investigated the vascular phenotype of *Nemo*^{beKO} *and Nemo*^{beKO}*Ripk3*$^{-/-}$ mice compared to the control groups. Analysis of string vessels revealed a tendency towards increased string vessel formation already two days after the induction of the *Ikbkg* knockout (Figure 25). After 28 days, the elevation in string vessel length was significantly different from that in *Nemo*^{fl} mice and string vessels were still observed 301 days after knockout induction. As shown before, RIPK3 deficiency prevented string vessel formation shortly after knockout induction, but at the last time point, *Nemo*^{beKO}*Ripk3*$^{-/-}$ mice showed an enormously increased formation of string vessels. According to this finding, we rather suggest a delay in string vessel formation than prevention as initially thought. Vessel length was measured and is shown in Supplement

Figure 35. No differences were observed at any time points for the genotypes. Nevertheless, a significant effect in time was detected. This effect likely occurred because of technical difficulties since the shift in time correlates with the time between staining and imaging (the higher the time difference, the higher the vessel length). Normalisation of the vessel length to the control group (*Nemo*^{fl}*)* for each time point diminished the time effect but did not reveal any significant differences between groups.

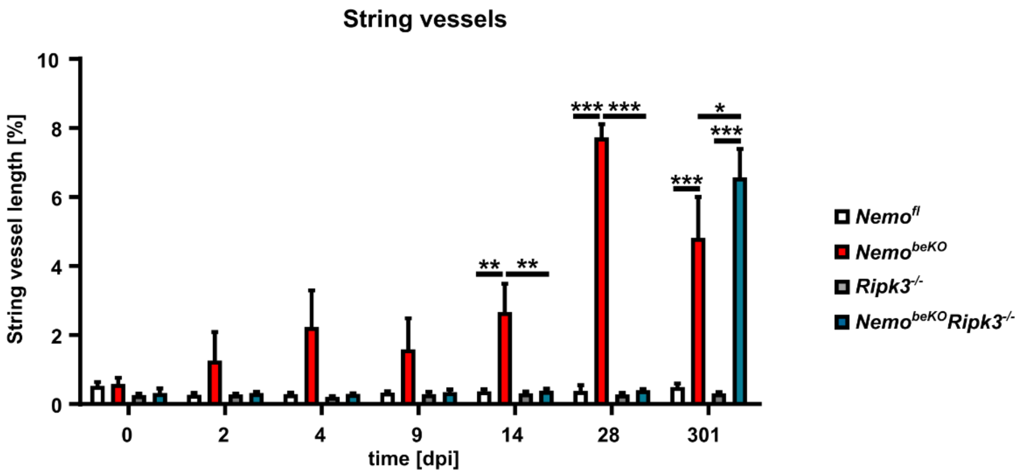

Figure 25: RIPK3 deficiency delayed string vessel formation in **Nemo**^{beKO} ***mice.*** *While RIPK3 deficiency prevented string vessel formation at least 28 days after* Nemo *knockout induction, a strongly increased string vessel formation was observed in* Nemo^{beKO}Ripk3$^{-/-}$ *mice 301 days after the first tamoxifen treatment. Two-way ANOVA followed by Tukey's post-hoc test, genotype: $F (3,106) = 43.7$, $p < 0.0001$; time: $F (6, 106) = 18.0$, $p < 0.0001$; interaction: $F (18, 106) = 11.7$, $p < 0.0001$; N = 3-7 animals/group and time point.* * $p < 0.05$; ** $p < 0.01$, ***$p < 0.001$.

Analysis of brain weights showed an increase in *Nemo*^{beKO} mice at 14 and 28 days after the first tamoxifen treatment (Figure 26a). *Ripk3* knockout completely prevented this increase, indicating that *Nemo*^{beKO}*Ripk3*$^{-/-}$ mice might not suffer from brain oedema. In contrast, IgG extravasation could not be prevented but only attenuated by RIPK3 deficiency (Figure 26b). Compared to the onset of elevated string vessel formation, *Nemo*^{beKO}*Ripk3*$^{-/-}$ mice started to have significantly higher extravasation already 28 days after the first tamoxifen dose. Noteworthy, in *Nemo*^{beKO} mice, IgG extravasation was already observed before tamoxifen treatment. Probably, the recombinase is already active at a low level before tamoxifen treatment. Similar to IgG extravasation, IgG vesicle number in *Nemo*^{beKO} was decreased by 50 % compared to *Nemo*^{fl} mice already before tamoxifen was administered (Figure 26c). IgG vesicle number in *Nemo*^{beKO}*Ripk3*$^{-/-}$ mice was not changed until nine days after the first tamoxifen treatment. After 28 days, an enormously low IgG vesicle number was observed in *Nemo*^{beKO} and *Nemo*^{beKO}*Ripk3*$^{-/-}$ mice. At this time point, the IgG vesicle numbers of *Nemo*^{beKO} mice was significantly lower than observed for *Nemo*^{beKO} mice without tamoxifen treatment ($p = 0.011$; not shown in the graph). After 301 days, IgG vesicle numbers in *Nemo*^{beKO} and *Nemo*^{beKO}*Ripk3*$^{-/-}$ mice were significantly different from those detected before tamoxifen treatment (*Nemo*^{beKO}*:* $p = 0.0481$;

Nemo^{beKO}*Ripk3*$^{-/-}$*:* p = 0.0098; not shown in the graph). Interestingly, a significant difference was also observed for the control group *Ripk3*$^{-/-}$ (p = 0.0485; not shown in the graph).

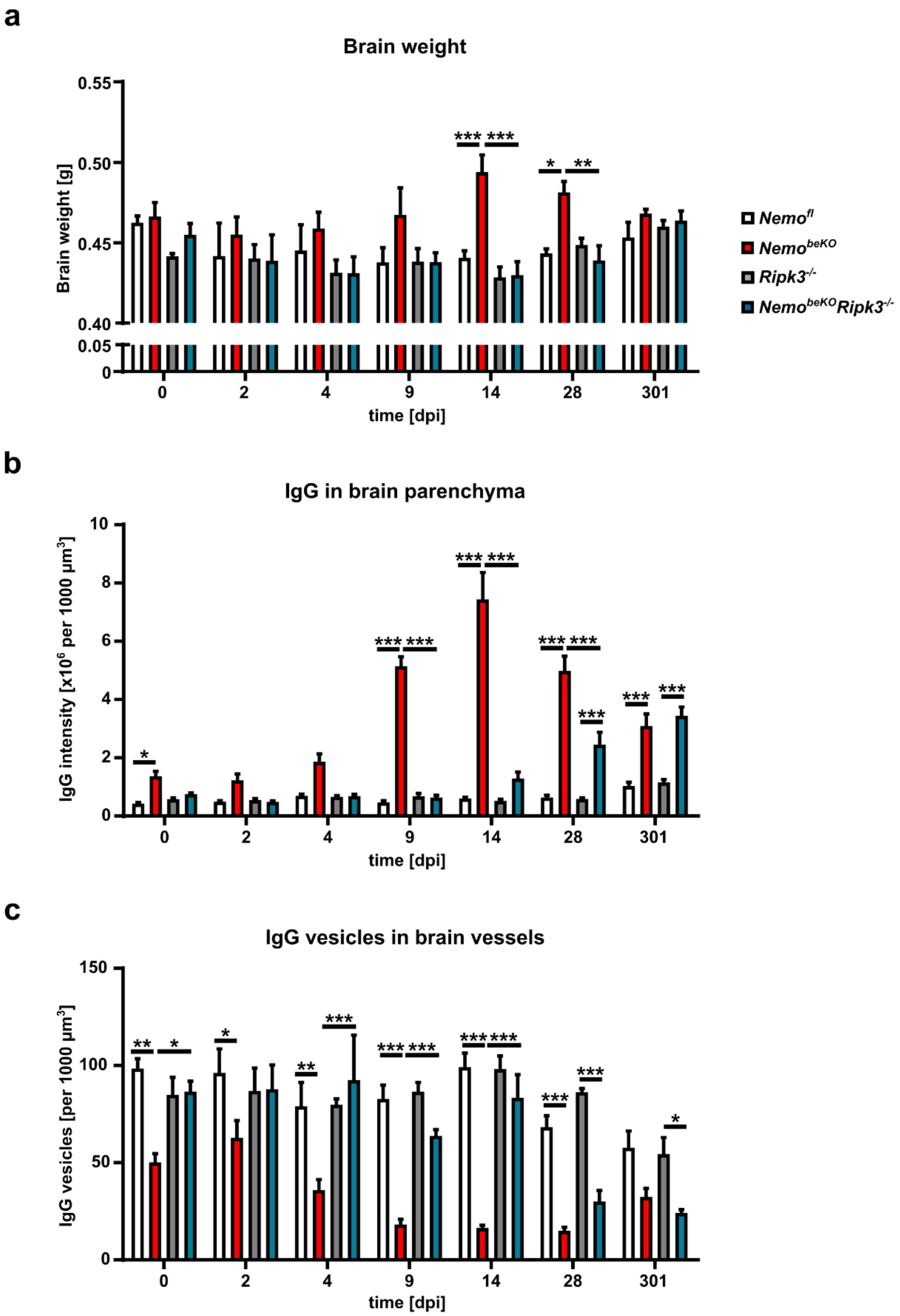

Figure 26: RIPK3 deficiency delayed IgG extravasation and reduction of IgG vesicle number in **Nemo**^{beKO} ***mice.*** *A) Brain weight is shown as an indicator for brain oedema. Brain weights of* Nemo^{beKO} *mice were significantly increased 14 and 28 days after tamoxifen treatment. Brain weights of* Nemo^{beKO}Ripk3$^{-/-}$ *mice did not increase at any time point. Two-way ANOVA followed by Tukey's posthoc test; time: F (6,110) = 2.6, p = 0.0225; genotype: F(3,110) = 15.2, p < 0.0001; interaction: F(18,110) = 1.355, p = 0.1693; N = 4-7 animals/group and time point. B)*

IgG extravasation in Nemo^{beKO} *mice brains started before tamoxifen treatment and lasted until the end of the experiment. RIPK3 deficiency attenuated this effect until day 28. Two-way ANOVA followed by Tukey's posthoc test, genotype: $F (3,108) = 154.3$, $p < 0.0001$; time: $F (6, 108) = 24.9$, $p < 0.0001$; interaction: $F (18, 108) = 18.6$, $p < 0.0001$; N = 3-7 animals/group and time point. C) The decrease in IgG vesicle number in* Nemo^{beKO} *mice was already present before tamoxifen treatment started and could be attenuated by RIPK3 deficiency until day 28. Two-way ANOVA followed by Tukey's posthoc test, genotype: $F (3,108) = 56.6$, $p < 0.0001$; time: $F (6, 108) = 15.4$, $p < 0.0001$; interaction: $F (18, 108) = 3.4$, $p < 0.0001$; N = 3-7 animals/ group and time point.* *p<0.05, ** p < 0.01, ***p < 0.001.

In addition to the main parameters of this study – string vessel formation, IgG extravasation and IgG vesicle number – we also investigated the occurrence of active astrocytes. Astrocytic activation is often associated with neuropathologies, such as epileptic seizures (Sano et al., 2021). We detected a significant increase in the GFAP$^+$ area in the *Nemo^{beKO}* mice 28 days after the first tamoxifen treatment (Figure 27). *Nemo^{beKO}Ripk3$^{-/-}$* mice did not show a significant elevation in the astrocytic area at any time point compared to its control group *Ripk3$^{-/-}$*.

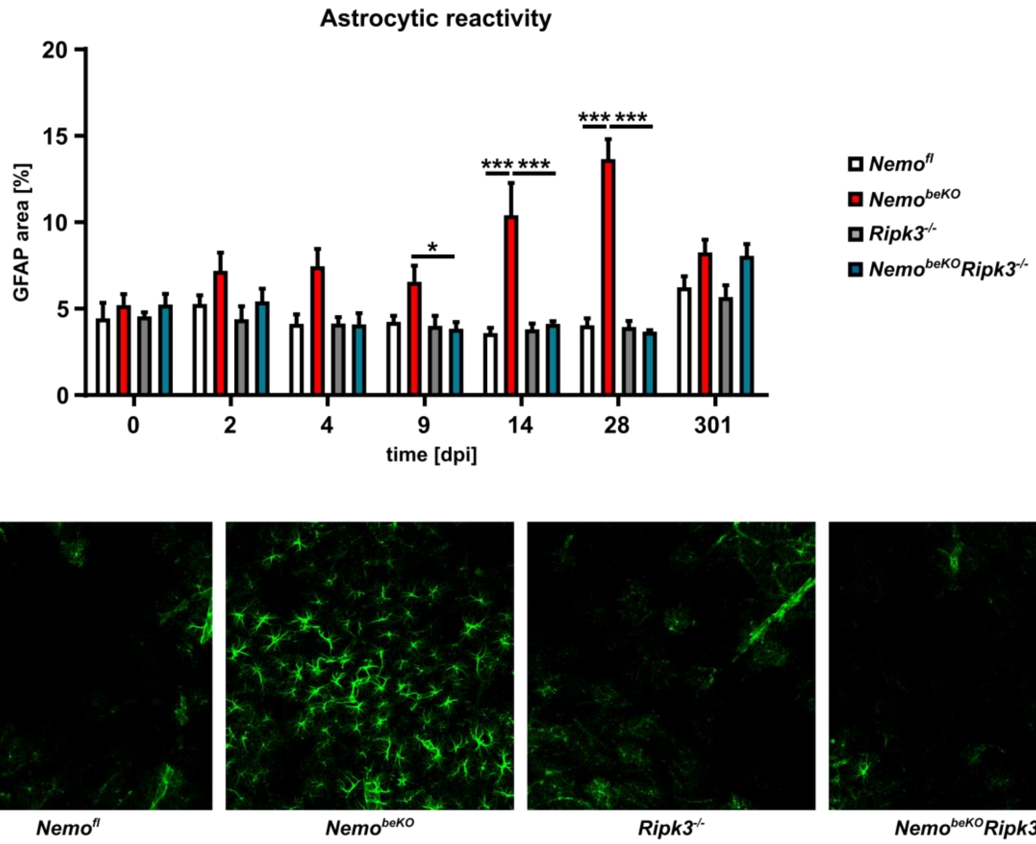

Figure 27: RIPK3 deficiency prevented the increase in astrocytic activity in the brains of* Nemo^{beKO} *mice. *In* Nemo^{beKO} *mice, increased astrocytic reactivity was observed starting at 9 days after the first tamoxifen dose, and it was prevented by RIPK3 ablation. Astrocytic reactivity was measured as the percentage of GFAP$^+$ area normalized to the total area of the image. Images below the graph show many GFAP$^+$ astrocytes in the cortex of* Nemo^{beKO} *mice, while in the cortices of the other genotypes only a small number of GFAP$^+$ astrocytes were observed. Two-way ANOVA followed by Tukey's posthoc test, genotype: $F (3,108) = 42.2$, $p < 0.0001$; time: $F (6, 108) = 6.7$, $p < 0.0001$; interaction: $F (18, 108) = 5.5$, $p < 0.0001$; N = 3-7 animals/group and time point. * $p < 0.05$; ***$p < 0.001$. Parts of figure 27a are published (Wenzel, Lampe, Müller-Fielitz et al., 2021).*

In summary, our data suggest that RIPK3 deficiency delays but does not prevent the vascular pathology and BBB interruptions of mice with brain endothelial knockout of *Ikbkg*. In addition, our data show that endothelial IgG vesicle transport seems to be the first parameter affected by NEMO ablation (Figure 28).

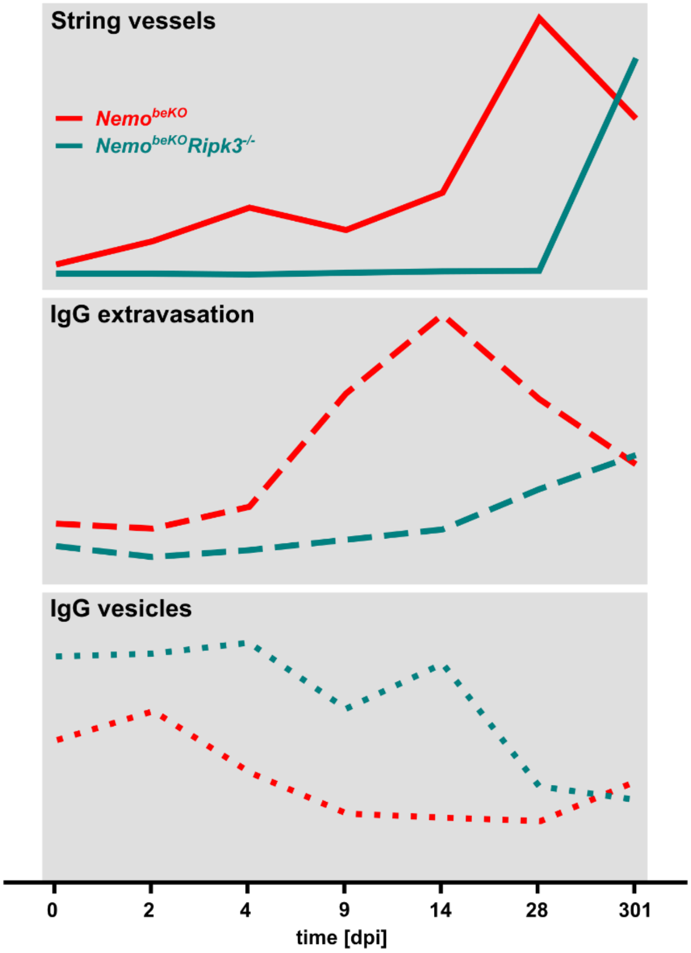

Figure 28: Progression of string vessel formation, IgG extravasation and IgG transcytosis disturbances were delayed by* Ripk3 *deletion in* Nemo^{beKO} *mice. *The scheme shows that string vessel formation is prevented by RIPK3 deficiency at least 28 days after tamoxifen treatment (upper graph). After 301 days, approximately the same increase in string vessel length can be observed for* Nemo^{beKO}Ripk3$^{-/-}$ *and* Nemo^{beKO} *mice. IgG extravasation (middle graph) and reduction in IgG vesicle number (lower graph) seem to have an earlier onset than the formation of string vessels. Especially in* Nemo^{beKO}Ripk3$^{-/-}$ *mice, the IgG vesicle number was already significantly reduced after nine days of the first tamoxifen treatment, whereas significantly elevated string vessel formation was observed after 301 days.*

5. Discussion

5.1. The brain vasculature in *Nemo*^{beKO} mice

Approximately one-third of all IP patients suffer from neurological symptoms typical for cSVD, such as seizures, mental retardation, stroke, and cerebellar ataxia (Müller et al., 2017). *Nemo*^{beKO} mice represent a well-established mouse model for the neurological symptoms of IP (Y. Jiang et al., 2020; Ridder et al., 2015). As in other cSVDs, hypoxic areas were found in the cerebrum leading to angiogenesis and vascular remodelling in the mouse model (Y. Jiang et al., 2020). In addition, endothelial cell death was discovered by the increased occurrence of string vessels and numerous BECs positive for cleaved Casp3, a marker for apoptosis (Ridder et al., 2015). The observation that string vessels have small diameters and seem to occur mainly in the capillary bed prompted the authors and others to assume that pathologies in *Nemo*^{beKO} mice are localised at the microvasculature, indicating IP as a cSVD (Y. Jiang et al., 2020; Müller et al., 2017; Ridder et al., 2015). In addition, it has been shown more recently that NEMO deficiency might also be the reason for brain pathologies observed in COVID-19 patients (Wenzel, Lampe, Müller-Fielitz et al., 2021). To date, COVID-19 has not been considered as cSVD, but M^{pro}-induced cleavage of NEMO leads to string vessels, vessel rarefaction and brain endothelial cell death. To this point, the localisation of BEC death and string vessels in the vascular tree in the brains of IP patients, COVID-19 patients or *Nemo*^{beKO} mice has been unknown.

Recent efforts aimed to prevent the *Nemo*^{beKO}-induced phenotype by constitutive *Ikk2* activation. Thus, NF-κB was activated, and high brain water content and IgG extravasation were partially compensated, but BEC death was not reduced. This discrepancy led to the hypothesis that brain endothelial NEMO ensures endothelial survival by gene expression independent effects. Accordingly, *in-vitro* studies have shown that NEMO deficient cells are more sensitive to TNF-induced cell death depending on RIPK1 than cells inhibited for NF-κB nuclear translocation (Legarda-Addison et al., 2009). Supporting this idea, Pescatore and colleagues compared cells expressing a NEMO-A323P mutant with *Ikbkg* knockout cells. They discovered that NEMO seems to have a scaffold function that prevents cell death independently from NF-κB activation (Pescatore et al., 2016). *In-vivo* studies on mice with NEMO-deficient intestinal epithelial cells or NEMO-deficient keratinocytes showed TNF-induced cell death resulting in colitis and skin lesions (Nenci et al., 2006, 2007). The deletion of TNFR could reverse these phenotypes, indicating NEMO's crucial importance to prevent specifically TNF-induced cell death. These results were confirmed by another *in-vivo* study, in which epithelial cell death caused by *Nemo* deficiency was diminished by the deletion of TNF-induced cell death executioners, such as RIPK1 or RIPK3 and FADD (Vlantis et al., 2016).

Based on these findings, we first evaluated the vascular phenotype of *Nemo*^{beKO} mice as a model for cSVD in more detail. Second, we examined if endothelial dysfunction in BECs due to *Ikbkg* inactivation is caused by TNF-induced cell death. Most of the investigations were done on *Nemo*^{beKO} samples achieved 14 days after the first tamoxifen treatment since former studies showed that neurological IP pathology is fully developed at this stage (Y. Jiang et al., 2020; Ridder et al., 2015)

5.1.1. cSVD characteristics in *Nemo*^{beKO} mice

To address the first point, we checked if *Nemo* deficiency in BECs leads to typical cSVD pathologies just as capillary cell death, microcirculation rarefaction, and pericyte dysfunction (Joutel et al., 2010; Uemura et al., 2020). As observed before, we detected numerous string vessels in the brain cortices of *Nemo*^{beKO} mice but not in *Nemo*^{fl} mice (Ridder et al., 2015; Wenzel, Lampe, Müller-Fielitz et al., 2021). These string vessels are thinner than normal capillaries and are probably reflected by a higher frequency of vessels smaller than approximately 1.7 µm in *Nemo*^{beKO} mice (Figure 6). Besides the increase in very thin vessels, we could observe an overall shift from vessels with smaller diameters to vessels with bigger diameters in NEMO deficient mice. Further, string vessels were primarily observed in higher branch orders of the vascular tree in different brain regions (Figure 7). Therefore, we conclude that BEC death predominantly occurs in smaller vessels in the brain of *Nemo*^{beKO} mice, leading to the formation of string vessels in the higher branch orders and rarefaction of capillaries (Wenzel, Lampe, Müller-Fielitz et al., 2021). As a consequence of the loss of microcirculation vessels, hypoxia occurs as observed by Jiang et al. (Y. Jiang et al., 2020). Thus, brain capillary rarefaction in *Nemo*^{beKO} mice, as assumed by Ridder and colleagues, could be confirmed by this study (Ridder et al., 2015).

Further, we showed reduced pericyte coverage in *Nemo*^{beKO} mice (Figure 6; Wenzel, Lampe, Müller-Fielitz et al., 2021). Pericytes have been often described as contractile cells regulating the blood flow, and lack of pericytes has been shown to increase capillary diameter (Hellström et al., 2001). Therefore, reduced pericyte coverage could result in disturbed microcirculation or dysfunctional neurovascular coupling (Hall et al., 2014; Kisler et al., 2017). Indeed, Ridder and colleagues observed impaired endothelial-mediated relaxation, reduced resting blood flow and reduced hyperemia in *Nemo*^{beKO} mice (Ridder et al., 2015). In addition, we observed a shift in the frequency of vessel diameters towards larger vessel diameters in *Nemo*^{beKO} mice (Wenzel, Lampe, Müller-Fielitz et al., 2021). This finding might result from increased endothelial cell death but could also be induced by pericyte loss.

In addition, pericyte deficiency has also been associated with BBB impairment by destabilising TJ and increasing endothelial transcytosis (S. Liu et al., 2012; Villaseñor, Kuennecke, et al., 2017). Our study observed both pathologies when NEMO was absent (Figure 12 and 15; Wenzel Lampe, Müller-Fielitz et al., 2021). With respect to the destabilizing effect on TJ, pericyte deficiency has been shown to cause occludin loss, leading to subsequent brain calcifications (Saitou et al., 2000; Zarb et al., 2019). These brain calcifications result from continuous, perivascular accumulations of calcium phosphate, are a typical feature of cSVD, and can lead to various neurological dysfunctions (Y. C. Chen et al., 2019; Loeb et al., 2006; Ramos et al., 2017). Although several mutations are linked to this phenomenon, the exact mechanism is still unknown (Keller et al., 2013; Ramos et al., 2017). Thus, we examined *Nemo*^{beKO} brains for calcifications but could not detect any (Supplemental Figure 33). It is not clear which mechanisms lead to pericyte loss in *Nemo*^{beKO} mice. Microarray data from *Nemo*^{beKO} vessel fragments do not indicate any loss of endothelial-pericyte communication since the expression of members of the Ang-1/Tie-2, PDGFβ/PDGFRβ, and TGFβ/TGFβR signalling pathways are unchanged or rather increased (Y. Jiang et al., 2020). BEC death and occludin TJ interruptions lead to BBB breakdown, which has been associated with cSVD (Schreiber et al., 2013). Besides these defects, we observed numerous other pieces of evidence for BBB breakdown in *Nemo*^{beKO} mice. These pieces of evidence include increased extravasation, astrogliosis and transcytotic changes and will be discussed later more in detail. Altogether, this study confirms IP as a cSVD in a mouse model by localising string vessels in the microvasculature, detecting pericyte deficiency and BBB impairment.

5.1.2. Endothelial cell death and the association with TNF-induced pathways

A significant increase in cleaved Casp3 levels in BECs and massive occurrence of string vessels has been associated with endothelial cell death in NEMO deficient mice (Ridder et al., 2015). The findings of our study revealed endothelial cell death by the TUNEL reaction and found a significant elevation in TUNEL^{+} vessels in the brains of *Nemo*^{beKO} mice (Figure 8; Wenzel, Lampe, Müller-Fielitz et al., 2021). Because the TUNEL reaction is less specific for apoptosis than cleaved Casp3, the quantification includes different cell death types and allows general information about BEC death. However, the number of TUNEL^{+} vessels per mm^2 in *Nemo*^{beKO} mice is meagre compared to the number of string vessels per mm^2. In our opinion, the time slot of cell death, especially the stage of DNA fragmentation detected by the TUNEL reaction, is probably smaller than the period in which a string vessel can be observed. For example, the duration of apoptosis has been estimated to be 6 to 24 h depending on the cell type (Saraste & Pulkki, 2000). Therefore, the number of dead endothelial cells might be strongly underestimated by quantifying TUNEL- or cleaved Casp3 signals and is probably better reflected by the quantification of string vessels.

Interestingly, some dying endothelial cells were detected in close proximity to string vessels (Figure 8; Wenzel, Lampe, Müller-Fielitz et al., 2021). To date, it is not known if cell death in *Nemo*^{beKO} brains occurs randomly within the capillary tree or if dying endothelial cells are clustered. If dying cells are more likely to die as well, cell death might be either induced by a local stimulus, such as hypoxia, or by paracrine signalling of dying cells. The latter issue might rely on the mode of cell death. For example, apoptotic cells are unlikely to induce cell death of neighbour cells. They instead secrete anti-inflammatory metabolites to suppress inflammation and promote cell proliferation and wound healing (Medina et al., 2020). Thus, apoptosis promotes the elimination of dying cells with phagocytotic signals while protecting the surrounding tissue. However, other cell death modes, such as necrosis or necroptosis, initiate inflammatory processes in the surrounding tissue, possibly leading to further cell death (Berghe et al., 2009; Bertheloot et al., 2021). Recently it was shown that the accumulation of phosphorylated MLKL from necroptotic epithelial cells at intercellular junctions promotes necroptosis of neighbouring cells (Samson et al., 2020). Enteropathies such as inflammatory bowel disease might be initiated in this manner. The close proximity of dying cells and string vessels observed in this study might indicate inflammatory cell death modes. This theory is strengthened by our finding of increased TNF expression and other reports showing upregulation of inflammation-associated genes in *Nemo*^{beKO} brain vessel fragments (Y. Jiang et al., 2020).

Increased TNF levels and absence of NEMO might lead to TNF-induced alternative pathways resulting in apoptosis and necroptosis (Figure 9). In the recent years, the mechanisms by which cells undergo TNF-induced apoptosis or necroptosis have been extensively studied. In brief, the kinase-active form of RIPK1 becomes activated if phosphorylation of serin-25 through the IKK complex is absent and ubiquitinylation is reduced due to low cIAP levels (Annibaldi et al., 2018; Dondelinger et al., 2019). Consequently, RIPK1 induces TNF-mediated cell death instead of complex I formation. In our study, NEMO deficiency probably results in an inactive IKK complex abolishing serin-25 phosphorylation of RIPK1. In addition, reduced NF-κB-induced gene expression might decrease cIAP levels (Lin et al., 2010). Therefore, RIPK1 recruits FADD, Casp8, and RIPK3 and thus, forms the ripoptosome. This complex, also known as TNF-induced complex IIb, promotes apoptosis dependent on RIPK1 kinase activation and RIPK3 scaffold function. Casp8 is cleaved and induces a Casp cascade to activate apoptosis (Tummers & Green, 2017). In addition, Casp8 cleaves RIPK1, RIPK3 and the necroptosis-promoting deubiquitinating enzyme CYLD and hence, usually prevents necroptosis (Tummers & Green, 2017). If the levels of active Casp8 or the adapter protein FADD are low, necroptosis is triggered by forming the RIPK1-RIPK3-MLKL necrosome (Manolis Pasparakis & Vandenabeele, 2015). This complex relies on the kinase function of both RIPK1 and RIPK3.

Based on these findings, we crossed our Nemo^{fl}*; Slco1c1-CreERT2* line with animals deficient for FADD and RIPK3, executioners of TNF-induced apoptosis or necroptosis (Manolis

Pasparakis & Vandenabeele, 2015; Pescatore et al., 2016; Vlantis et al., 2016). Surprisingly, *Nemo*^{beKO}*FADD*^{beKO} mice died within nine days after the start of tamoxifen treatment (Figure 10; Wenzel, Lampe, Müller-Fielitz et al., 2021). Further, the additional *Fadd* knockout did not ameliorate string vessel formation or vessel rarefaction in *Nemo*^{beKO} mice. These findings agree with observations in a colitis mouse model induced by *Ikbkg* inactivation. Here, a conditional knockout of *Fadd* could not prevent colon inflammation. (Vlantis et al., 2016). In addition, the ubiquitous deletion of *Fadd* is lethal *in-utero* (Yeh et al., 1998; Zhao et al., 2017). In fact, the absence of FADD does prevent TNF-induced apoptosis but, intriguingly, might induce RIPK3-mediated necroptosis leading to increased mortality and inflammation as observed before (Ranjan & Pathak, 2016; Schock et al., 2015; Zhao et al., 2017).

In contrast, RIPK3 ablation was sufficient to prevent string vessel formation and vessel rarefaction 14 days after the start of tamoxifen treatment (Wenzel, Lampe, Müller-Fielitz et al., 2021). Besides, the elevated mortality in *Nemo*^{beKO} mice was entirely abolished by RIPK3 deficiency. Further analyses showed that *Ripk3* deletion prevents occludin TJ interruptions and reduces BBB permeability partially in *Nemo*^{beKO} mice (Figure 11, Figure 12; Wenzel, Lampe, Müller-Fielitz et al., 2021). In accordance, a study by Newton and colleagues showed improved outcomes of kidney ischemia-reperfusion injury, myocardial infarction and systemic inflammation when *Ripk3* was deleted (Newton et al., 2016). Interestingly, the knockout of Nemo, FADD and RIPK3 still led to slightly increased formation of string vessels in our study (Wenzel, Lampe, Müller-Fielitz et al., 2021). This result contrasts with a study using the triple knockout in a colitis model that could fully rescue the phenotype observed by *Nemo* inactivation alone (Vlantis et al., 2016). Thus, it cannot be excluded that FADD deficiency might also trigger other forms of cell death in BECs than RIPK3-mediated necroptosis.

Since *Nemo*^{beKO} mice showed an inflammatory phenotype and RIPK3 ablation normalized the vascular phenotype, we speculated that brain endothelial *Nemo* inactivation leads to necroptosis by the TNF-induced formation of the necrosome. Thus, we focussed on further investigations with RIPK3 deletion.

5.1.3. *Ripk3* deletion and the *Nemo*^{beKO} pathology in a long-term study

In a study by Nenci et al., skin lesions after birth in mice with *Ikbkg* deficiency were rescued by a simultaneous knockout of *Tnfr1* (Nenci et al., 2006). In accordance with our findings, they revealed TNF-induced cell death responsible for the observed IP phenotype. Surprisingly, four to six months later, most NEMO^{EKO}/TNFRI-deficient mice developed skin lesions. Based on these observations, we wondered if RIPK3 deletion prevents the vascular phenotype of *Nemo*^{beKO} mice permanently or delays the onset of the symptoms. Following time-course experiments with *Nemo*^{beKO} mice performed by Ridder and al., we sacrificed mice with *Ikbkg* and

Ripk3 deletion before tamoxifen treatment and 2, 4, 9, 14, 28 and 301 days after the start of tamoxifen injection (Ridder et al., 2015). Again, string vessel formation was normal in mice with combined NEMO and RIPK3 deficiency up to 28 days after the start of tamoxifen injection, but at day 301, an enormously increased string vessel formation could be observed even with *Ripk3* deletion (Figure 25). In addition, IgG extravasation was similarly elevated as observed in *Nemo*^{beKO} mice without RIPK3 deficiency at this time point (Figure 26). Besides, the body weight of *Nemo*^{beKO}*Ripk3*$^{-/-}$ mice decreased 28 days after the first tamoxifen dose (Figure 24). Body weight is a reliable welfare indicator of mice, and hence, in our study, body weight decrease could indicate the onset of neurological symptoms, such as seizures (Campos-Luna et al., 2019). Accordingly, *Nemo*^{beKO} mice started to lose body weight eight days after the start of tamoxifen injection and reached the minimum weight at day 20 when BBB impairment had manifested and seizures were detected (Ridder et al., 2015). The body weight decrease in *Nemo*^{beKO}*Ripk3*$^{-/-}$ mice was mild compared to *Nemo*^{beKO} mice and manifested later. Therefore, it might be speculated that neurological symptoms are less pronounced when RIPK3 is absent. These findings indicate that necroptosis and BBB impairment can be prevented by *Ripk3* deletion shortly after *Ikbkg* knockout induction, but not at later stages.

Nenci and colleagues hypothesized that TNF signalling is necessary for the onset of the disease early after birth, but in adulthood, secondary skin lesion development is mediated by other processes. This hypothesis cannot be translated to our findings with RIPK3 ablation since our *Nemo*^{beKO} mice are already adult when the *Ikbkg* knockout is induced. However, it might be possible that other factors lead to a switch in cell death signalling. Nenci et al. found increased Il-1β levels and apoptotic basal keratinocytes in the skin of the older NEMO^{EKO}/TNFRI-deficient mice, indicating that Il-1β-dependent pathways might lead to keratinocyte death at later stages. Knowledge about the cytokines released in the brain parenchyma of *Nemo*^{beKO}*Ripk3*$^{-/-}$ mice compared to the cytokine profile of *Nemo*^{beKO} and control mice might help test this hypothesis for our model. Perhaps, several cell death mechanisms are induced in parallel in *Nemo*^{beKO} mice with different temporal onsets. Thus, TNF-induced necroptosis might be the first pathway activated by the destabilisation of TNF-induced complex I. Eventually, RIPK3-independent cell death might be induced by inflammatory and angiogenic processes that develop later.

An instance of an alternative pathway with later onset in *Nemo*^{beKO} mice might be RIPK1-dependent and RIPK3-independent apoptosis. Vlantis and colleagues observed Paneth cell death and colitis mediated by Nemo inactivation in the intestinal epithelium of mice (*Nemo*$^{IEC-KO}$). Upon *Ripk3* deletion, only a slight improvement of the phenotype was detected (Vlantis et al., 2016). Further, they found Casp3 positive cells in the absence of *Nemo* and *Ripk3*. We did not check for apoptosis marker in the *Nemo*^{beKO}*Ripk3*$^{-/-}$ vasculature but detected Casp3 positive endothelial cells in *Nemo*^{beKO} mice, suggesting apoptosis as an additional cell death pathway next to necroptosis. Gathering information about the cell death mode in *Nemo*^{beKO}*Ripk3*$^{-/-}$ by investigating apoptosis marker (e. g. cleaved Casp3) and necroptosis marker (e. g. pMLKL) in the brain vasculature would clarify if necroptosis is prevented and RIPK3-independent apoptosis activated. However, cell death was fully diminished when Vlantis and colleagues inhibited RIPK1 kinase activity in *Nemo*$^{IEC\text{-}KO}$ mice. More recently, we could reverse increased string vessel formation entirely by the pharmacological inhibition of RIPK1 in a SARS-CoV2 mouse model where NEMO was cleaved by M^{pro} in BEC (Wenzel, Lampe, Müller-Fielitz et al., 2021). RIPK3 ablation only partially improved the phenotype. Thus, in contrast to the RIPK3 knockout, the absence of RIPK1 kinase activity might protect from both, apoptosis and necroptosis. This conclusion has also been drawn in numerous other studies (Laurien et al., 2020; Polykratis et al., 2014; Van et al., 2017). Remarkably, null-knockout of *Ripk1* leads to severe inflammatory processes indicating that the scaffold function of RIPK1 is needed for the vitality of a cell (Berger et al., 2014; Y. Li et al., 2019; Van et al., 2017).

Activation of RIPK1 kinase is regulated by post-translational modifications, such as S166 phosphorylation, and might be cell-type- and stimuli-dependent (Laurien et al., 2020; Mifflin et al., 2020). Some reports could show that different NF-κB pathway members interact with RIPK1 to regulate kinase activity (Dondelinger et al., 2019; Geng et al., 2017; Lafont et al., 2018; Xu et al., 2018). Thus, it is reasonable to assume that the deficiency of NEMO might lead to an imbalance of the scaffold-dependent survival function and the kinase-dependent cell death function of RIPK1. Notably, inhibition of RIPK1 by Nec-1s did not ameliorate the vascular pathology in *Nemo*^{beKO} mice (Figure 32). In our opinion, technical issues might be the reason for the outcome of this study. Necrostatins have a short half-life time and, thus, should be administered intracerebroventricularly via an osmotic pump (S. Zhu et al., 2011). Since Nec-1s has low solubility in suitable solvents and a large volume is needed to treat animals for at least 14 days, this route of administration could not be used in our experiments. Instead, we decided on intraperitoneal treatment as done by Wang and colleagues (Q. Wang et al., 2017). We think the administration route and the used concentration were probably unsuitable for brain endothelial RIPK1 inhibition. In addition, it has not been investigated if necrostatins can cross the BBB. Some studies claim BBB-penetrating characteristics for necrostatins and refer to the work of Jagtab and colleagues (Liang et al., 2019; S. Zhu et al., 2011). Although Jagtab and colleagues did great work on pharmacokinetic investigations for necrostatins, they did not examine BBB permeability for any necrostatin (Jagtap et al., 2007). Consequently, we cannot be sure if Nec-1s even penetrated the BBB in our experiment.

As already mentioned, inhibition of RIPK1 kinase function by the oral gavage of GSK′547 was very successful in a mouse model for brain pathologies of COVID-19 (Wenzel, Lampe, Müller-

Fielitz et al., 2021). According to these findings, further investigations aiming to find therapeutical options to treat neurological symptoms of IP or COVID-19 should not focus on RIPK3 inhibition but rather on diminishing RIPK1 kinase activity. Inhibition of Ripk1 kinase activity by treating with an inhibitor or using the recently established *Ripk1*$^{D138N/D138N}$ knock-in mouse model, which expresses RIPK1 with impaired kinase activity, might prevent cell death entirely and permanently and could be tested in *Nemo*^{beKO} mice (Mifflin et al., 2020; Polykratis et al., 2014).

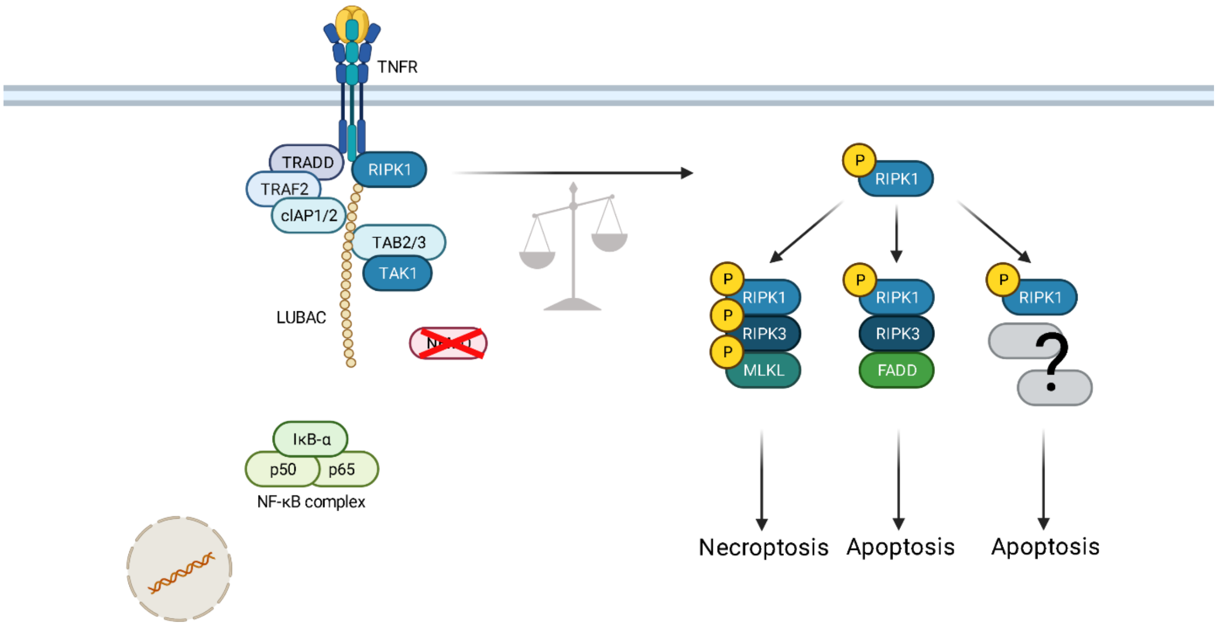

Figure 29: Ablation of NEMO triggers TNF-induced cell death dependent on the RIPK1 kinase activity. *Deleting* Ikbkg *not only abolishes NF-κB-induced gene expression but might also lead to kinase-activating phosphorylation of RIPK1. In turn, RIPK1 kinase activity mediates cell death via the necrosome (necroptosis) or the ripoptosome and FADD (apoptosis). According to recent findings, apoptosis might also be triggered in a RIPK3- and FADD-independent fashion. The figure was created with Biorender.com.*

5.1.4. *Nemo* deletion might induce non-productive angiogenesis

As early as 14 days after the start of tamoxifen treatment, *Nemo*^{beKO}*Ripk3*$^{-/-}$ mice did not show any signs of BEC death or interruption in TJ structure. Still, the BBB was impaired, as shown by increased extravasation of several endogenous markers and 4-kDa-FITC-dextran (Figure 11). In addition, we observed a decreased number of endothelial IgG vesicles indicating altered IgG transcytosis (Figure 15). We concluded that endothelial cell death and TJ interruptions in *Nemo*^{beKO} mice might be RIPK3-mediated while IgG transcytosis is influenced by altered gene expression due to inactivation of the NF-κB pathway. Thus, we performed microarray analysis from vessel fragments to uncover NF-κB activated genes with potential function in brain endothelial transcytosis.

Interestingly, only 25 genes were regulated in *Nemo*^{beKO}*Ripk3*$^{-/-}$ vessel fragments compared to 1097 regulated genes in *Nemo*^{beKO} vessel fragments (Figure 22; Y. Jiang et al., 2020). Notably, 21 of 25 regulated genes from *Nemo*^{beKO}*Ripk3*$^{-/-}$ vessel fragments were also regulated in *Nemo*^{beKO} vessel fragments, indicating that *Ripk3* deletion attenuates the effects on gene expression caused by *Ikbkg* inactivation. For both genotypes, Functional Annotation Clustering analysis revealed that the cluster with the highest enrichment score is associated with cell cycle/cell division/mitosis (Table 7; Y. Jiang et al., 2020). Following these results, Jiang and colleagues could show increased angiogenesis in all branches of the vascular tree in *Nemo*^{beKO} mice. Further, they observed a correlation in the chronological onset of capillary cell death, hypoxia, and angiogenesis and found a spatial relationship between string vessels, hypoxic areas and newly formed vessels. This observation indicates elevated angiogenesis in the brain as a consequence of a pathological event, and indeed, increased angiogenesis is associated with numerous neurological diseases, such as AD, ischemic stroke or traumatic brain injury (Alvarez-Vergara et al., 2021; Zhang et al., 2014; H. Zhu et al., 2021).

Based on these findings, we performed Ki67 staining in *Nemo*^{beKO}*Ripk3*$^{-/-}$ mice and found elevated endothelial proliferation (Figure 23). However, the number of proliferative endothelial cells were not as high as observed in *Nemo*^{beKO} mice (Y. Jiang et al., 2020). It is still elusive how angiogenesis is initiated in *Nemo*^{beKO}*Ripk3*$^{-/-}$ mice. To this point, it has not been tested if hypoxic areas can also be detected in *Nemo*^{beKO}*Ripk3*$^{-/-}$ mice and thus might trigger angiogenesis. Further, string vessels are not observed at this time point. However, cell death might already appear but probably at a low level, which does not lead to string vessel formation or vessel rarefaction.

However, if angiogenesis is productive, it has a beneficial function by compensating for the loss of vessels, as shown in several diseases (Krupinski et al., 1994; Yanlu Zhang et al., 2014). Since elevated angiogenesis does not lead to an increased vessel density in *Nemo*^{beKO} and *Nemo*^{beKO}*Ripk3*$^{-/-}$ mice (Figure 10), the angiogenesis in our mouse model might be non-productive. A recent study using mouse models for AD suggests vascular dysfunction and vessel rarefaction due to non-productive angiogenesis (Alvarez-Vergara et al., 2021). The authors observed hypoxia areas close to amyloid-beta plaques promoting the release of angiogenic vascular endothelial growth factor (VEGF). Signalling through the VEGF receptor induces the formation of tip cells as observed by higher *Plaur* expression, but a dysfunctional gamma-secretase blocks the further angiogenic process. Consequently, the number of tip cells is increased, but the formation of new vessels is dysfunctional and leads to vascular scars. Moreover, they detected microglial cleavage of abnormal vessels leading to vessel loss. Likewise the AD mouse model, *Nemo*^{beKO} mice show increased formation of tip cells, activated *Plaur* expression (Table 6) and microglial activation (Y. Jiang et al., 2020; Wenzel, Lampe, Müller-Fielitz et al., 2021). If NF-κB signalling promotes or inhibits angiogenesis is still under debate

(L. Jiang et al., 2013; Tabruyn & Griffioen, 2008; Tu et al., 2021). However, it might be speculated that NF-κB-mediated gene expression contributes to the efficient formation of new vessels. Thus, non-productive angiogenesis resulting from *Ikbkg* inactivation might contribute to the vascular pathology observed in *Nemo*^{beKO} and *Nemo*^{beKO}*Ripk3*$^{-/-}$ mice at later stages.

It is still elusive if the upregulation of angiogenesis-related genes is associated with transcytosis changes and BBB impairment. None of the functional annotation clusters was associated with cellular transport, and for none of the regulated genes, we found any direct association to transcytosis. However, transcytotic mechanisms at the BBB are largely unknown, and therefore, it might be worth investigating if inhibition or overexpression of the regulated genes has any effect on brain endothelial transcytosis.

5.2. The influence of NEMO on TJ and brain endothelial transcytosis

5.2.1. The contribution of occludin to brain parenchymal extravasation

RIPK3 deficiency prevented the vascular phenotype observed by brain endothelial-specific ablation of *Ikbkg* 14 days after the start of tamoxifen treatment. However, the BBB was still impaired, as shown by higher IgG, albumin, fibrinogen and 4-kDa FITC-dextran extravasation (Figure 11). A possible explanation for the leaky BBB might be increased paracellular extravasation due to interrupted TJ. Previous research observed decreased occludin expression in *Nemo*^{beKO} cerebral vessels while other TJ proteins, such as Claudin-5 or ZO-1, had no changed expression (Ridder et al., 2015). According to some studies, loss of occludin is sufficient to induce increased BBB permeability (Eum et al., 2015; Kim et al., 2020). Analysis of the TJ morphology by super-resolution microscopy revealed occludin interruptions leading to an overall reduction in the length of occludin TJ (Figure 12; Wenzel, Lampe, Müller-Fielitz et al., 2021). In former times, occludin degradation in *Nemo*^{beKO} mice was associated with reduced endothelial expression of the deubiquitinase A20, preventing proteasomal degradation of occludin (Ridder et al., 2015). A20 is a target of NF-κB-mediated gene expression, and thus, occludin TJ integrity might be regulated by the NF-κB pathway (Shembade & Harhaj, 2012). However, *Ripk3* deletion prevents interruptions in occludin TJ structure in *Nemo*^{beKO} mice, arguing against NF-κB-mediated occludin degradation. In accordance, other studies reported that NF-κB inhibition leads to reduced MMP-9 expression, an enzyme able to degrade occludin (Bond et al., 2001; Brilha et al., 2017; Guarneri et al., 2017). Hence, increased levels of occludin would be expected in the *Nemo*^{beKO} mice. Accordingly, brain endothelial *A20* deletion in mice did not reduce occludin expression or led to interrupted TJ structure (unpublished data by Lisa Hill).

In conclusion, we speculated if occludin TJ interruptions in *Nemo*^{beKO} mice appear independent of attenuated NF-κB gene expression. Occludin delocalisation or degradation in *Nemo*^{beKO} mice can have various reasons, such as MMP-induced degradation initiated by NF-κB-independent processes or cytokine-induced processes (Yuan et al., 2020). For example, many studies describe hypoxia-reperfusion-induced destabilisation of occludin TJ (Lochhead et al., 2010; McCaffrey et al., 2009; Witt et al., 2003). Thus, McCaffrey and colleagues found occludin morphology changes at the BBB when hypoxia was induced, which has a similar structure to the occludin disintegrations we found in *Nemo*^{beKO} mice. They investigated the molecular structure of occludin and suggested conformational changes in occludin oligomers induced by changes in oxygen availability and subsequent reperfusion. In addition, signals for occludin degradation could also arise from other cells of the NVU. For example, astrocytes and pericytes can induce glutathione (GSH)-,IL-1β-, and VEGF-mediated degradation or delocalisation of occludin due to hypoxic stimuli, inflammation or melatonin loss (Bauer et al., 2010; Huang et al., 2020; J. Liu et al., 2012; Qin et al., 2019; Y. Yang et al., 2007). In most of the reports, degradation is mediated by elevated MMP expression either in astrocytes or endothelial cells.

Interestingly, increased astrocytic activation was observed in the *Nemo*^{beKO} mice and was normal in *Nemo*^{beKO}mice with additional RIPK3 ablation (Figure 27; Wenzel, Lampe, Müller-Fielitz et al., 2021). In addition, hypoxic areas were observed in *Nemo*^{beKO} mice (Y. Jiang et al., 2020). Future experiments should aim to investigate if close proximity of occludin interruptions to hypoxic areas indicate hypoxia-induced occludin degradation in our mouse model of IP. In addition, it would be worth checking if *Ripk3* deficiency prevents hypoxia and thus, might attenuate occludin degradation this way.

5.2.2. Endothelial transcytosis changes in *Nemo*^{beKO} mice

In contrast to *Nemo*^{beKO} mice, BBB leakage in *Nemo*^{beKO}*Ripk3*$^{-/-}$ mice could not be explained by vascular and TJ defects. A conceivable explanation for increased BBB permeability could be found in altered transcellular transport. It is assumed that the physiological transcytosis rate in the brain endothelium is low to restrict the transport of plasma proteins that could potentially harm the neuronal tissue. Nowadays, it is known that endothelial cells at the BBB have a complex endosomal system regulating transcytosis by sorting tubules to various cellular destinations and that these structures can be dysregulated in different neurological disorders (Villaseñor et al., 2019). Therefore, we tested if transcytosis changes might be the reason for the elevated BBB permeability in *Nemo*^{beKO} mice with RIPK3 deficiency.

First, we investigated the number of cytosolic vesicles in *Nemo*^{beKO} capillaries compared to *Nemo*^{fl} capillaries by electron microscopy of cortical brain sections. However, our analysis did not detect any significant differences between the genotypes for the cytosolic vesicle number

(Figure 13). Nonetheless, we decided to quantify transcytosis more specifically by fluorescent stainings and high-resolution light microscopy. This decision was based on two considerations: First, Stewart and colleagues compared vesicular densities measured by electron microscopy with protein permeability data in vascular beds of different tissues from quantitative, morphometric studies (Stewart, 2000). Surprisingly, they observed only a weak correlation and assumed that vesicle quantification by electron microscopy could not be used as the only predictor of tissue permeability. Second, our electron microscopy images presented only a small fraction of vessels per genotype and did not distinguish between different endosomal structures or vesicle cargos. Guided by the protocol of Villasenor et al., we established IgG vesicle staining in our laboratory (Figure 14).

By staining with anti-mouse antibodies, we detected numerous IgG puncta in wild-type brains. We demonstrated the specificity of the IgG staining by using different anti-mouse antibodies, which all showed the same pattern of IgG puncta. In addition, no signal was observed when using an anti-rabbit antibody. Quantification of this punta by confocal microscopy observed a significant reduction in IgG vesicle number in *Nemo*^{beKO} mice (Figure 15; Wenzel, Lampe, Müller-Fielitz et al., 2021). STED imaging of a small number of samples confirmed the finding of numerous IgG puncta in the capillaries of the control mice, but significantly fewer IgG-filled vesicles were detected in *Nemo*^{beKO} mice (Figure 16; Wenzel, Lampe, Müller-Fielitz et al., 2021). Moreover, the same effect was observed in *Nemo*^{beKO}*Ripk3*$^{-/-}$ mice. We, therefore, concluded that *Ikbkg* inactivation influences IgG transcytosis in BECs independent of RIPK3-mediated endothelial cell death and thus, BBB permeability is increased even if RIPK3 is deleted.

To date, not much is known about IgG transport across the BBB. Like in many other organs, IgG crosses the BBB by transcytosis, but the uptake mechanisms are still under debate. Zlocovic et al. proposed in 1990 a specific transfer mechanism for IgG at the BBB, which is saturated at physiological IgG plasma levels (Zlokovic et al., 1990). Later, studies on intravenously injected fluorescently labelled IgG and IgG fragment crystallizable (Fc) fragments confirmed this assumption and IgG recycling were proposed as the responsible mechanism for saturation (St-Amour et al., 2013; Tuma & Hubbard, 2003; Zhang & Pardridge, 2001). More recently, it has been shown that BECs express the neonatal Fc receptor (FcR_n), but binding of IgG to this receptor at the luminal membrane is rather unlikely (Schlachetzki et al., 2002; Tuma & Hubbard, 2003; Villasenõr et al., 2016). According to recent studies, IgG is uptaken by fluid-phase endocytosis (Mantle & Lee, 2019; Ruano-Salguero & Lee, 2020). Once internalized, IgG is binding to its membrane receptor FcR_n if the endosomal compartment's pH decreases below 6.5 (Challa et al., 2014; Schlachetzki et al., 2002). IgG bound to FcR_n is probably destined for recycling to the luminal membrane by Rab11 positive endosomes, while unbound IgG is sorted for lysosomal degradation (Ruano-Salguero & Lee, 2020; Villasenõr et al., 2016). It is assumed that the different binding behaviour of IgG relies on different binding affinity among the IgG molecules or competition between IgG molecules with a limited pool of FcR_n (Bruhns et al., 2009; Ober et al., 2004). Both mechanisms prevent abluminal transport of IgG and, therefore, reduce the extravasation of IgG to the brain parenchyma, as shown in Figure 30.

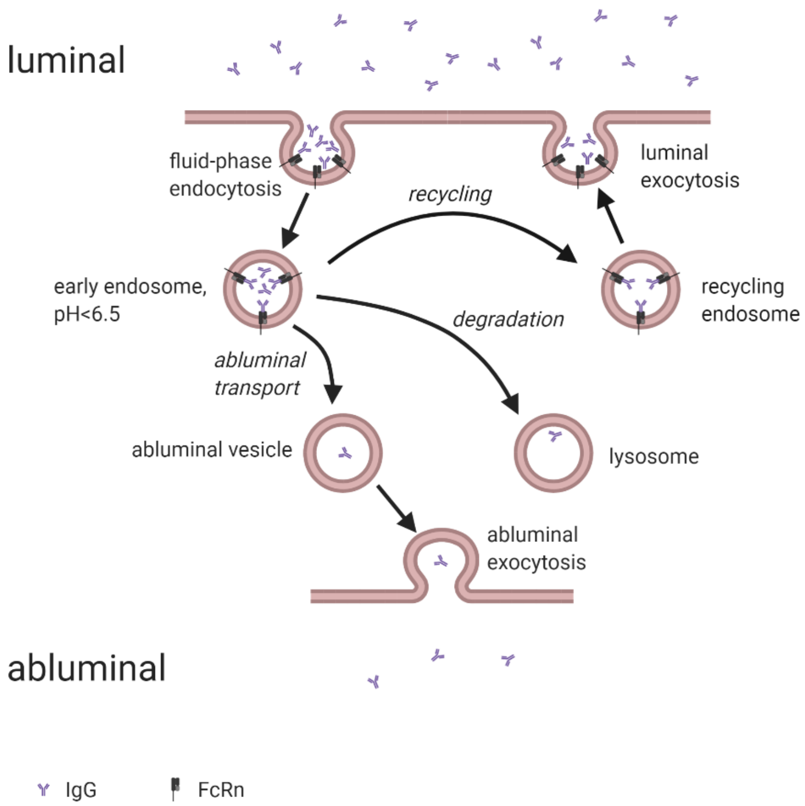

Figure 30: IgG transcytosis at the BBB. *The figure suggests possible mechanisms by which IgG transport to the brain parenchyma is hindered. These mechanisms include fluid-phase endocytosis of IgG, binding to the FcR_n in the early endosome and subsequent IgG recycling if IgG is bound to its receptor or lysosomal degradation of non-receptor bound IgG. Thus, only a few IgG molecules are exocytosed at the abluminal membrane. The figure was created with Biorender.com.*

Several studies indicate that an increased number of vesicles corresponds to increased transcytosis and, mostly, is accompanied by increased extravasation (Mathiesen Janiurek et al., 2019; Stewart, 2000). Our study observed increased IgG extravasation and a reduced number of IgG-filled vesicles in *Nemo*^{beKO} mice. This apparently paradoxical association persisted in the absence of cell death and TJ interruptions in *Nemo*^{beKO}*Ripk3*$^{-/-}$ mice. Therefore, we suggest that in our case, a lower number of IgG vesicles corresponds with an increased transcytosis of IgG to the brain parenchyma. This hypothesis is consistent with a previous report of Villasenor and colleagues (Villasenõr et al., 2016). They found a decreased number of IgG-filled vesicles accompanied by increased IgG extravasation in the brain capillaries of *Pdgf*$^{ret/ret}$ mice, a mouse model in which the deletion of the PDGF-B retention motif leads to the detachment of pericytes from the vessel walls (Lindblom et al., 2003). In addition, they administered a humanized IgG (Mab86) and found it colocalised with IgG vesicles in wildtype mice but observed no vesicles in *Pdgf*$^{ret/ret}$ mice, although extravasation of Mab86 was increased. Since EM analysis of endothelial vesicles in *Pdgf*$^{ret/ret}$ mice revealed no difference in vesicle uptake but increased cytosolic and abluminal vesicles, they assumed changes in mechanisms downstream of the uptake leading to increased transport to the brain parenchyma. In accordance, they found less IgG localised in lysosomes in the *Pdgf*$^{ret/ret}$ mice, indicating disturbed IgG clearance in BECs. For our *Nemo*^{beKO} mice, we observed no change in the number of LAMP2$^+$ lysosomes but a reduced number of vesicles positive for TfR, a recycling endosome marker (Figure 17; Hua et al., 1998; Ober et al., 2004). This finding might indicate decreased IgG recycling in BECs lacking NEMO and thus, suggest that NF-κB signalling contributes to IgG clearance by regulating transcytotic recycling processes. Consequently, reduced recycling might lead to a change in intracellular IgG sorting mechanisms towards the increased abluminal release of IgG (Figure 31). However, future investigations should intend detailed colocalisation studies of IgG and TfR, other recycling compartment markers, and different endosomal compartment markers in general to get more insight into possible connections of endothelial IgG sorting and the NF-κB pathway.

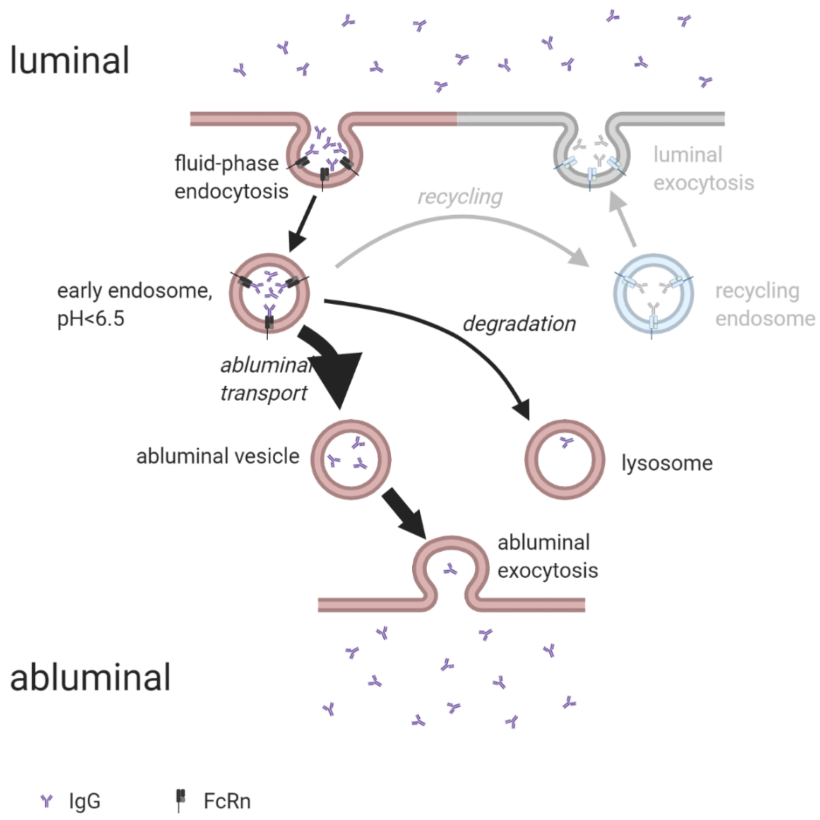

Figure 31: **Ikbkg** ***inactivation might lead to changes in IgG sorting mechanisms.*** *According to our concept, IgG recycling in BECs of* Nemo^{beKO} *mice might be reduced. Consequently, more IgG-filled vesicles are sorted for abluminal release, increasing IgG extravasation. The figure was created with Biorender.com.*

To this point, it is not clear how extravasated IgG is processed in the brain parenchyma. Investigations in the cortex of *Nemo*^{beKO} mice revealed IgG accumulations that colocalised with Iba1^{+} microglia (Figure 18). Expansion microscopy showed IgG accumulations as puncta that were mainly localised in microglial processes. A similar pattern was observed by a study investigating peripherally administered IgG antibodies against amyloid-β (Bard et al., 2000). Here, the therapeutic antibodies colocalised with amyloid-β plaques and microglia. According to the authors, microglial cells clear plaques by initiating FcR_n-mediated phagocytosis and degradation of IgG-coated amyloid-β. Future stainings of IgG, microglia, the FcR_n receptor, and lysosome markers could reveal if such a mechanism is activated to clear the brain parenchyma from IgG in *Nemo*^{beKO} mice. Notably, microglia occurrence and microglial activity are significantly higher in *Nemo*^{beKO} mice, suggesting increased clearing activity of microglial cells (Wenzel, Lampe, Müller-Fielitz et al., 2021).

We next approached if forced NF-κB activation by constitutive activation of *Ikk2* can reverse transcytotic changes caused by the absence of NF-κB signalling. For this reason, we used *Tak1*^{beKO} mice and crossed them with *IKK2*^{ca} mice, in which constitutive activation of IKK2 is induced by removing a *loxP*-flanked STOP cassette upon Cre recombinase activity (Sasaki et al., 2006). Similar to endothelial NEMO deficiency, endothelial loss of TAK1 caused increased IgG extravasation and a decreased number of capillary IgG-filled vesicles (Figure 20). This observation fits a study from Ridder et al., in which *Nemo*^{beKO} and *Tak1*^{beKO} mice showed the same phenotype regarding brain vasculature defects and BBB impairment (Ridder et al., 2015). In the same study, constitutive *Ikk2* activation prevented increased brain weight, elevated mortality and led to a partial decrease in IgG extravasation but could not prevent vascular defects in *Tak1*^{beKO} mice. Surprisingly, additional *Ikk2* activation in *Tak1*^{beKO} mice in our study could not improve the observed increase in IgG extravasation (Figure 20).

Moreover, *Tak1*^{beKO}*IKK2*^{ca} mice showed a similar reduction in the IgG vesicle number as observed in *Tak1*^{beKO} mice. A reason for this unexpected result might be an overactivation of NF-κB. As already shown in Figure 3, the relationship between BBB integrity and NF-κB activity might be explained by a bell-shaped curve. On the one hand, low NF-κB activity, such as in the absence of NEMO, results in BBB impairment probably due to disturbed transcytosis regulation. On the other hand, strongly increased NF-κB activity, which might be the case if *Ikk2* is constitutively active, could lead to BBB leakage due to increased expression of inflammation-associated genes. Accordingly, it was shown that *IKK2*^{ca} in *Tak1*^{beKO} cells leads to a significantly higher expression of NF-κB target genes than in control cells presenting basal NF-κB activity (Ridder et al., 2015). However, to evaluate this theory, NF-κB activity should be quantified in the different knockout models with or without the constitutively active mutant of *Ikk2*.

5.2.3. The contribution of RIPK3 on endothelial transcytosis

Following the findings for IgG transcytosis, we planned vesicle quantifications for other plasma proteins. Fibrinogen is a 340-kDa glycoprotein involved in blood coagulation, which shows increased extravasation to the brain parenchyma in *Nemo*^{beKO} mice (Figure 11). Studies about the physiological occurrence of fibrinogen in the brain parenchyma are contradictory. Some studies claim that fibrinogen is not detectable in the healthy brain, while others showed fibrinogen chains in the paravascular space produced by astrocytes and neurons (Golanov et al., 2019; Petersen et al., 2018). However, in our experiments, we could find a basal level of fibrinogen staining in the brain parenchyma of all genotypes and puncta-like structures in brain vessels. We observed a decreased number of fibrinogen-filled vesicles in the brain capillaries of *Nemo*^{beKO} mice. Although IgG transcytosis alterations in *Nemo*^{beKO} mice persisted even in the absence of RIPK3, the number of fibrinogen vesicles was normalized when RIPK3 was ablated (Figure 19). A possible explanation for this discrepancy might be different intracellular sorting mechanisms for IgG and fibrinogen. Indeed, co-staining of IgG and fibrinogen revealed only rare colocalisation events of endothelial IgG- and fibrinogen-filled vesicles. As described above, IgG is probably internalized by a fluid-phase mechanism, and its transport to the brain parenchyma might be limited primarily by recycling mechanisms and lysosomal degradation. To date, nothing is known about fibrinogen transcytosis and its intracellular sorting mechanisms in the brain endothelium. However, fibrinogen transcytosis has been investigated in megakaryocytes. Here, fibrinogen is endocytosed clathrin-dependent and receptor-mediated by integrin alpha II b beta 3 as the primary receptor (Handagama et al., 1993; Hung et al., 2012). In another study using A549 lung epithelial type II-like cells, fibrinogen is endocytosed dependent on the integrin alpha v beta 3 and, subsequently, is degraded by lysosomes (Odrljin et al., 2001). Interestingly, the authors assume non-clathrin mediated endocytosis and could not find colocalisation of fibrinogen and transferrin vesicles. Probably, endocytosis mode and subsequent processing might depend on the tissue. Therefore, general assumptions about intracellular fibrinogen trafficking might not be valid for the brain endothelium. Co-stainings of fibrinogen and markers for different intracellular sorting vesicles, such as clathrin-, caveolin-, LAMP2- or TfR-antibodies, might help to gain insight into transcellular fibrinogen transport in the brain. Since RIPK3 deficiency prevents fibrinogen transcytosis and extravasation changes, it might be possible that NF-κB independent effects regulate fibrinogen transport while IgG transcytosis is mediated by NF-κB dependent gene expression.

5.2.4. Outlook: Transcytosis changes as an early marker for brain pathologies?

By performing a time-course experiment, we observed that an increase in IgG extravasation and a reduction of IgG-filled vesicles are the first symptoms of BBB impairment in NEMO deficient mice (Figure 26). Interestingly, the number of IgG-filled vesicles was already markedly reduced before mice were treated with tamoxifen. We assume that the Cre recombinase has a low basal activity before tamoxifen is injected. RIPK3 deficiency is sufficient to prevent the effects of basal Cre recombinase activity on the BBB for at least 14 days after the start of tamoxifen treatment. Vascular defects, such as string vessel formation, were observed after the increase in BBB leakage for IgG, indicating that changes in IgG transcytosis are the first event upon *Ikbkg* inactivation that leads to BBB impairment (Figure 25, Figure 28). Therefore, we conclude that changes in transcytosis are an early marker for a beginning disruption of the BBB.

Some evidence for transcytosis changes as an early biomarker for BBB leakage has recently been achieved. For instance, brain vascular leakage for albumin and IgG early after stroke occurred without alterations of the tight-junction structures, but transendothelial trafficking was already changed (Haley & Lawrence, 2017; Krueger et al., 2013). Further, Knowland and colleagues found that BBB integrity is disturbed stepwise in stroke, with increased endothelial caveolae numbers and changed transcytosis rates occurring first (Knowland et al., 2014). In addition, further investigations showed a clear correlation between the change in vesicle number and spatial and temporal leakage of the microvasculature, pointing out the importance of endothelial transcytosis as an indicator of BBB breakdown (Haley & Lawrence, 2017). Besides pathological conditions, it is known that BBB leakage and elevation of brain endothelial transcytosis correlates with age. A recent study reported increased plasma uptake in the ageing brain correlating with a shift from clathrin-mediated transcytosis to non-specific caveolae-mediated transcytosis (Yang et al., 2020). Interestingly, Yang et al. also observed decreased endothelial TfR expression and reduced pericyte coverage of the brain vasculature in the aged mice. According to their theory, TfR expression is mediated by pericytes and thus, reduced by the loss of pericytes. Our study detected reduced pericyte coverage and fewer TfR^+ vesicles in capillaries of *Nemo*^{beKO} mice. Hence, a decreased pericyte occurence might be another reason for decreased IgG recycling and increased transcellular trafficking to the brain parenchyma in *Nemo*^{beKO} mice.

However, changes in brain endothelial transcytosis are likely to reflect the first intracellular imbalances due to brain pathologies or ageing. Unfortunately, assessment of brain endothelial transcytosis in living subjects is complicated since vesicle quantification needs high-resolution microscopy techniques. Janiurek et al. recently investigated the vesicular density of intravenously injected BSA-Alexa488 in living anaesthetized mice through an acute craniotomy by two-photon fluorescence imaging (Mathiesen Janiurek et al., 2019). Such *in-vivo* techniques would offer information about the speed, directionality and pathways of transcytosis and, hence, would be able to track endothelial IgG recycling. Moreover, a detailed understanding of transcellular trafficking and associated signalling pathways in the brain endothelium would allow interfering with the cellular machinery to overcome inefficient drug delivery through the BBB. Thus, our study pointed out the importance of NF-κB signalling for brain endothelial transcytosis.

Nevertheless, many questions need to be addressed in the future to confirm our findings and gain detailed insight into the pathogenesis evoked by NEMO deficiency. First of all, IgG transcytosis should be investigated more in detail since IgG leakage is assumed to contribute to neuronal dysfunctions leading to epilepsy (Michalak et al., 2012). IgG colocalised with neurons could be found in epileptic patients but not in control patients and is associated with degenerative neuronal changes, such as neuronal shrinkage. For this reason, it would be of great interest to investigate if IgG extravasation in $Nemo^{beKO}Ripk3^{-/-}$ mice is sufficient to cause epileptic seizures. To limit excessive IgG leakage, knowledge about the pathways mediating IgG transcytosis is needed. Which mechanisms regulate recycling or degradation of uptaken IgG, and how do they depend on NEMO and NF-κB signalling? Furthermore, transcellular transport of other plasma proteins than IgG and fibrinogen should be quantified, if possible, in acute craniotomy experiments in living $Nemo^{beKO}$ animals.

However, another promising finding of this study is that RIPK3 deficiency prevents vascular defects – at least 28 days after the first dose of tamoxifen. Until that point, animals showed no increase in string vessel formation, normal astrocytic reactivity and only partially increased BBB leakage for IgG. Further studies could check if $Nemo^{beKO}$ animals with $Ripk1^{D138N/D138N}$ mutation prevents vascular defects permanently. If so, do animals still show increased IgG extravasation and alterations in IgG transcytosis? If the deletion of RIPK1 kinase activity is not preventing changes in transcellular transport in the brain endothelium, it would be of great interest to investigate if these animals still suffer from neurological symptoms, such as seizures. In case the ablation of RIPK1 kinase activity successfully prevents the neurological symptoms of the $Nemo^{beKO}$ phenotype, specific inhibitors for RIPK1 kinase function could be tested in mouse experiments. GSK′547 is such an inhibitor and has been successfully used to prevent increased string vessel formation in a mouse model mimicking the brain pathology of SARS-CoV-2. This inhibitor would also hold great therapeutical potential for treating IP since no specific treatment exists to date.

6. Supplement

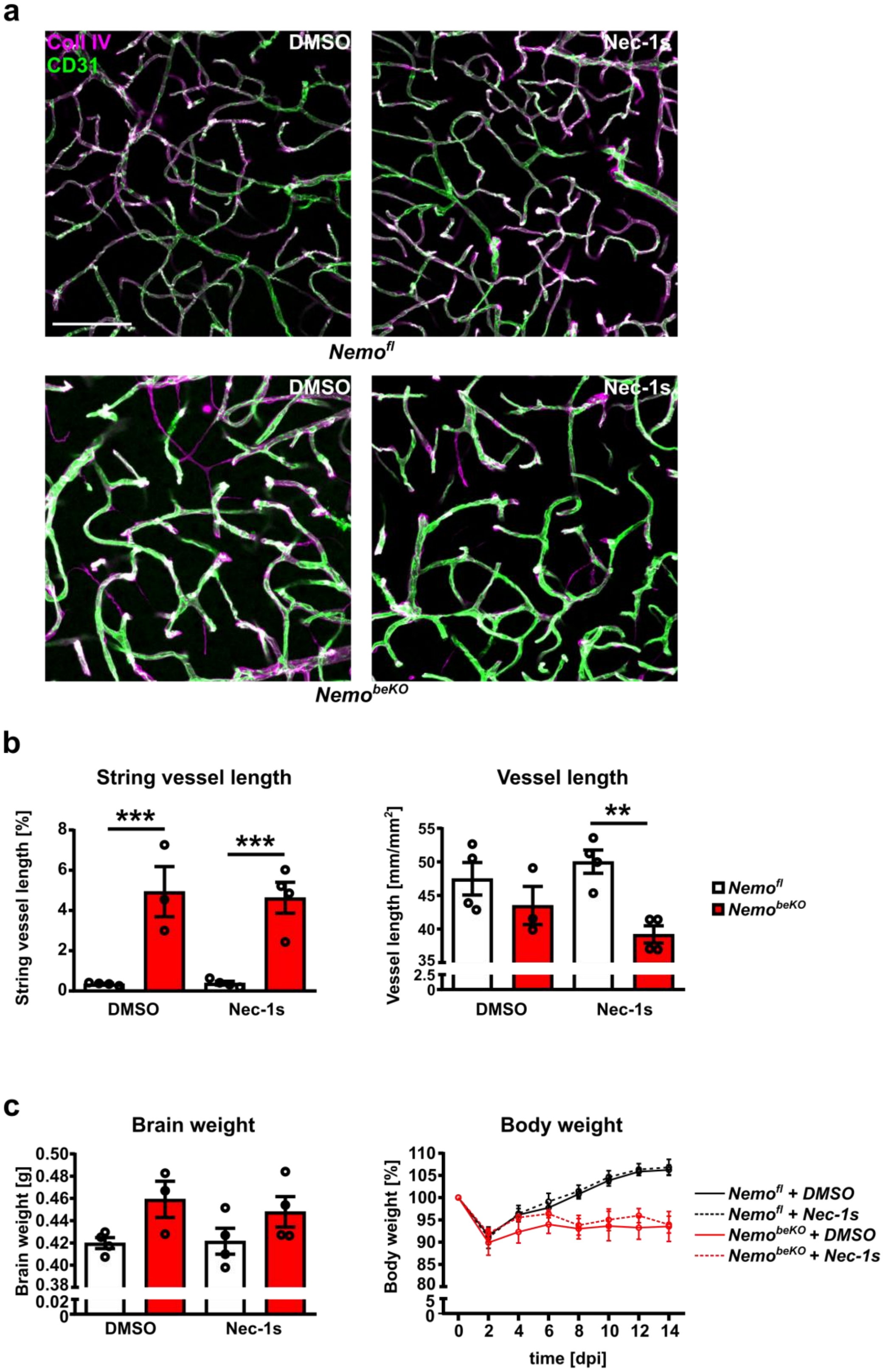

Figure 32: Pharmacological inhibition of RIPK1 by Necrostatin-1s did not improve the phenotype of **Nemo^{beKO}** ***mice.*** *A) Staining of the vasculature showed increased formation of string vessels in vehicle-treated (DMSO) and Necrostatin-1s treated* Nemo^{beKO} *mice. Scale bar, 100 µm. B)* Nemo^{beKO} *mice had a significantly higher number of string vessels and a significantly decreased vessel length. Treatment with Necrostatin-1s did not improve the vascular phenotype of* Nemo^{beKO} *mice. Two-way ANOVA followed by Sidaks posthoc test; (string vessel length:genotype: $F(1,11) = 47.8$, $p < 0.001$; treatment: $F(1,11) < 0.1$, $p = 0.839$; interaction: $F(1,11) = 0.1$, $p = 0.794$;*

vessel length: genotype: F(1,11) = 12.8, p = 0.004; treatment: F(1,11) = 0.2, p = 0.680; interaction: F(1,11) = 2.7, p = 0.126; N = 3-4 animals/group. C) Analysis of the brain weight did not show any significant differences between the groups, but a tendency for higher brain weights in the Nemo^{beKO} *mice unless the treatment. Two-way ANOVA followed by Sidaks posthoc test; genotype: F(1,11) = 7.6, p = 0.018; treatment: F(1,11) = 0.2, p = 0.697; interaction: F(1,11) = 0.3, p = 0.5964; N = 3-4 animals/group.* Nemo^{beKO} *mice lost significantly more weight than control mice independent of the treatment. Three-Way ANOVA followed by Tukey's post-hoc test (genotype: F (1,91) = 97.43, p < 0.001; time: F (7,91) = 14.4, p < 0.001; treatment: F (1,91) = 3.0, p = 0.08; interaction: significant for time x genotype, F(7,91) = 9.0, p < 0.001).* p < 0.05; ** p < 0.01.*

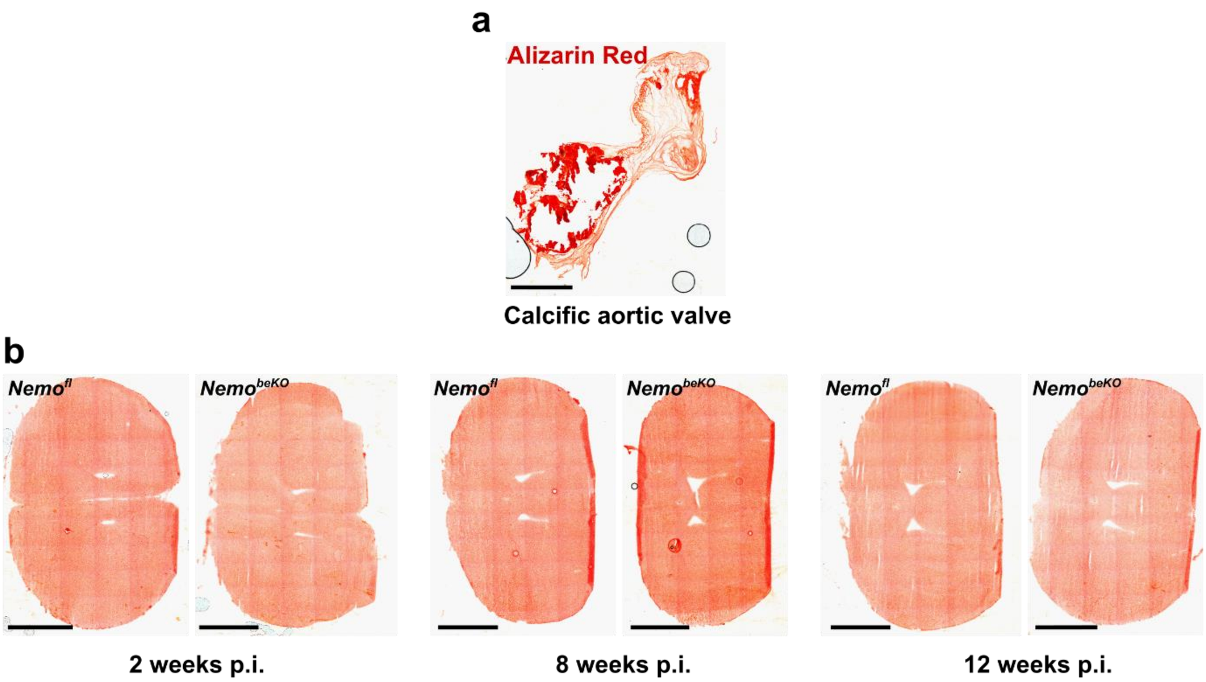

Figure 33: Nemo^{beKO} ***mice show no brain calcifications.*** *A) A calcific aortic valve served as a positive control for Alizarin-Red S staining of calcification. In the presence of calcium, Alizarin-Red S forms a complex, which is red. B)* Nemo^{beKO} *mice show no brain calcifications after two weeks, eight weeks or 12 weeks after tamoxifen injection. Scale bar, 2 mm.*

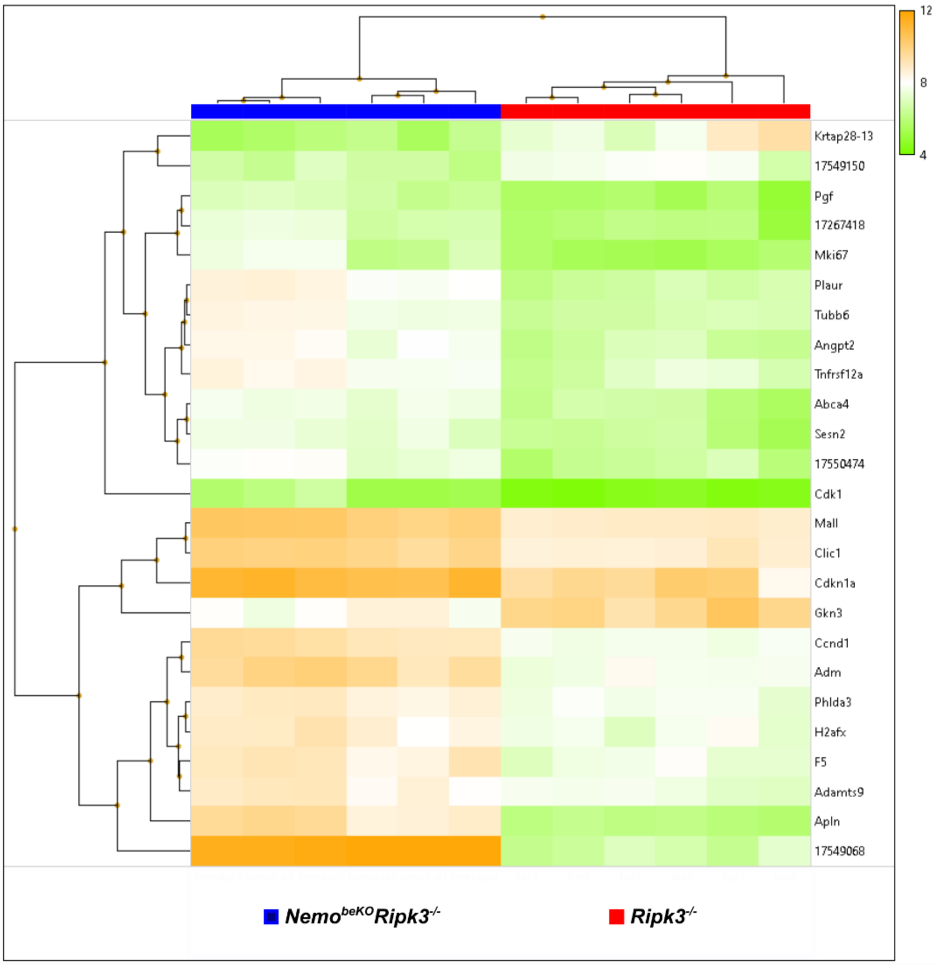

Figure 34: Heat-map analysis of significantly regulated genes in* Nemo^{beKO}Ripk3$^{-/-}$ *mice. *Shown are the log2-intensities for significant, two-fold regulated genes for each animal.*

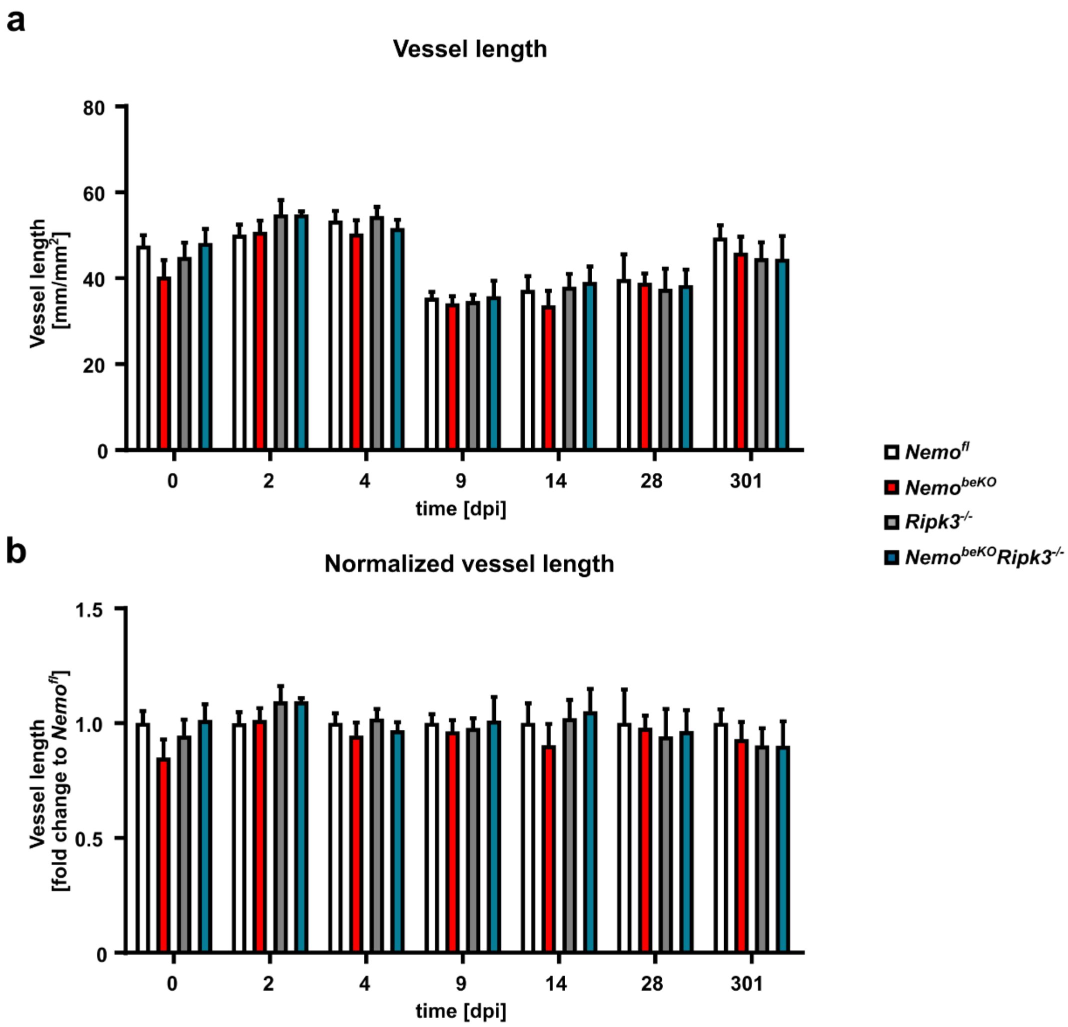

***Figure 35: No differences in vessel length were detected for mice with* NEMO *deficiency**. *A) Vessel length was measured by Coll IV staining. Two-way ANOVA followed by Tukey's post-hoc test, genotype: $F (3,106) = 0.9$, $p = 0.4684$; time: $F (6,106) = 16.6$, $p < 0.001$; interaction: $F (18, 106) = 0.3$, $p =0.997$. N = 3 – 7 animals/group and timepoint. B) Vessel length normalized to the vessel length of* Nemo^{fl} *group for each time point. Two-way ANOVA followed by Tukey's post-hoc test, genotype: $F (3,106) = 0.8$, $p = 0.510$; time: $F (6, 106) = 0.8$, $p = 0.601$; interaction: $F (18, 106) = 0.3$, $p =0.999$; N = 3 – 7 animals/group and timepoint*

7. References

Alarcon-Martinez, L., Villafranca-Baughman, D., Quintero, H., Kacerovsky, J. B., Dotigny, F., Murai, K. K., Prat, A., Drapeau, P., & Di Polo, A. (2020). Interpericyte tunnelling nanotubes regulate neurovascular coupling. *Nature*. https://doi.org/10.1038/s41586-020-2589-x

Alvarez-Vergara, M. I., Rosales-Nieves, A. E., March-Diaz, R., Rodriguez-Perinan, G., Lara-Ureña, N., Luis, C. O. S., Sanchez-Garcia, M. A., Martin-Bornez, M., Gómez-Gálvez, P., Vicente-Munuera, P., Fernandez-Gomez, B., Marchena, M. A., Bullones-Bolanos, A. S., Davila, J. C., Gonzalez-Martinez, R., Trillo-Contreras, J. L., Sanchez-Hidalgo, A. C., Toro, R. del, Scholl, F. G., … Pascual, A. (2021). Non-productive angiogenesis disassembles Aß plaque-associated blood vessels. *Nature Communications 2021 12:1*, *12*(1), 1–16. https://doi.org/10.1038/s41467-021-23337-z

Alvarez, J. I., Dodelet-Devillers, A., Kebir, H., Ifergan, I., Fabre, P. J., Terouz, S., Sabbagh, M., Wosik, K., Bourbonni??re, L., Bernard, M., Van Horssen, J., De Vries, H. E., Charron, F., & Prat, A. (2011). The hedgehog pathway promotes blood-brain barrier integrity and CNS immune quiescence. *Science*, *334*(6063), 1727–1731. https://doi.org/10.1126/science.1206936

Ando, Y., Okada, H., Takemura, G., Suzuki, K., Takada, C., Tomita, H., Zaikokuji, R., Hotta, Y., Miyazaki, N., Yano, H., Muraki, I., Kuroda, A., Fukuda, H., Kawasaki, Y., Okamoto, H., Kawaguchi, T., Watanabe, T., Doi, T., Yoshida, T., … Ogura, S. (2018). Brain-Specific Ultrastructure of Capillary Endothelial Glycocalyx and Its Possible Contribution for Blood Brain Barrier. *Scientific Reports*. https://doi.org/10.1038/s41598-018-35976-2

Andreone, B. J., Chow, B. W., Tata, A., Lacoste, B., Ben-Zvi, A., Bullock, K., Deik, A. A., Ginty, D. D., Clish, C. B., & Gu, C. (2017). Blood-Brain Barrier Permeability Is Regulated by Lipid Transport-Dependent Suppression of Caveolae-Mediated Transcytosis. *Neuron*, *94*(3), 581-594.e5. https://doi.org/10.1016/j.neuron.2017.03.043

Anerson, J. M., Stevenson, B. R., Jesaitis, L. A., Goodenough, D. A., & Mooseker, M. S. (1988). Characterization of ZO-1, a protein component of the tight junction from mouse liver and Madin-Darby canine kidney cells. *Journal of Cell Biology*, *106*(4), 1141–1149. https://doi.org/10.1083/jcb.106.4.1141

Annibaldi, A., Wicky John, S., Vanden Berghe, T., Swatek, K. N., Ruan, J., Liccardi, G., Bianchi, K., Elliott, P. R., Choi, S. M., Van Coillie, S., Bertin, J., Wu, H., Komander, D., Vandenabeele, P., Silke, J., & Meier, P. (2018). Ubiquitin-Mediated Regulation of RIPK1 Kinase Activity Independent of IKK and MK2. *Molecular Cell*, *69*(4), 566. https://doi.org/10.1016/J.MOLCEL.2018.01.027

Arthur, F. E., Shivers, R. R., & Bowman, P. D. (1987). Astrocyte-mediated induction of tight junctions in brain capillary endothelium: an efficient in vitro model. *Developmental Brain Research*, *36*(1), 155–159. https://doi.org/10.1016/0165-3806(87)90075-7

Attwell, D., Buchan, A. M., Charpak, S., Lauritzen, M., MacVicar, B. A., & Newman, E. A. (2010). Glial and neuronal control of brain blood flow. In *Nature* (Vol. 468, Issue 7321, pp. 232–243). https://doi.org/10.1038/nature09613

Barar, J., Rafi, M. A., Pourseif, M. M., & Omidi, Y. (2016). Blood-brain barrier transport machineries and targeted therapy of brain diseases. *BioImpacts*, *6*(4), 225–248. https://doi.org/10.15171/bi.2016.30

Bard, F., Cannon, C., Barbour, R., Burke, R. L., Games, D., Grajeda, H., Guido, T., Hu, K., Huang, J., Johnson-Wood, K., Khan, K., Kholodenko, D., Lee, M., Lieberburg, I., Motter, R., Nguyen, M., Soriano, F., Vasquez, N., Weiss, K., … Yednock, T. (2000). Peripherally administered antibodies against amyloid β-peptide enter the central nervous system and reduce pathology in a mouse model of Alzheimer disease. *Nature Medicine*, *6*(8), 916–919. https://doi.org/10.1038/78682

Bauer, A. T., Bürgers, H. F., Rabie, T., & Marti, H. H. (2010). Matrix metalloproteinase-9 mediates hypoxia-induced vascular leakage in the brain via tight junction rearrangement. *Journal of Cerebral Blood Flow and Metabolism*, *30*(4), 837–848. https://doi.org/10.1038/jcbfm.2009.248

Bazzoni, G., Martìnez-Estrada, O. M., Mueller, F., Nelboeck, P., Schmid, G., Bartfai, T., Dejana, E., & Brockhaus, M. (2000). Homophilic interaction of junctional adhesion molecule. *Journal of Biological Chemistry*, *275*(40), 30970–30976. https://doi.org/10.1074/jbc.M003946200

Behl, C., Davis, J. B., Lesley, R., & Schubert, D. (1994). Hydrogen peroxide mediates amyloid β protein toxicity. *Cell*, *77*(6), 817–827. https://doi.org/10.1016/0092-8674(94)90131-7

Bell, R. D., Winkler, E. A., Singh, I., Sagare, A. P., Deane, R., Wu, Z., Holtzman, D. M., Betsholtz, C., Armulik, A., Sallstrom, J., Berk, B. C., & Zlokovic, B. V. (2012). Apolipoprotein e controls cerebrovascular integrity via cyclophilin A. *Nature*, *485*(7399), 512–516. https://doi.org/10.1038/nature11087

Bellmann, C., Schreivogel, S., Günther, R., Dabrowski, S., Schümann, M., Wolburg, H., & Blasig, I. E. (2014).

Highly conserved cysteines are involved in the oligomerization of occludin-Redox dependency of the second extracellular loop. *Antioxidants and Redox Signaling*, *20*(6), 855–867. https://doi.org/10.1089/ars.2013.5288

Ben-Zvi, A., Lacoste, B., Kur, E., Andreone, B. J., Mayshar, Y., Yan, H., & Gu, C. (2014). Mfsd2a is critical for the formation and function of the blood-brain barrier. *Nature*, *509*(7501), 507–511. https://doi.org/10.1038/nature13324

Bennett, R. E., Robbins, A. B., Hu, M., Cao, X., Betensky, R. A., Clark, T., Das, S., & Hyman, B. T. (2018). Tau induces blood vessel abnormalities and angiogenesis-related gene expression in P301L transgenic mice and human Alzheimer's disease. *Proceedings of the National Academy of Sciences of the United States of America*. https://doi.org/10.1073/pnas.1710329115

Berger, S. B., Kasparcova, V., Hoffman, S., Swift, B., Dare, L., Schaeffer, M., Capriotti, C., Cook, M., Finger, J., Hughes-Earle, A., Harris, P. A., Kaiser, W. J., Mocarski, E. S., Bertin, J., & Gough, P. J. (2014). RIP1 kinase activity is dispensable for normal development but is a key regulator of inflammation in SHARPIN-deficient mice. *Journal of Immunology (Baltimore, Md. : 1950)*, *192*(12), 5476. https://doi.org/10.4049/JIMMUNOL.1400499

Berghe, T. Vanden, Vanlangenakker, N., Parthoens, E., Deckers, W., Devos, M., Festjens, N., Guerin, C. J., Brunk, U. T., Declercq, W., & Vandenabeele, P. (2009). Necroptosis, necrosis and secondary necrosis converge on similar cellular disintegration features. *Cell Death & Differentiation 2010 17:6*, *17*(6), 922–930. https://doi.org/10.1038/cdd.2009.184

Bertheloot, D., Latz, E., & Franklin, B. S. (2021). Necroptosis, pyroptosis and apoptosis: an intricate game of cell death. *Cellular & Molecular Immunology 2021 18:5*, *18*(5), 1106–1121. https://doi.org/10.1038/s41423-020-00630-3

Bond, M., Chase, A. J., Baker, A. H., & Newby, A. C. (2001). Inhibition of transcription factor NF-kB reduces matrix metalloproteinase-1,-3 and-9 production by vascular smooth muscle cells. *Cardiovascular Research*, *50*, 556–565. www.elsevier.com/locate/cardioreswww.elsevier.nl/locate/cardiores

Brilha, S., Ong, C. W. M., Weksler, B., Romero, N., Couraud, P.-O., & Friedland, J. S. (2017). *Matrix metalloproteinase-9 activity and a downregulated Hedgehog pathway impair blood-brain barrier function in an in vitro model of CNS tuberculosis*. https://doi.org/10.1038/s41598-017-16250-3

Brodsky, F. M. (2016). Clathrin and Clathrin-Dependent Endocytosis. *Encyclopedia of Cell Biology*, *2*, 384–393. https://doi.org/10.1016/B978-0-12-394447-4.20038-2

Brown, W. R. (2010). A review of string vessels or collapsed, empty basement membrane tubes. In *Journal of Alzheimer's Disease*. https://doi.org/10.3233/JAD-2010-100219

Bruckner, B. A., Ammini, C. V, Otal, M. P., Raizada, M. K., & Stacpoole, P. W. (1999). Regulation of brain glucose transporters by glucose and oxygen deprivation. *Metabolism: Clinical and Experimental*, *48*(4), 422–431. https://doi.org/http://dx.doi.org/10.1016/S0026-0495(99)90098-7

Bruhns, P., Iannascoli, B., England, P., Mancardi, D. A., Fernandez, N., Jorieux, S., & Daëron, M. (2009). Specificity and affinity of human Fcγ receptors and their polymorphic variants for human IgG subclasses. *Blood*, *113*(16), 3716–3725. https://doi.org/10.1182/BLOOD-2008-09-179754

Butt, A. M., Jones, H. C., & Abbott, N. J. (1990). Electrical resistance across the blood-brain barrier in anaesthetized rats: a developmental study. *The Journal of Physiology*, *429*(1), 47–62. https://doi.org/10.1113/jphysiol.1990.sp018243

Campos-Luna, I., Miller, A., Beard, A., & Leach, M. (2019). Validation of mouse welfare indicators: a Delphi consultation survey. *Scientific Reports 2019 9:1*, *9*(1), 1–11. https://doi.org/10.1038/s41598-019-45810-y

Candé, C., Vahsen, N., Garrido, C., & Kroemer, G. (2004). Apoptosis-inducing factor (AIF): Caspase-independent after all. In *Cell Death and Differentiation* (Vol. 11, Issue 6, pp. 591–595). Nature Publishing Group. https://doi.org/10.1038/sj.cdd.4401400

Carter, B. D., Kaltschmidt, C., Kaltschmidt, B., Offenhäuser, N., Böhm-Matthaei, R., Baeuerle, P. A., & Barde, Y. A. (1996). Selective activation of NF-kappa B by nerve growth factor through the neurotrophin receptor p75. *Science (New York, N.Y.)*, *272*(5261), 542–545. https://doi.org/10.1126/SCIENCE.272.5261.542

Caruso, R. A., Bonanno, A., Finocchiaro, G., Cavaliere, R., Gitto, G., Plutino, F. M., Quattrocchi, E., Cuppari, M. C., Fabiano, V., & Basile, G. (2009). Ultrastructural observations on inflammatory angiogenesis in gastric carcinomas with massive neutrophil infiltration. *Ultrastructural Pathology*, *33*(1), 1–5. https://doi.org/10.1080/01913120802636696

Castro Dias, M., Coisne, C., Baden, P., Enzmann, G., Garrett, L., Becker, L., Hölter, S. M., Aguilar-Pimentel, A., Adler, T., Busch, D. H., Spielmann, N., Moreth, K., Hans, W., Amarie, O., Graw, J., Rozman, J., Radc, I., Neff, F., Calzada-Wack, J., … Engelhardt, B. (2019). Claudin-12 is not required for blood-brain barrier tight junction function. *Fluids and Barriers of the CNS*, *16*(1). https://doi.org/10.1186/S12987-019-0150-9

Castro Dias, M., Coisne, C., Lazarevic, I., Baden, P., Hata, M., Iwamoto, N., Francisco, D. M. F., Vanlandewijck, M., He, L., Baier, F. A., Stroka, D., Bruggmann, R., Lyck, R., Enzmann, G., Deutsch, U., Betsholtz, C., Furuse, M., Tsukita, S., & Engelhardt, B. (2019). Claudin-3-deficient C57BL/6J mice display intact brain barriers. *Scientific Reports*, *9*(1). https://doi.org/10.1038/S41598-018-36731-3

Challa, D. K., Velmurugan, R., Ober, R. J., & Ward, E. S. (2014). FcRn: From molecular interactions to regulation of IgG pharmacokinetics and functions. In *Current Topics in Microbiology and Immunology* (Vol. 382, pp. 249–272). Curr Top Microbiol Immunol. https://doi.org/10.1007/978-3-319-07911-0_12

Challa, V. R., Thore, C. R., Moody, D. M., Anstrom, J. A., & Brown, W. R. (2004). Increase of white matter string vessels in Alzheimer's disease. *Journal of Alzheimer's Disease*, *6*(4), 379–383. https://doi.org/10.3233/JAD-2004-6404

Chau, B. N., Chen, T.-T., Wan, Y. Y., DeGregori, J., & Wang, J. Y. J. (2004). Tumor Necrosis Factor Alpha-Induced Apoptosis Requires p73 and c-ABL Activation Downstream of RB Degradation. *Molecular and Cellular Biology*, *24*(10), 4438–4447. https://doi.org/10.1128/mcb.24.10.4438-4447.2004

Chen, A. Q., Fang, Z., Chen, X. L., Yang, S., Zhou, Y. F., Mao, L., Xia, Y. P., Jin, H. J., Li, Y. N., You, M. F., Wang, X. X., Lei, H., He, Q. W., & Hu, B. (2019). Microglia-derived TNF-α mediates endothelial necroptosis aggravating blood brain–barrier disruption after ischemic stroke. *Cell Death and Disease*, *10*(7), 1–18. https://doi.org/10.1038/s41419-019-1716-9

Chen, D., Yu, J., & Zhang, L. (2016). Necroptosis: An alternative cell death program defending against cancer. In *Biochimica et Biophysica Acta - Reviews on Cancer* (Vol. 1865, Issue 2, pp. 228–236). Elsevier B.V. https://doi.org/10.1016/j.bbcan.2016.03.003

Chen, Q., Jiang, L., Li, C., Hu, D., Bu, J., Cai, D., & Du, J. (2012). Haemodynamics-Driven Developmental Pruning of Brain Vasculature in Zebrafish. *PLoS Biology*, *10*(8), e1001374. https://doi.org/10.1371/journal.pbio.1001374

Chen, Y. C., Wei, X. E., Lu, J., Qiao, R. H., Shen, X. F., & Li, Y. H. (2019). Correlation between intracranial arterial calcification and imaging of cerebral small vessel disease. *Frontiers in Neurology*, *10*(MAY). https://doi.org/10.3389/fneur.2019.00426

Chen, Y. S., Chen, K. H., Liu, C. C., Lee, C. Te, Yang, C. H., Chuang, K. C., & Lin, C. R. (2007). Propofol-induced vascular permeability change is related to the nitric oxide signaling pathway and occludin phosphorylation. *Journal of Biomedical Science*, *14*(5), 629–636. https://doi.org/10.1007/s11373-007-9164-4

Chishty, M., Begley, D. J., Abbott, N. J., & Reichel, A. (2003). Functional characterisation of nucleoside transport in rat brain endothelial cells. *Neuroreport*, *14*(7), 1087–1090. https://doi.org/10.1097/01.wnr.0000072843.93264.ff

Choi, K. H., Kim, H. S., Park, M. S., Kim, J. T., Kim, J. H., Cho, K. A., Lee, M. C., Lee, H. J., & Cho, K. H. (2016). Regulation of Caveolin-1 Expression Determines Early Brain Edema After Experimental Focal Cerebral Ischemia. *Stroke*, *47*(5), 1336–1343. https://doi.org/10.1161/STROKEAHA.116.013205

Clarke, D. D., & Sokoloff, L. (1999). *Regulation of Cerebral Metabolic Rate*. https://www.ncbi.nlm.nih.gov/books/NBK28194/

Coelho-Santos, V., Leitão, R. A., Cardoso, F. L., Palmela, I., Rito, M., Barbosa, M., Brito, M. A., Fontes-Ribeiro, C. A., & Silva, A. P. (2015). The TNF-α/NF-κB signaling pathway has a key role in methamphetamine-induced blood-brain barrier dysfunction. *Journal of Cerebral Blood Flow and Metabolism*, *35*(8), 1260–1271. https://doi.org/10.1038/jcbfm.2015.59

Colgan, O. C., Ferguson, G., Collins, N. T., Murphy, R. P., Meade, G., Cahill, P. A., & Cummins, P. M. (2007). Regulation of bovine brain microvascular endothelial tight junction assembly and barrier function by laminar shear stress. *American Journal of Physiology - Heart and Circulatory Physiology*, *292*(6). https://doi.org/10.1152/ajpheart.01177.2006

Cory, S., & Adams, J. M. (2002). The BCL2 family: Regulators of the cellular life-or-death switch. In *Nature Reviews Cancer* (Vol. 2, Issue 9, pp. 647–656). Nature Publishing Group. https://doi.org/10.1038/nrc883

Cuadrado-Godia, E., Dwivedi, P., Sharma, S., Santiago, A. O., Gonzalez, J. R., Balcells, M., Laird, J., Turk, M., Suri, H. S., Nicolaides, A., Saba, L., Khanna, N. N., & Suri, J. S. (2018). Cerebral Small Vessel Disease: A Review Focusing on Pathophysiology, Biomarkers, and Machine Learning Strategies. *Journal of Stroke*, *20*(3), 302. https://doi.org/10.5853/JOS.2017.02922

Cummins, P. M. (2011). *Occludin: One Protein, Many Forms Downloaded from*. https://doi.org/10.1128/MCB.06029-11

Daneman, R., Zhou, L., Kebede, A. A., & Barres, B. A. (2010). Pericytes are required for blood?????"brain barrier integrity during embryogenesis. *Nature*, *468*(7323), 562–566. https://doi.org/10.1038/nature09513

DeMaio, L., Rouhanizadeh, M., Reddy, S., Sevanian, A., Hwang, J., & Hsiai, T. K. (2006). Oxidized phospholipids mediate occludin expression and phosphorylation in vascular endothelial cells. *American Journal of Physiology - Heart and Circulatory Physiology*, *290*(2). https://doi.org/10.1152/ajpheart.00554.2005

Deng, Z., Liu, D., Fu, T., Jiang, W., Qiu, M., Xiao, X., Xu, J., Feng, Y., Li, D., & Zeng, H. (2019). NF-κB mediates early blood-brain barrier disruption in a rat model of traumatic shock. *Journal of Trauma and Acute Care Surgery*, *86*(2), 240–249. https://doi.org/10.1097/TA.0000000000002124

DeOre, B. J., Partyka, P. P., Fan, F., & Galie, P. A. (2020). CD44 regulates blood-brain barrier integrity in response to fluid shear stress. In *bioRxiv* (p. 2020.01.28.924043). bioRxiv. https://doi.org/10.1101/2020.01.28.924043

DeStefano, J. G., Xu, Z. S., Williams, A. J., Yimam, N., & Searson, P. C. (2017). Effect of shear stress on iPSC-derived human brain microvascular endothelial cells (dhBMECs). *Fluids and Barriers of the CNS*, *14*(1), 20. https://doi.org/10.1186/s12987-017-0068-z

Dondelinger, Y., Delanghe, T., Priem, D., Wynosky-Dolfi, M. A., Sorobetea, D., Rojas-Rivera, D., Giansanti, P., Roelandt, R., Gropengiesser, J., Ruckdeschel, K., Savvides, S. N., Heck, A. J. R., Vandenabeele, P., Brodsky, I. E., & Bertrand, M. J. M. (2019). Serine 25 phosphorylation inhibits RIPK1 kinase-dependent cell death in models of infection and inflammation. *Nature Communications*, *10*(1), 1–16. https://doi.org/10.1038/s41467-019-09690-0

Dovey, C. M., Diep, J., Clarke, B. P., Hale, A. T., McNamara, D. E., Guo, H., Brown, N. W., Cao, J. Y., Grace, C. R., Gough, P. J., Bertin, J., Dixon, S. J., Fiedler, D., Mocarski, E. S., Kaiser, W. J., Moldoveanu, T., York, J. D., & Carette, J. E. (2018). MLKL Requires the Inositol Phosphate Code to Execute Necroptosis. *Molecular Cell*, *70*(5), 936-948.e7. https://doi.org/10.1016/j.molcel.2018.05.010

Elmore, S. (2007). Apoptosis: A Review of Programmed Cell Death. In *Toxicologic Pathology* (Vol. 35, Issue 4, pp. 495–516). NIH Public Access. https://doi.org/10.1080/01926230701320337

Esnault, C., Priet, S., Ribet, D., Vernochet, C., Bruls, T., Lavialle, C., Weissenbach, J., & Heidmann, T. (2008). A placenta-specific receptor for the fusogenic, endogenous retrovirus-derived, human syncytin-2. *Proceedings of the National Academy of Sciences of the United States of America*. https://doi.org/10.1073/pnas.0807413105

Eum, S. Y., Jaraki, D., András, I. E., & Toborek, M. (2015). Lipid rafts regulate PCB153-induced disruption of occludin and brain endothelial barrier function through protein phosphatase 2A and matrix metalloproteinase-2. *Toxicology and Applied Pharmacology*, *287*(3), 258–266. https://doi.org/10.1016/j.taap.2015.06.011

Feng, S., Zou, L., Wang, H., He, R., Liu, K., & Zhu, H. (2018). RhoA/ROCK-2 Pathway Inhibition and Tight Junction Protein Upregulation by Catalpol Suppresses Lipopolysaccaride-Induced Disruption of Blood-Brain Barrier Permeability. *Molecules*, *23*(9), 2371. https://doi.org/10.3390/molecules23092371

Fernández-Klett, F., & Priller, J. (2015). Diverse functions of pericytes in cerebral blood flow regulation and ischemia. In *Journal of Cerebral Blood Flow and Metabolism* (Vol. 35, Issue 6, pp. 883–887). SAGE Publications. https://doi.org/10.1038/jcbfm.2015.60

Fielding, C. J., & Fielding, P. E. (2000). Cholesterol and caveolae: Structural and functional relationships. In *Biochimica et Biophysica Acta - Molecular and Cell Biology of Lipids*. https://doi.org/10.1016/S1388-1981(00)00150-5

Forsberg, K. M. E., Zhang, Y., Reiners, J., Ander, M., Niedermayer, A., Fang, L., Neugebauer, H., Kassubek, J., Katona, I., Weis, J., Ludolph, A. C., Del Tredici, K., Braak, H., & Yilmazer-Hanke, D. (2018). Endothelial damage, vascular bagging and remodeling of the microvascular bed in human microangiopathy with deep white matter lesions. *Acta Neuropathologica Communications*, *6*(1), 128. https://doi.org/10.1186/s40478-018-0632-z

Frösen, J., Cebral, J., Robertson, A. M., & Aoki, T. (2019). Flow-induced, inflammation-mediated arterial wall remodeling in the formation and progression of intracranial aneurysms. *Neurosurgical Focus*, *47*(1). https://doi.org/10.3171/2019.5.FOCUS19234

Fujimoto, K. (1995). Pericyte-endothelial gap junctions in developing rat cerebral capillaries: A fine structural study. *The Anatomical Record*, *242*(4), 562–565. https://doi.org/10.1002/ar.1092420412

Furuse, M., Hirase, T., Itoh, M., Nagafuchi, A., Yonemura, S., Tsukita, S., & Tsukita, S. (1993). Occludin: A novel integral membrane protein localizing at tight junctions. *Journal of Cell Biology*, *123*(6 II), 1777–1788. https://doi.org/10.1083/jcb.123.6.1777

Galluzzi, L., Vitale, I., Aaronson, S. A., Abrams, J. M., Adam, D., Agostinis, P., Alnemri, E. S., Altucci, L., Amelio, I., Andrews, D. W., Annicchiarico-Petruzzelli, M., Antonov, A. V., Arama, E., Baehrecke, E. H., Barlev, N. A., Bazan, N. G., Bernassola, F., Bertrand, M. J. M., Bianchi, K., … Kroemer, G. (2018). Molecular mechanisms of cell death: Recommendations of the Nomenclature Committee on Cell Death 2018. In *Cell Death and Differentiation* (Vol. 25, Issue 3, pp. 486–541). Nature Publishing Group. https://doi.org/10.1038/s41418-017-0012-4

Geng, J., Ito, Y., Shi, L., Amin, P., Chu, J., Ouchida, A. T., Mookhtiar, A. K., Zhao, H., Xu, D., Shan, B., Najafov, A., Gao, G., Akira, S., & Yuan, J. (2017). Regulation of RIPK1 activation by TAK1-mediated phosphorylation dictates apoptosis and necroptosis. *Nature Communications 2017 8:1*, *8*(1), 1–12. https://doi.org/10.1038/s41467-017-00406-w

Geranmayeh, M. H., Rahbarghazi, R., & Farhoudi, M. (2019). Targeting pericytes for neurovascular regeneration. In *Cell Communication and Signaling* (Vol. 17, Issue 1, pp. 1–13). BioMed Central Ltd. https://doi.org/10.1186/s12964-019-0340-8

Golanov, E. V., Sharpe, M. A., Regnier-Golanov, A. S., Zoppo, G. J. Del, Baskin, D. S., & Britz, G. W. (2019). Fibrinogen Chains Intrinsic to the Brain. *Frontiers in Neuroscience*, *13*(MAY). https://doi.org/10.3389/FNINS.2019.00541

Golgi-Apparat Dr.Jastrows EM-Atlas. (n.d.). Retrieved September 13, 2021, from http://www.drjastrow.de/WAI/EM/EMGolgi.html

Gong, Y. N., Guy, C., Crawford, J. C., & Green, D. R. (2017). Biological events and molecular signaling following MLKL activation during necroptosis. *Cell Cycle*, *16*(19), 1748–1760. https://doi.org/10.1080/15384101.2017.1371889

Gong, Y. N., Guy, C., Olauson, H., Becker, J. U., Yang, M., Fitzgerald, P., Linkermann, A., & Green, D. R. (2017). ESCRT-III Acts Downstream of MLKL to Regulate Necroptotic Cell Death and Its Consequences. *Cell*, *169*(2), 286-300.e16. https://doi.org/10.1016/j.cell.2017.03.020

González-Mariscal, L., Betanzos, A., & Ávila-Flores, A. (2000). MAGUK proteins: Structure and role in the tight junction. *Seminars in Cell and Developmental Biology*, *11*(4), 315–324. https://doi.org/10.1006/scdb.2000.0178

Govindpani, K., McNamara, L. G., Smith, N. R., Vinnakota, C., Waldvogel, H. J., Faull, R. L., & Kwakowsky, A. (2019). Vascular Dysfunction in Alzheimer's Disease: A Prelude to the Pathological Process or a Consequence of It? *Journal of Clinical Medicine*, *8*(5), 651. https://doi.org/10.3390/JCM8050651

Gray, C. M., Remouchamps, C., McCorkell, K. A., Solt, L. A., Dejardin, E., Orange, J. S., & May, M. J. (2014). Noncanonical NF-κB signaling is limited by classical NF-κB activity. *Science Signaling*, *7*(311). https://doi.org/10.1126/scisignal.2004557

Greene, C., Hanley, N., & Campbell, M. (2019). Claudin-5: Gatekeeper of neurological function. In *Fluids and Barriers of the CNS* (Vol. 16, Issue 1, pp. 1–15). BioMed Central Ltd. https://doi.org/10.1186/s12987-019-0123-z

Grilli, M., Goffi, F., Memo, M., & Spano, P. (1996). Interleukin-1beta and glutamate activate the NF-kappaB/Rel binding site from the regulatory region of the amyloid precursor protein gene in primary neuronal cultures. *The Journal of Biological Chemistry*, *271*(25), 15002–15007. https://doi.org/10.1074/JBC.271.25.15002

Guarneri, C., Bevelacqua, V., Polesel, J., Falzone, L., Cannavo, P. S., Spandidos, D. A., Malaponte, G., & Libra, M. (2017). NF-κB inhibition is associated with OPN/MMP-9 downregulation in cutaneous melanoma. *Oncology Reports*, *37*(2), 737. https://doi.org/10.3892/OR.2017.5362

Guérit, S., Fidan, E., Macas, J., Czupalla, C. J., Figueiredo, R., Vijikumar, A., Yalcin, B. H., Thom, S., Winter, P., Gerhardt, H., Devraj, K., & Liebner, S. (2020). Astrocyte-derived Wnt growth factors are required for endothelial blood-brain barrier maintenance. *Progress in Neurobiology*, 101937. https://doi.org/10.1016/j.pneurobio.2020.101937

Gumbiner, B., Lowenkopf, T., & Apatira, D. (1991). Identification of a 160-kDa polypeptide that binds to the tight junction protein ZO-1. *Proceedings of the National Academy of Sciences of the United States of America*, *88*(8), 3460–3464. https://doi.org/10.1073/pnas.88.8.3460

Haley, M. J., & Lawrence, C. B. (2017). The blood-brain barrier after stroke: Structural studies and the role of transcytotic vesicles. *Journal of Cerebral Blood Flow and Metabolism*, *37*(2), 456–470. https://doi.org/10.1177/0271678X16629976

Hall, C. N., Reynell, C., Gesslein, B., Hamilton, N. B., Mishra, A., Sutherland, B. A., Oâ Farrell, F. M., Buchan, A. M., Lauritzen, M., & Attwell, D. (2014). Capillary pericytes regulate cerebral blood flow in health and disease. *Nature*, *508*(1), 55–60. https://doi.org/10.1038/nature13165

Han, Z., Boyle, D. L., Manning, A. M., & Firestein, G. S. (1998). AP-1 and NF-κB regulation in rheumatoid arthritis and murine collagen-induced arthritis. *Autoimmunity*, *28*(4), 197–208. https://doi.org/10.3109/08916939808995367

Handagama, P., Scarborough, R. M., Shuman, M. A., & Bainton, D. F. (1993). Endocytosis of fibrinogen into megakaryocyte and platelet α-granules is mediated by α(IIb)β3 (glycoprotein IIb-IIIa). *Blood*, *82*(1), 135–138. https://doi.org/10.1182/blood.v82.1.135.bloodjournal821135

Hart, L. A., Krishnan, V. L., Adcock, I. M., Barnes, P. J., & Chung, K. F. (1998). Activation and localization of transcription factor, nuclear factor-κB, in asthma. *American Journal of Respiratory and Critical Care Medicine*, *158*(5 PART I), 1585–1592. https://doi.org/10.1164/ajrccm.158.5.9706116

Haruwaka, K., Ikegami, A., Tachibana, Y., Ohno, N., Konishi, H., Hashimoto, A., Matsumoto, M., Kato, D., Ono, R., Kiyama, H., Moorhouse, A. J., Nabekura, J., & Wake, H. (2019). Dual microglia effects on blood brain barrier permeability induced by systemic inflammation. *Nature Communications*, *10*(1), 1–17. https://doi.org/10.1038/s41467-019-13812-z

Hase, M., Araki, S., & Hayashi, H. (1997). Fragments of amyloid β induce apoptosis in vascular endothelial cells. *Endothelium: Journal of Endothelial Cell Research*, *5*(4), 221–229. https://doi.org/10.3109/10623329709052587

Hase, Y., Ding, R., Harrison, G., Hawthorne, E., King, A., Gettings, S., Platten, C., Stevenson, W., Craggs, L. J. L., & Kalaria, R. N. (2019). White matter capillaries in vascular and neurodegenerative dementias. *Acta Neuropathologica Communications*, *7*(1), 16. https://doi.org/10.1186/s40478-019-0666-x

Haskins, J., Gu, L., Wittchen, E. S., Hibbard, J., & Stevenson, B. R. (1998). ZO-3, a novel member of the MAGUK protein family found at the tight junction, interacts with ZO-1 and occludin. *Journal of Cell Biology*, *141*(1), 199–208. https://doi.org/10.1083/jcb.141.1.199

Hellström, M., Gerhardt, H., Kalén, M., Li, X., Eriksson, U., Wolburg, H., & Betsholtz, C. (2001). Lack of Pericytes Leads to Endothelial Hyperplasia and Abnormal Vascular Morphogenesis. *Journal of Cell Biology*, *153*(3), 543–554. https://doi.org/10.1083/JCB.153.3.543

Henle, F. (1838). Ueber die Ausbreitung des Epithelium im menschlichen Koerper. *Muellers Arch.Fuer Anatomie, Physiologie Und Wissenschaftliche Medicin*, *1*, 103–128. https://ci.nii.ac.jp/naid/10004989971

Hill, R. A., Tong, L., Yuan, P., Murikinati, S., Gupta, S., & Grutzendler, J. (2015). Regional Blood Flow in the Normal and Ischemic Brain Is Controlled by Arteriolar Smooth Muscle Cell Contractility and Not by Capillary Pericytes. *Neuron*, *87*(1), 95–110. https://doi.org/10.1016/j.neuron.2015.06.001

Hirano, A., Kawanami, T., & Llena, J. F. (1994). Electron microscopy of the blood-brain barrier in disease. *Microscopy Research and Technique*, *27*(6), 543–556. https://doi.org/10.1002/jemt.1070270609

Holmström, T. H., Tran, S. E. F., Johnson, V. L., Ahn, N. G., Chow, S. C., & Eriksson, J. E. (1999). Inhibition of Mitogen-Activated Kinase Signaling Sensitizes HeLa Cells to Fas Receptor-Mediated Apoptosis. *Molecular and Cellular Biology*, *19*(9), 5991–6002. https://doi.org/10.1128/mcb.19.9.5991

Hori, S., Ohtsuki, S., Hosoya, K. I., Nakashima, E., & Terasaki, T. (2004). A pericyte-derived angiopoietin-1 multimeric complex induces occludin gene expression in brain capillary endothelial cells through Tie-2 activation in vitro. *Journal of Neurochemistry*, *89*(2), 503–513. https://doi.org/10.1111/j.1471-4159.2004.02343.x

Hua, C. T., Hopwood, J. J., Carlsson, S. R., Harris, R. J., & Meikle, P. J. (1998). Evaluation of the lysosome-associated membrane protein LAMP-2 as a marker for lysosomal storage disorders. *Clinical Chemistry*, *44*(10), 2094–2102. https://doi.org/10.1093/clinchem/44.10.2094

Huang, S. F., Othman, A., Koshkin, A., Fischer, S., Fischer, D., Zamboni, N., Ono, K., Sawa, T., & Ogunshola, O. O. (2020). Astrocyte glutathione maintains endothelial barrier stability. *Redox Biology*, *34*, 101576. https://doi.org/10.1016/J.REDOX.2020.101576

Hung, W. S., Huang, C. L., Fan, J. T., Huang, D. Y., Yeh, C. F., Cheng, J. C., & Tseng, C. P. (2012). The endocytic adaptor protein Disabled-2 is required for cellular uptake of fibrinogen. *Biochimica et Biophysica Acta (BBA) - Molecular Cell Research*, *1823*(10), 1778–1788. https://doi.org/10.1016/J.BBAMCR.2012.06.008

Hunter, J. M., Kwan, J., Malek-Ahmadi, M., Maarouf, C. L., Kokjohn, T. A., Belden, C., Sabbagh, M. N., Beach, T. G., & Roher, A. E. (2012). Morphological and pathological evolution of the brain microcirculation in aging and Alzheimer's disease. *PLoS ONE*, *7*(5). https://doi.org/10.1371/journal.pone.0036893

Iadecola, C. (2004). Neurovascular regulation in the normal brain and in Alzheimer's disease. *Nature Reviews Neuroscience*, *5*(5), 347–360. https://doi.org/10.1038/nrn1387

Inoue, K., Shinohara, H., Behar, M., Yumoto, N., Tanaka, G., Hoffmann, A., Aihara, K., & Okada-Hatakeyama, M.

(2016). Oscillation dynamics underlie functional switching of NF-κB for B-cell activation. *Npj Systems Biology and Applications*, *2*(1), 1–9. https://doi.org/10.1038/npjsba.2016.24

Ishizaki, T., Chiba, H., Kojima, T., Fujibe, M., Soma, T., Miyajima, H., Nagasawa, K., Wada, I., & Sawada, N. (2003). Cyclic AMP induces phosphorylation of claudin-5 immunoprecipitates and expression of claudin-5 gene in blood-brain-barrier endothelial cells via protein kinase A-dependent and -independent pathways. *Experimental Cell Research*, *290*(2), 275–288. https://doi.org/10.1016/S0014-4827(03)00354-9

Jagtap, P. G., Degterev, A., Choi, S., Keys, H., Yuan, J., & Cuny, G. D. (2007). Structure-activity relationship study of tricyclic necroptosis inhibitors. *Journal of Medicinal Chemistry*. https://doi.org/10.1021/jm061016o

Jastrow, H. (2018). *Endocytosis Dr.Jastrow's electron microscopic atlas*. http://www.drjastrow.de/WAI/EM/EMEndocytoseE.html

Jia, W., Martin, T. A., Zhang, G., & Jiang, W. G. (2013). Junctional adhesion molecules in cerebral endothelial tight junction and brain metastasis. In *Anticancer Research* (Vol. 33, Issue 6, pp. 2353–2359). https://pubmed.ncbi.nlm.nih.gov/23749882/

Jiang, L., Song, L., Wu, J., Yang, Y., Zhu, X., Hu, B., Cheng, S.-Y., & Li, M. (2013). Bmi-1 Promotes Glioma Angiogenesis by Activating NF-κB Signaling. *PLOS ONE*, *8*(1), e55527. https://doi.org/10.1371/JOURNAL.PONE.0055527

Jiang, Y., Müller, K., Khan, M. A., Assmann, J. C., Lampe, J., Kilau, K., Richter, M., Kleint, M., Ridder, D. A., Hübner, N., Schmidt-Supprian, M., Wenzel, J., & Schwaninger, M. (2020). Cerebral angiogenesis ameliorates pathological disorders in Nemo-deficient mice with small-vessel disease. *Journal of Cerebral Blood Flow and Metabolism*, *41*(2), 219–235. https://doi.org/10.1177/0271678X20910522

Joutel, A., Monet-Leprêtre, M., Gosele, C., Baron-Menguy, C., Hammes, A., Schmidt, S., Lemaire-Carrette, B., Domenga, V., Schedl, A., Lacombe, P., & Hubner, N. (2010). Cerebrovascular dysfunction and microcirculation rarefaction precede white matter lesions in a mouse genetic model of cerebral ischemic small vessel disease. *Journal of Clinical Investigation*, *120*(2), 433–445. https://doi.org/10.1172/JCI39733

Ju Hwang, C., Choi, D.-Y., Park, M. H., & Hong, J. T. (2017). NF-κB as a Key Mediator of Brain Inflammation in Alzheimer's Disease. *CNS & Neurological Disorders - Drug Targets*, *18*(1), 3–10. https://doi.org/10.2174/1871527316666170807130011

Kageyama, T., Nakamura, M., Matsuo, A., Yamasaki, Y., Takakura, Y., Hashida, M., Kanai, Y., Naito, M., Tsuruo, T., Minato, N., & Shimohama, S. (2000). The 4F2hc/LAT1 complex transports L-DOPA across the blood-brain barrier. *Brain Research*, *879*(1–2), 115–121. https://doi.org/10.1016/S0006-8993(00)02758-X

Kaltschmidt, B., & Kaltschmidt, C. (2009). NF-kappaB in the nervous system. In *Cold Spring Harbor perspectives in biology* (Vol. 1, Issue 3). Cold Spring Harbor Laboratory Press. https://doi.org/10.1101/cshperspect.a001271

Kanayama, A., Seth, R. B., Sun, L., Ea, C. K., Hong, M., Shaito, A., Chiu, Y. H., Deng, L., & Chen, Z. J. (2004). TAB2 and TAB3 Activate the NF-κB Pathway through Binding to Polyubiquitin Chains. *Molecular Cell*, *15*(4), 535–548. https://doi.org/10.1016/J.MOLCEL.2004.08.008

Kang, D. E., Saitoh, T., Chen, X., Xia, Y., Masliah, E., Hansen, L. A., Thomas, R. G., Thal, L. J., & Katzman, R. (1997). Genetic association of the low-density lipoprotein receptor-related protein gene (LRP), an apolipoprotein E receptor, with late-onset Alzheimer's disease. *Neurology*, *49*(1), 56–61. https://doi.org/10.1212/WNL.49.1.56

Keller, A., Westenberger, A., Sobrido, M. J., García-Murias, M., Domingo, A., Sears, R. L., Lemos, R. R., Ordoñez-Ugalde, A., Nicolas, G., Da Cunha, J. E. G., Rushing, E. J., Hugelshofer, M., Wurnig, M. C., Kaech, A., Reimann, R., Lohmann, K., Dobričić, V., Carracedo, A., Petrović, I., … Oliveira, J. R. M. (2013). Mutations in the gene encoding PDGF-B cause brain calcifications in humans and mice. *Nature Genetics*, *45*(9), 1077–1082. https://doi.org/10.1038/ng.2723

Kendellen, M. F., Bradford, J. W., Lawrence, C. L., Clark, K. S., & Baldwin, A. S. (2014). Canonical and non-canonical NF-κB signaling promotes breast cancer tumor-initiating cells. *Oncogene*, *33*(10), 1297–1305. https://doi.org/10.1038/onc.2013.64

Khalid, N., & Azimpouran, M. (2021). *Necrosis - StatPearls - NCBI Bookshelf*. https://www.ncbi.nlm.nih.gov/books/NBK557627/

Kim, K. A., Kim, D., Kim, J. H., Shin, Y. J., Kim, E. S., Akram, M., Kim, E. H., Majid, A., Baek, S. H., & Bae, O. N. (2020). Autophagy-mediated occludin degradation contributes to blood-brain barrier disruption during ischemia in bEnd.3 brain endothelial cells and rat ischemic stroke models. *Fluids and Barriers of the CNS*, *17*(1), 21. https://doi.org/10.1186/s12987-020-00182-8

Kimelberg, H. K., & Nedergaard, M. (2010). Functions of Astrocytes and their Potential As Therapeutic Targets.

Neurotherapeutics, *7*(4), 338–353. https://doi.org/10.1016/j.nurt.2010.07.006

Kisler, K., Nelson, A. R., Rege, S. V., Ramanathan, A., Wang, Y., Ahuja, A., Lazic, D., Tsai, P. S., Zhao, Z., Zhou, Y., Boas, D. A., Sakadžić, S., & Zlokovic, B. V. (2017). Pericyte degeneration leads to neurovascular uncoupling and limits oxygen supply to brain. *Nature Neuroscience*, *20*(3), 406–416. https://doi.org/10.1038/nn.4489

Kniesel, U., & Wolburg, H. (2000). Tight junctions of the blood-brain barrier. *Cellular and Molecular Neurobiology*, *20*(1), 57–76. https://doi.org/10.1023/A:1006995910836

Knowland, D., Arac, A., Sekiguchi, K. J., Hsu, M., Lutz, S. E., Perrino, J., Steinberg, G. K., Barres, B. A., Nimmerjahn, A., & Agalliu, D. (2014). Stepwise Recruitment of Transcellular and Paracellular Pathways Underlies Blood-Brain Barrier Breakdown in Stroke. *Neuron*. https://doi.org/10.1016/j.neuron.2014.03.003

Kolodziej, L. E., Lodolce, J. P., Chang, J. E., Schneider, J. R., Grimm, W. A., Bartulis, S. J., Zhu, X., Messer, J. S., Murphy, S. F., Reddy, N., Turner, J. R., & Boone, D. L. (2011). TNFAIP3 maintains intestinal barrier function and supports epithelial cell tight junctions. *PLoS ONE*, *6*(10), 26352. https://doi.org/10.1371/journal.pone.0026352

Kondylis, V., Kumari, S., Vlantis, K., & Pasparakis, M. (2017). The interplay of IKK, NF-κB and RIPK1 signaling in the regulation of cell death, tissue homeostasis and inflammation. In *Immunological Reviews* (Vol. 277, Issue 1, pp. 113–127). Blackwell Publishing Ltd. https://doi.org/10.1111/imr.12550

Körbelin, J., Dogbevia, G., Michelfelder, S., Ridder, D. A., Hunger, A., Wenzel, J., Seismann, H., Lampe, M., Bannach, J., Pasparakis, M., Kleinschmidt, J. A., Schwaninger, M., & Trepel, M. (2016). A brain microvasculature endothelial cell-specific viral vector with the potential to treat neurovascular and neurological diseases. *EMBO Molecular Medicine*, *8*(6), 609–625. https://doi.org/10.15252/emmm.201506078

Ková, L. (2010). The 20 W sleep-walkers. *EMBO Reports*, *11*(1), 2. https://doi.org/10.1038/EMBOR.2009.266

Kraupp, B. G., Ruttkay-Nedecky, B., Koudelka, H., Bukowska, K., Bursch, W., & Schulte-Hermann, R. (1995). In situ detection of fragmented dna (tunel assay) fails to discriminate among apoptosis, necrosis, and autolytic cell death: A cautionary note. *Hepatology*, *21*(5), 1465–1468. https://doi.org/10.1002/hep.1840210534

Kroemer, G., El-Deiry, W. S., Golstein, P., Vaux, D., Vandenabeele, P., Zhivotovsky, B., Blagosklonny, M. V, Malorni, W., Knight, R. A., Piacentini, M., Nagata, S., & Melino, G. (2005). News and Commentary Classification of cell death: recommendations of the Nomenclature Committee on Cell Death. *Cell Death and Differentiation*, *12*, 1463–1467. https://doi.org/10.1038/sj.cdd.4401724

Kroemer, G., Galluzzi, L., Vandenabeele, P., Abrams, J., Alnemri, E. S., Baehrecke, E. H., Blagosklonny, M. V., El-Deiry, W. S., Golstein, P., Green, D. R., Hengartner, M., Knight, R. A., Kumar, S., Lipton, S. A., Malorni, W., Nuñez, G., Peter, M. E., Tschopp, J., Yuan, J., … Melino, G. (2009). Classification of cell death: Recommendations of the Nomenclature Committee on Cell Death 2009. In *Cell Death and Differentiation* (Vol. 16, Issue 1, pp. 3–11). NIH Public Access. https://doi.org/10.1038/cdd.2008.150

Krueger, M., Härtig, W., Reichenbach, A., Bechmann, I., & Michalski, D. (2013). Blood-Brain Barrier Breakdown after Embolic Stroke in Rats Occurs without Ultrastructural Evidence for Disrupting Tight Junctions. *PLoS ONE*, *8*(2), e56419. https://doi.org/10.1371/journal.pone.0056419

Krupinski, J., Kaluza, J., Kumar, P., Kumar, S., & Wang, J. M. (1994). Role of angiogenesis in patients with cerebral ischemic stroke. *Stroke*, *25*(9), 1794–1798. https://doi.org/10.1161/01.STR.25.9.1794

Krushel, L. A., Cunningham, B. A., Edelman, G. M., & Crossin, K. L. (1999). NF-κB Activity Is Induced by Neural Cell Adhesion Molecule Binding to Neurons and Astrocytes *. *Journal of Biological Chemistry*, *274*(4), 2432–2439. https://doi.org/10.1074/JBC.274.4.2432

Kumari, S., Mg, S., & Mayor, S. (2010). Endocytosis unplugged: Multiple ways to enter the cell. In *Cell Research* (Vol. 20, Issue 3, pp. 256–275). Nature Publishing Group. https://doi.org/10.1038/cr.2010.19

Kutuzov, N., Flyvbjerg, H., & Lauritzen, M. (2018). Contributions of the glycocalyx, endothelium, and extravascular compartment to the blood–brain Barrier. *Proceedings of the National Academy of Sciences of the United States of America*. https://doi.org/10.1073/pnas.1802155115

Lafont, E., Draber, P., Rieser, E., Reichert, M., Kupka, S., de Miguel, D., Draberova, H., von Mässenhausen, A., Bhamra, A., Henderson, S., Wojdyla, K., Chalk, A., Surinova, S., Linkermann, A., & Walczak, H. (2018). TBK1 and IKKε prevent TNF-induced cell death by RIPK1 phosphorylation. *Nature Cell Biology 2018 20:12*, *20*(12), 1389–1399. https://doi.org/10.1038/s41556-018-0229-6

Lagas, J. S., Van Waterschoot, R. A. B., Van Tilburg, V. A. C. J., Hillebrand, M. J., Lankheet, N., Rosing, H., Beijnen, J. H., & Schinkel, A. H. (2009). Brain accumulation of dasatinib is restricted by P-glycoprotein (ABCB1) and breast cancer resistance protein (ABCG2) and can be enhanced by elacridar treatment.

Clinical Cancer Research, *15*(7), 2344–2351. https://doi.org/10.1158/1078-0432.CCR-08-2253

Larson, D. M., Carson, M. P., & Haudenschild, C. C. (1987). Junctional transfer of small molecules in cultured bovine brain microvascular endothelial cells and pericytes. *Microvascular Research*, *34*(2), 184–199. https://doi.org/10.1016/0026-2862(87)90052-5

Laurien, L., Nagata, M., Schünke, H., Delanghe, T., Wiederstein, J. L., Kumari, S., Schwarzer, R., Corona, T., Krüger, M., Bertrand, M. J. M., Kondylis, V., & Pasparakis, M. (2020). Autophosphorylation at serine 166 regulates RIP kinase 1-mediated cell death and inflammation. *Nature Communications 2020 11:1*, *11*(1), 1–16. https://doi.org/10.1038/s41467-020-15466-8

Lee, E. G., Boone, D. L., Chai, S., Libby, S. L., Chien, M., Lodolce, J. P., & Ma, A. (2000). Failure to regulate TNF-induced NF-κB and cell death responses in A20-deficient mice. *Science*, *289*(5488), 2350–2354. https://doi.org/10.1126/science.289.5488.2350

Legarda-Addison, D., Hase, H., O'Donnell, M. A., & Ting, A. T. (2009). NEMO/IKKγ regulates an early NF-κB-independent cell-death checkpoint during TNF signaling. *Cell Death and Differentiation*. https://doi.org/10.1038/cdd.2009.41

Li, Q., Han, X., Lan, X., Gao, Y., Wan, J., Durham, F., Cheng, T., Yang, J., Wang, Z., Jiang, C., Ying, M., Koehler, R. C., Stockwell, B. R., & Wang, J. (2017). Inhibition of neuronal ferroptosis protects hemorrhagic brain. *JCI Insight*, *2*(7), e90777. https://doi.org/10.1172/jci.insight.90777

Li, W. P., Chan, W. Y., Lai, H. W. L., & Yew, D. T. (1997). Terminal dUTP nick end labeling (TUNEL) positive cells in the different regions of the brain in normal aging and Alzheimer patients. *Journal of Molecular Neuroscience*, *8*(2), 75–82. https://doi.org/10.1007/BF02736774

Li, Y., Führer, M., Bahrami, E., Socha, P., Klaudel-Dreszler, M., Bouzidi, A., Liu, Y., Lehle, A. S., Magg, T., Hollizeck, S., Rohlfs, M., Conca, R., Field, M., Warner, N., Mordechai, S., Shteyer, E., Turner, D., Boukari, R., Belbouab, R., … Kotlarz, D. (2019). Human RIPK1 deficiency causes combined immunodeficiency and inflammatory bowel diseases. *Proceedings of the National Academy of Sciences*, *116*(3), 970–975. https://doi.org/10.1073/PNAS.1813582116

Liang, Y. X., Wang, N. N., Zhang, Z. Y., Juan, Z. D., & Zhang, C. (2019). Necrostatin-1 ameliorates peripheral nerve injury-induced neuropathic pain by inhibiting the RIP1/RIP3 pathway. *Frontiers in Cellular Neuroscience*, *13*, 211. https://doi.org/10.3389/fncel.2019.00211

Liebner, S., Corada, M., Bangsow, T., Babbage, J., Taddei, A., Czupalla, C. J., Reis, M., Felici, A., Wolburg, H., Fruttiger, M., Taketo, M. M., Von Melchner, H., Plate, K. H., Gerhardt, H., & Dejana, E. (2008). Wnt/β-catenin signaling controls development of the blood - brain barrier. *Journal of Cell Biology*, *183*(3), 409–417. https://doi.org/10.1083/jcb.200806024

Lin, Y., Bai, L., Chen, W., & Xu, S. (2010). The NF-κB activation pathways, emerging molecular targets for cancer prevention and therapy. *Expert Opinion on Therapeutic Targets*, *14*(1), 45. https://doi.org/10.1517/14728220903431069

Lindblom, P., Gerhardt, H., Liebner, S., Abramsson, A., Enge, M., Hellström, M., Bäckström, G., Fredriksson, S., Landegren, U., Nyström, H. C., Bergström, G., Dejana, E., Östman, A., Lindahl, P., & Betsholtz, C. (2003). Endothelial PDGF-B retention is required for proper investment of pericytes in the microvessel wall. *Genes and Development*. https://doi.org/10.1101/gad.266803

Linton, K. J. (2007). Structure and function of ABC transporters. *Physiology (Bethesda, Md.)*, *22*, 122–130. https://doi.org/10.1152/physiol.00046.2006

Liu, C., Zhang, K., Shen, H., Yao, X., Sun, Q., & Chen, G. (2018). Necroptosis: A novel manner of cell death, associated with stroke (Review). In *International Journal of Molecular Medicine* (Vol. 41, Issue 2, pp. 624–630). Spandidos Publications. https://doi.org/10.3892/ijmm.2017.3279

Liu, H., Ma, Y., Pagliari, L. J., Perlman, H., Yu, C., Lin, A., & Pope, R. M. (2004). TNF-α-Induced Apoptosis of Macrophages Following Inhibition of NF-κB: A Central Role for Disruption of Mitochondria. *The Journal of Immunology*, *172*(3), 1907–1915. https://doi.org/10.4049/jimmunol.172.3.1907

Liu, J., Jin, X., Liu, K. J., & Liu, W. (2012). Matrix metalloproteinase-2-mediated occludin degradation and caveolin-1-mediated claudin-5 redistribution contribute to blood-brain barrier damage in early ischemic stroke stage. *Journal of Neuroscience*, *32*(9), 3044–3057. https://doi.org/10.1523/JNEUROSCI.6409-11.2012

Liu, S., Agalliu, D., Yu, C., & Fisher, M. (2012). The Role of Pericytes in Blood-Brain Barrier Function and Stroke. *Current Pharmaceutical Design*, *18*(25), 3653–3662. https://doi.org/10.2174/138161212802002706

Liu, T., Zhang, L., Joo, D., & Sun, S. C. (2017). NF-κB signaling in inflammation. In *Signal Transduction and Targeted Therapy*. https://doi.org/10.1038/sigtrans.2017.23

Liu, W., Wang, P., Shang, C., Chen, L., Cai, H., Ma, J., Yao, Y., Shang, X., & Xue, Y. (2014). Endophilin-1 regulates blood-brain barrier permeability by controlling ZO-1 and occludin expression via the EGFR-ERK1/2 pathway. *Brain Research*, *1573*, 17–26. https://doi.org/10.1016/j.brainres.2014.05.022

Lochhead, J. J., McCaffrey, G., Quigley, C. E., Finch, J., Demarco, K. M., Nametz, N., & Davis, T. P. (2010). Oxidative stress increases blood-brain barrier permeability and induces alterations in occludin during hypoxia-reoxygenation. *Journal of Cerebral Blood Flow and Metabolism*, *30*(9), 1625–1636. https://doi.org/10.1038/jcbfm.2010.29

Loeb, J. A., Sohrab, S. A., Huq, M., & Fuerst, D. R. (2006). Brain calcifications induce neurological dysfunction that can be reversed by a bone drug. *Journal of the Neurological Sciences*, *243*(1–2), 77–81. https://doi.org/10.1016/J.JNS.2005.11.033

Luissint, A. C., Artus, C., Glacial, F., Ganeshamoorthy, K., & Couraud, P. O. (2012). Tight junctions at the blood brain barrier: Physiological architecture and disease-associated dysregulation. In *Fluids and Barriers of the CNS* (Vol. 9, Issue 1). https://doi.org/10.1186/2045-8118-9-23

Luna-Tortós, C., Fedrowitz, M., & Löscher, W. (2008). Several major antiepileptic drugs are substrates for human P-glycoprotein. *Neuropharmacology*, *55*(8), 1364–1375. https://doi.org/10.1016/j.neuropharm.2008.08.032

Mahringer, A., & Fricker, G. (2016). ABC transporters at the blood-brain barrier. In *Expert Opinion on Drug Metabolism and Toxicology* (Vol. 12, Issue 5, pp. 499–508). Taylor and Francis Ltd. https://doi.org/10.1517/17425255.2016.1168804

Mantle, J. L., & Lee, K. H. (2019). Immunoglobulin G transport increases in an in vitro blood–brain barrier model with amyloid-β and with neuroinflammatory cytokines. *Biotechnology and Bioengineering*, *116*(7), 1752–1761. https://doi.org/10.1002/BIT.26967

Martìn-Padura, I., Lostaglio, S., Schneemann, M., Williams, L., Romano, M., Fruscella, P., Panzeri, C., Stoppacciaro, A., Ruco, L., Villa, A., Simmons, D., & Dejana, E. (1998). Junctional adhesion molecule, a novel member of the immunoglobulin superfamily that distributes at intercellular junctions and modulates monocyte transmigration. *Journal of Cell Biology*, *142*(1), 117–127. https://doi.org/10.1083/jcb.142.1.117

Mathiesen Janiurek, M., Soylu-Kucharz, R., Christoffersen, C., Kucharz, K., & Lauritzen, M. (2019). Apolipoprotein M-bound sphingosine-1-phosphate regulates blood-brain barrier paracellular permeability and transcytosis. *ELife*. https://doi.org/10.7554/eLife.49405

May, M. J., D'Acquisto, F., Madge, L. A., Glockner, J., Pober, J. S., & Ghosh, S. (2000). Selective inhibition of NF-κB activation by a peptide that blocks the interaction of NEMO with the IκB kinase complex. *Science*. https://doi.org/10.1126/science.289.5484.1550

McCaffrey, G., Willis, C. L., Staatz, W. D., Nametz, N., Quigley, C. A., Hom, S., Lochhead, J. J., & Davis, T. P. (2009). Occludin oligomeric assemblies at tight junctions of the blood-brain barrier are altered by hypoxia and reoxygenation stress. *Journal of Neurochemistry*, *110*(1), 58–71. https://doi.org/10.1111/j.1471-4159.2009.06113.x

Medina, C. B., Mehrotra, P., Arandjelovic, S., Perry, J. S. A., Guo, Y., Morioka, S., Barron, B., Walk, S. F., Ghesquière, B., Krupnick, A. S., Lorenz, U., & Ravichandran, K. S. (2020). Metabolites released from apoptotic cells act as tissue messengers. *Nature 2020 580:7801*, *580*(7801), 130–135. https://doi.org/10.1038/s41586-020-2121-3

Mehrabadi, A. R., Korolainen, M. A., Odero, G., Miller, D. W., & Kauppinen, T. M. (2017). Poly(ADP-ribose) polymerase-1 regulates microglia mediated decrease of endothelial tight junction integrity. *Neurochemistry International*, *108*, 266–271. https://doi.org/10.1016/j.neuint.2017.04.014

Mercurio, F., Zhu, H., Murray, B. W., Shevchenko, A., Bennett, B. L., Li, J. W., Young, D. B., Barbosa, M., Mann, M., Manning, A., & Rao, A. (1997). IKK-1 and IKK-2: Cytokine-activated IκB kinases essential for NF-κB activation. *Science*. https://doi.org/10.1126/science.278.5339.860

Meuwissen, M. E. C., & Mancini, G. M. S. (2012). Neurological findings in incontinentia pigmenti; a review. In *European Journal of Medical Genetics*. https://doi.org/10.1016/j.ejmg.2012.04.007

Mezzano, S., Aros, C., Droguett, A., Burgos, M. E., Ardiles, L., Flores, C., Schneider, H., Ruiz-Ortega, M., & Egido, J. (2004). NF-κB activation and overexpression of regulated genes in human diabetic nephropathy. *Nephrology Dialysis Transplantation*, *19*(10), 2505–2512. https://doi.org/10.1093/ndt/gfh207

Michalak, Z., Lebrun, A., Miceli, M. Di, Rousset, M.-C., Crespel, A., Coubes, P., Henshall, D. C., Lerner-Natoli, M., & Rigau, V. (2012). IgG Leakage May Contribute to Neuronal Dysfunction in Drug-Refractory Epilepsies With Blood-Brain Barrier Disruption. *Journal of Neuropathology & Experimental Neurology*, *71*(9), 826–838. https://doi.org/10.1097/NEN.0B013E31826809A6

Mifflin, L., Ofengeim, D., & Yuan, J. (2020). Receptor-interacting protein kinase 1 (RIPK1) as a therapeutic target.

In *Nature Reviews Drug Discovery* (Vol. 19, Issue 8, pp. 553–571). Nature Publishing Group. https://doi.org/10.1038/s41573-020-0071-y

Möckl, L. (2020). The Emerging Role of the Mammalian Glycocalyx in Functional Membrane Organization and Immune System Regulation. In *Frontiers in Cell and Developmental Biology*. https://doi.org/10.3389/fcell.2020.00253

Mondal, A., Ashiq, K. A., Phulpagar, P., Singh, D. K., & Shiras, A. (2019). Effective Visualization and Easy Tracking of Extracellular Vesicles in Glioma Cells. *Biological Procedures Online 2019 21:1*, *21*(1), 1–12. https://doi.org/10.1186/S12575-019-0092-2

Morgan, L., Shah, B., Rivers, L. E., Barden, L., Groom, A. J., Chung, R., Higazi, D., Desmond, H., Smith, T., & Staddon, J. M. (2007). Inflammation and dephosphorylation of the tight junction protein occludin in an experimental model of multiple sclerosis. *Neuroscience*, *147*(3), 664–673. https://doi.org/10.1016/j.neuroscience.2007.04.051

Müller, K., Courtois, G., Ursini, M. V., & Schwaninger, M. (2017). New Insight into the Pathogenesis of Cerebral Small-Vessel Diseases. *Stroke*, *48*(2), 520–527. https://doi.org/10.1161/STROKEAHA.116.012888

Murakami, T., Felinski, E. A., & Antonetti, D. A. (2009). Occludin phosphorylation and ubiquitination regulate tight junction trafficking and vascular endothelial growth factor-induced permeability. *Journal of Biological Chemistry*, *284*(31), 21036–21046. https://doi.org/10.1074/jbc.M109.016766

Nenci, A., Becker, C., Wullaert, A., Gareus, R., Van Loo, G., Danese, S., Huth, M., Nikolaev, A., Neufert, C., Madison, B., Gumucio, D., Neurath, M. F., & Pasparakis, M. (2007). Epithelial NEMO links innate immunity to chronic intestinal inflammation. *Nature*, *446*(7135), 557–561. https://doi.org/10.1038/nature05698

Nenci, A., Huth, M., Funteh, A., Schmidt-Supprian, M., Bloch, W., Metzger, D., Chambon, P., Rajewsky, K., Krieg, T., Haase, I., & Pasparakis, M. (2006). Skin lesion development in a mouse model of incontinentia pigmenti is triggered by NEMO deficiency in epidermal keratinocytes and requires TNF signaling. *Human Molecular Genetics*, *15*(4), 531–542. https://doi.org/10.1093/hmg/ddi470

Newton, K, Dugger, D. L., Maltzman, A., Greve, J. M., Hedehus, M., Martin-McNulty, B., Carano, R. A. D., Cao, T. C., Bruggen, N. van, Bernstein, L., Lee, W. P., Wu, X., DeVoss, J., Zhang, J., Jeet, S., Peng, I., McKenzie, B. S., Roose-Girma, M., Caplazi, P., … Vucic, D. (2016). RIPK3 deficiency or catalytically inactive RIPK1 provides greater benefit than MLKL deficiency in mouse models of inflammation and tissue injury. *Cell Death and Differentiation*, *23*(9), 1565. https://doi.org/10.1038/CDD.2016.46

Newton, Kim. (2020). Multitasking kinase ripk1 regulates cell death and inflammation. *Cold Spring Harbor Perspectives in Medicine*, *10*(3). https://doi.org/10.1101/cshperspect.a036368

Newton, Kim, Sun, X., & Dixit, V. M. (2004). Kinase RIP3 Is Dispensable for Normal NF-κBs, Signaling by the B-Cell and T-Cell Receptors, Tumor Necrosis Factor Receptor 1, and Toll-Like Receptors 2 and 4. *Molecular and Cellular Biology*, *24*(4), 1464–1469. https://doi.org/10.1128/mcb.24.4.1464-1469.2004

Nguyen, L. N., Ma, D., Shui, G., Wong, P., Cazenave-Gassiot, A., Zhang, X., Wenk, M. R., Goh, E. L. K., & Silver, D. L. (2014). Mfsd2a is a transporter for the essential omega-3 fatty acid docosahexaenoic acid. *Nature*, *509*(7501), 503–506. https://doi.org/10.1038/nature13241

Nitta, T., Hata, M., Gotoh, S., Seo, Y., Sasaki, H., Hashimoto, N., Furuse, M., & Tsukita, S. (2003). Size-selective loosening of the blood-brain barrier in claudin-5-deficient mice. *Journal of Cell Biology*, *161*(3), 653–660. https://doi.org/10.1083/jcb.200302070

Ober, R. J., Martinez, C., Vaccaro, C., Zhou, J., & Ward, E. S. (2004). Visualizing the Site and Dynamics of IgG Salvage by the MHC Class I-Related Receptor, FcRn. *The Journal of Immunology*, *172*(4), 2021–2029. https://doi.org/10.4049/JIMMUNOL.172.4.2021

Obermeier, B., Daneman, R., & Ransohoff, R. M. (2013). Development, maintenance and disruption of the blood-brain barrier. In *Nature Medicine* (Vol. 19, Issue 12, pp. 1584–1596). https://doi.org/10.1038/nm.3407

Odrljin, T. M., Haidaris, C. G., Lerner, N. B., & Simpson-Haidaris, P. J. (2001). Integrin v 3-Mediated Endocytosis of Immobilized Fibrinogen by A549 Lung Alveolar Epithelial Cells. *Am. J. Respir. Cell Mol. Biol*, *24*, 12–21. www.atsjournals.org

Oeckinghaus, A., & Ghosh, S. (2009). The NF-kappaB family of transcription factors and its regulation. In *Cold Spring Harbor perspectives in biology* (Vol. 1, Issue 4). Cold Spring Harbor Laboratory Press. https://doi.org/10.1101/cshperspect.a000034

Pantoni, L. (2010). Cerebral small vessel disease: from pathogenesis and clinical characteristics to therapeutic challenges. *The Lancet Neurology*, *9*(7), 689–701. https://doi.org/10.1016/S1474-4422(10)70104-6

Pardridge, W. M. (2002). Drug and Gene Delivery to the Brain: The Vascular Route. *Neuron*, *36*(4), 555–558. https://doi.org/10.1016/S0896-6273(02)01054-1

Pasparakis, M, Luedde, T., & Schmidt-Supprian, M. (2006). Dissection of the NF-κB signalling cascade in transgenic and knockout mice. In *Cell Death and Differentiation* (Vol. 13, Issue 5, pp. 861–872). Nature Publishing Group. https://doi.org/10.1038/sj.cdd.4401870

Pasparakis, Manolis, & Vandenabeele, P. (2015). Necroptosis and its role in inflammation. In *Nature* (Vol. 517, Issue 7534, pp. 311–320). Nature Publishing Group. https://doi.org/10.1038/nature14191

Pescatore, A., Esposito, E., Draber, P., Walczak, H., & Ursini, M. V. (2016). NEMO regulates a cell death switch in TNF signaling by inhibiting recruitment of ripk3 to the cell death-inducing complex II. *Cell Death and Disease*, *7*(8), e2346–e2346. https://doi.org/10.1038/cddis.2016.245

Petersen, M. A., Ryu, J. K., & Akassoglou, K. (2018). Fibrinogen in neurological diseases: mechanisms, imaging and therapeutics. *Nature Reviews. Neuroscience*, *19*(5), 283. https://doi.org/10.1038/NRN.2018.13

Pierre, K., Pellerin, L., Debernardi, R., Riederer, B. M., & Magistretti, P. J. (2000). Cell-specific localization of monocarboxylate transporters, MCT1 and MCT2, in the adult mouse brain revealed by double immunohistochemical labeling and confocal microscopy. *Neuroscience*, *100*(3), 617–627. https://doi.org/10.1016/S0306-4522(00)00294-3

Polykratis, A., Hermance, N., Zelic, M., Roderick, J., Kim, C., Van, T.-M., Lee, T. H., Chan, F. K. M., Pasparakis, M., & Kelliher, M. A. (2014). Cutting Edge: RIPK1 Kinase Inactive Mice Are Viable and Protected from TNF-Induced Necroptosis In Vivo. *The Journal of Immunology*, *193*(4), 1539–1543. https://doi.org/10.4049/jimmunol.1400590

Poole, R. C., & Halestrap, A. P. (1993). Transport of lactate and other monocarboxylates across mammalian plasma membranes. *The American Journal of Physiology*, *264*(4 Pt 1), C761-82. http://eutils.ncbi.nlm.nih.gov/entrez/eutils/elink.fcgi?dbfrom=pubmed&id=8476015&retmode=ref&cmd=prlinks%5Cnpapers2://publication/uuid/4E583622-CA11-4A50-A331-052F5CD8276B

Poziomczyk, C. S., Maria, F. D. S., Freitas, A. M., Fiegenbaum, M., Bau, A. E. K., Recuero, J. K., Campos, C. W., Maahs, M. A. P., De Almeida, S. T., Bringhenti, L., Travi, G. M., Zen, P. R. G., & Bonamigo, R. R. (2014). Incontinentia pigmenti. *Anais Brasileiros de Dermatologia*, *89*(1), 26–36. https://doi.org/10.1590/abd1806-4841.20142584

Preston, J. E., Joan Abbott, N., & Begley, D. J. (2014). Transcytosis of macromolecules at the blood-brain barrier. In *Advances in Pharmacology* (Vol. 71, pp. 147–163). Academic Press Inc. https://doi.org/10.1016/bs.apha.2014.06.001

Pulgar, V. M. (2019). Transcytosis to Cross the Blood Brain Barrier, New Advancements and Challenges. *Frontiers in Neuroscience*, *0*(JAN), 1019. https://doi.org/10.3389/FNINS.2018.01019

Qin, W., Li, J., Zhu, R., Gao, S., Fan, J., Xia, M., Zhao, R. C., & Zhang, J. (2019). Melatonin protects blood-brain barrier integrity and permeability by inhibiting matrix metalloproteinase-9 via the NOTCH3/NF-kB pathway. *Aging*, *11*(23), 11391–11415. https://doi.org/10.18632/aging.102537

Rahighi, S., Ikeda, F., Kawasaki, M., Akutsu, M., Suzuki, N., Kato, R., Kensche, T., Uejima, T., Bloor, S., Komander, D., Randow, F., Wakatsuki, S., & Dikic, I. (2009). Specific Recognition of Linear Ubiquitin Chains by NEMO Is Important for NF-κB Activation. *Cell*, *136*(6), 1098–1109. https://doi.org/10.1016/J.CELL.2009.03.007

Ramos, E. M., Oliveira, J., Sobrido, M. J., & Coppola, G. (2017). Primary Familial Brain Calcification. *GeneReviews®*. https://www.ncbi.nlm.nih.gov/books/NBK1421/

Ranjan, K., & Pathak, C. (2016). FADD regulates NF-κB activation and promotes ubiquitination of cFLIP L to induce apoptosis. *Scientific Reports*, *6*. https://doi.org/10.1038/srep22787

Reese, T. S., & Karnovsky, M. J. (1967). Fine structural localization of a blood-brain barrier to exogenous peroxidase. *Journal of Cell Biology*, *34*(1), 207–217. https://doi.org/10.1083/jcb.34.1.207

Reeson, P., Choi, K., & Brown, C. E. (2018). VEGF signaling regulates the fate of obstructed capillaries in mouse cortex. *ELife*. https://doi.org/10.7554/eLife.33670

Reinecke, R. D., Kuwabara, T., Cogan, D. G., & Weis, D. R. (1962). Retinal Vascular Patterns: Part V: Experimental Ischemia of the Cat Eye. *Archives of Ophthalmology*, *67*(4), 470–475. https://doi.org/10.1001/archopht.1962.00960020470015

Renner, F., & Schmitz, M. L. (2009). Autoregulatory feedback loops terminating the NF-κB response. In *Trends in Biochemical Sciences* (Vol. 34, Issue 3, pp. 128–135). https://doi.org/10.1016/j.tibs.2008.12.003

Reynolds, A. B., Herbert, L., Cleveland, J. L., Berg, S. T., & Gaut, J. R. (1992). P120, a novel substrate of protein tyrosine kinase receptors and of p60(v-src) is related to cadherin-binding factors β-catenin, plakoglobin and armadillo. *Oncogene*, *7*(12), 2439–2445. https://pubmed.ncbi.nlm.nih.gov/1334250/

Ridder, D. A., Lang, M.-F., Salinin, S., Röderer, J.-P., Struss, M., Maser-Gluth, C., & Schwaninger, M. (2011). TAK1 in brain endothelial cells mediates fever and lethargy. *The Journal of Experimental Medicine*. https://doi.org/10.1084/jem.20110398

Ridder, D. A., Wenzel, J., Müller, K., Töllner, K., Tong, X.-K., Assmann, J. C., Stroobants, S., Weber, T., Niturad, C., Fischer, L., Lembrich, B., Wolburg, H., Grand'Maison, M., Papadopoulos, P., Korpos, E., Truchetet, F., Rades, D., Sorokin, L. M., Schmidt-Supprian, M., … Schwaninger, M. (2015). Brain endothelial TAK1 and NEMO safeguard the neurovascular unit. *The Journal of Experimental Medicine*, *212*(10), 1529–1549. https://doi.org/10.1084/jem.20150165

Rizzo, M. T., & Leaver, H. A. (2010). Brain endothelial cell death: Modes, signaling pathways, and relevance to neural development, homeostasis, and disease. In *Molecular Neurobiology*. https://doi.org/10.1007/s12035-010-8132-6

Ruano-Salguero, J. S., & Lee, K. H. (2020). Antibody transcytosis across brain endothelial-like cells occurs nonspecifically and independent of FcRn. *Scientific Reports*, *10*(1). https://doi.org/10.1038/s41598-020-60438-z

Rüffer, C., & Gerke, V. (2004). The C-terminal cytoplasmic tail of claudins 1 and 5 but not its PDZ-binding motif is required for apical localization at epithelial and endothelial tight junctions. *European Journal of Cell Biology*, *83*(4), 135–144. https://doi.org/10.1078/0171-9335-00366

Saitou, M., Furuse, M., Sasaki, H., Schulzke, J.-D., Fromm, M., Takano, H., Noda, T., & Tsukita, S. (2000). Complex Phenotype of Mice Lacking Occludin, a Component of Tight Junction Strands. *Molecular Biology of the Cell*, *11*(12), 4131–4142. https://doi.org/10.1091/mbc.11.12.4131

Salhia, B., Angelov, L., Roncari, L., Wu, X., Shannon, P., & Guha, a. (2000). Expression of vascular endothelial growth factor by reactive astrocytes and associated neoangiogenesis. *Brain Research*, *883*(1), 87–97. http://www.ncbi.nlm.nih.gov/pubmed/11063991

Samson, A. L., Zhang, Y., Geoghegan, N. D., Gavin, X. J., Davies, K. A., Mlodzianoski, M. J., Whitehead, L. W., Frank, D., Garnish, S. E., Fitzgibbon, C., Hempel, A., Young, S. N., Jacobsen, A. V., Cawthorne, W., Petrie, E. J., Faux, M. C., Shield-Artin, K., Lalaoui, N., Hildebrand, J. M., … Murphy, J. M. (2020). MLKL trafficking and accumulation at the plasma membrane control the kinetics and threshold for necroptosis. *Nature Communications 2020 11:1*, *11*(1), 1–17. https://doi.org/10.1038/s41467-020-16887-1

Sano, F., Shigetomi, E., Shinozaki, Y., Tsuzukiyama, H., Saito, K., Mikoshiba, K., Horiuchi, H., Cheung, D. L., Nabekura, J., Sugita, K., Aihara, M., & Koizumi, S. (2021). Reactive astrocyte-driven epileptogenesis is induced by microglia initially activated following status epilepticus. *JCI Insight*, *6*(9). https://doi.org/10.1172/JCI.INSIGHT.135391

Saraste, A., & Pulkki, K. (2000). Morphologic and biochemical hallmarks of apoptosis. In *Cardiovascular Research* (Vol. 45, Issue 3, pp. 528–537). Oxford Academic. https://doi.org/10.1016/S0008-6363(99)00384-3

Sasaki, Y., Derudder, E., Hobeika, E., Pelanda, R., Reth, M., Rajewsky, K., & Schmidt-Supprian, M. (2006). Canonical NF-κB Activity, Dispensable for B Cell Development, Replaces BAFF-Receptor Signals and Promotes B Cell Proliferation upon Activation. *Immunity*, *24*(6), 729–739. https://doi.org/10.1016/j.immuni.2006.04.005

Schlachetzki, F., Zhu, C., & Pardridge, W. M. (2002). Expression of the neonatal Fc receptor (FcRn) at the blood-brain barrier. *Journal of Neurochemistry*. https://doi.org/10.1046/j.1471-4159.2002.00840.x

Schock, S. N., Young, J. A., He, T. H., Sun, Y., & Winoto, A. (2015). Deletion of FADD in macrophages and granulocytes results in RIP3- and MyD88-dependent systemic inflammation. *PLoS ONE*, *10*(4). https://doi.org/10.1371/journal.pone.0124391

Schreiber, S., Bueche, C. Z., Garz, C., & Braun, H. (2013). Blood brain barrier breakdown as the starting point of cerebral small vessel disease? - New insights from a rat model. *Experimental and Translational Stroke Medicine*, *5*(1), 1–8. https://doi.org/10.1186/2040-7378-5-4/FIGURES/2

Seifert, L., Werba, G., Tiwari, S., Giao Ly, N. N., Alothman, S., Alqunaibit, D., Avanzi, A., Barilla, R., Daley, D., Greco, S. H., Torres-Hernandez, A., Pergamo, M., Ochi, A., Zambirinis, C. P., Pansari, M., Rendon, M., Tippens, D., Hundeyin, M., Mani, V. R., … Miller, G. (2016). The necrosome promotes pancreatic oncogenesis via CXCL1 and Mincle-induced immune suppression. *Nature*. https://doi.org/10.1038/nature17403

Shembade, N., & Harhaj, E. W. (2012). Regulation of NF-κB signaling by the A20 deubiquitinase. In *Cellular and Molecular Immunology* (Vol. 9, Issue 2, pp. 123–130). Nature Publishing Group. https://doi.org/10.1038/cmi.2011.59

Shen, J., Xu, G., Zhu, R., Yuan, J., Ishii, Y., Hamashima, T., Matsushima, T., Yamamoto, S., Takatsuru, Y., Nabekura, J., & Sasahara, M. (2019). PDGFR-β restores blood-brain barrier functions in a mouse model of focal cerebral ischemia. *Journal of Cerebral Blood Flow and Metabolism*, *39*(8), 1501–1515. https://doi.org/10.1177/0271678X18769515

Shi, Y., Zhang, L., Pu, H., Mao, L., Hu, X., Jiang, X., Xu, N., Stetler, R. A., Zhang, F., Liu, X., Leak, R. K., Keep, R. F., Ji, X., & Chen, J. (2016). Rapid endothelial cytoskeletal reorganization enables early blood-brain barrier disruption and long-term ischaemic reperfusion brain injury. *Nature Communications*, *7*. https://doi.org/10.1038/ncomms10523

Shibamoto, S., Hayakawa, M., Takeuchi, K., Hori, T., Miyazawa, K., Kitamura, N., Johnson, K. R., Wheelock, M. J., Matsuyoshi, N., Takeichi, M., & Ito, F. (1995). Association of p120, a tyrosine kinase substrate, with E-cadherin/catenin complexes. *Journal of Cell Biology*, *128*(5), 949–957. https://doi.org/10.1083/jcb.128.5.949

Shibata, M., Yamada, S., Ram Kumar, S., Calero, M., Bading, J., Frangione, B., Holtzman, D. M., Miller, C. A., Strickland, D. K., Ghiso, J., & Zlokovic, B. V. (2000). Clearance of Alzheimer's amyloid-β1-40 peptide from brain by LDL receptor-related protein-1 at the blood-brain barrier. *Journal of Clinical Investigation*, *106*(12), 1489–1499. https://doi.org/10.1172/JCI10498

Shpetner, H. S., & Vallee, R. B. (1989). Identification of dynamin, a novel mechanochemical enzyme that mediates interactions between microtubules. *Cell*. https://doi.org/10.1016/0092-8674(89)90027-5

Silva, M. T., Do Vale, A., & Dos Santos, N. M. N. (2008). Secondary necrosis in multicellular animals: An outcome of apoptosis with pathogenic implications. In *Apoptosis* (Vol. 13, Issue 4, pp. 463–482). Springer. https://doi.org/10.1007/s10495-008-0187-8

Sofroniew, M. V. (2015). Astrogliosis. *Cold Spring Harbor Perspectives in Biology*, *7*(2). https://doi.org/10.1101/cshperspect.a020420

Song, J., Choi, S. M., Whitcomb, D. J., & Kim, B. C. (2017). Adiponectin controls the apoptosis and the expression of tight junction proteins in brain endothelial cells through AdipoR1 under beta amyloid toxicity. *Cell Death and Disease*, *8*(10), 3102. https://doi.org/10.1038/cddis.2017.491

St-Amour, I., Paré, I., Alata, W., Coulombe, K., Ringuette-Goulet, C., Drouin-Ouellet, J., Vandal, M., Soulet, D., Bazin, R., & Calon, F. (2013). Brain bioavailability of human intravenous immunoglobulin and its transport through the murine blood–brain barrier. *Journal of Cerebral Blood Flow & Metabolism*, *33*(12), 1983. https://doi.org/10.1038/JCBFM.2013.160

Stamatovic, S. M., Sladojevic, N., Keep, R. F., & Andjelkovic, A. V. (2012). Relocalization of junctional adhesion molecule A during inflammatory stimulation of brain endothelial cells. *Molecular and Cellular Biology*, *32*(17), 3414–3427. https://doi.org/10.1128/MCB.06678-11

Stewart, P. A. (2000). Endothelial vesicles in the blood-brain barrier: Are they related to permeability? In *Cellular and Molecular Neurobiology* (Vol. 20, Issue 2, pp. 149–163). https://doi.org/10.1023/A:1007026504843

Storck, S. E., Meister, S., Nahrath, J., Meißner, J. N., Schubert, N., Spiezio, A. Di, Baches, S., Vandenbroucke, R. E., Bouter, Y., Prikulis, I., Korth, C., Weggen, S., Heimann, A., Schwaninger, M., Bayer, T. A., & Pietrzik, C. U. (2016). Endothelial LRP1 transports amyloid-β1–42 across the blood-brain barrier. *The Journal of Clinical Investigation*, *126*(1), 123–136. https://doi.org/10.1172/JCI81108

Sun, S. C. (2017). The non-canonical NF-κB pathway in immunity and inflammation. In *Nature Reviews Immunology* (Vol. 17, Issue 9, pp. 545–558). Nature Publishing Group. https://doi.org/10.1038/nri.2017.52

Sweeney, M. D., Sagare, A. P., & Zlokovic, B. V. (2018). Blood-brain barrier breakdown in Alzheimer disease and other neurodegenerative disorders. In *Nature Reviews Neurology* (Vol. 14, Issue 3, pp. 133–150). Nat Rev Neurol. https://doi.org/10.1038/nrneurol.2017.188

Tabruyn, S. P., & Griffioen, A. W. (2008). NF-κB: a new player in angiostatic therapy. *Angiogenesis*, *11*(1), 101. https://doi.org/10.1007/S10456-008-9094-4

Tabruyn, S. P., Mémet, S., Avé, P., Verhaeghe, C., Mayo, K. H., Struman, I., Martial, J. A., & Griffioen, A. W. (2009). NF-κB activation in endothelial cells is critical for the activity of angiostatic agents. *Molecular Cancer Therapeutics*, *8*(9), 2645–2654. https://doi.org/10.1158/1535-7163.MCT-09-0383

Takaesu, G., Surabhi, R. M., Park, K. J., Ninomiya-Tsuji, J., Matsumoto, K., & Gaynor, R. B. (2003). TAK1 is critical for IκB kinase-mediated activation of the NF-κB pathway. *Journal of Molecular Biology*. https://doi.org/10.1016/S0022-2836(02)01404-3

Takata, F., Dohgu, S., Matsumoto, J., Takahashi, H., Machida, T., Wakigawa, T., Harada, E., Miyaji, H., Koga, M., Nishioku, T., Yamauchi, A., & Kataoka, Y. (2011). Brain pericytes among cells constituting the blood-brain barrier are highly sensitive to tumor necrosis factor-α, releasing matrix metalloproteinase-9 and migrating in vitro. *Journal of Neuroinflammation*, *8*(1), 106. https://doi.org/10.1186/1742-2094-8-106

Tang, S. C., Lagas, J. S., Lankheet, N. A. G., Poller, B., Hillebrand, M. J., Rosing, H., Beijnen, J. H., & Schinkel,

A. H. (2012). Brain accumulation of sunitinib is restricted by P-glycoprotein (ABCB1) and breast cancer resistance protein (ABCG2) and can be enhanced by oral elacridar and sunitinib coadministration. *International Journal of Cancer*, *130*(1), 223–233. https://doi.org/10.1002/ijc.26000

Teichert, M., Milde, L., Holm, A., Stanicek, L., Gengenbacher, N., Savant, S., Ruckdeschel, T., Hasanov, Z., Srivastava, K., Hu, J., Hertel, S., Bartol, A., Schlereth, K., & Augustin, H. G. (2017). Pericyte-expressed Tie2 controls angiogenesis and vessel maturation. *Nature Communications*, *8*. https://doi.org/10.1038/ncomms16106

Tian, X., Leite, D. M., Scarpa, E., Nyberg, S., Fullstone, G., Forth, J., Matias, D., Apriceno, A., Poma, A., Duro-Castano, A., Vuyyuru, M., Harker-Kirschneck, L., Šarić, A., Zhang, Z., Xiang, P., Fang, B., Tian, Y., Luo, L., Rizzello, L., & Battaglia, G. (2020). On the shuttling across the blood-brain barrier via tubule formation: Mechanism and cargo avidity bias. *Science Advances*, *6*(48), 4397–4424. https://doi.org/10.1126/sciadv.abc4397

Tornavaca, O., Chia, M., Dufton, N., Almagro, L. O., Conway, D. E., Randi, A. M., Schwartz, M. A., Matter, K., & Balda, M. S. (2015). ZO-1 controls endothelial adherens junctions, cell-cell tension, angiogenesis, and barrier formation. *Journal of Cell Biology*, *208*(6), 821–838. https://doi.org/10.1083/jcb.201404140

Traweger, A., Fang, D., Liu, Y. C., Stelzhammer, W., Krizbai, I. A., Fresser, F., Bauer, H. C., & Bauer, H. (2002). The tight junction-specific protein occludin is a functional target of the E3 ubiquitin-protein ligase itch. *Journal of Biological Chemistry*, *277*(12), 10201–10208. https://doi.org/10.1074/jbc.M111384200

Tsuge, M., Yasui, K., Ichiyawa, T., Saito, Y., Nagaoka, Y., Yashiro, M., Yamashita, N., & Morishima, T. (2010). Increase of tumor necrosis factor-α in the blood induces early activation of matrix metalloproteinase-9 in the brain. *Microbiology and Immunology*, *54*(7), 417–424. https://doi.org/10.1111/j.1348-0421.2010.00226.x

Tu, J., Fang, Y., Han, D., Tan, X., Jiang, H., Gong, X., Wang, X., Hong, W., & Wei, W. (2021). Activation of nuclear factor-κB in the angiogenesis of glioma: Insights into the associated molecular mechanisms and targeted therapies. *Cell Proliferation*, *54*(2), e12929. https://doi.org/10.1111/CPR.12929

Tuma, P. L., & Hubbard, A. L. (2003). Transcytosis: Crossing cellular barriers. In *Physiological Reviews* (Vol. 83, Issue 3, pp. 871–932). American Physiological Society. https://doi.org/10.1152/physrev.00001.2003

Tummers, B., & Green, D. R. (2017). Caspase-8; regulating life and death. *Immunological Reviews*, *277*(1), 76. https://doi.org/10.1111/IMR.12541

Uemura, M. T., Maki, T., Ihara, M., Lee, V. M. Y., & Trojanowski, J. Q. (2020). Brain Microvascular Pericytes in Vascular Cognitive Impairment and Dementia. *Frontiers in Aging Neuroscience*, *12*, 80. https://doi.org/10.3389/FNAGI.2020.00080

Valerio, A., Boroni, F., Benarese, M., Sarnico, I., Ghisi, V., Bresciani, L. G., Ferrario, M., Borsani, G., Spano, P., & Pizzi, M. (2006). NF-kappaB pathway: a target for preventing beta-amyloid (Abeta)-induced neuronal damage and Abeta42 production. *The European Journal of Neuroscience*, *23*(7), 1711–1720. https://doi.org/10.1111/J.1460-9568.2006.04722.X

van den Brink, G. R., ten Kate, F. J., Ponsioen, C. Y., Rive, M. M., Tytgat, G. N., van Deventer, S. J. H., & Peppelenbosch, M. P. (2000). Expression and Activation of NF-κB in the Antrum of the Human Stomach. *The Journal of Immunology*, *164*(6), 3353–3359. https://doi.org/10.4049/jimmunol.164.6.3353

Van, T. M., Polykratis, A., Straub, B. K., Kondylis, V., Papadopoulou, N., & Pasparakis, M. (2017). Kinase-independent functions of RIPK1 regulate hepatocyte survival and liver carcinogenesis. *Journal of Clinical Investigation*, *127*(7), 2662–2677. https://doi.org/10.1172/JCI92508

Varga, I., Ghallab, A., & Danisovic, L. (2020). LETTER TO THE EDITOR Artifacts in Electron Microscopic Research. *Physiol. Res*, *69*(4), 405–413. www.biomed.cas.cz/physiolres

Villaseñor, R., Kuennecke, B., Ozmen, L., Ammann, M., Kugler, C., Grüninger, F., Loetscher, H., Freskgård, P. O., & Collin, L. (2017). Region-specific permeability of the blood–brain barrier upon pericyte loss. *Journal of Cerebral Blood Flow and Metabolism*, *37*(12), 3683–3694. https://doi.org/10.1177/0271678X17697340

Villaseñor, R., Lampe, J., Schwaninger, M., & Collin, L. (2019). Intracellular transport and regulation of transcytosis across the blood–brain barrier. In *Cellular and Molecular Life Sciences*. https://doi.org/10.1007/s00018-018-2982-x

Villasenõr, R., Ozmen, L., Messaddeq, N., Grüninger, F., Loetscher, H., Keller, A., Betsholtz, C., Freskgård, P. O., & Collin, L. (2016). Trafficking of Endogenous Immunoglobulins by Endothelial Cells at the Blood-Brain Barrier. *Scientific Reports*. https://doi.org/10.1038/srep25658

Villaseñor, R., Schilling, M., Sundaresan, J., Lutz, Y., & Collin, L. (2017). Sorting Tubules Regulate Blood-Brain Barrier Transcytosis. *Cell Reports*, *21*(11), 3256–3270. https://doi.org/10.1016/j.celrep.2017.11.055

Vlantis, K., Wullaert, A., Polykratis, A., Kondylis, V., Dannappel, M., Schwarzer, R., Welz, P., Corona, T., Walczak, H., Weih, F., Klein, U., Kelliher, M., & Pasparakis, M. (2016). NEMO Prevents RIP Kinase 1-Mediated Epithelial Cell Death and Chronic Intestinal Inflammation by NF-κB-Dependent and -Independent Functions. *Immunity*, *44*(3), 553–567. https://doi.org/10.1016/j.immuni.2016.02.020

Wang, Q., Zhou, T., Liu, Z., Ren, J., Phan, N., Gupta, K., Stewart, D. M., Morgan, S., Assa, C., Kent, K. C., & Liu, B. (2017). Inhibition of Receptor-Interacting Protein Kinase 1 with Necrostatin-1s ameliorates disease progression in elastase-induced mouse abdominal aortic aneurysm model. *Scientific Reports*. https://doi.org/10.1038/srep42159

Wang, Y., Liu, S., Wang, J., Zhang, J., Hua, Y., Li, H., Tan, H., Kuai, B., Wang, B., & Sheng, S. (2017). Association between LRP1 C766T polymorphism and Alzheimer's disease susceptibility: a meta-analysis. *Scientific Reports 2017 7:1*, *7*(1), 1–10. https://doi.org/10.1038/s41598-017-08335-w

Wei, L., Ying, D. J., Cui, L., Langsdorf, J., & Ping Yu, S. (2004). Necrosis, apoptosis and hybrid death in the cortex and thalamus after barrel cortex ischemia in rats. *Brain Research*, *1022*(1–2), 54–61. https://doi.org/10.1016/j.brainres.2004.06.080

Wenzel, J., Lampe, J., Müller-Fielitz, H., Schuster, R., Zille, M., Müller, K., Krohn, M., Körbelin, J., Zhang, L., Özorhan, Ü., Neve, V., Wagner, J. U. G., Bojkova, D., Shumliakivska, M., Jiang, Y., Fähnrich, A., Ott, F., Sencio, V., Robil, C., … Schwaninger, M. (2021). The SARS-CoV-2 main protease Mpro causes microvascular brain pathology by cleaving NEMO in brain endothelial cells. *Nature Neuroscience 2021*, 1–12. https://doi.org/10.1038/s41593-021-00926-1

Wenzel, J., & Schwaninger, M. (2016). The blood–brain barrier and its regulation by NF-κB. *E-Neuroforum*, *7*(2), 23–30. https://doi.org/10.1007/s13295-016-0022-6

Witt, K. a, Mark, K. S., Hom, S., & Davis, T. P. (2003). Effects of hypoxia-reoxygenation on rat blood-brain barrier permeability and tight junctional protein expression. *American Journal of Physiology. Heart and Circulatory Physiology*, *285*(6), H2820--31. https://doi.org/10.1152/ajpheart.00589.2003

Wooten, M. W. (1999). Function for NF-kB in neuronal survival: Regulation by atypical protein kinase C. Journal of Neuroscience Research, 58(5), 607–611 | 10.1002/(sici)1097-4547(19991201)58:5<607::aid-jnr1>3.0.co;2-m. *Journal of Neuroscience*, 607–611. https://sci-hub.se/https://doi.org/10.1002/(SICI)1097-4547(19991201)58:5%3C607::AID-JNR1%3E3.0.CO;2-M

Xia, Y., Shen, S., & Verma, I. M. (2014). NF-κB, an active player in human cancers. In *Cancer immunology research* (Vol. 2, Issue 9, pp. 823–830). NIH Public Access. https://doi.org/10.1158/2326-6066.CIR-14-0112

Xiao, G., & Gan, L.-S. (2013). Receptor-mediated endocytosis and brain delivery of therapeutic biologics. *International Journal of Cell Biology*, *2013*, 703545. https://doi.org/10.1155/2013/703545

Xu, D., Jin, T., Zhu, H., Chen, H., Ofengeim, D., Zou, C., Mifflin, L., Pan, L., Amin, P., Li, W., Shan, B., Naito, M. G., Meng, H., Li, Y., Pan, H., Aron, L., Adiconis, X., Levin, J. Z., Yankner, B. A., & Yuan, J. (2018). TBK1 Suppresses RIPK1-Driven Apoptosis and Inflammation during Development and in Aging. *Cell*, *174*(6), 1477-1491.e19. https://doi.org/10.1016/j.cell.2018.07.041

Yang, A. C., Stevens, M. Y., Chen, M. B., Lee, D. P., Stähli, D., Gate, D., Contrepois, K., Chen, W., Iram, T., Zhang, L., Vest, R. T., Chaney, A., Lehallier, B., Olsson, N., du Bois, H., Hsieh, R., Cropper, H. C., Berdnik, D., Li, L., … Wyss-Coray, T. (2020). Physiological blood–brain transport is impaired with age by a shift in transcytosis. *Nature*, *583*(7816), 425–430. https://doi.org/10.1038/s41586-020-2453-z

Yang, P., Pavlovic, D., Waldvogel, H., Dragunow, M., Synek, B., Turner, C., Faull, R., & Guan, J. (2015). String vessel formation is increased in the brain of Parkinson disease. *Journal of Parkinson's Disease*, *5*(4), 821–836. https://doi.org/10.3233/JPD-140454

Yang, Y., Estrada, E. Y., Thompson, J. F., Liu, W., & Rosenberg, G. A. (2007). Matrix metalloproteinase-mediated disruption of tight junction proteins in cerebral vessels is reversed by synthetic matrix metalloproteinase inhibitor in focal ischemia in rat. *Journal of Cerebral Blood Flow and Metabolism*, *27*(4), 697–709. https://doi.org/10.1038/sj.jcbfm.9600375

Yeh, W., JL, de la P., ME, M., HB, S., AJ, E., A, S., M, N., A, W., W, K., K, M., WS, E.-D., SW, L., DV, G., & TW, M. (1998). FADD: essential for embryo development and signaling from some, but not all, inducers of apoptosis. *Science (New York, N.Y.)*, *279*(5358), 1954–1958. https://doi.org/10.1126/SCIENCE.279.5358.1954

You, W. C., Wang, C. X., Pan, Y. X., Zhang, X., Zhou, X. M., Zhang, X. S., Shi, J. X., & Zhou, M. L. (2013). Activation of Nuclear Factor-κB in the Brain after Experimental Subarachnoid Hemorrhage and Its Potential Role in Delayed Brain Injury. *PLoS ONE*, *8*(3). https://doi.org/10.1371/journal.pone.0060290

Yu, H., Lin, L., Zhang, Z., Zhang, H., & Hu, H. (2020). Targeting NF-κB pathway for the therapy of diseases: mechanism and clinical study. In *Signal Transduction and Targeted Therapy* (Vol. 5, Issue 1, pp. 1–23). Springer Nature. https://doi.org/10.1038/s41392-020-00312-6

Yuan, Liu, K. J., & Qi, Z. (2020). Occludin regulation of blood–brain barrier and potential therapeutic target in ischemic stroke. *Brain Circulation*, *6*(3), 152. https://doi.org/10.4103/BC.BC_29_20

Zandi, E., Rothwarf, D. M., Delhase, M., Hayakawa, M., & Karin, M. (1997). The IκB kinase complex (IKK) contains two kinase subunits, IKKα and IKKβ, necessary for Iκb phosphorylation and NF-κB activation. *Cell*. https://doi.org/10.1016/S0092-8674(00)80406-7

Zarb, Y., Franzoso, F. D., & Keller, A. (2019). Pericytes in Primary Familial Brain Calcification. In *Advances in Experimental Medicine and Biology* (Vol. 1147, pp. 247–264). Adv Exp Med Biol. https://doi.org/10.1007/978-3-030-16908-4_11

Zhang, Yanlu, Xiong, Y., Mahmood, A., Zhang, Z. G., & Chopp, M. (2014). Angiogenesis and functional recovery after traumatic brain injury. In *Vascular Mechanisms in CNS Trauma* (pp. 141–156). Springer, New York, NY. https://doi.org/10.1007/978-1-4614-8690-9_8

Zhang, Yuan, Li, X., Qiao, S., Yang, D., Li, Z., Xu, J., Li, W., Su, L., & Liu, W. (2021). Occludin degradation makes brain microvascular endothelial cells more vulnerable to reperfusion injury in vitro. *Journal of Neurochemistry*, *156*(3), 352–366. https://doi.org/10.1111/jnc.15102

Zhang, Yun, & Pardridge, W. M. (2001). Mediated efflux of IgG molecules from brain to blood across the blood–brain barrier. *Journal of Neuroimmunology*, *114*(1–2), 168–172. https://doi.org/10.1016/S0165-5728(01)00242-9

Zhao, Q., Yu, X. J., Zhang, H. W., Liu, Y. B., Zhang, X. X., Wu, X. X., Xie, Q., Li, M., Ying, H., & Zhang, H. (2017). RIPK3 Mediates Necroptosis during Embryonic Development and Postnatal Inflammation in Fadd-Deficient Mice. *Cell Reports*, *19*(4), 798–808. https://doi.org/10.1016/j.celrep.2017.04.011

Zheng, P. P., Romme, E., Van Der Spek, P. J., Dirven, C. M. F., Willemsen, R., & Kros, J. M. (2010). Glut1/SLC2A1 is crucial for the development of the blood-brain barrier in vivo. *Annals of Neurology*, *68*(6), 835–844. https://doi.org/10.1002/ana.22318

Zhivotovsky, B., & Orrenius, S. (2001). Current Concepts in Cell Death. *Current Protocols in Cell Biology*, *11*(1). https://doi.org/10.1002/0471143030.cb1801s11

Zhou, H. J., Qin, L., Jiang, Q., Murray, K. N., Zhang, H., Li, B., Lin, Q., Graham, M., Liu, X., Grutzendler, J., & Min, W. (2021). Caveolae-mediated Tie2 signaling contributes to CCM pathogenesis in a brain endothelial cell-specific Pdcd10-deficient mouse model. *Nature Communications 2021 12:1*, *12*(1), 1–22. https://doi.org/10.1038/s41467-020-20774-0

Zhu, H., Zhang, Y., Zhong, Y., Ye, Y., Hu, X., Gu, L., & Xiong, X. (2021). Inflammation-Mediated Angiogenesis in Ischemic Stroke. *Frontiers in Cellular Neuroscience*, *0*, 57. https://doi.org/10.3389/FNCEL.2021.652647

Zhu, J., Li, X., Yin, J., Hu, Y., Gu, Y., & Pan, S. (2018). Glycocalyx degradation leads to blood–brain barrier dysfunction and brain edema after asphyxia cardiac arrest in rats. *Journal of Cerebral Blood Flow and Metabolism*. https://doi.org/10.1177/0271678X17726062

Zhu, S., Zhang, Y., Bai, G., & Li, H. (2011). Necrostatin-1 ameliorates symptoms in R6/2 transgenic mouse model of Huntington's disease. In *Cell Death and Disease* (Vol. 2, Issue 1). https://doi.org/10.1038/cddis.2010.94

Zihni, C., Mills, C., Matter, K., & Balda, M. S. (2016). Tight junctions: From simple barriers to multifunctional molecular gates. In *Nature Reviews Molecular Cell Biology* (Vol. 17, Issue 9, pp. 564–580). Nature Publishing Group. https://doi.org/10.1038/nrm.2016.80

Zille, M., Ikhsan, M., Jiang, Y., Lampe, J., Wenzel, J., & Schwaninger, M. (2019). The impact of endothelial cell death in the brain and its role after stroke: A systematic review. In *Cell Stress*. https://doi.org/10.15698/cst2019.11.203

Zlokovic, B. V., Skundric, D. S., Segal, M. B., Lipovac, M. N., Mackic, J. B., & Davson, H. (1990). A saturable mechanism for transport of immunoglobulin G across the blood-brain barrier of the guinea pig. *Experimental Neurology*, *107*(3), 263–270. https://doi.org/10.1016/0014-4886(90)90144-H

Eidesstattliche Erklärung

Hiermit versichere ich an Eides statt, dass ich die vorliegende Dissertation ohne fremde Hilfe und ohne Benutzung anderer als der angegebenen Quellen und Hilfsmittel angefertigt und die den benutzten Quellen wörtlich oder inhaltlich entnommenen Stellen als solche kenntlich gemacht habe.

Diese Arbeit wurde in gleicher oder ähnlicher Form noch bei keinem anderen Prüfenden als Prüfungsleistung eingereicht.

Josephine Lampe

Acknowledgements/Danksagung

Ein besonderer Dank gilt zunächst Herrn Prof.Schwaninger, der mir ermöglicht hat meine Doktorarbeit in der Pharmakologie anzufertigen und mich stets mit großem Interesse und Optimismus am Nemo-Projekt unterstützt hat. Vielen Dank auch für die zahlreichen Möglichkeiten, die zu meiner wissenschaftlichen Karriere beigetragen haben, sei es der Aufenthalt bei Roche in der Schweiz, der CAJAL-Kurs in Bordeaux oder die zahlreichen anderen Seminare und Konferenzen die ich besuchen durfte. Ebenfalls bedanke ich mich bei Frau Prof. Kusche-Vihrog für die Übernahme des Zweitgutachtens und Herrn Prof. Tautz für den Prüfungsvorsitz.

Many thanks to Ludovic Collin and Roberto Villasenor for the fantastic cooperation and the amazing support when I did my internship in Basel. The time I spent in Basel led to many figures in my thesis but also helped me a lot with gaining expertise in many regards of my career.

This thesis wouldn’t have been possible without the support of all the great people in the Institute for Pharmacology. Even in times of greatest despair, the lunchbreaks with the other PhD students cheered up my mood. Many of you helped me also with experiments, advice and support in the form of enjoyable conversations, cake and chocolate. Many thanks also to Sina, Julian, Kristin and Yun – the former generation of PhD students who supported and helped me a lot when I started here – and to Ellie, who has shared an office with me for the longest time!

Daran anknüpfend möchte ich mich auch ganz herzlich bei unseren TAs Ines, Beate, Frauke und Wiebke bedanken, die mir bei vielen Experimenten geholfen haben, bei Schwierigkeiten immer eine gute Lösung (und das nicht nur im chemischen Sinne) parat haben und das Chaos aufräumen, das manchmal verursacht wird wenn viele Doktoranden im Labor arbeiten :) Vielen Dank auch an unsere Post-Docs! Besonders seien dabei Jan Wenzel und Marietta Zille erwähnt, die mich oft beim Nemo-Projekt unterstützt haben, und mir auch ansonsten mit wertvollen Tipps und Hilfe zur Seite standen.

Der Weg zur Doktorarbeit war so manches Mal stressig. Umso wichtiger waren die Auszeiten und aufmunternden Gespräche mit meinen Freunden und mit Yves. Vielen Dank auch für euer Verständnis!

Diese Doktorarbeit und mein Werdegang bis dahin wären nicht ohne meine Eltern, meine Großeltern und meiner Schwester Marie möglich gewesen. Die regelmäßige Versorgung mit „Fresspaketen“ oder das „offene Ohr“ zu jeder Zeit sind nur ein paar Dinge von der langen Liste an praktischer und emotionaler Unterstützung, die ihr geleistet habt. Danke, dass ihr immer an mich geglaubt habt!

Curriculum vitae

Josephine Lampe

Personal Profile

Date of birth: 21.05.1993
Place of birth: Parchim
Nationality: german

Education

PhD student – Institute of Pharmacology, University of Lübeck (Germany)
From 01/2017

- Project: "The NF-kappa-B essential modulator (NEMO) is crucial for the functionality of brain endothelial properties."
- Supervisor: Prof. Dr. med. Markus Schwaninger

M. Sc. Human Biology – Institute of Physiology, University of Greifswald (Germany)
02/2016-11/2016

- Final grade: 1.0
- Thesis project: „The influence of thiazide-sensitive sodium reabsorption on the progression of the tyrosine kinase inhibitor-induced arterial hypertension. "
- Supervisor: Prof. Dr. med. Olaf Grisk

B. Sc. Human Biology – Institute of Anatomy, University of Greifswald (Germany)
04/2014-09/2014

- Final grade: 1.4
- Thesis project: "The influence of angiotensin 1-7 derivatives on the brain morphology in an animal model of Huntington's disease."
- Supervisor: Prof. Dr. rer. nat. Oliver von Bohlen und Halbach

Abitur – Friedrich-Franz-Gymnasium Parchim (Germany)
08/2006-06/2011

- Final grade: 1.2

Employments and Internships

RiSE Intern - Roche Pharma Research and Early Development in Basel (Switzerland)
09/2017-06/2018

- Scientist in Neuroimmunology (Tasks: cell culture experiments, western blots, histological stainings, expansion microscopy of sections, confocal microscopy)
- Supervisors: Dr. rer. nat. Ludovic Collin, Dr. rer. nat. Roberto Villasenor

Undergraduate Teaching Assistant – Institute of Physiology, University of Greifswald (Germany)
04/2016-08/2016

- Tasks: supervision of medical students in practical seminars

Intern - Sleep Laboratory and Institute of Medical Research and Sleep Medicine Somni Bene in Schwerin (Germany)
08/2015-10/2015
- Tasks: caretaking and preparation of probands, analysis of sleep and EEG recording
- Supervisors: Dr. med. Katharina Börsch, Dr. med. Heike Benes

Student Laboratory Assistant – Institute of Physiology, University of Greifswald (Germany)
04/2015-01/2016
- Tasks: Histological stainings, qPCR
- Supervisor: Dr. rer. nat. Anna Koenen

Skills and Certificates

Laboratory
- **Microscopy:** fluorescence microscopy, confocal microscopy, expansion microscopy technique
- **Animal and human studies:** oral gavage, intraperitoneal injections, intracardiac perfusions, blood sampling and organ collection from mice; *in-vivo* studies of blood circulation and kidney function in rats; preparation and analysis of overnight polysomnography from humans, assistance tasks in clinical trials
- **Molecular biology:** cryostat and vibratome sectioning, histological stainings, brain vessel fragment isolation, cell culture and cell assays (primary cells and immortalized cell lines), real-time PCR, western blot, fluorescence-based assays
- **Certificates:** 3-week CAJAL Course on “Brain Homeostasis and neurovascular coupling” (2019), FELASA B (2015)

Software
- **Image editing software:** ImageJ, Imaris, Leica LAS, BioRender, Inkscape, Adobe Illustrator
- **Statistics:** Prism
- **Others:** Microsoft Office (Excel, Powerpoint, Word)

Communication
- **Teaching:** giving lectures and supervising internships for undergraduates, mentoring of a bachelor student
- **Scientific Writing:** participation in the certified course “Nature Master Class in Publishing and Scientific Writing.” (2019)

Languages
- **German:** native speaker
- **English:** fluent
- **French:** basic communication skills

Awards
- Science Award from the University of Lübeck (Wissenschaftspreis der Universität zu Lübeck, 2021)
- Poster award on the 8th NCCR Retreat DZHK (2019)
- PhD Oral Prize 4th European NF-κB Subunit Workshop (2018)

Publications

2021

- Wenzel, J.*, **Lampe, J.*,** Müller-Fielitz, H.*, Schuster, R., Zille, M., Müller, K., Krohn, M., Körbelin, J., Zhang, L., Özorhan, Ü., Neve, V., Wagner, J. U. G., Bojkova, D., Shumliakivska, M., Jiang, Y., Fähnrich, A., Ott, F., Sencio, V., Robil, C., … Schwaninger, M. (2021). The SARS-CoV-2 main protease Mpro causes microvascular brain pathology by cleaving NEMO in brain endothelial cells. Nature Neuroscience 2021, 1–12. https://doi.org/10.1038/s41593-021-00926-1

** = the authors contributed equally*

2020

- Jiang, Y., Müller, K., Khan, M. A., Assmann, J. C., **Lampe, J**., Kilau, K., Richter, M., Kleint, M., Ridder, D. A., Hübner, N., Schmidt-Supprian, M., Wenzel, J., & Schwaninger, M. (2020). Cerebral angiogenesis ameliorates pathological disorders in Nemo-deficient mice with small-vessel disease. Journal of Cerebral Blood Flow and Metabolism, 41(2), 219–235. https://doi.org/10.1177/0271678X20910522

2019

- Zille, M., Ikhsan, M., Jiang, Y., **Lampe, J.,** Wenzel, J., & Schwaninger, M. (2019). The impact of endothelial cell death in the brain and its role after stroke: A systematic review. In Cell Stress. https://doi.org/10.15698/cst2019.11.203

- Villaseñor, R., **Lampe, J.,** Schwaninger, M., & Collin, L. (2019). Intracellular transport and regulation of transcytosis across the blood–brain barrier. In Cellular and Molecular Life Sciences. https://doi.org/10.1007/s00018-018-2982-x

2018

- Witte, J., **Lampe, J**., Koenen, A., Urbaneck, I., Steinbach, A., Rettig, R., & Grisk, O (2018). The role of distal tubule and collecting duct sodium reabsorption in sunitinib-induced hypertension. Journal of hypertension, 36(4), 892–903. https://doi.org/10.1097/HJH.0000000000001650